Numerical and experimental studies to model and reduce the impedance in the CERN Super Proton Synchrotron (SPS)

Dissertation

zur

Erlangung des akademischen Grades
Doktor-Ingenieur (Dr.-Ing.)
der Fakultät für Informatik und Elektrotechnik
der Universität Rostock

vorgelegt von

Mario Beck, geboren am 10.08.1988 in Stuttgart Bad-Canstatt
aus Genf

Rostock, 20.12.2018

Tag der Einreichung: 20.12.2018
Tag der Verteidigung: 08.05.2019

Gutachter:

Prof. Dr. Ursula van Rienen, Universität Rostock, Deutschland
Prof. Dr. Mauro Migliorati, Università di Roma, Italien
Dr. Giovanni Rumolo, CERN, Genf, Schweiz

Abstract

Intensity-driven beam instabilities are studied in simulations with a refined impedance model and in experimental measurements for this thesis.

The High Luminosity Large Hadron Collider (HL-LHC) project at CERN aims for an increase in the integrated luminosity in the Large Hadron Collider (LHC). To achieve this goal the LHC injector chain has to be upgraded. These upgrades are summarized in the LHC Injectors Upgrade (LIU) project. The last LHC injector, the Super Proton Synchrotron (SPS), intends to accelerate beams with twice the present intensity. To successfully accelerate beams with such intensities, impedance-driven instabilities have to be studied. In accelerator physics the impedance describes the interaction between the particle beam and the accelerator. Impedances can drive beams unstable and can result in particle losses. To model these effects in the SPS its impedance model is updated and completed. An impedance model merges all design related impedance contributions of the different accelerator components. To obtain a reliable model, the included components have to be modelled realistically.

The CST PARTICLE STUDIO® code is used to further improve the model of the extraction and injection kickers impedance in the SPS. The simulations are validated by bench measurements. Also the Electrostatic Septum (ZS) in the SPS is initially characterized in terms of impedance. A scaling technique is used to determine the contribution of the whole ZS chain. Simulations show that the proposed ZS upgrade will significantly reduce its impedance contribution. These simulations are then included in the impedance model of the SPS.

The updated models include two new versions, that model the SPS impedance in the year 2018 and after the next Long Shutdown (LS2) in 2021. The models are validated by beam-based measurements in the accelerator and are then used to study observations in the SPS. The horizontal instability occurring in the SPS during high intensity operations for example, is also observed in beam dynamics simulations. This instability can be damped with higher chromaticity values. Beam dynamics simulations are used to support the initial measurements of the intensity threshold in a newly proposed configuration of the SPS, the so-called Q22 optics. The post-LIU operation of the SPS may benefit from this optics. The intensity threshold is measured in detail and is found at $N_{thr} = 2.5 \cdot 10^{11}$ ppb for a longitudinal beam emittance of $\epsilon_z = 0.32\,\mathrm{eVs}$. These values are also obtained in beam dynamics simulations.

Finally, measurements investigating the stabilizing effects of the octupole magnets on instabilities in the horizontal plane are presented.

With all this research this thesis contributes to the impedance modelling of accelerators and to their operation with high intensity beams.

Kurzfassung

Intensitätsgetriebene Strahlinstabilitäten werden in dieser Arbeit mit einem vervollständigten Impedanzmodell in Teilchensimulationen und in experimentellen Messungen untersucht.

Das High Luminosity Large Hadron Collider (HL-LHC)-Projekt am CERN hat eine Erhöhung der integrierten Luminosität im Large Hadron Collider (LHC) als Ziel. Um dieses Ziel zu erreichen müssen auch die Vorbeschleuniger des LHC aufgerüstet werden. Diese Aufrüstungen sind im LHC Injectors Upgrade (LIU)-Projekt zusammengefasst. Der direkte LHC Injektor, das Super Proton Synchrotron (SPS), soll Teilchenstrahlen mit der doppelten derzeitigen Intensität beschleunigen.

Um Strahlen mit solcher Intensität erfolgreich beschleunigen zu können müssen impedanzgetriebene Instabilitäten studiert werden. Die Impedanz beschreibt in der Beschleunigerphysik die Interaktion zwischen dem Beschleuniger und dem Teilchenstrahl. Sie kann zu einer Instabilität des Teilchenstrahls führen und dadurch zu Teilchenverlust. Um diese Effekte im SPS zu modellieren wird dessen Impedanzmodell aktualisiert und vervollständigt. Das Impedanzmodell eines Beschleunigers fasst alle konstruktionsbedingten Impedanzen der Beschleunigerkomponenten zusammen. Um ein zuverlässiges Modell zu erhalten müssen die einzelnen Komponenten realitätsnah im Modell eingebunden sein.

Die CST PARTICLE STUDIO® Software wird verwendet, um das Modell der Kickermagnete für Extraktion und Injektion im SPS zu präzisieren. Die Simulationen werden anschließend mit Labormessungen verglichen und verifiziert. Auch wird im Rahmen dieser Arbeit erstmals das Elektrostatische Septum (ZS) im SPS auf seine Impedanz untersucht. Mithilfe einer neuen Skalierungsmethode wird der komplette Beitrag des ZS zur Beschleunigerimpedanz berechnet. Simulationen zeigen, dass das vorgeschlagene ZS-Upgrade den Impedanzbeitrag bedeutend verringern wird. Diese Simulationen werden dann in das SPS Impedanzmodell integriert.

Das aktualisierte Beschleunigerimpedanzmodell führt zwei neue Versionen ein, welche das SPS im Jahr 2018 und nach der nächsten langen Abschaltung von 2019 bis 2020 modellieren. Das Modell wird durch Messungen im Beschleuniger validiert und dann verwendet, um Observationen im SPS zu verstehen. Zum Beispiel kann die Instabilität in der horizontalen Ebene, unter welcher Hochintensitätsstrahlen im SPS leiden, in Strahldynamiksimulationen reproduziert werden. Die Instabilität kann mit höheren Chromatizitätswerten stabilisiert werden. Auch werden Strahldynamiksimulationen verwendet um die Messung des Intensitätsgrenzwert in einer neu vorgeschlagenen Konfiguration des Beschleunigers, der sogenannten Q22 Optik zu

begleiten. Das Betreiben des SPS nach dem LIU-Projekt könnte eventuell durch diese Optik erleichtert werden. Der Intensitätsgrenzwert wird zum ersten Mal gründlich untersucht und bei einer Intensität von $N_{thr} = 2.5 \cdot 10^{11}$ ppb für eine longitudinale Strahlemittanz von $\epsilon_z = 0.32\,\text{eVs}$ gemessen. Diese Werte werden auch von Strahldynamiksimulationen berechnet.

Abschließend wird der Stabilisierungseffekt von Oktupolmagneten auf Instabilitäten in der horizontalen Ebene des Beschleunigers in Messungen untersucht.

Damit leistet diese Arbeit einen Beitrag, um Beschleuniger mit hohen Intensitäten betreiben zu können.

Acknowledgement

Contents

List of Figures

List of Tables

Acronyms

CERN   European Organization for Nuclear Research

PSB   Proton Synchrotron Booster

PS   Proton Synchrotron

SPS   Super Proton Synchrotron

LHC   Large Hadron Collider

LEIR   Low Energy Ion Ring

LINAC   LINear ACcelerator

HL-LHC   High Luminosity LHC

LIU   LHC Injector Upgrade

LOD   Vertical Landau Octupoles

LOE   Landau Octupoles for Extraction

LOF   Horizontal Landau Octupoles

MKP   Magnetic Injection Kicker

MKE   Magnetic Extraction Kicker

MKQ   Magnetic Tune Kicker

MKD   Magnetic Dump Kicker

ZS   Electrostatic Septa

MS   Magnetic Septa

EM   Electromagnetic

TEM   Transverse Electromagnetic

HV   High-Voltage

GND	Ground
RF	Radio Frequency
VNA	Vector Network Analyser
DUT	Device Under Test
PFN	Pulse Forming Network
TDR	Time Domain Response
LSS	Long Straight Section
LS	Long Shutdown
MAD	Methodical Accelerator Design
CST	CST STUDIO SUITE®
CST PS	CST PARTICLE STUDIO®
CST MWS	CST MICROWAVE STUDIO®
HPC	High Performance Computing
PEC	Perfect Electrical Conductor
MD	Machine Development
BPM	Beam Position Monitor
BCT	Beam Current Transformer
ISC	Indirect Space Charge
TMCI	Transverse Mode Coupling Instability
SBA	Single Bunch Approximation

1 Introduction

This thesis was carried out at the European Organization for Nuclear Research (CERN). The mission of the organisation is to perform fundamental physical research, with the aim to better understand the structure of the universe. Its main task is to provide and operate the world's largest particle accelerators. Therefore, a brief overview over accelerator technology is given in the following. After, the thesis is motivated and in the end of this chapter an outline of the thesis is given.

1.1 Technology - Particle accelerators

1.1.1 Purpose of accelerators

Accelerators are devices that increase the energy of particles, with the chief aim to create the conditions needed to study very small structures. Nowadays, they become more and more popular in medicine and industry applications, but a main purpose remains fundamental research. Particles (electrons, protons or ions) are grouped together in so-called bunches in order to be accelerated. All bunches in an accelerator form the particle beam. These beams are then collided, either against a fixed target, where the particle beam hits a block of known material, or against a beam travelling in opposite directions in a collider ring. As a product of the collisions, fundamental particles are created and examined through detectors. Hence, detectors can be described as microscopes for the smallest structures. The higher the collision energy, the smaller is the observable de Broglie wavelength λ of the fundamental particles. This can be seen from the following equation [Wie15]:

$$\lambda = \frac{h}{p} = \frac{h \cdot c}{E}. \tag{1.1}$$

Here h is the Planck constant, c is the speed of light, p the momentum and E the energy of the particle. As the energy is also described by $E = m \cdot c^2$ it is evident, that the higher the energy, the heavier and energy-richer the discoverable particles can get [Hin08].

There are multiple types of particle accelerators each one with its own advantages and drawbacks. At CERN only linear accelerators and synchrotrons are used. In the following only some basics of this type of accelerators are briefly revised, while more detailed descriptions can be found in the appropriate references, for example [Wie15]. Please note that the term machine is used as a synonym for particle accelerators here, as that is customary in the field of accelerator physics.

Linear accelerators

The basic idea of particle accelerators is simple: Electromagnetic (EM) fields are used to guide charged particles on wanted trajectories and increase their energy. The first machines used an electrostatic field for the acceleration [Wie15]. The voltages needed to accelerate particles using this technique however are limited by breakdown effects. For this reason, nowadays Radio Frequency (RF) alternating electric fields are used. This technique used in a linear arrangement creates a so-called LINear ACcelerator (LINAC). It has to be pointed out that the term LINAC is only used for a linear arrangement of a machine in combination with RF acceleration. They are not used for linear machines using electrostatic acceleration [Hin08].

A way to realize RF acceleration are cavity resonators, which are mostly symmetric, i.e. rotationally symmetric around the beam axis. The most important mode for acceleration in cavities is the Transverse Magnetic eigenmode TM_{010} [Hin08]: This mode sustains an electrical field in longitudinal direction only. The particle bunch has to be timed to arrive in the cavity when the field is accelerating for the particle type used. Advantages of this technology are a relatively compact design and that the cavity can be adjusted to different particle velocities by controlling the phase in the resonator [Hin08].

Circular accelerators - Synchrotrons

Linear accelerators would need to be prohibitively long to achieve particle energies beyond MeV. The idea behind circular accelerators is to use the same accelerating structure multiple times [Hin08]. Thus, higher energies can be achieved while occupying less space. The price to pay is that the beam has to follow a curved trajectory to periodically return into the accelerating structure, which requires magnetic fields. Here, the principle of the synchrotron is focused on.

The synchrotron uses deflecting magnets in a circular arrangement (also referred to as ring) in order to bend the beam. To accelerate the particles, mostly cavities are used. In case of acceleration, the frequnecy of the cavity has to be increased synchronously with the magnetic field (the origin of the term synchrotron) [Wie15]. Thus, when the magnetic field is increased the momentum of the particle increases accordingly and the orbit of the particles stays the same. As the magnetic field achievable, even with superconducting magnets, is limited, in order to reach very high energies the circumference of the accelerator has to become larger.

A disadvantage of this concept is that, because the beam is constantly bent, the particles loose energy through the so-called synchrotron radiation [Hin08]. This loss of energy has to be compensated by the accelerating cavities.

A synchrotron can be operated as a storage ring, when the beam is not accelerated but kept at a constant energy level.

1.1.2 The CERN accelerator chain

Accelerators are limited by the range of particle energy they can handle. In order to accelerate the particles to very high energies, several accelerators have to be employed in a cascade. The CERN accelerator chain (displayed in Fig. 1.1) is able to increase the energy of protons and ions to up to 6.5 TeV. Currently, CERN runs two linear accelerators, four synchrotrons and one collider. Directly after the particle sources, the LINACs are the first machines in the accelerator chain. Depending on particle type and experiment, one LINAC is combined with up to three synchrotrons, to provide the demanded particle energy. LINAC2 is connected to the proton source while the ion source feeds LINAC3. The synchrotrons then, after further accelerating the beam, deliver it either to the next link in the chain or to the fixed target experiments.

The Proton Synchrotron (PS) and the Super Proton Synchrotron (SPS) [CER72] are used to accelerate a single beam of either protons or ions. On the contrary, the Proton Synchrotron Booster (PSB) only accelerates protons delivered by LINAC2 whereas the Low Energy Ion Ring (LEIR) only accelerates ions provided by LINAC3. Different from the other synchrotrons, the PSB uses four rings, stacked on top of each other, to accelerate the protons. The beams of all four rings are recombined into one single beam, before being delivered to the PS.

The Large Hadron Collider (LHC) [BCM+04] functions as a circular accelerator for two counter-rotating beams and as a collider at points where its two beam pipes are merged into single beam chambers. When providing a particle beam to the LHC, the other machines work as pre-accelerators. Thereby the SPS with its 7 km long circumference is the last pre-accelerator in the chain and injects alternately into the two rings of the LHC. In the LHC, the beams are first brought to higher energies and then collided at the four intersections where the experiments ALICE, ATLAS, CMS and LHCb are installed. As both proton beams currently can be accelerated up to 6.5 TeV, the maximum center-of-mass energy for proton collisions is 13 GeV.
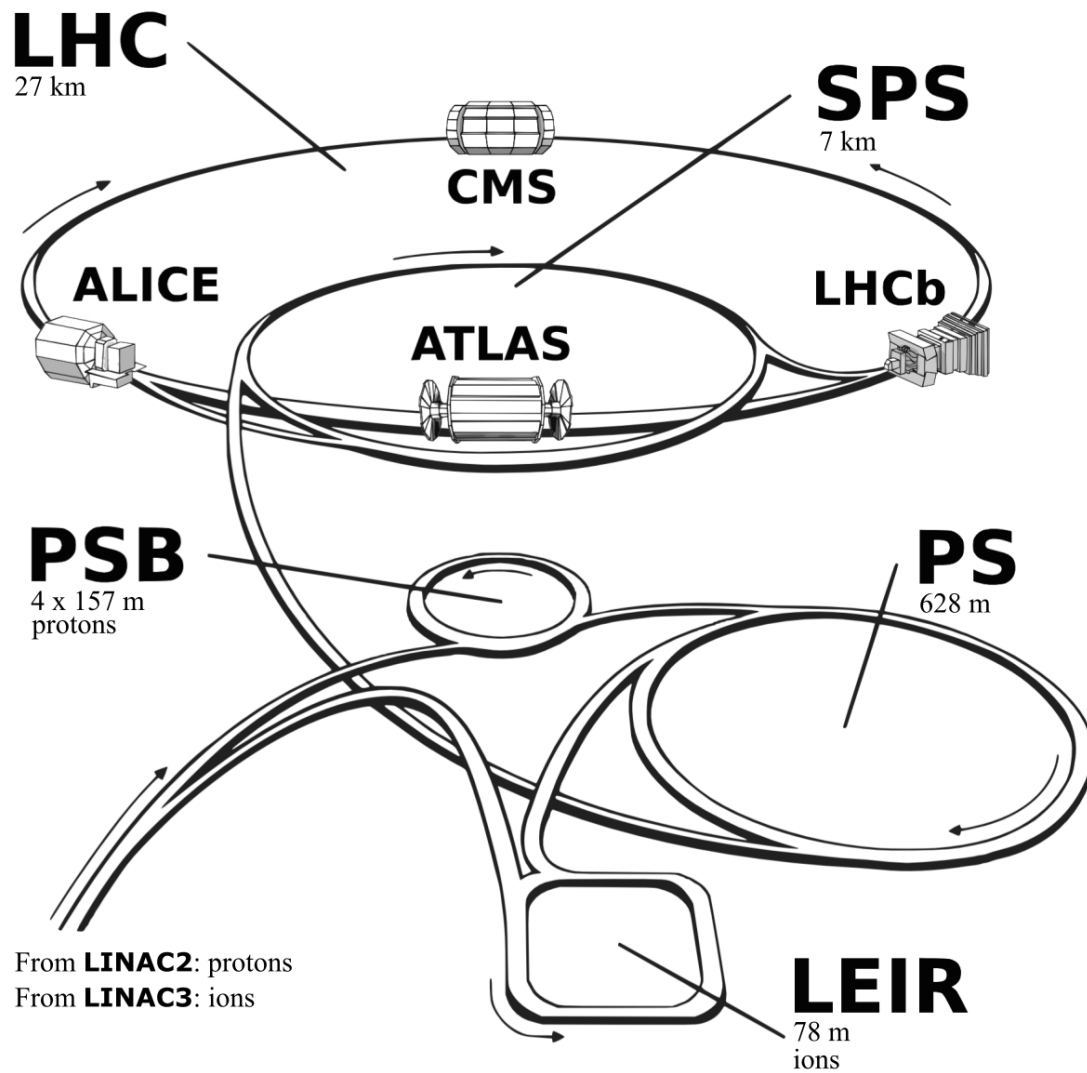
Figure 1.1: The CERN accelerator chain. The circumferences of the different accelerators is noted next to their abbreviations. If a machine only accelerates either protons or ions, that is indicated, too. Adapted from: jetgoodson.com/thesisGallery.html

1.2 Motivation

At CERN the High Luminosity LHC (HL-LHC) [ABAB$^+$17] project is currently underway. The main aim of this project is to achieve a total integrated luminosity of 3000 /fb over the LHC run four (2026-2037). For this purpose it is necessary to increase the instantaneous rate of collisions

$$\frac{dR}{dt} = \mathcal{L} \cdot \sigma_p \tag{1.2}$$

in the interaction points of the LHC [HM06]. The collision rate is only dependent on the peak luminosity $\mathcal{L}$ and the cross section σ_p of the used particle (Eq. (1.2)). Thus, to increase the collisions, the luminosity has to be increased. $\mathcal{L}$ of two head-on colliding Gaussian shaped beams can be expressed by [HM06]:

$$\mathcal{L} = \frac{N_1 N_2 f N_b}{4\pi \sigma_x \sigma_y}, \tag{1.3}$$

where $N_{1,2}$ are the number of particles in the two colliding bunches, the intensity respectively, N_b is the number of colliding bunches, the revolution frequency f of the particles and σ_x / σ_y the rms horizontal / vertical beam sizes. As f is basically constant in the LHC, to increase $\mathcal{L}$ the intensity of the beam has to be maximised and / or the transverse σ has to be minimized. The beam for the HL-LHC will be produced and delivered by the injectors. As beam quality can only deteriorate along the transport to the LHC, the injector chain plays an important role for the project. For the injectors to become capable of delivering the demanded beam intensity and quality to the HL-LHC, they have to be upgraded, too. These upgrades are coordinated through another project named the LHC Injector Upgrade (LIU) [DFG$^+$14, HDD$^+$14].

The goal of the LIU project is to allow the injectors to produce beams with double intensity and brightness values with respect to the values delivered nowadays. This relies on the implementation of a series of upgrades throughout the injector chain, which can lift the present intensity and brightness limitations and improve beam performance. A combination of machine studies and simulations are used to predict the future performance of the different machines. These rely on detailed knowledge of optical aperture and beam coupling impedance of the machine. As will be explained later in this thesis, the beam coupling impedance of a machine results from a linear combination of the contributors of the single devices composing the machine. For example, the kickers, i.e. the fast pulsed magnets for beam injection and extraction, have been long identified as a major source of impedance in the SPS in all planes, and therefore they also play an important role for impedance-driven instabilities [FBRV18]. Consequently the correct characterisation of the kickers is crucial to access the SPS performance. Furthermore, the impedance model has to be adapted for the different machine optics and compared to observations in the machine.

First experiences of operating the SPS with intensities higher than the nominal LHC beam have shown that coherent instabilities in both transverse planes may develop at injection energy. As these instabilities could potentially become a limitation for the future high intensity operation, they need to be studied in detail. In particular, a transverse mode coupling instability is encountered in the vertical plane. This instability threshold has to be determined in measurements and simulations for a new optics, proposed to relax the demands on the RF-system. In the horizontal plane, a head-tail instability of individual bunches is observed in multi-bunch operation. To understand the occurring mechanisms, beam dynamics simulations employing the SPS impedance model should be used. The possibility of mitigating this instability with stabilization mechanisms like transverse dampers, octupoles and chromaticity should be studied as well.

1.3 Thesis outline

To reproduce beam dynamics in simulations, first the accelerator's impedance has to be modelled. Nowadays, the impedance of the different accelerator components is mainly determined with commercial codes in combination with bench measurements for validation of the EM models. The impedances of the different components are then combined in a global impedance model, representing the impedance of the whole accelerator. This model is subsequently used as input for beam dynamics simulations. The results of these simulations are compared to beam measurements in the accelerator to confirm the correctness of the model. If differences between beam dynamics simulations and beam measurements are observed, or if components in the accelerator do change, the procedure can be iterated. This process is illustrated in Fig. 1.2.

This thesis focuses on the impedance and beam dynamics in the SPS and follows the work-flow illustrated in Fig. 1.2 in its structure: In the next chapter, Ch. 2, the concepts of wake and impedance are introduced, together with the simulation and bench measurement methods used for this thesis. After that, the impedance of individual SPS components is investigated in depth with simulations and bench measurements in Ch. 3. Following, in Ch. 4, the creation of an impedance model for an accelerator is explained and the transverse impedance model of the SPS is introduced. Also, fundamentals of beam dynamics are introduced, together with a short introduction to the PyHEADTAIL code, used for beam dynamics simulations within this thesis. The beam dynamics simulations are presented and compared to beam measurements, in Ch. 5. In the same chapter the SPS impedance model is thus validated by measurements. The last chapter, Ch. 6, concludes this thesis.
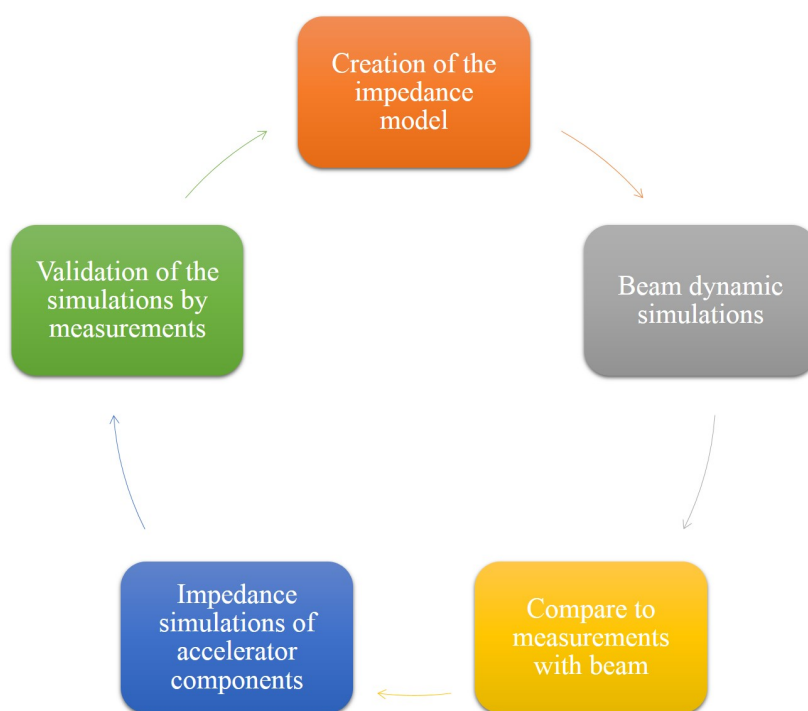
Figure 1.2: Flowchart of the creation of an impedance model.

2 Impedance characterisation

In this chapter, the theory of wake and beam coupling impedance (hereafter simply impedance) is introduced. Then, methods used to obtain the impedances of components in simulations and measurements are discussed.

2.1 Fundamentals on wake and impedance

Here the concept of wake and impedance is briefly introduced followed by the derivation of the power loss calculation and an overview over the methods used for simulations and measurements within this thesis. This section closely follows [Zan13] and [Wie15] in the derivation of the wake function. Broader summaries of the topic can be found e.g. in [WW91, Wil89, Stu01, RvR18].

Assume a charged particle bunch is travelling through a beam pipe at high energy. Further, the beam pipe is assumed to be a uniform and perfectly conducting tube in vacuum. An electrical field extends from the bunch to the walls of the beam pipe, as shown in Fig. 2.1 on the left hand side. For ultra-relativistic beams this field has no component in longitudinal direction and travels together with the beam. If the beam encounters a geometric discontinuity the EM field is forced to bend to satisfy the boundary conditions and some parts of the field stay behind. Especially, they remain within the structure for a certain time, possibly even after the bunch has left the structure, as shown in Fig. 2.1 on the right hand side. The created field is called wake field (or simply wake). By creating this wake field, the particles within the bunch can happen to influence themselves. But not only geometric discontinues are an origin of wake fields. The bunch induces a current into the beam pipe, which follows the bunch [Ng06]. If the beam pipe is now assumed to be resistive, this current gets delayed and can act back on trailing particles [Wie15]. In general, all materials surrounding the bunch other than a Perfect Electrical Conductor (PEC) can generate wake fields. The interactions between the particles via the wake fields can lead to instabilities of the particle beam, which consists of multiple consecutive bunches, in accelerators [Cha93].

To describe the wake mathematically, a system of two charges q and q_0 which are travelling at the speed of light c on the axis and are separated by a distance z is introduced and shown in Fig. 2.2. The longitudinal wake function $W_{||}(z)$ is defined as the integral of the Lorentz force $F_{||}$ felt by the trailing (witness) particle q due to the field induced by the source particle q_0 over the length L of the structure which
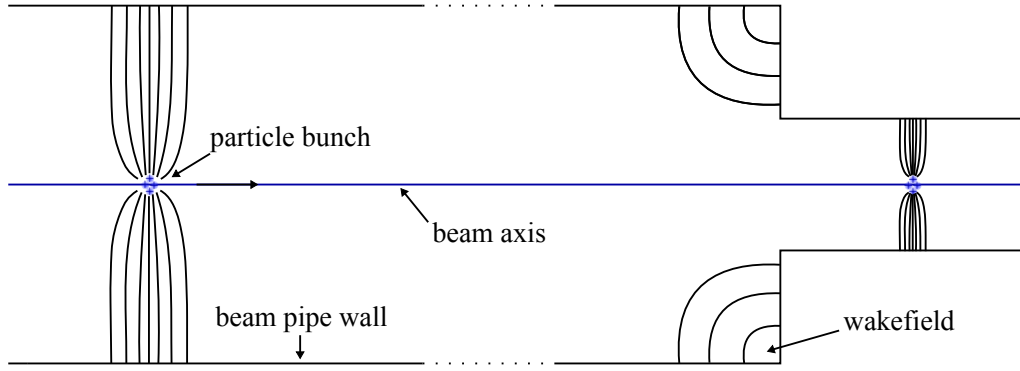
Figure 2.1: Creation of wake fields due to the interaction of a charge distribution with its environment, in combination with a change of the beam pipe diameter. Adapted from: [Wie15]

the particles are travelling through $(s(0, L))$ [Rum14].

$$W_{||}(z) = \frac{1}{q_0 q} \int_0^L F_{||}(s, z) \, \mathrm{d}s. \tag{2.1}$$

In the absence of magnetic fields, the force can also be described as q multiplied by $E_{||}$, the longitudinal electrical field induced by q_0. Inserting that into Eq. (2.1) leads to:

$$W_{||}(z) = \frac{1}{q_0} \int_0^L E_{||}(s, z) \, \mathrm{d}s. \tag{2.2}$$

The unit of the wake function is V/C (or Ω/s).
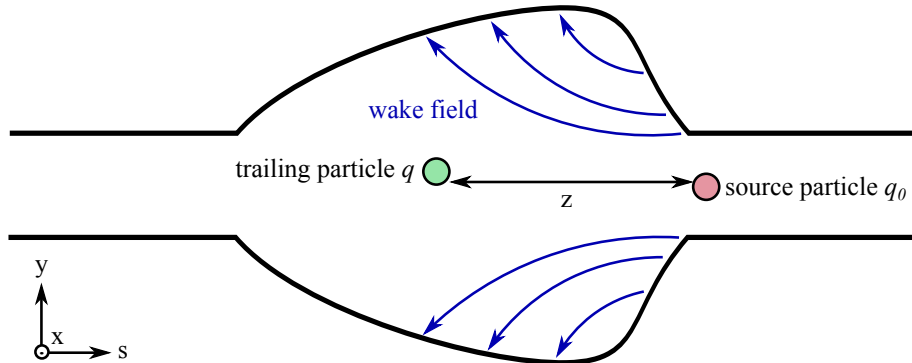
Figure 2.2: The particle model. Two ultra-relativistic particles are spaced by the longitudinal distance z. The source particle q_0 creates a wake field due to changes in the surrounding geometry. This wake field influences the trailing particle q.

The wake function describes the interaction of the particles with their environment in the time domain. The impedance describes this interaction in the frequency

domain [Wie15]. Thus, the longitudinal impedance $Z_{||}(\omega)$ is defined by the Fourier transform of the longitudinal wake function $W_{||}(z)$:

$$Z_{||}(\omega) = \frac{1}{c} \int_{-\infty}^{\infty} W_{||}(z) e^{\frac{-j\omega z}{c}} \, \mathrm{d}z. \tag{2.3}$$

Because of its relation to the wake function, this quantity has a unit of Ω. Using Eq. (2.3), changes in the diameter, or material surrounding the beam, can be described as a frequency-dependent impedance. Thus, all sections in an accelerator can be described as impedances.

In beam physics, broadband impedances, which extend over wide frequency ranges, and their associated short-lived wake functions typically provoke single bunch or intra-bunch (head-tail) instabilities. Conversely, narrowband impedances, which are sharply peaked functions around a certain frequency, with their long-lived wake functions typically couple several subsequent bunches or even the same bunch over several turns and thus may lead to multi-bunch or multi-turn instabilities.

2.1.1 Transverse wake and impedance

Similar to the longitudinal plane, a general wake function can be defined in both transverse planes [Ng06]:

$$W_{x,y}(z) = \frac{1}{q_0 q} \int_0^L F_{x,y}(s, z) \, \mathrm{d}s, \tag{2.4}$$

where $F_{x,y}$ are the components of the Lorentz force in the horizontal (x) and vertical (y) plane respectively. The transverse wake function can also be defined by its expansion into a power series [Zan13, HWZ98]. It is then described by the driving wake function $W_{x,y}^{driv}$ and the detuning wake function $W_{x,y}^{det}(z)$ in the horizontal / vertical planes. If the beam chamber is asymmetric, or if the beam travels off-axis in a symmetric structure, that results in:

$$\begin{aligned} W_x(z) &= A_x(z) + W_x^{driv}(z)x_0 + W_x^{det}(z)x, \\ W_y(z) &= A_y(z) + W_y^{driv}(z)x_0 + W_y^{det}(z)y, \end{aligned} \tag{2.5}$$

The constant terms $A_{x,y}(z)$ are defined as:

$$A_x(z) = W_x(z)|_{x=x_0=0}, \quad \text{and} \quad A_y(z) = W_y(z)|_{y=y_0=0}. \tag{2.6}$$

Higher order and coupling terms are neglected here, but for small offsets of the source particle position (x_0, y_0) and the test particle position (x, y) from the center of the structure, this approximation is valid [Zan13]. In literature, the driving impedance is often referred to as dipolar impedance and the detuning impedance is often called quadrupolar impedance. As they are dependent on the particle position their unit

is V/C/m (or Ω/s/m). In case of a top / bottom and left / right symmetry the constant terms in Eq. (2.6) are zero and Eq. (2.5) reads:

$$W_x(z) = W_x^{driv}(z)x_0 + W_x^{det}(z)x,$$
$$W_y(z) = W_y^{driv}(z)x_0 + W_y^{det}(z)y. \tag{2.7}$$

For rotational symmetric structures and an ultra-relativistic beam which travels in its center, this equation can be further simplified as the detuning terms are zero.

For particle simulations these driving and detuning terms of the transverse wake function are very useful, as they relate the perturbations of the source and witness particles to the associated kicks (x' and y') on the trailing particle by [Rum14]:

$$\Delta x'(z) = -\left(\frac{qq_0}{E_0}\right)[W_x^{driv}(z)x_0 + W_x^{det}(z)x],$$
$$\Delta y'(z) = -\left(\frac{qq_0}{E_0}\right)[W_y^{driv}(z)y_0 + W_y^{det}(z)y]. \tag{2.8}$$

The transverse impedance is again defined by transforming the transverse wake functions into the frequency domain:

$$Z_{x,y}(\omega) = \frac{j}{c} \int_{-\infty}^{\infty} W_{x,y}(z)e^{\frac{-j\omega z}{c}} \, \mathrm{d}z. \tag{2.9}$$

Also equation (2.5) can be expressed in the frequency domain by:

$$Z_x(\omega) = a_x(\omega) + Z_x^{driv}(\omega)x_0 + Z_x^{det}(\omega)x,$$
$$Z_y(\omega) = a_y(\omega) + Z_y^{driv}(\omega)x_0 + Z_y^{det}(\omega)y, \tag{2.10}$$

where the Fourier transform of $A_x(z)$ and $A_y(z)$ are $a_x(\omega)$ and $a_y(\omega)$, respectively.

The wake function, discussed above, describes the influence of a single particle on a trailing or witness particle. To describe the influence of a charged particle distribution on a trailing particle, all source terms have to be superimposed. This is done by convoluting the wake function with the charge distribution. The convolution of wake function and charge distribution is called the wake potential.

2.1.2 Power loss calculation

The derivation of the power loss in this thesis follows [Zan13].
In order to calculate the power loss, first the energy loss for a bunch passing once through an accelerator structure is derived. The total energy loss E_L of a bunch of particles with the line density $\lambda(z)$ can be found by integrating its longitudinal wake function over all particles. To describe the interaction between the particles, the bunch is divided into slices. A source slice $eN_{\mathrm{bunch}}\lambda(z')\mathrm{d}z'$ of the bunch shall affect a witness slice $eN_{\mathrm{bunch}}\lambda(z)\mathrm{d}z$ behind it. Here, e is the charge of a particle and

N_{bunch} the number of particles in the bunch, as $\lambda(z)$ is assumed to be normalized to unity. Now, the wake functions of all preceding source slices are integrated for every witness slice. To calculate the total energy loss, the energy that is lost by the source slices must be integrated over the full bunch extension.

$$E_L = e^2 N_{\text{bunch}}^2 \int_{-\infty}^{\infty} \lambda(z)\mathrm{d}z \int_{-\infty}^{\infty} \lambda(z')W_{\|}(z - z')\mathrm{d}z'. \qquad (2.11)$$

In a circular accelerator, the bunch passes through the same element multiple times. In this scenario, to calculate the total energy lost per passage, the revolutions have to be taken into account, as well. In an accelerator with the circumference C, adding up the wakes created by every turn leads to:

$$E_L = e^2 N_{\text{bunch}}^2 \int_{-\infty}^{\infty} \lambda(z)\mathrm{d}z \int_{-\infty}^{\infty} \lambda(z') \sum_{k=-\infty}^{\infty} W_{\|}(kC + z - z')\mathrm{d}z'. \qquad (2.12)$$

All integrals and summations in this section are formally extended from $-\infty$ as the wake function vanishes for positive values of z. The energy loss can also be represented in the frequency domain using impedances (see Sec. 2.1). With the relation

$$\sum_{k=-\infty}^{\infty} W_{\|}(kC + z - z') = \frac{\omega_0}{2\pi} \sum_{p=-\infty}^{\infty} Z_{\|}(p\omega_0)e^{-\frac{jp\omega_0(z-z')}{c}}, \qquad (2.13)$$

where $\omega_0 = 2\pi f_0$ and f_0 is the frequency with which the particle bunch is rotating through an accelerator with the circumference C. The Fourier transform of Eq. (2.12) results in:

$$E_L = \frac{e^2 N_{\text{bunch}}^2 \omega_0}{2\pi} \sum_{p=-\infty}^{\infty} (|\overline{\lambda}(p\omega_0)|^2 Re[Z_{\|}(p\omega_0)]). \qquad (2.14)$$

Here $\overline{\lambda}(p\omega_0)$ is the frequency domain representation of $\lambda(z)$ and $Z_{\|}(p\omega_0)$ the longitudinal impedance of the structure, the particle bunch is travelling through.

Multiplying Eq. (2.14) by the frequency f_0 leads to W_L, the power loss in this device [Zan13]. If the beam consists of a number of consecutive bunches n_{bunches}, the Single Bunch Approximation (SBA) of the beam power loss in Eq. (2.15) can be employed. However, this formula is only valid if the wake fields induced by one bunch are assumed to vanish before the next bunch passes by [Zan13].

$$W_{L_{\text{SBA}}} = n_{\text{bunches}}(f_0 e N_{\text{bunch}})^2 \sum_{p=-\infty}^{\infty} (|\overline{\lambda}(p\omega_0)|^2 Re[Z_{\|}(p\omega_0)]). \qquad (2.15)$$

The power loss of a beam can be calculated by replacing $\overline{\lambda}(\omega)$ with the beam spectrum $\overline{\Lambda}(\omega)$. The total number of particles in this case is $N_{\text{beam}} = n_{\text{bunches}} \cdot N_{\text{bunch}}$. The formula for the power loss of a beam then results in:

$$W_L = (f_0 e N_{\text{beam}})^2 \sum_{p=-\infty}^{\infty} (|\overline{\Lambda}(p\omega_0)|^2 Re[Z_{\|}(p\omega_0)]). \qquad (2.16)$$

Beam structure in the SPS

For the power loss calculation the beam spectrum needs to be known. The beam's shape in time and frequency domain is defined by the production scheme of the pre-injectors and thus cannot be changed. First, the beam is described in the time domain. The SPS accelerates two main proton beam types for the LHC. A beam that has bunches of particles spaced by 25 ns and one that contains spaces of 50 ns. The 50 ns beam can be simply described as a 25 ns beam where every second bunch is left out. So, the space in the machine can also be described as divided into 25 ns slots. 72 bunches in a row form a so-called train. This corresponds to one PS fill that is injected into the SPS. When the SPS is filled, it houses four trains spaced by 200 ns (eight slots) as displayed in Fig. 2.3. In total that leads to a time domain
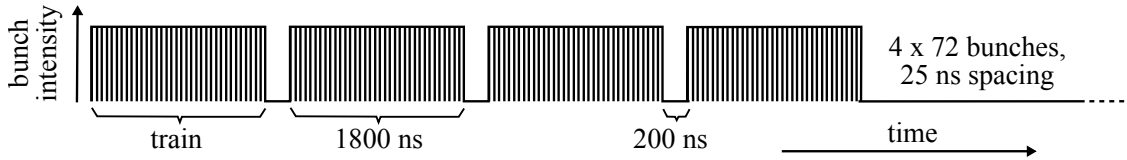
Figure 2.3: The 25 ns SPS beam composition in the time domain.

beam length of $72 \cdot 4 \cdot 25\text{ns} + 3 \cdot 200\text{ns} = 7.8\mu$s. Travelling with the speed of light, a particle needs approximately $23\,\mu$s to travel around the 7 km long SPS circumference. Thus, the whole beam occupies around 1/3 of the machine.

The particles in one bunch are assumed to have a Gaussian distribution, with a standard deviation of 0.7 ns (~ 0.2 m) [Zan13] in the longitudinal direction at injection energy. This is called the average bunch length σ. In Fig. 2.4 the Fourier transform of the 25 ns beam is shown. The peaks with 40 MHz spacing refer to the 25 ns bunch spacing in the time domain. The figure also shows that, as expected, the whole beam spectrum is enveloped by the Gaussian distribution that represents the spectrum of the Gaussian bunch.

2.2 Methods - Impedance and wake simulations

The wake potential, respectively the impedance, can be calculated analytically, only for simple structures. Therefore, numerical codes are used to study more complex structures [NG16]. An example is the 3D EM simulation software CST STUDIO SUITE® (CST) [CST]. To determine the wake potential and with it the impedance of a 3D modelled accelerator component, the wake field solver of CST PARTICLE STUDIO® (CST PS) can be used, with a simulated particle beam as excitation source. The particle beam is represented by a line current with a charge distribution which is Gaussian shaped in the longitudinal direction. The wake field solver employs a time domain solver to calculate the EM fields created by the moving beam and
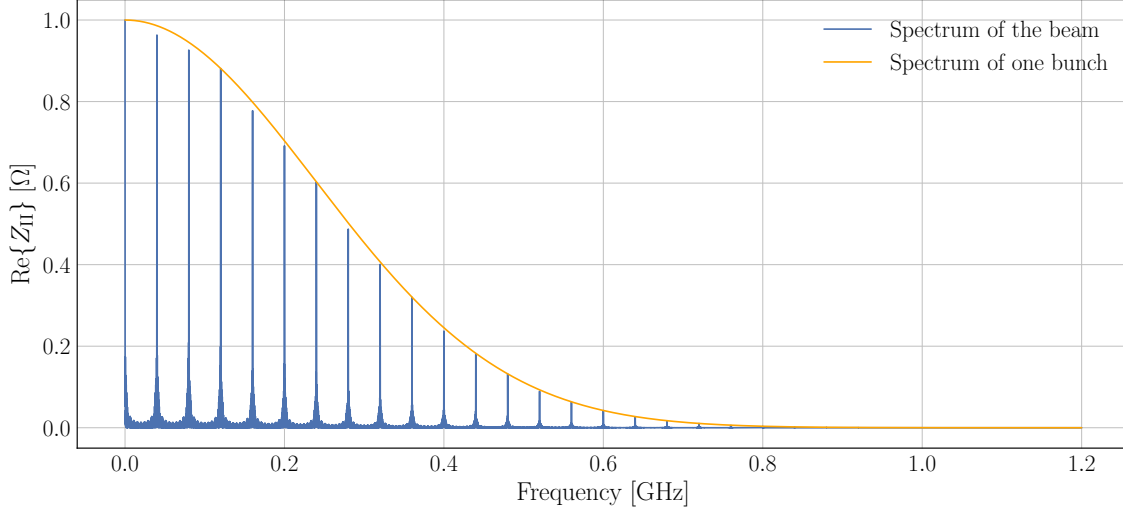
Figure 2.4: Spectra of the 25 ns beam and a bunch in the SPS.

integrates along the beam axis to compute the wake potential. The impedance is then obtained by a Fourier transform of the wake potential in post-processing. Wake and impedance results obtained with the CST code have been compared to theory and analytical models in [Zan13].

The longitudinal wake potential of a simulated model is the direct output of the CST wake field solver. Furthermore, it is possible in CST to place the path of a source beam independently of the path of the test beam (integration path). This allows the calculation of the transverse driving and detuning terms discussed above. From Eqs. (2.5) follows:

$$
\begin{aligned}
W_x^{driv}(z) &= \left.\frac{W_x(z) - A_x(z)}{x_0}\right|_{x=0}, \\
W_x^{det}(z) &= \left.\frac{W_x(z) - A_x(z)}{x}\right|_{x_0=0}, \\
W_y^{driv}(z) &= \left.\frac{W_y(z) - A_y(z)}{y_0}\right|_{y=0}, \\
W_y^{det}(z) &= \left.\frac{W_y(z) - A_y(z)}{y}\right|_{y_0=0}.
\end{aligned}
\tag{2.17}
$$

As the driving terms are only dependent on the offset of the source path, they can be obtained by simulating the structure with the integration path in the center and the beam path offset by x_0 or by y_0, respectively. Similarly, as the detuning terms are only dependent on the offset of the integration path, they can be simulated by offsetting the integration path by x or y and defining the source path in the middle

of the structure (see Eq. (2.17)). This is clarified in Fig. 2.5 for an axis symmetric structure. In that case the $A_x(z)$ and $A_y(z)$ terms vanish.
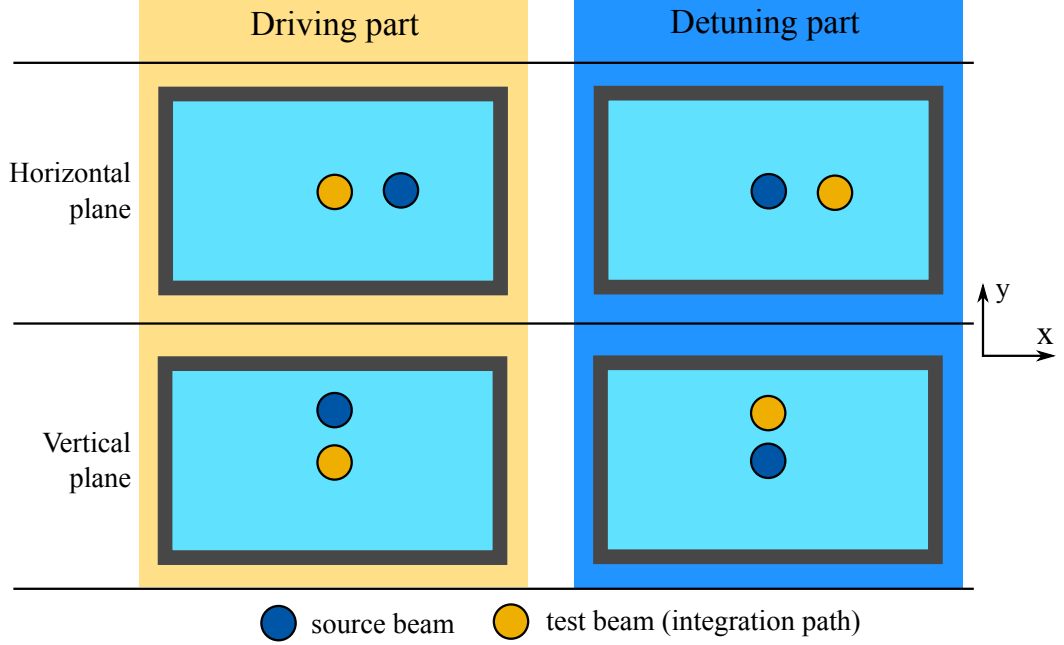
Figure 2.5: Setup of the transverse driving and detuning components simulations.

In conclusion, to obtain a full wake potential characterization of a non-rotational symmetric 3D structure with a numerical code, five simulations of the model with different source and test beam positions have to be launched; one for the longitudinal plane and four for the transverse planes.

CST PS calculates the longitudinal impedance out of the wake potential by dividing its Fourier transform by the Fourier transform of the charge distribution. Again, the Eqs. (2.17) can also be written in the frequency domain and the driving and detuning impedances can be obtained analogously, which follows from Eqs. (2.10):

$$
\begin{aligned}
Z_x^{driv}(\omega) &= \left.\frac{Z_x(\omega) - a_x(\omega)}{x_0}\right|_{x=0}, \\
Z_x^{det}(\omega) &= \left.\frac{Z_x(\omega) - a_x(\omega)}{x}\right|_{x_0=0}, \\
Z_y^{driv}(\omega) &= \left.\frac{Z_y(\omega) - a_y(\omega)}{y_0}\right|_{y=0}, \\
Z_y^{det}(\omega) &= \left.\frac{Z_y(\omega) - a_y(\omega)}{y}\right|_{y_0=0}.
\end{aligned}
\tag{2.18}
$$

Depending on the requirements on the simulations, the excitation pulse (bunch length of the beam) and the wake length (how long the wake is simulated) can be

adapted. Very short excitation pulses are needed to access high frequencies. To reproduce multi-bunch effects or to have a good frequency resolution, long wake lengths have to be simulated. Also the available computation resources have to be taken into account. The longer the wake length and the finer the discretization mesh, the more time consuming the simulations become.

The longitudinal impedance results of the wake field simulations can be compared to the impedance obtained by eigenmode simulations in CST MICROWAVE STUDIO$^{®}$ (CST MWS), if the structure under investigation allows it (strongly resonant and approximately loss free structure). However, the eigenmode results have to be treated with care, as the eigenmode solver calculates all principally excitable modes, even those that may not be excited by the beam in reality.

All CST simulations executed for this thesis were computed on a node of a Windows High Performance Computing (HPC) cluster, with 128 GB of RAM and two sockets holding each a Intel Xeon E5-2650 v2 processor with a base frequency of 2.6 GHz. As each of the processors has eight cores, one HPC node has 16 cores at its disposal. All computing times presented in this thesis refer to the total simulation time documented in the solver logfile by CST.

Codes computing the impedance directly in the frequency domain are also available, but are not discussed here, as there are no high performant solvers available to calculate the beam coupling impedance of 3D structures [NG16].

2.3 Methods - Impedance measurements

Simulations can be supported and / or validated by means of bench measurements. The figure of interest is the impedance seen by the particle beam in the accelerator. Bench measurements to obtain the impedance rely on the wire method [BCK^{+}09, DBC^{+}11]. For this purpose, a wire is stretched on the axis of the Device Under Test (DUT). To imitate the beam's EM field a pulse is sent through it. Due to the presence of the wire in the structure, a Transverse Electromagnetic (TEM) mode can propagate, which reproduces the field of ultra-relativistic particles. The pulse is created by a Vector Network Analyser (VNA) which is matched to the DUT. For simplicity, matching for measurements within this thesis is executed resistively. The measurement setup is illustrated in Fig. 2.6. The value of this matching resistor R_s can be found with [TWK98]:

$$R_s = Z_L - Z_0, \tag{2.19}$$

where Z_0 is the characteristic impedance of the VNA system and Z_L is the characteristic impedance of the DUT. Z_L can be either measured in a Time Domain Response (TDR) measurement (with an unmatched wire), or calculated analytically for simple structures. For example the Z_L of a round beam pipe can be found by

[KCG07]:

$$Z_L/\Omega = 60\ln(\frac{D}{d}), \tag{2.20}$$

where D is the beam pipe diameter and d the diameter of the wire used for measurements and enabling the TEM mode to propagate. In case of a flat beam chamber a formula describing the characteristic impedance of a wire between two plates can be used [KCG07]:

$$Z_L/\Omega = 60\ln(1.27\frac{D}{d}). \tag{2.21}$$

Here D refers to the distance between the two parallel plates.
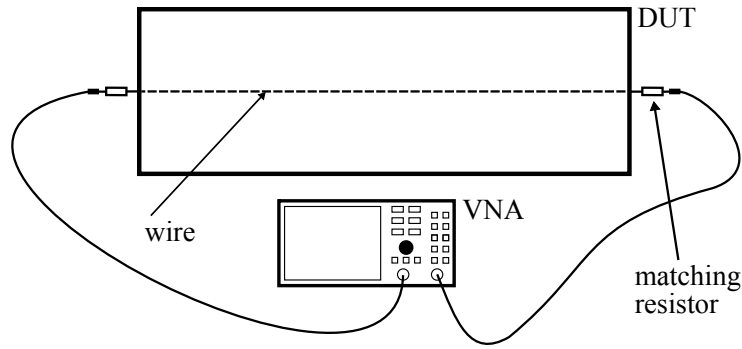
Figure 2.6: Setup for a wire measurement of the longitudinal impedance. The wire is inserted in the DUT.

To convert the scattering parameter (S-parameter) measured by the VNA into an impedance, which can be compared to the simulations, the LOG-formula [KCG07]:

$$Z = -2Z_L\ln(S_{21}), \tag{2.22}$$

is used.

The measurements are only valid for frequencies below the cut-off frequency of the first higher order mode that is able to propagate in the measurement setup [Mos16]. Also resonance frequencies obtained with the wire method have to be handled with care, as the introduction of the wire could shift their position and alter their breadth. The transverse impedance (driving and detuning part) can also be measured with two wires stretched in the DUT. Therefore, the current has to be sent over one wire and the response has to be measured on the other, similar to the procedure discussed in Sec. 2.2 for simulations.

3 Impedance of selected accelerator components

To determine the impedance of complex accelerator components a combination of simulation codes and bench measurements is used. The measurements for this thesis were done to gain an insight into the impedance and to support the simulations. Simulation and measurement methods were introduced in the two preceding sections.

In this chapter the impedance characterization and reduction is discussed on the example of three specific SPS devices. The devices investigated for this thesis exhibit both broadband and narrowband contributions to the global impedance of the machine. One of the largest contributors to the broadband impedance in the SPS are the injection and extraction kickers. Besides, in their present configuration, they also have non-negligible narrowband components. The narrowband impedance of the SPS has been in general not yet investigated as deep as the broadband part. The extraction septum which and the Y-chamber discussed below both exhibit resonant modes which could contribute significantly to the global narrowband impedance in the SPS.

3.1 The Y-chamber

One of the measures to increase the peak luminosity of the LHC within the HL-LHC project (discussed in Ch. 1) involves restoring fully head-on bunch collisions at the interaction points by compensating for the crossing angle with which the beams are brought to collision. This shall be done with so-called crab cavities that provide a transverse rotational kick to the bunches before collision. Two superconducting prototype crab cavities were installed on a test stand in the SPS to provide the first demonstration of vertical crabbing of protons. The cavities can only be moved in the beam path of the SPS when they are tested. During normal operation they have to be mechanically moved out of the ring. To achieve this task without breaking the vacuum every time, a beam pipe is installed in parallel to the test stand, providing a path for the beam during normal operation. The photo in Fig. 3.1 clarifies the setup in the SPS tunnel.

Y-shaped beam pipes, the so-called Y-chamber shown in Fig. 3.2, connect the test stand and the beam pipe in parallel to the SPS via long bellows. These bellows are necessary to allow the transverse shift of the whole test stand without generating vacuum leaks. The opening angle of the Y-chamber is 12° and the cut-off frequency
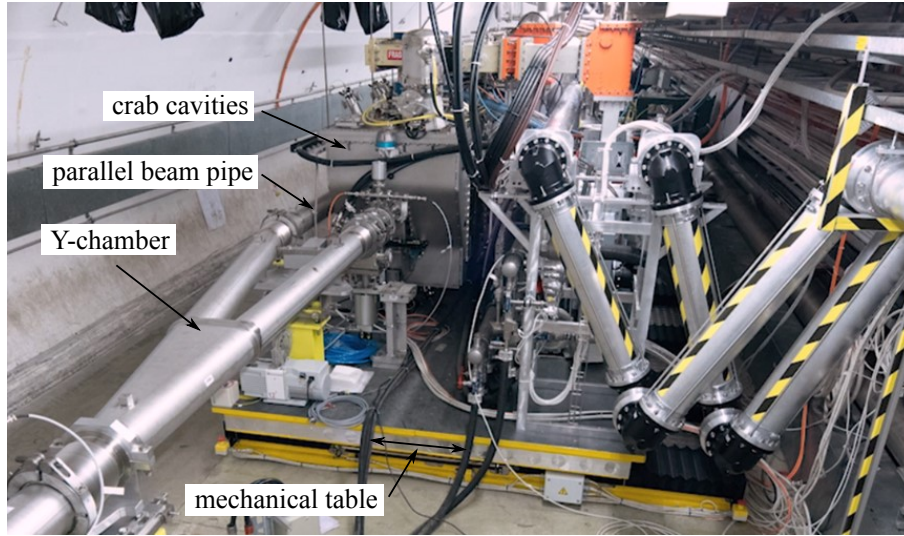
Figure 3.1: A picture of the crab-cavity test stand. The crab cavities are installed on a movable mechanical table together with all the equipment needed for its operation and the parallel beam pipe. A second Y-chamber is installed behind the crab cavities.

f_c of its 151 mm diameter stainless steel beam pipe is 1.127 GHz.

To investigate its impedance, the Y-chamber was modelled in its real dimensions, which is important to reproduce the frequency of occurring resonances. The three bellows are included into simulations to see if they contribute to the frequency range of interest. A drawback of this approach is that due to the size of the chamber and the bellows a high number of mesh cells is needed for an accurate simulation. Calculating the impedance with the wake field solver results in the blue curve in Fig. 3.4. This type of simulation with 6.6 million hexahedral mesh cells and a wake length of 300 m takes 15 hours on the 16 cores HPC node described in Sec. 2.2. In
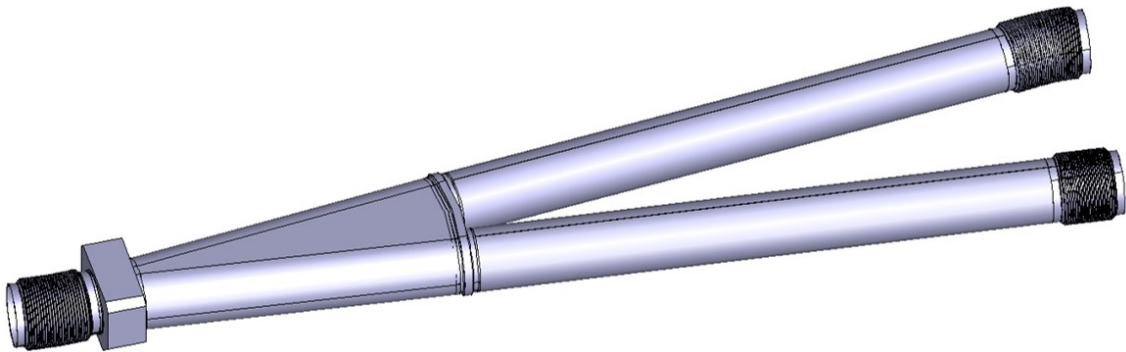
Figure 3.2: Model of the Y-chamber installed in the SPS before and after the crab-cavity test stand.

Fig. 3.4, the mode excited in the cavity introduced due to the transition from one into two beam pipes at 1.078 GHz is clearly visible. This mode is within to the beam spectrum and thus potentially harmful, as the impedances of both Y-chambers add up.

(a) No shield

(b) Perfect transition

(c) Sheet shield

(d) Sheet shield details
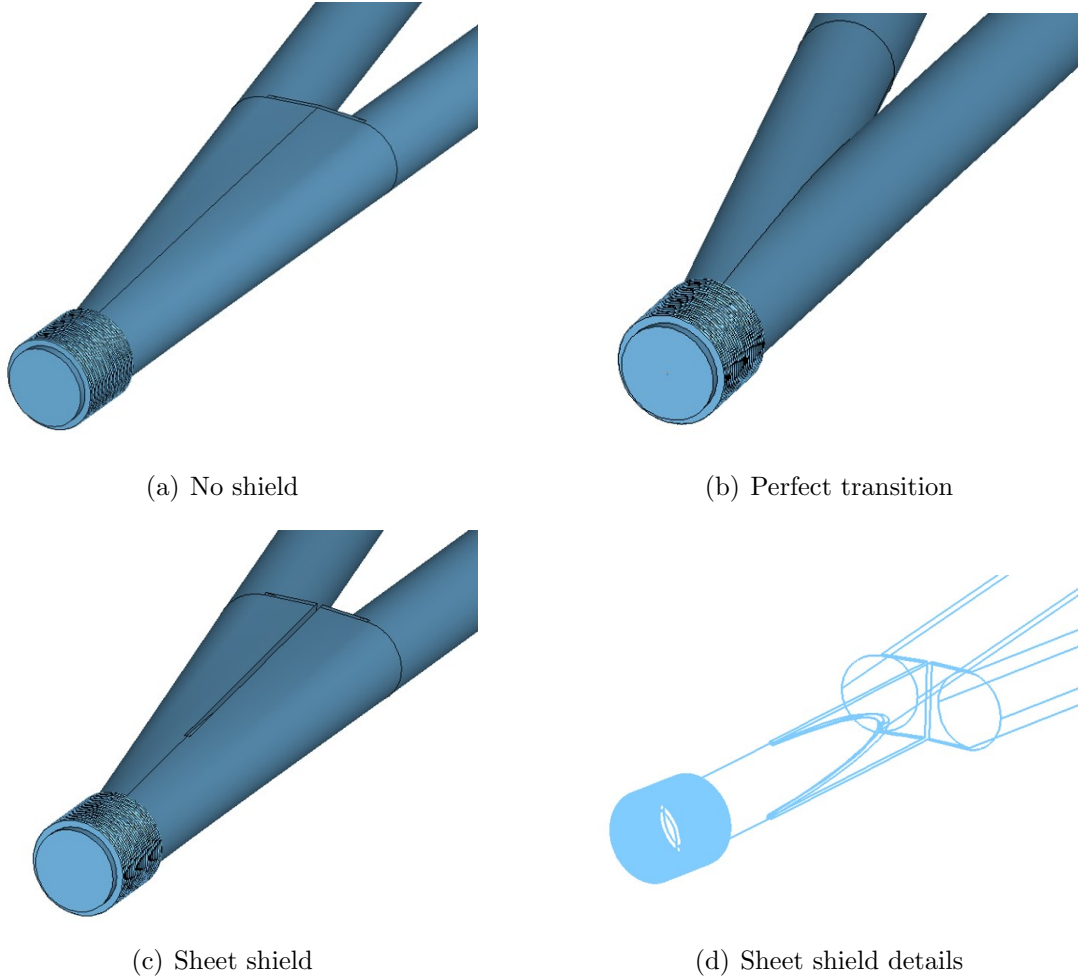
Figure 3.3: CST models of the three different Y-chamber models. Shown here is only the vacuum inside the chamber. To reduce simulation complexity a lossy metal material with the conductivity of stainless steel is surrounding the whole model, imitating the beam pipe.

Different approaches to reduce this mode were investigated. First a Y-chamber with a perfect transition from one into two beam pipes, shown in Fig. 3.3 (b) was studied. The perfect transition is modelled by adding two beam pipes in the wanted angle and cutting away the overlapping parts. The resulting impedance (red curve in Fig. 3.4) does not show the resonant mode at 1.078 GHz. Another solution, to mitigate this resonant mode, is to modify the existing design of the Y-chamber.
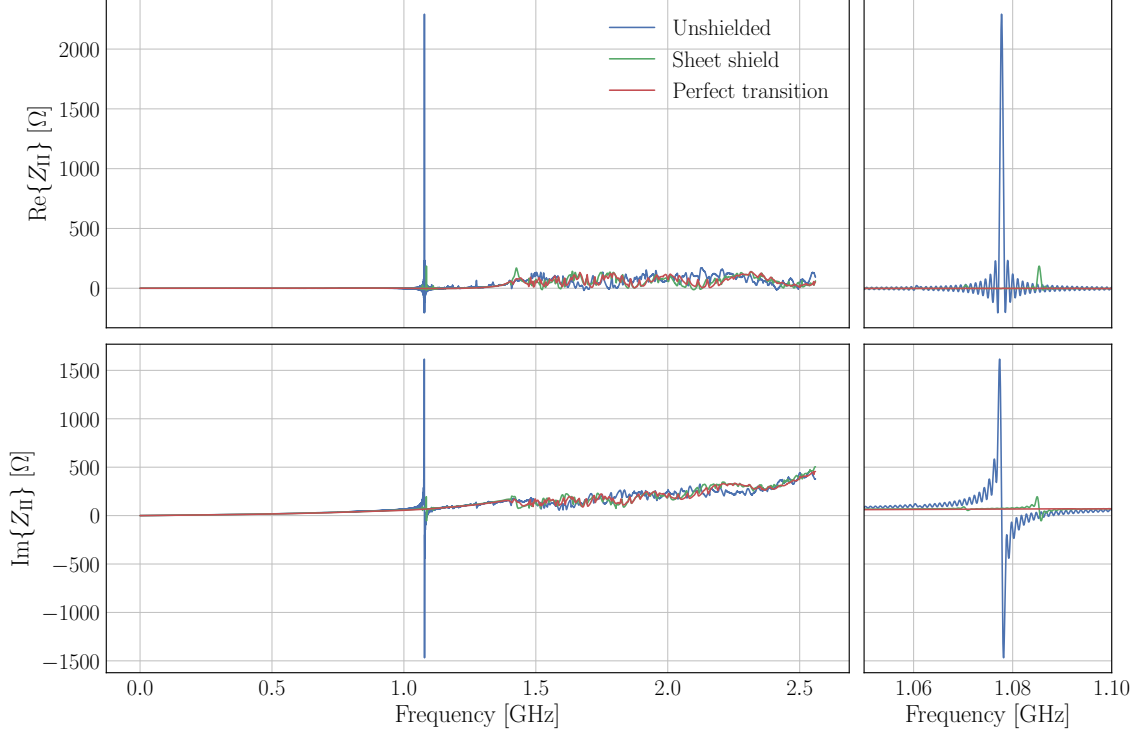
Figure 3.4: Simulated impedance of the different Y-chamber models.

Similar as proposed in [CMS01] for the LHC interaction region, the mode can be damped by introducing a vertical plate with a cut of the perfect transition profile. For the case of the Y-chamber that is a parabola. This "sheet shield" approach is clarified in Fig. 3.3 (c) and (d). The resulting impedance of a Y-chamber with this shield installed (green curve in Fig. 3.4), shows a reduction of the peak's height by a factor of about ten and a shift in frequency of 7.5 MHz.

Wake field simulations of resonating structures with a high electrical conductivity need a very long wake to have a good resolution in frequency domain and in particular to access the low frequency part of the impedance spectrum. The wakes of the simulations in Fig. 3.4 are not completely decayed, which leads to the artificial contribution of the sync function to the impedance around the 1.078 GHz mode (a truncated time domain signal leads to the convolution with a sinc function in the frequency domain, which means that a single frequency can be spread over the spectrum with the decay of the sinc function). The walls surrounding the cavity housing the modes have a high conductivity and thus the resonant modes are indeed hardly damped. Investigating the impedance of the mode with the wake field solver (time domain) would imply simulating the wake until this mode vanishes. This would require a around four times longer wake length and therefore a approximately four times longer computation time.

As the mode is trapped, the eigenmode solver can be used to calculate the resonant mode and its parameters directly. For the eigenmode simulation, all three ports of the Y-chamber are closed with either an electrical or a magnetic boundary. An eigenmode simulation of the first 20 modes of the Y-chamber model discretised by 1.2 million tetrahedral mesh cells on the 16 cores HPC node lasts around seven hours. These modes are plotted together with the wake field results in Fig. 3.5 for the unshielded Y-chamber. The impedance value of the 1.078 GHz mode from eigenmode simulations is approximately 4400 Ω, around double the wake field simulation value. As the eigenmode simulations calculate the mode directly their results can be trusted. The impedance value of the resonant mode is thus characterized in about one-eighth of the computation time compared to what would be needed with the wake field solver.
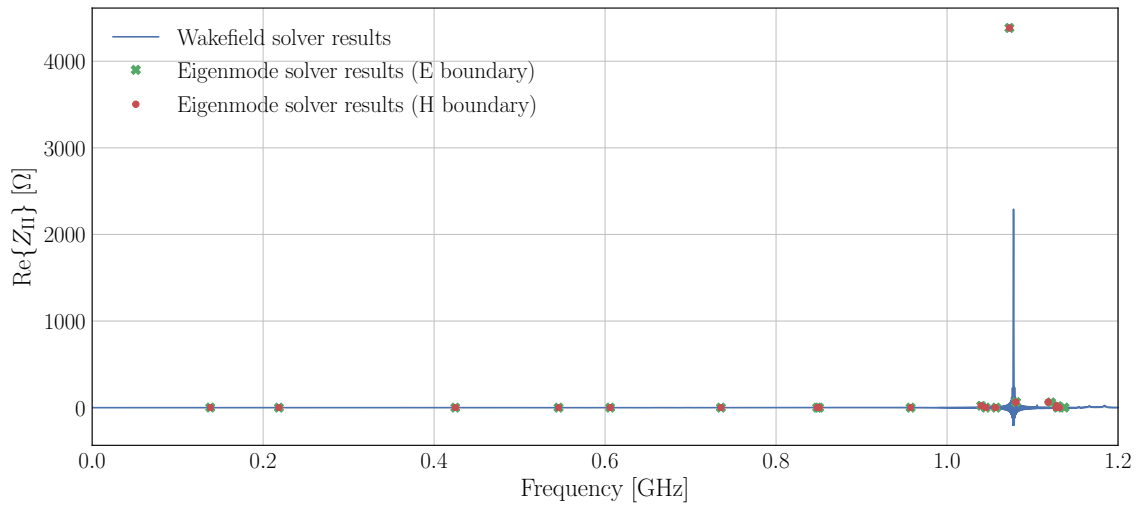
Figure 3.5: Comparison of the simulated Y-chamber impedance achieved with the wake field solver to the mode impedance calculated with the eigenmode solver. The eigenmode solver results are calculated for two cases, terminated with an electric and a magnetic boundary, respectively.

3.2 The kickers

The dynamic range in terms of acceleration is limited for circular accelerators. To reach high particle energies several accelerators have to be cascaded. Thus, there is a need to transfer the beam from one machine to another. To inject or extract the particle beam out of or into an accelerator, kicker magnets are used. As these devices often contain ferrite and they feature relatively small apertures, have a large contribution to the broadband impedance of a machine.

In the following, the impedance of the injection and extraction kickers in the SPS is investigated in depth. First, the operating principle of a kicker is explained followed by a motivation for the studies conducted.

3.2.1 Structure, operating principle and characteristics

The basic task of a kicker is to create a magnetic field perpendicular to the beam axis. As the charged particles in the beam are travelling through that field they experience a deflection (kick) by the Lorentz force which is perpendicular to the beam axis and the kicker field. The SPS injection and extraction kickers use ferrites whose magnetic field is induced by a fast current pulse [FFH$^+$76]. The ferrite is C-shaped and therefore also referred to as ferrite yoke. The beam is travelling in the aperture of the yoke, experiencing the magnetic field whenever the kicker is pulsed. This is clarified in Fig. 3.6 which represents the typical cross section of a kicker magnet. The plate on the left of the aperture is called the High-Voltage (HV) bus-bar and is faced by the Ground (GND) bus-bar. Both bus-bars extend over the full kicker length. With the equation of the Lorentz force for a magnetic flux $\vec{B}$ on a moving charge,

$$\vec{F} = q(\vec{v} \times \vec{B}), \qquad (3.1)$$

the direction of the deflection of a particle with the charge q and the speed $\vec{v}$ can be determined.
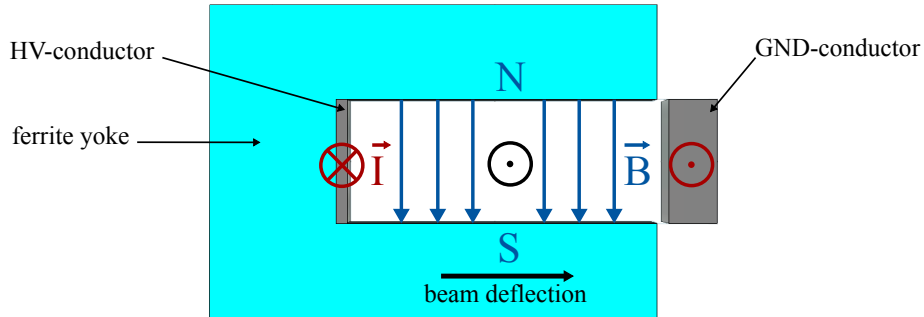
Figure 3.6: Kicker operating principle. The flux of the magnetic field (blue) is induced by the pulsed current (red) and deflects the proton beam to the right (black). The north-(N) and south-pole (S) of the magnetic field are also marked.

For a uniform steering of the beam the pulse shape has to be as flat as possible during the beam passage. To avoid reflections that could alter the waveform, the kicker has to be matched to the cable. Therefore the kickers are constructed in a way that their schematic emulates a coaxial cable. To achieve this, the kicker is divided into cells [BCC$^+$09]. One cell is consisting of a ferrite core clamped between two metal plates. The number and length of the cells depend on the requirements of the kicker. The HV bus-bar is connected to the plates clamping the ferrite (HV-plates).

These plates exhibit a capacitive coupling to ground. The resulting schematic circuit diagram is shown in Fig. 3.7. L_c represents the inductance of a kicker cell and C_c its capacitance [BDF$^+$10]. As two ferrite blocks are separated by one metal plate, a cell extends from the middle of one plate to the middle of the next one. Consequently an inductive connection stretches between two $C_c/2$ capacitances. As currents travelling on the HV-conductor experience the described electric circuit, the kicker can easily be matched to a given cable during design phase. Kickers arranged as described above, are called fast pulsed transmission line kickers.
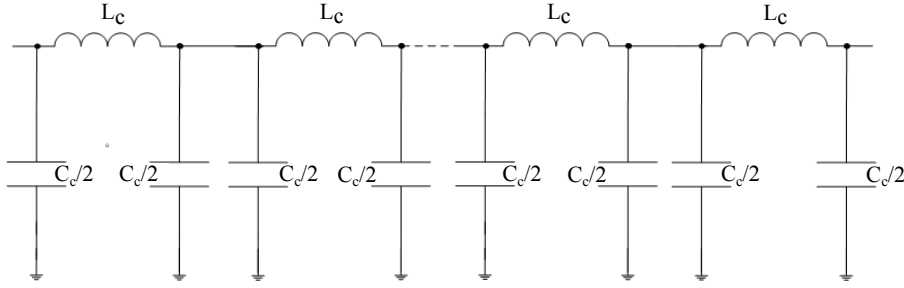
Figure 3.7: Schematic circuit diagram of a transmission line kicker. Source: [BCC$^+$09]

Kicker characteristics   To get the characteristic impedance Z of one cell, the transmission line model can be used [BCC$^+$09]:

$$Z = \sqrt{\frac{L_c}{C_c}}. \tag{3.2}$$

Every cell delays the pulse by [BCC$^+$09]:

$$\tau_c = \sqrt{L_c \cdot C_c}. \tag{3.3}$$

The HV bus-bar is now assumed to be connected to a Pulse Forming Network (PFN) on one side and terminated with the kicker's characteristic impedance on the other side. In this scenario, the magnetic field can be considered as completely built up when the edge of the pulse travelled through the whole kicker with n cells. The rise time τ of the magnetic field can be expressed as $\tau = n \cdot \tau_c + t_{\text{pulse}}$ where t_{pulse} describes the rise time of the pulsed current. If the kicker is terminated in a short-circuit, the pulse gets reflected and travels a second time over the HV-plate. This leads to a higher field strength but also to a twofold rise time.

   As stated before, the pulse should not be degraded while travelling through the kicker to ensure a uniform deflection of the beam. Due to the presence of L and C the kicker structure acts as a filter for pulses running on the HV-conductor. Fast rise times require sharp pulse edges and thus a wide frequency spectrum. To not

degrade the pulse shape the cut-off frequency f_c introduced by the filter structure of the kicker to the pulse needs to be high. A high f_c also reduces the so-called flat-top ripple of the pulse, smoothening it further. f_c can be calculated by [Duc05]:

$$f_c = \frac{Z}{\pi \cdot \sqrt{(L_c + 4L_{cs}) \cdot L_c}}. \tag{3.4}$$

where L_{cs} is the parasitic inductance occurring in series with C_c in reality. The cell length is proportional to L_c and can be adapted in the design phase to achieve different performances [BW96].

3.2.2 Motivation to study the kickers

The SPS is the last machine in the CERN accelerator chain before the LHC. To extract the beam from the SPS into the LHC the Magnetic Extraction Kicker (MKE) kicker and the Magnetic Septa (MS) are used in a procedure called a one-turn-extraction. The kicker produces a fast pulsed magnetic field that deflects the beam into the region where the MS creates a constant magnetic field. This field bends the beam into the transfer line to the LHC. The rise-time of the MKE is imposed by the difference between the length of the beam ($8\,\mu$s) and the time the beam takes to complete one turn in the accelerator ($23\,\mu$s). The kicker's field is not sufficient to guide the beam directly into the transfer line, that's why the MS is used in addition.

The LHC as a collider has two beams travelling in opposite directions, thus two regions of extraction are needed (Long Straight Section (LSS) 4 and LSS6 [GCD+06]). In the SPS, two types of extraction kickers are used: The MKE-S with a small aperture (width 135 mm, height 32 mm) and the MKE-L with a large aperture (width 147.7 mm, height 35 mm). The larger aperture size of the MKE-L allows the beam to travel further off-center without hitting the kicker. All MKE kickers consists of seven cells with a length of 237.5 mm each. Every extraction region uses several MKE-S and MKE-L kickers.

Compared to the MKE the Magnetic Injection Kicker (MKP) in the SPS requires a faster field rise-, and fall-time (200 ns), to achieve a close spacing between the bunch-trains injected from the PS. For that reason the kicker cells are shorter. The MKP also has L and S versions. The L and the S refer to the larger (width 141.5 mm, height 54 mm) and smaller (width 100 mm, height 61 mm) horizontal aperture. In addition the L version is longer (22 cells) than the S version (17 cells). A MKP cell is 27.5 mm long. All these dimensions are summarized in Tab. 3.1.

Even when the kickers are not active the beam passes through them every turn, as they are situated in the machine. The parasitic EM interaction between the beam and the kickers results in beam-induced heating and possible beam instability [ABC+04]. The consequences can be very serious. In the following the questions of the ferrite heating will be analysed closely.

Table 3.1: Dimensions of the SPS injection and extraction kickers.

	MKE-L	MKE-S	MKP-L	MKP-S
Aperture height	32 mm	35 mm	54 mm	61 mm
Aperture width	147.7 mm	135 mm	141.5 mm	100 mm
Cell length	237.5 mm	237.5 mm	27.5 mm	27.5 mm
Number of cells	7	7	22	17
Total length	1662.5 mm	1662.5 mm	605 mm	467.5 mm

The heated ferrite tends to outgas and so degrades the vacuum. In the worst case, if the ferrite exceeds its Curie temperature, the kicker loses its functionality. To avert this scenario, water-cooling has been installed in the MKE tanks in the past [TBGU06]. To avoid collisions between the beam and the outgassing particles, additional vacuum pumps were installed, as well. However, these measures only act on the symptoms. Another approach was followed with the installation of the serigraphy. There the aim was to act on the root cause of the MKE ferrite heating, i.e. the EM interaction between the beam and the kicker. A coupler with stripes of silver paste (very good conductor) is painted (serigraphed) on the ferrite of every cell of the kicker following the pattern illustrated in Fig. 3.8. The electromagnetic field induced by the beam can couple with the serigraphy and its penetration into the ferrite is therefore strongly reduced.

Lately, to further reduce the power lost in the ferrite the length of the serigraphy stripes was optimised to minimize the EM interaction of the kicker with the 25 ns spaced beam [DFG+14]. This beam is routinely used for the filling of the LHC and exhibits spectral lines spaced by 40 MHz as shown in Subsec. 2.1.2. The serigraphy as a coupler has a resonance frequency depending, among others, on its layout. Power loss estimations suppose that this resonance peak laid on, or close to, a beam spectrum line, contributing largely to the power loss (see Eq. (2.16)). By changing the layout of the serigraphy, its resonance frequency shifts further away from the spectral line, effectively reducing the power loss. This approach required shortening the length of the serigraphy stripes from 200 mm to 180 mm [BBD+17]. In Tab. 3.2 the changes in the kickers of the extraction regions over several years have been listed.

The impact of the shortening of the serigraphy length was observed during the high intensity run in the SPS in October 2017. Beams with more particles than used in daily operations were injected and increased the power loss. The temperature and the vacuum pressure in the kicker's vacuum tanks were monitored during this run and are displayed in Fig. 3.9. The values for the temperature curves are obtained from temperature probes mounted on the GND bus-bar and thus, capture the tank temperature rather than the ferrite temperature. From Fig. 3.9 (upper plot) a main
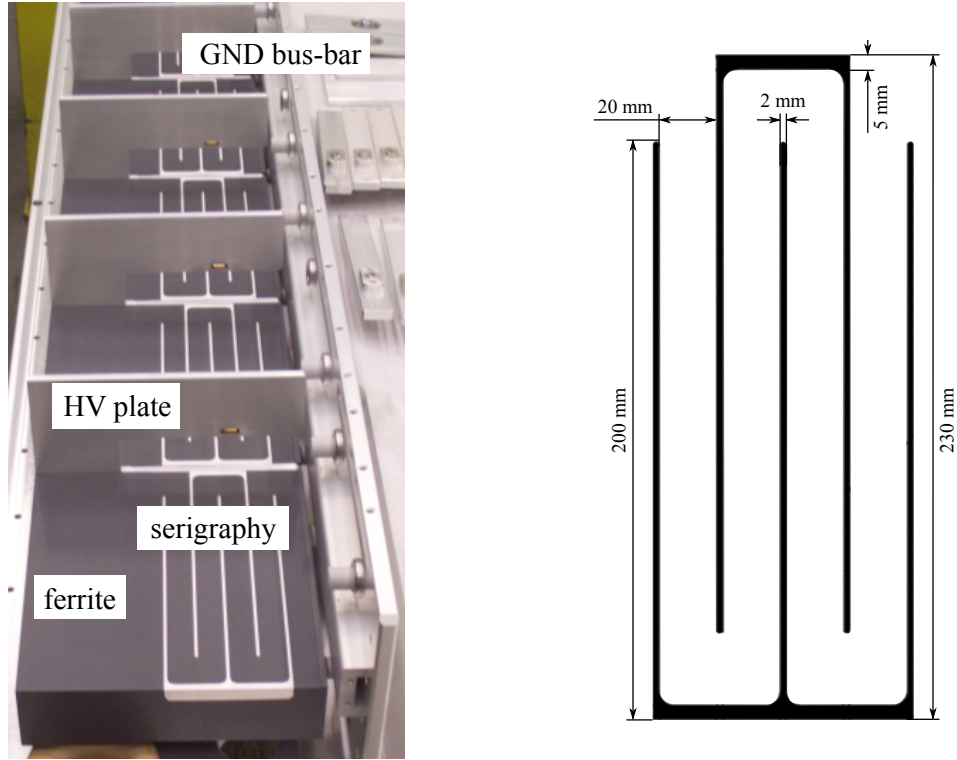
Figure 3.8: On the left, the MKE kicker with serigraphy applied during assembly is displayed. The C-shaped HV-plates separating the cells are visible. The GND-conductor can be seen on the right hand side of the picture. The serigraphy is also printed on the ferrite surface exposed to the beam from the top. On the right the layout of the 200 mm long serigraphy is shown.

observation for the MKE kickers was that the tank temperature of the MKEs in LSS4 with the 180 mm serigraphy rises approximately half as fast as the one of the MKEs in LSS6 with 200 mm serigraphy (see Tab. 3.2) as anticipated in [DFG+14].

For the MKPs the data shows that the MKP-L tank generated the highest temperature increase, whereas the MKP-S tank hardly heats up. This is not only due to the fact that the MKP-L is longer but also that its aperture, besides being wider, is lower than the one of the MKP-S. However, the absolute temperature of the MKEs cannot be compared to the MKP's absolute temperature, as the MKP kickers are installed in a region with limited physical space and thus no water cooling can be installed. That is also the reason why the kicker temperature curves start at different values. To reduce the temperature rise, the MKE type serigraphy cannot be transferred to the MKP either, as the shorter cell length prevents sufficient coupling between the serigraphy stripes. An adapted MKP serigraphy concept was proposed in [Bec15]. The serigraphy layout presented expands over the whole kicker and needs to be insulated from the kicker's surface to not short-circuit the HV-plates and impair the

Table 3.2: Changes of the MKE kicker configuration in the SPS over the years. (ser. stands for serigraphy)

Period	Kicker in LSS4 (short-circuit termination[*])
From Feb. 2017	2 MKE-L and 2 MKE-S with 180 mm ser.
Jan. 2016 - Dec. 2016	2 MKE-L and 2 MKE-S (1 S with 180 mm ser.)
Jan. 2014 - Dec. 2015	3 MKE-L and 2 MKE-S with 200 mm ser.
Jan. 2012 - Dec. 2013	3 MKE-L and 2 MKE-S (2 L and 2 S with 200 mm ser.)
Jan. 2011 - Dec. 2011	3 MKE-L and 2 MKE-S (2 S with 200 mm ser.)
Jan. 2003 - Dec. 2010	3 MKE-L and 2 MKE-S not serigraphed
Before 2003	No MKE installed
Kicker in LSS6 (short-circuit termination)	
From Jan. 2018	2 MKE-L and 1 MKE-S with 180 mm ser.
Jan. 2009 - Feb. 2017	2 MKE-L and 1 MKE-S with 200 mm ser.
Jan. 2007 - Dec. 2008	2 MKE-L and 1 MKE-S (1 L with 200 mm ser. and 2 cells of 1 S with 200 mm ser.)
Jan. 2006 - Dec. 2007	2 MKE-L and 2 MKE-S (2 cells of 1 S with 200 mm ser.)
Before 2006	No MKE installed

[*] With the removing of one MKE-L from LSS4 end of 2015 the kickers in that section were changed from terminated to short-circuit mode.

kicker's function.

The second plot of Fig. 3.9 shows the vacuum pressure for the same tanks. Two components can be recognised; a fast one (dynamic pressure rise in presence of the beam), creating all the spikes in the measured curve and a slow drift of the baseline value (static pressure). The spikes are mainly related to the electron cloud created in the kicker when the high intensity beam passes through. Comparing the curves, further observations can be made:

- The slow drift of the vacuum pressure in the MKP-L tank is correlated to the increasing temperature in the tank. The heated ferrite outgasses more the increased amount of the desorbed molecules and degrades the vacuum quality.

- Between the MKE curves, a higher vacuum pressure is observed in the tank with the higher temperature. Thus the reduction of the heating achieved with the 180 mm serigraphy mitigates the degradation of the vacuum.

- Contrary to the MKP-L, the MKP-S does not degrade the vacuum, as the temperature in its tank is not changing significantly.

To avoid collisions between the residual particles and the beam, the vacuum pressure in the machine is desired to be kept as low as possible. Hence, especially the MKP-L,
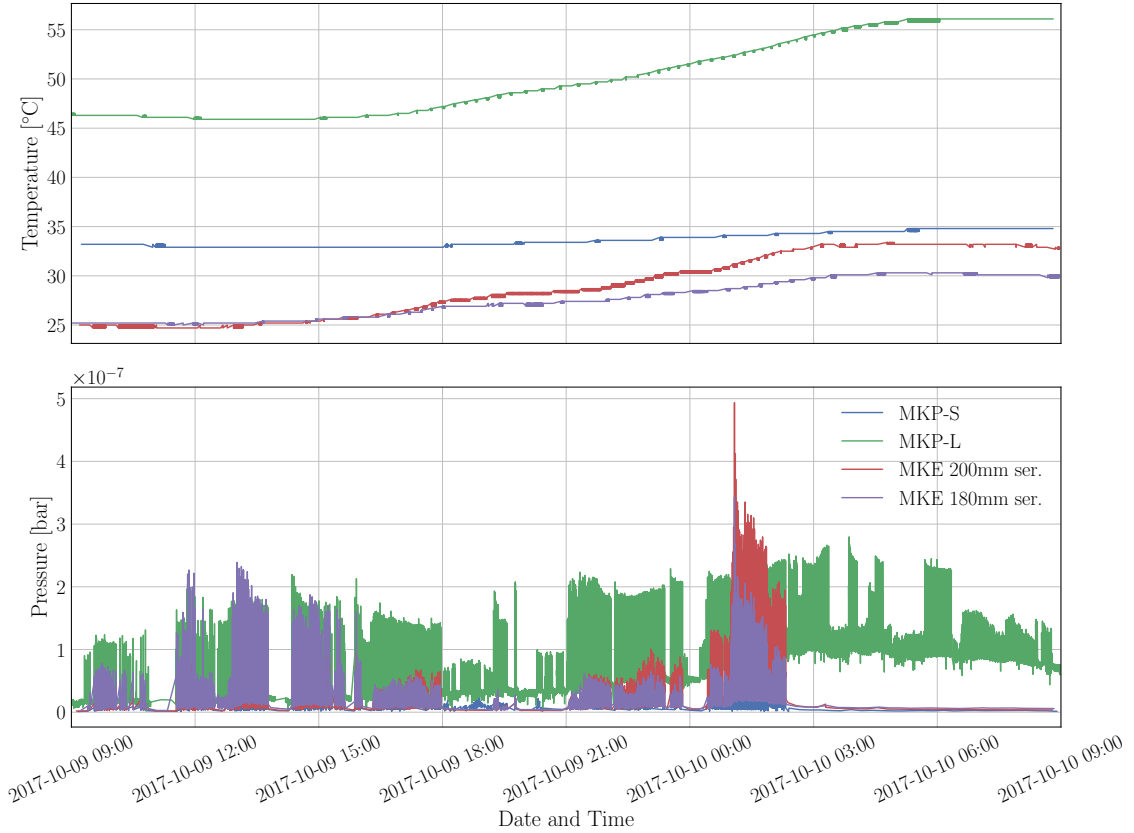
Figure 3.9: Development of injection and extraction kicker tank temperature and pressure during the 2017 SPS high intensity run. The temperatures in the tanks of the two different extraction regions are averaged and thus represent the heating of the two different serigraphy length (see Tab. 3.2).

which shows a 10° increase in temperature during the run, the heating could become a limiting factor during operations, as it exhibits the largest change in temperature, the vacuum pressure in its tank is the highest. To understand the heating of the kickers and to be able to mitigate it, their accurate impedance modelling is crucial.

Furthermore, recent measurements of the longitudinal SPS impedance in the machine pointed to a missing impedance in the longitudinal impedance model [LS17]. The longitudinal impedance model is very important to predict the instability threshold for the future LHC beams in the SPS. Therefore a precise characterization of the broadband contribution of the kickers impedance in the longitudinal plane is needed in the framework of the LIU project.

For these reasons the kickers have been reinvestigated in depth in the framework of this thesis. The aim was to develop a model that is consistent with both, the results of bench measurements and the heating observations in the machine. For the latter the accuracy in the characterisation of the serigraphy's resonance frequency is

crucial. Accordingly, after a short overview over previous work done on the kickers, the MKE and MKP impedance, respectively, is investigated in depth.

Previous studies on the SPS injection and extraction kickers

Since the usage of the SPS as an injector for the LHC, the impedance of the fast extraction kickers has been the objective of analytical studies as well as of dedicated measurements and simulations. In 2000, H.Tsutsui presented a theoretical formula to estimate the impedance of the kicker, in the longitudinal [Tsu00b, Tsu00a] and later in the transverse plane [TV00]. The transverse formula was benchmarked with a simple 3D electromagnetic simulation. In the same year, F. Caspers measured the kicker with and without transition pieces shielding the beam from the kickers vacuum tank [CGD+00, CMT00]. Three years later H.Tsutsui investigated the calculation of the kicker heating [TCV03]. In 2007, the kicker was remeasured by T. Kroyer, this time with the serigraphy installed [KCG07]. In 2013, C. Zannini presented detailed electromagnetic simulations of the MKE with and without serigraphy [Zan13] using CST and benchmarked those aginst analytical models (further simulations were presented in [SMZ+10, ZMS+10, ZVM+11]). In the same thesis, a first model of the MKP was also introduced. In [Bec15] that model was refined and validated by measurements. In addition a serigraphy layout to reduce the heating of the MKP was proposed.

3.3 Investigation of the extraction kicker

The MKE kickers are first studied in simulations and then compared to measurements in a following subsection. At the end, the impedance of the final model is presented.

3.3.1 Simulations

The wake field solver of CST introduced in Sec. 2.2 is used for the following simulations. To determine the impedance of the MKE kickers they are first modelled with their real dimensions including all seven cells with ferrite, HV-plates, the HV and GND bus-bars and the serigraphy. The model is depicted in Fig. 3.10. A particle beam is chosen as a source. In reality the kicker is housed in a support frame inside a vacuum tank. To reduce simulation time the modelled kicker is inserted in a vacuum block the size of the support frame. The vacuum block is in contact with PEC boundaries, as the system is assumed to be electromagnetically shielded by the support frame. Boundaries in beam direction are chosen to be absorbing (open boundaries in CST), assuming a perfectly matched tank. Furthermore, all metal parts are modelled as PEC, which is a good approximation for good conductors. As the MKE-S and MKE-L have different apertures they have to be modelled individually.
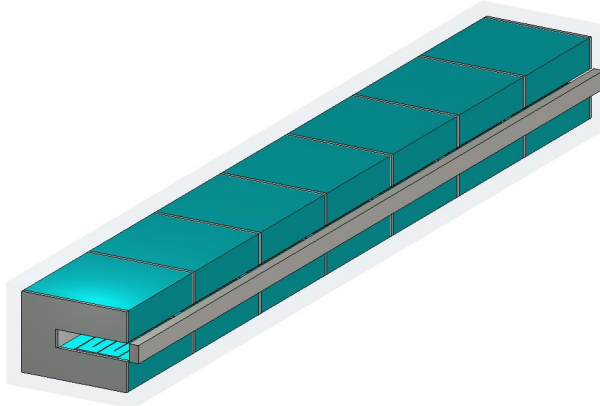
Figure 3.10: MKE-L model used for simulations.

Simulating the MKE-L model with a 200 mm serigraphy reveals the impedance curve in Fig 3.11. The expected resonance peak of the serigraphy is visible at 47 GHz.

The precise modelling of this peak is crucial, so the parameters influencing it have to be studied in depth. These parameters have to be determined first. Therefore, the serigraphy is described as a coupler implemented using micro-strip lines on ferrite. With the group velocity of a TEM mode in a waveguide [Poz12], the coupler's
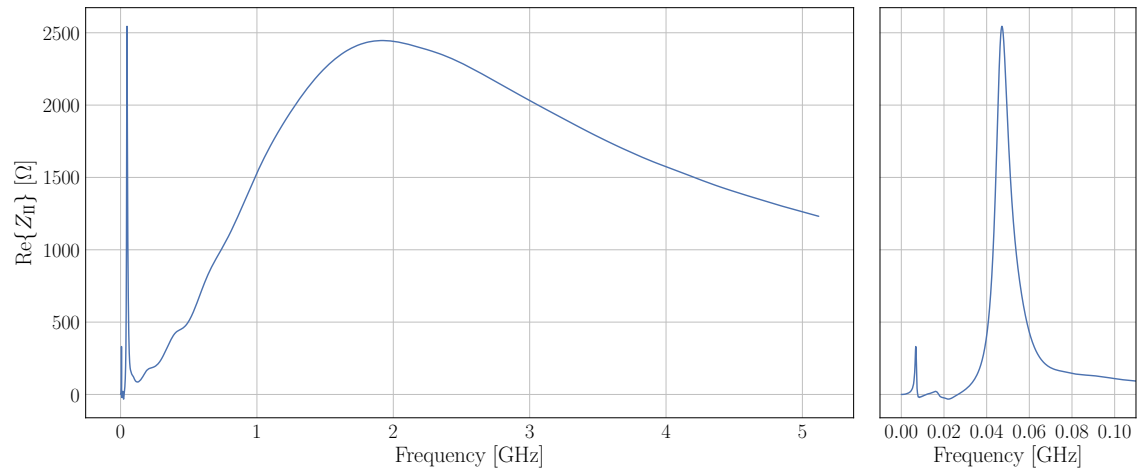
Figure 3.11: First simulation results of the MKE-L with the 200 mm serigraphy. The real part of the longitudinal impedance is plotted over the frequency. On the right-hand-side a zoom on lower frequency regions is displayed.

resonance frequency can be described as:

$$f_r = \frac{2c}{l\sqrt{\epsilon_{eff}\mu_{eff}}}. \tag{3.5}$$

Here l refers to the overlapping length of the serigraphy coupler's stripes and the effective permittivity ϵ_{eff} as well as the effective permeability μ_{eff} describe the EM property of a material surrounding the serigraphy which reproduces the effect of the given layout. If the height of the ferrite block is much larger than the width of a serigraphy stripe, the effective permittivity and permeability values can be calculated from their relative values by [Poz12]:

$$\epsilon_{eff} = \frac{\epsilon_r + 1}{2} \qquad \text{and} \qquad \mu_{eff} = \frac{\mu_r + 1}{2}. \tag{3.6}$$

From Eq. (3.5) it is evident that the resonance peak of the serigraphy is strongly dependent on the properties of the ferrite and the overlapping length of the serigraphy. In addition, as the serigraphy is very thin and therefore challenging to model, the implementation of the serigraphy in the model also has a strong influence. The influence of the determined parameters on the resonance peak or the serigraphy is investigated in depth for each item in the following order:

- Modelling of the serigraphy

- Investigating the influence of the relative permeability μ_r

- Investigating the influence of the relative permittivity ϵ_r

- Simulated influence of the serigraphy length on the impedance

To illustrate the effects only the real part of the longitudinal impedance is plotted. The imaginary part of the longitudinal impedance and the transverse components of the final model are presented at the end of the section.

Modelling of the serigraphy

In cooperation with CST AG in Darmstadt (Germany) three approaches to model the serigraphy have been established:

1. Using the tabulated surface impedance macro with one layer;

2. Using a coated material with zero thickness;

3. Using the thin panel material option to create a material.

For all these approaches the serigraphy layout in Fig. 3.25 is modelled as a surface (without any thickness) and its thickness is then considered as an electrical parameter of the material instead of as a geometric property. The tabulated surface impedance material is impenetrable by the EM field and if used to model serigraphy it would shield the ferrite underneath from penetration through EM waves. To implement the serigraphy with the second approach, a material with zero thickness, but coated with a material that has the properties of the serigraphy's silver paste, is defined. Testing reveals, that the properties of the underlying material with zero thickness do not influence the result and that the combination of material and coating is penetrable by EM fields. This method was used in [Zan13]. The third approach, the thin panel material, was recently introduced in CST and creates a thin, not fully electromagnetically shielding material.
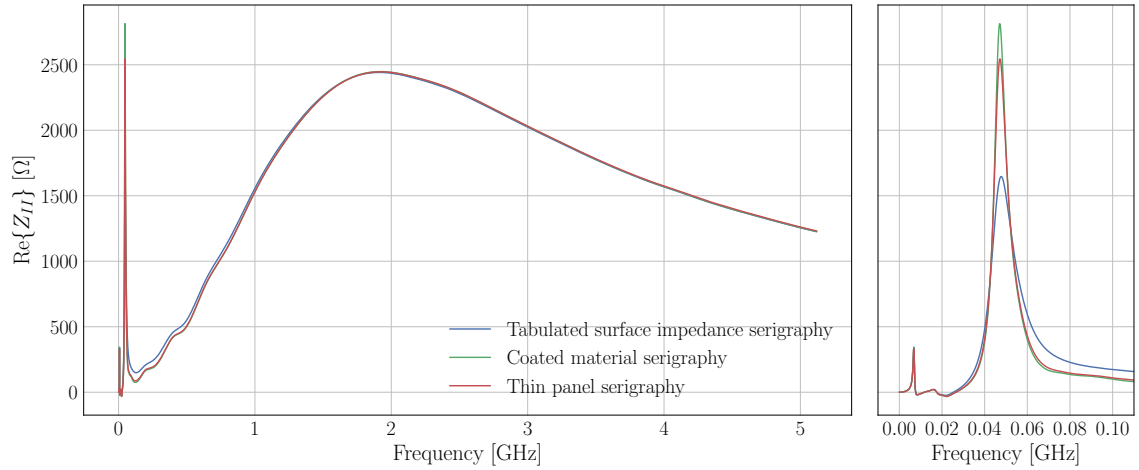
Figure 3.12: The simulated real part of the longitudinal impedance for the three approaches of modelling the serigraphy. On the right-hand-side a zoom on lower frequency regions is displayed. The model used is an MKE-L with the 200 mm serigraphy.

In Fig. 3.12 results from the wake field simulation of the MKE-L with the 200 mm serigraphy are shown for all three modelling approaches. The second and third modelling approach give nearly the same results, whereas the first method differs at low frequencies. Especially the resonance peak of the serigraphy structure around 40 MHz is wider and has a lower amplitude. The skin-depth calculated with the formula [Poz12]

$$\delta_s = \sqrt{\frac{2}{\omega\sigma\mu}} \qquad \text{with} \qquad \mu = \mu_0 \cdot \mu_r, \qquad (3.7)$$

at a frequency of 40 MHz with an assumed serigraphy silver conductivity σ_{ser} of $1 \cdot 10^7$ S/m and the relative permeability μ_r^{ser} of one is around 25 μm. As the painted serigraphy is only 30 μm thick, approximately the value of the skin depth, the first approach of modelling the serigraphy as impenetrable is inappropriate. The third

modelling method was chosen for the kicker models as it represents the easiest and most intuitive way to implement the serigraphy. The supplier states conductivity values up to $4.2 \cdot 10^7 \, \text{S/m}$ for the silver paste used to paint the serigraphy [Her11]. In simulations the conductivity of the serigraphy material was chosen to $1 \cdot 10^7 \, \text{S/m}$, to take into account a possible degradation in conductivity occurring from the manual application process of the silver paste. Simulations comparing these two values lead to exactly the same impedance results (see Appendix A). It is crucial to refine the mesh along the serigraphy width to make the results converge. A simulation with 44 million mesh cells and a wake length of $500 \, \text{m}$ lasts about 58 hours on the 16 cores HPC node described in Sec. 2.2. Convergence studies with more mesh cells were done and led to very similar impedance curves (see Appendix A).

The small peak at around $10 \, \text{MHz}$ is the TEM mode propagating between the HV and the GND bus-bar described in [ZRV12]. The HV bus-bar is modelled floating (electrically not connected), so this mode is hardly damped. In reality the HV bus-bar is connected to the PFN through cables. The effect of these cables is investigated in measurement later within this section.

Influence of the relative permeability μ_r

As discussed above, the kicker heats up during operation. As the ferrite's EM-properties change with temperature this could have an effect on the impedance. In [CBC$^+$18], measurements of the changing EM-properties over frequency for different temperatures are presented. Note that the Ceramic Magnetic, Inc CMD5005 ferrite measured there is the same ferrite type as the 8C11 from another supplier. A kicker simulated with the measured 8C11 ferrite properties leads to nearly the identical impedance curve as obtained with the 25° CMD5005 ferrite properties. In Fig. 3.13 the simulated impedance of the MKE-L the with the $200 \, \text{mm}$ thin panel serigraphy is presented for ferrites modelled after the relative permeability curves measured at different temperatures. The broadband impedance decreases for higher temperatures, whereas the changing temperature has no sizeable effect on the serigraphy resonance peak. As in operation the MKE stays far below 50° (see Fig. 3.9) the effect of changing magnetic properties for heated ferrite can be neglected in the MKE model.

A ferrite relative permittivity ϵ_r of 12 was used for all these simulations. This value was measured in [CBC$^+$18] at 25° and in a range of frequencies between $400 \, \text{MHz}$ and $1.5 \, \text{GHz}$. The dependency of the permittivity on temperature was not measured, nor the value at lower frequencies. The effects of the relative permittivity on the kicker impedance is investigated below.

Influence of the relative permittivity ϵ_r

The ferrite used for the kicker magnets is the Ferroxcube 8C11. To establish a reliable impedance model it is absolutely crucial that the ferrite is adequately represented.
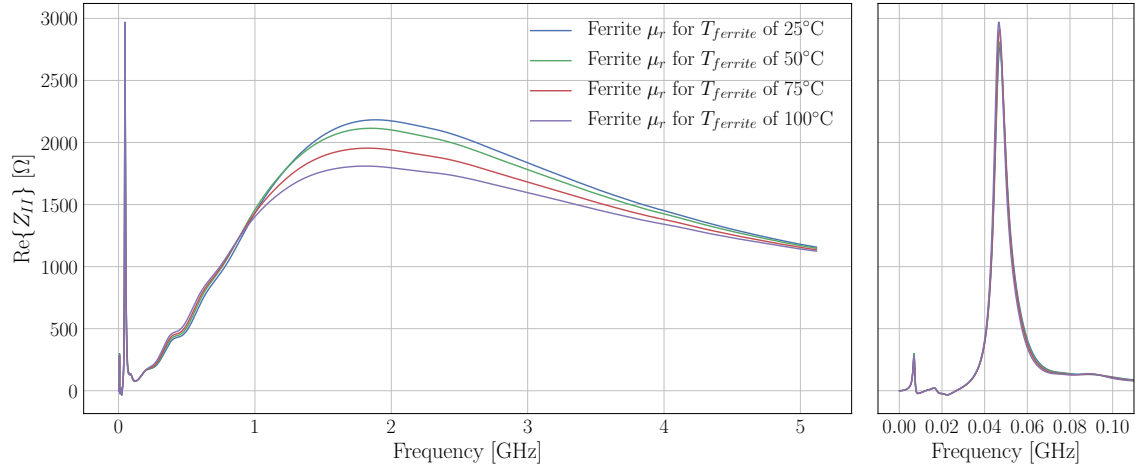
Figure 3.13: The simulated real part of the longitudinal impedance for different ferrite temperatures. On the right-hand-side a zoom on lower frequency regions is attached. The model used is an MKE-L with the 200 mm thin panel serigraphy. The relative permittivity ϵ_r of the ferrite was always set to 12.

Therefore the measured frequency-dependent relative permeability μ_r values of the 8C11 ferrite are imported into CST and their fit is used for simulations. The conductivity of the ferrite is set to $1 \cdot 10^{-5}$ S/m as given in the data sheet [Fer08]. A scan to test the sensitivity of this parameter showed changes in the impedance of the resonance peak only for a conductivity value that is a factor 10^4 smaller than the value used (see Appendix A).

Permittivity measurements of the 8C11 shown in [KCG07] suppose a growing relative permittivity ϵ_r for lower frequencies, with values up to 16 for frequencies around 40 MHz. In theory, according to Eq. (3.5) the influence of the relative permittivity and the relative permeability on the serigraphy's resonance frequency should be equal. But as the value of the relative permittivity ϵ_r is much smaller than the value of the relative permeability μ_r, the influence of small changes on the resonance frequency is larger. To investigate the effect of changing relative permittivity ϵ_r values on the simulated kicker impedance, a scan over the relative permittivity ϵ_r was executed and the results are shown in Fig. 3.14. As expected from theory, the relative permittivity ϵ_r has a large influence on the frequency of the serigraphy's resonance peak. Table 3.3 shows that for the MKE-L with the 200 mm serigraphy the resonance frequency varies from 50.6 MHz for a relative permittivity ϵ_r of ten to 41.6 MHz for a relative permittivity ϵ_r of 16. It is also visible that equidistant changes in the relative permittivity do not lead to a equidistant changes in frequency. In addition, the relative permittivity also influences the broadband impedance above 1.75 GHz (Fig. 3.14). From heating observations the resonance peak of the 200 mm serigraphy is suspected to be situated close to 40 MHz, which

supports a relative permittivity ϵ_r of 16.
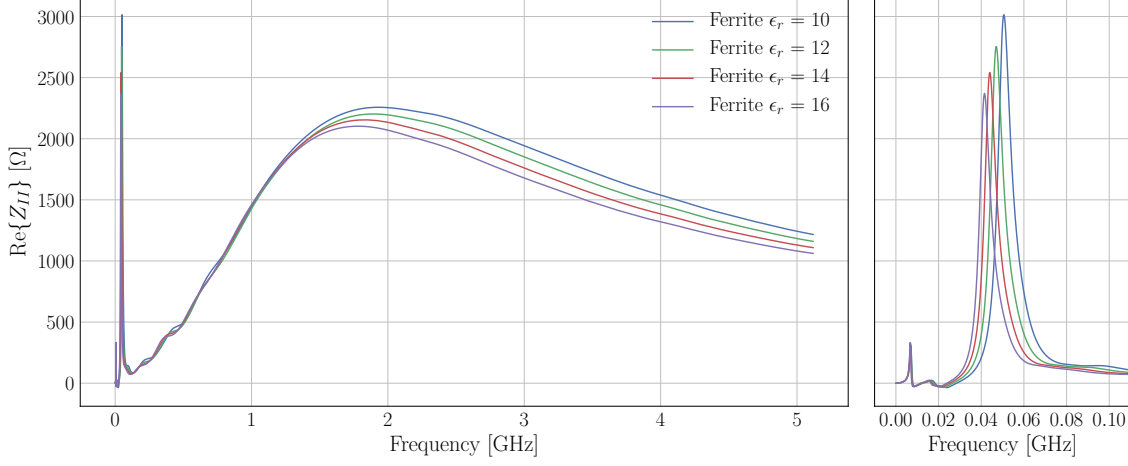
Figure 3.14: The simulated real part of the longitudinal impedance for different values of the relative permittivity of the ferrite. On the right-hand-side a zoom on lower frequency regions is attached. The model used is an MKE-L the with the 200 mm thin panel serigraphy.

Table 3.3: Simulated frequency of the MKE serigraphy resonance dependent on the relative permittivity ϵ_r.

	MKE-L 200 mm serigraphy
$\epsilon_r = 10$	50.6 MHz
$\epsilon_r = 12$	47.0 MHz
$\epsilon_r = 14$	44.0 MHz
$\epsilon_r = 16$	41.6 MHz

CST only allows to introduce either relative permeability or relative permittivity as a frequency-dependent value. Thus, for the relative permeability μ_r the measured frequency-dependent values are used. The main interest for beam dynamics simulations lies in frequencies up to 2 GHz, where the simulations do not show any major difference. Therefore, a constant relative permittivity ϵ_r of 16 was chosen for the MKE simulation model. Hence, one model reproduces heating observations and impedance measurements simultaneously.

Simulated influence of the serigraphy length on the impedance

As described before, shortening the serigraphy stripes by 20 mm reduces the heating of the kicker. This effect was anticipated in simulations by C. Zannini and initially

documented in [DFG$^+$14]. In Fig. 3.15 the simulated impedances of the MKE-S and MKE-L model described above with the different serigraphy length are shown. As expected from Eq. (3.5) the serigraphy's resonance frequency peak moves to higher frequencies for a shorter serigraphy. For the MKE-L and the MKE-S simulated resonance frequency values are documented in Tab. 3.4. The simulated shift in frequency is 5.0 MHz. To understand the effect of this shift on the heating, the power loss has to be considered as it is proportional to the heating. The bunch spacing of 25 ns in the SPS leads to beam spectrum peaks spaced by 40 MHz (see Fig. 2.4). The reduction of the serigraphy length moves the serigraphy's resonance peak away from the beam spectrum line at 40 MHz and thus lowers the power loss (Eq. (2.16)). The broadband impedance above 1 GHz on the other hand slightly increases for a shortened serigraphy, which is expected as the coupling between the serigraphy stripes becomes weaker. These effects of the shorter stripes on the impedance are confirmed by measurements (see below). In general, the broadband impedance of the MKE-S is higher than the one of the MKE-L. This can be explained due to the lower aperture height of the MKE-S.

Table 3.4: Simulated frequency of the MKE serigraphy resonance.

	MKE-L	**MKE-S**
200 mm serigraphy	41.4 MHz	42.6 MHz
180 mm serigraphy	46.4 MHz	47.6 MHz
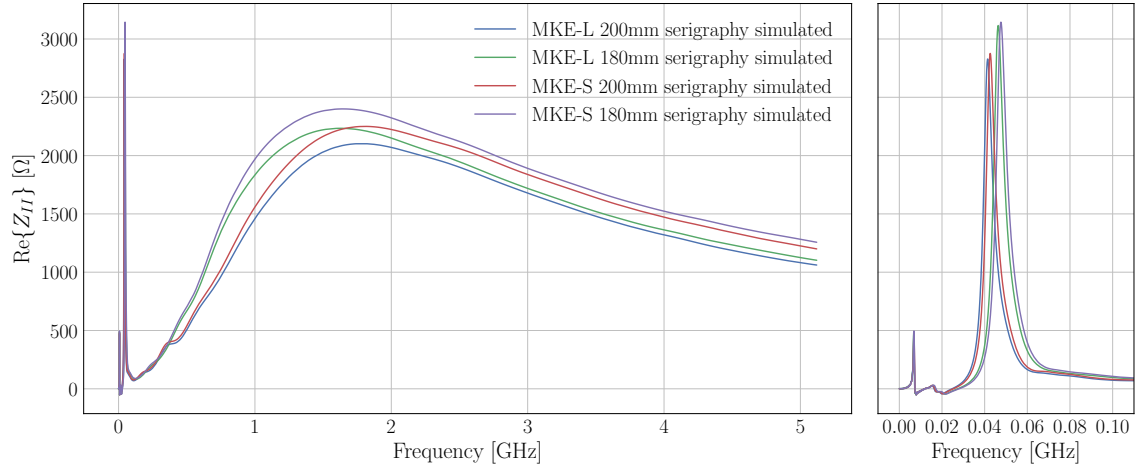
Figure 3.15: The simulated real part of the longitudinal impedance for MKE kickers with different serigraphy lengths. The serigraphy was modelled with the thin panel approach and the relative ferrite permittivity ϵ_r was always set to 16.

3.3.2 Measurements

Bench measurements were done to study the impedance of the kicker experimentally and to support the simulations. This subsection presents the bench measurements of the MKE done for this thesis. First, the measurements are reproduced in simulations to understand the correlation. Then, the measured impedance of the 200 mm and 180 mm serigraphy are presented. Finally, the effect of a connected HV bus-bar on the impedance is investigated in measurements.

Comparing measurements to simulations

To validate the simulations, the MKE kickers have been measured with the wire method introduced in Sec. 2.3 and discussed extensively in [CGD$^+$00, CMT00, KCG07] for the MKEs. The kickers were measured in their vacuum tanks. The wire was thus stretched through the tank and attached to two metal plates, which were flanged to the beam pipe connectors of the tank. The wire was streched in the same position as the circulating beam would travel when the kicker is inactive. It was resistively matched to the VNA used for the measurement by soldering a matching resistor to each of the wire's ends. The values of this matching resistor were found with Eq. (2.19). The characteristic impedance of the kicker was calculated with Eq. (2.21) where D is the distance between the HV- and the GND bus-bar as the formula is derived form a parallel plates conductor [MLGL92].

The first step to compare the measurements to simulations is to reproduce the complete measurement setup in simulations ("numerical measurement"). As the impedance is not measured directly but calculated from the S-parameters, it is important to understand the effects of this conversion. Therefore, an improved model representing the measurements was built in CST (see Fig. 3.16). The transition tapers [CMT00] from the tanks beam pipe connector into the kicker are added to the model in Fig. 3.10. To reproduce the measurements, a wire is used as a source. As in reality, the wire is simulated to be mounted on flanges closing off the tank. The matching resistors are implemented as lumped elements. The $S21$-parameter obtained from the time domain simulations is compared to measurement in Fig. 3.17.

The results are generally in good agreement. Again, the frequency dependency of the relative permittivity ϵ_r of the ferrite is clearly visible. For higher frequencies, a relative permittivity ϵ_r of 16 leads to a standing wave pattern due to a mismatch, but the resonance peak frequency seems to be perfectly reproduced. A relative permittivity ϵ_r of 12 does not show a mismatch for higher frequencies but does not satisfactorily reproduce the resonance peak at lower frequencies. From around 0.75 GHz to ca. 1.5 GHz the simulation differs slightly from the measurement. This can be attributed to measurement errors. To cover the worst case the simulated impedance is assumed from here on.

The peak at 1.75 GHz seen in measurements and simulations occurs due to the fact
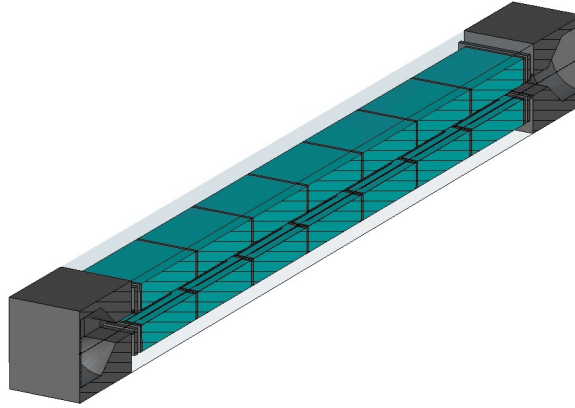
Figure 3.16: Model used to reproduce the measurement. To enable a view inside, the model is cut open through the center of the vertical plane for the plot. The wire is visible in the center of the aperture.
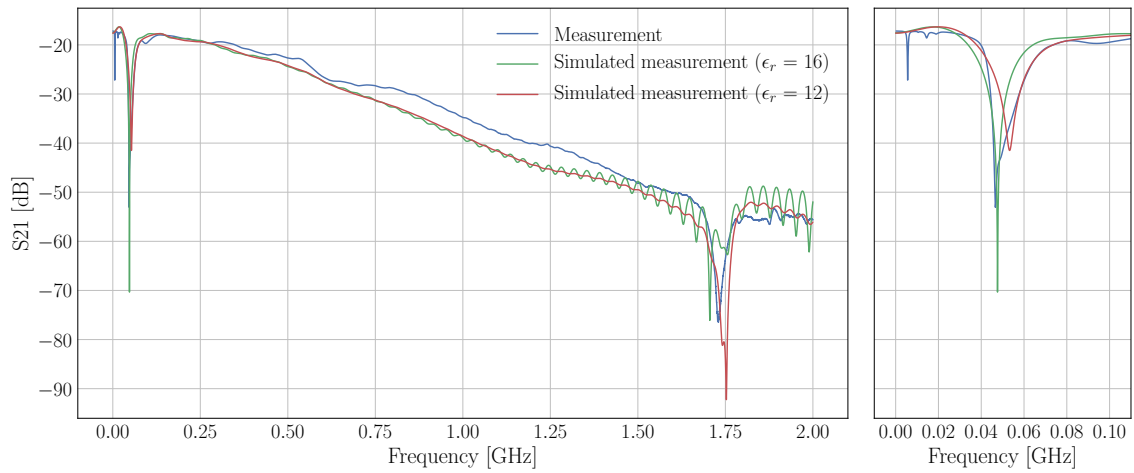
Figure 3.17: The measured $S21$-parameter of the MKE-L kicker with the $200\,\mathrm{mm}$ serigraphy compared to the one obtained from simulations of the measurement setup with the serigraphy modelled as thin panel material.

that the tank is closed by flanges for measurements. These flanges, in combination with the aperture taper from the round beam pipe to the square aperture of the tank, lead to a resonating cavity. When the tanks are installed in the machine these flanges are not present, so this peak is a measurement artefact and can be ignored.

To obtain the impedance curves, the $S21$-parameters displayed in Fig. 3.17 can be converted into an impedance using the LOG-formula (Eq. (2.3)). The improved LOG-formula presented in [Jen00] was also tested and gave similar results. In Fig. 3.18, the curves are compared to the wake field simulation of the regular model as shown

in Fig. 3.10 and the wake field results of the model for the measurement setup from Fig. 3.16 (the flanges are removed for that simulation). As a first observation, the two curves achieved by the wake field simulations are very similar. But the computation time for the regular model without the transition tapers is around 15 hours shorter. Hence, it is going to be used to simulate the impedance of the kicker. Another observation is that for frequencies above $0.75\,\mathrm{GHz}$, or for impedance values above $1000\,\Omega$, the LOG-formula introduces an error in the impedance. Comparing the transformed impedance to the wake field simulation results obtained with the same model, the difference becomes evident. From around $600\,\mathrm{MHz}$ on the two curves start to drift apart. Around $1.8\,\mathrm{GHz}$ the impedance obtained with the LOG formula shows impedance values that are approximately $500\,\Omega$ higher than the one obtained by the wake field simulation. Note that for the wake field results the peak at $1.75\,\mathrm{GHz}$ is not visible any more (no flanges) but a small bump at around $1.6\,\mathrm{GHz}$ arising from the transition taper is however noticeable.
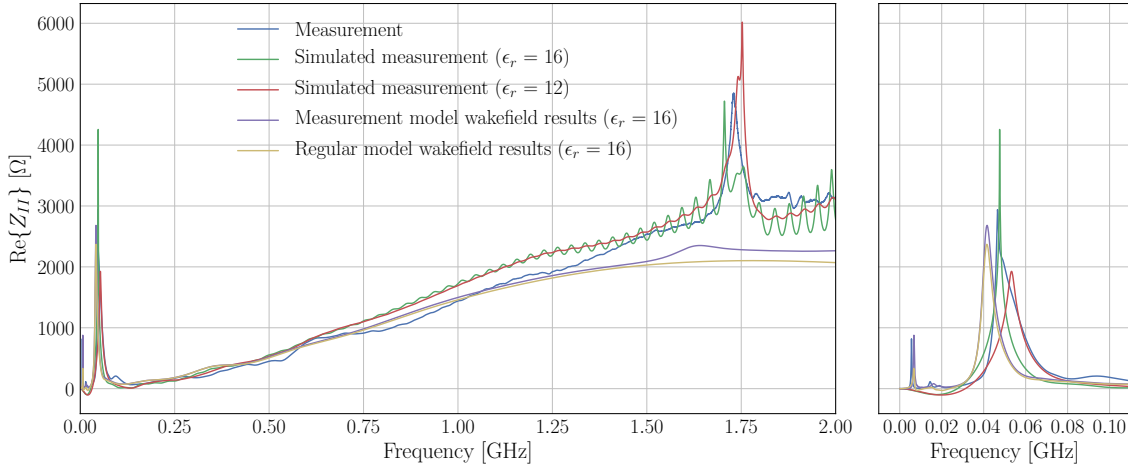
Figure 3.18: The measured real part of the longitudinal impedance from a MKE-L kicker with the 200 mm serigraphy compared to the one of the simulated measurement setup with the thin panel serigraphy. The $S21$-parameter are converted into impedance using the LOG-formula.

Comparing the serigraphy resonance frequency of the simulated measurement to the one of the wake field simulations a shift of $6.7\,\mathrm{MHz}$ is observed. This shift to higher frequencies for the measurement setup is due to the introduction of the wire, which influences the position of the resonance. Subtracting this shift in frequency from the measured resonance frequency of $46.6\,\mathrm{MHz}$ leads to a frequency close to the $40\,\mathrm{MHz}$ beam spectrum line.

Measured effect of the serigraphy length on the impedance

As already stated above, the comparison of the two different serigraphy lengths in measurements (see Fig. 3.19) supports the effects observed in simulations: The measured broadband impedance of the MKE-L with 200 mm serigraphy is lower than the one of the MKE-L with 180 mm serigraphy length. Also, the frequency of the 180 mm serigraphy resonance shifts to higher values. The measured resonance frequencies are collected in Tab. 3.5. In case of the MKE-L the peak of the 200 mm serigraphy at 46.6 MHz shifts by 5.8 MHz to 52.2 MHz for the 180 mm serigraphy, what is in good accordance with the shift predicted by simulations. The 1 MHz difference in resonance frequency, comparing the same serigraphy stripe length attached to the different kicker versions (see Tab. 3.4), is also measured.
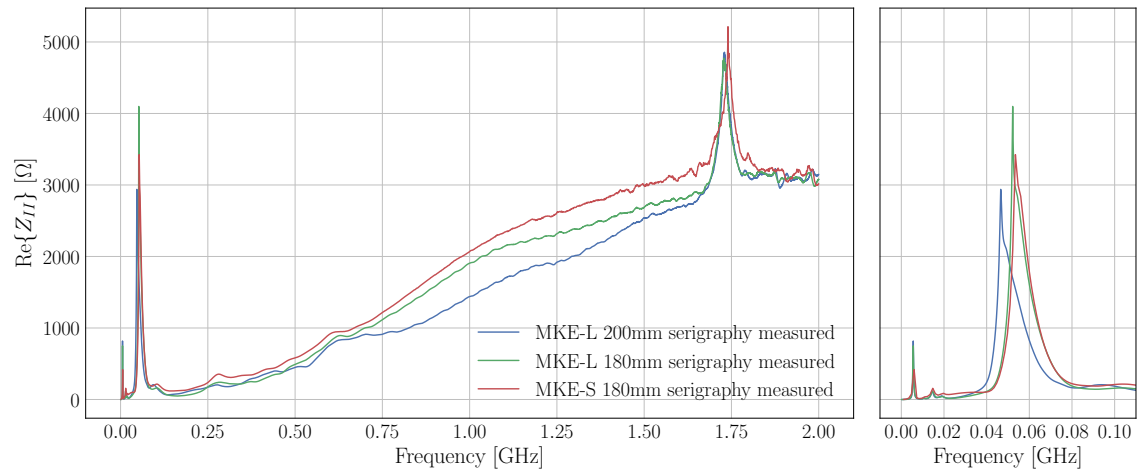
Figure 3.19: Measured real part of the longitudinal impedance of the two versions of the MKE kicker with the different serigraphy length attached. On the right-hand-side a zoom on lower frequency regions is attached. The impedance has been calculated out of the S-parameters by means of the LOG-formula.

Unfortunately it has not been possible to measure the MKE-S with the 200 mm serigraphy applied. The measurement of the MKE-S with the 180 mm serigraphy in Fig. 3.19 supports the observations of simulations that the broadband impedance of a MKE-S is slightly larger than the one of the MKE-L.

Table 3.5: Measured frequency of the MKE serigraphy resonance.

	MKE-L	MKE-S
200 mm serigraphy	46.6 MHz	-
180 mm serigraphy	52.2 MHz	53.5 MHz

Effect of a connected HV bus-bar

When installed in the tunnel, the HV bus-bar of the kickers is connected to a PFN via long cables. The other end of the HV bus-bar can be either terminated or short-circuited. Additional capacitors decoupling the HV plates clamping the ferrite blocks and creating the coaxial line characteristic of the kicker are also connected during operation. As the serigraphy is connected to the HV plates, these added loads could influence its resonance frequency. Theoretically neither the cables nor the capacitors have an impact on frequencies above several MHz, as the cutoff frequency of a MKE kicker cell (Eq. (3.4)) is in that order. To confirm this hypothesis, a MKE-L kicker with 200 mm serigraphy has been measured with attached cables, capacitors and different terminations of the HV bus-bar.

In Fig. 3.20 the measured S-parameters of three different scenarios are shown. It is clearly visible that the attachments hardly affect the measurement above a frequency of 100 MHz. The main difference is that the TEM mode at 10 MHz is damped for a short-circuited HV-bus-bar. This is expected as a short-cut conductor prevents a TEM from propagating. As all kickers are short-circuited in operation (see Tab. 3.2), the TEM mode peaks can be ignored. Overall, the attachment of cables, capacitors and the termination do not influence the S-parameters in the region of interest in a significant way. However, in the region from 0.75 GHz to around 1.5 GHz the S-parameters are slightly lower, approaching the measurement results to the curve obtained for the simulated measurement setup in Fig. 3.17 and thus validating the simulations additionally.
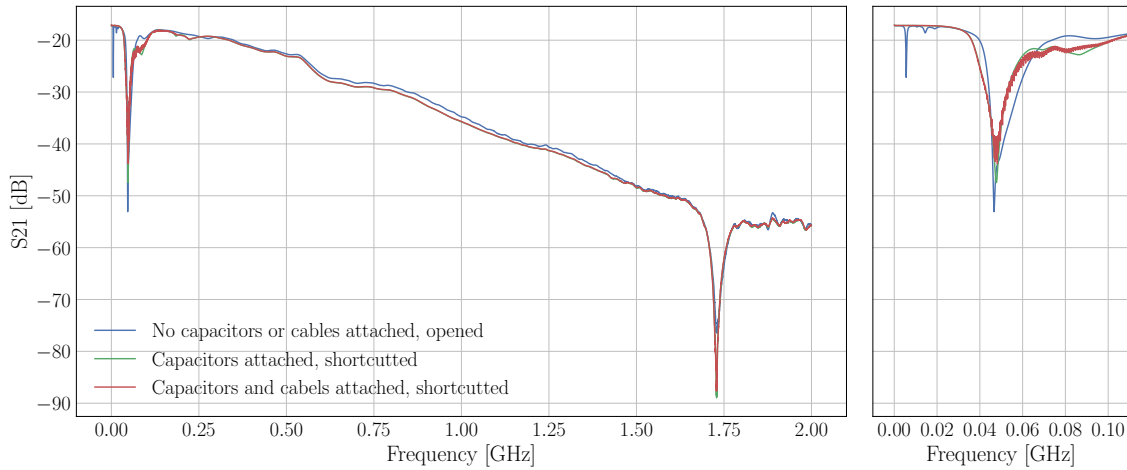
Figure 3.20: The measured $S21$-parameter of the MKE-L kicker with the 200 mm serigraphy attached. In the measurements the effect of the capacitors an cables connected during operation are investigated. Also different HV bus-bar terminations were measured. On the right-hand-side a zoom on lower frequency regions is attached.

Note that the measurements show two ambiguous peaks for the serigraphy's reso-

nance peak (bump on the right side of the resonance). This is due to the fact that a wire is introduced allowing a TEM mode propagating between it and the HV bus-bar. When the HV bus-bar is short-circuited, this mode disappears (see Fig. 3.20).

3.3.3 Impedance results of the final model

The kicker model as developed and benchmarked above was used to simulate the impedance of the MKE-L with the 180 mm serigraphy in all three dimensions, in longitudinal, horizontal and vertical. The final simulations use the following parameters and modelling approaches:

- **Ferrite:** Based on the measured, frequency-dependent relative permeability μ_r of the 8C11 ferrite with an relative permittivity ϵ_r of 16 and a conductivity σ_{Fer} of $1 \cdot 10^{-5}$ S/m.

- **Serigraphy:** Implemented as thin panel material and with a conductivity σ_{Ser} of $1 \cdot 10^7$ S/m.

For completeness the imaginary part which was not shown during the development of the model is now presented, as well. The results of further simulations and measurements executed within this thesis can be found in Appendix A.

First, the longitudinal impedance is presented in Fig. 3.21. The simulated impedances are compared to the impedance values measured on the modelled kicker. Again, a very good agreement between measurements and simulations can be observed, also for the imaginary part.

Second, as the kicker magnets significantly contribute to the broadband impedance of the SPS in all planes, the driving and detuning parts of their transverse impedance have been calculated for this thesis. The results are displayed in Figs. 3.22.

3.3.4 Power loss calculation and comparison to heating observation

To investigate the effect of the serigraphy length on the heating, the power loss values of the different models are calculated for the spectrum of the 25 ns beam described in Subsec. 2.1.2. This beam will be used for the filling of the HL-LHC with the intensities and horizontal bunch length (σ_z) evolution as displayed in Fig. 3.23.

The intensity is assumed to be $2.6 \cdot 10^{11}$ particles per bunch (ppb) at injection. The injection, acceleration and scraper losses are accounted for [1]. The evolution of the bunch length is plotted with the values as used for the power loss calculation. The power loss is calculated with Eq. (2.16) for every intensity / bunch length combination. These values are then averaged over the cycle. The power loss ratios obtained for the different serigraphy length in this manner are presented in Tab. 3.6.

---

[1]Uncaptured particles that are lost or removed.
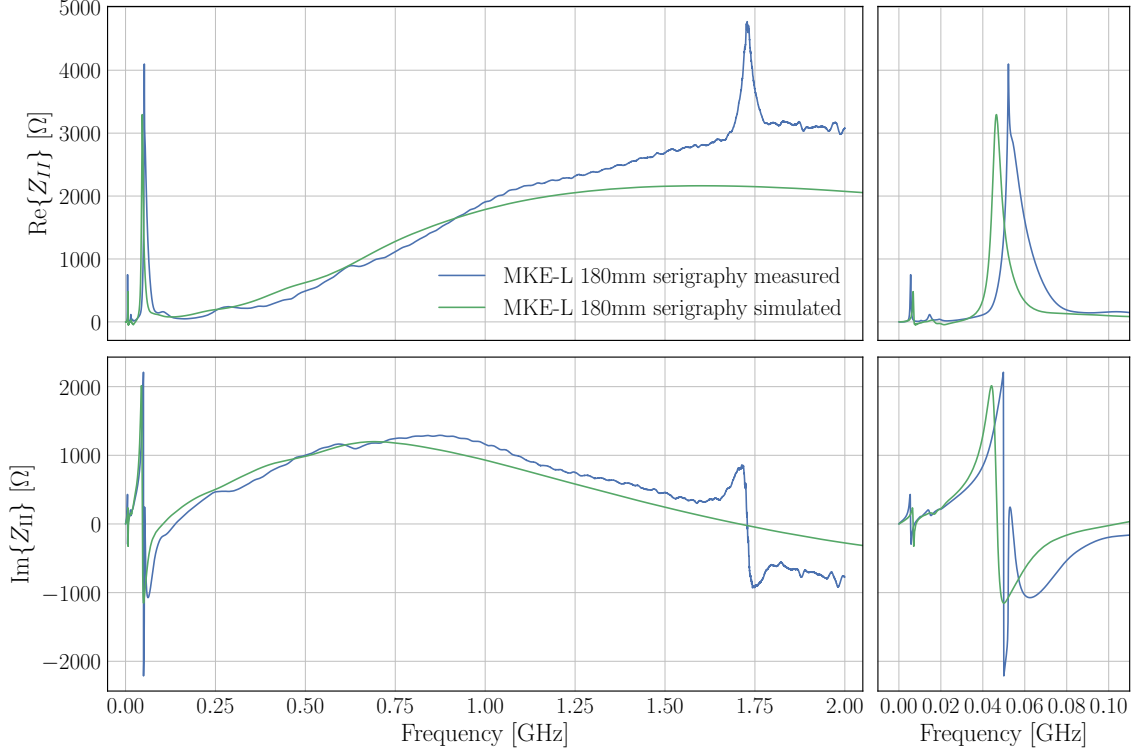
Figure 3.21: MKE-L 180 mm serigraphy: Comparing impedance measurements to the results of wake field simulations with the model shown in Fig. 3.10. The impedance of the measurement has been calculated from the S-parameters by means of the LOG-formula. On the right-hand-side a zoom on lower frequency regions is attached.

Table 3.6: Predicted difference in MKE power loss for the high intensity beam.

Power loss ratio	MKE-L	MKE-S
$W_{\mathrm{ser200}}/W_{\mathrm{ser180}}$	2.37	1.84

As the power loss is proportional to the heating, power loss ratios can be directly compared to heating observations in the machine. Comparing the power loss for the models with the 200 mm serigraphy to the power loss of those with the 180 mm serigraphy, shows an average power loss reduction by a factor of about two for the 180 mm serigraphy. This is in good agreement with the heating observations in the machine (Fig. 3.9).

The reason for this reduction in power loss is that the resonance peak of the 180 mm serigraphy is further away from the 40 MHz beam spectrum line. This can be visualised by plotting the beam spectrum together with the simulated MKE-L kicker impedances for different serigraphy lengths, as shown in Fig. 3.24.
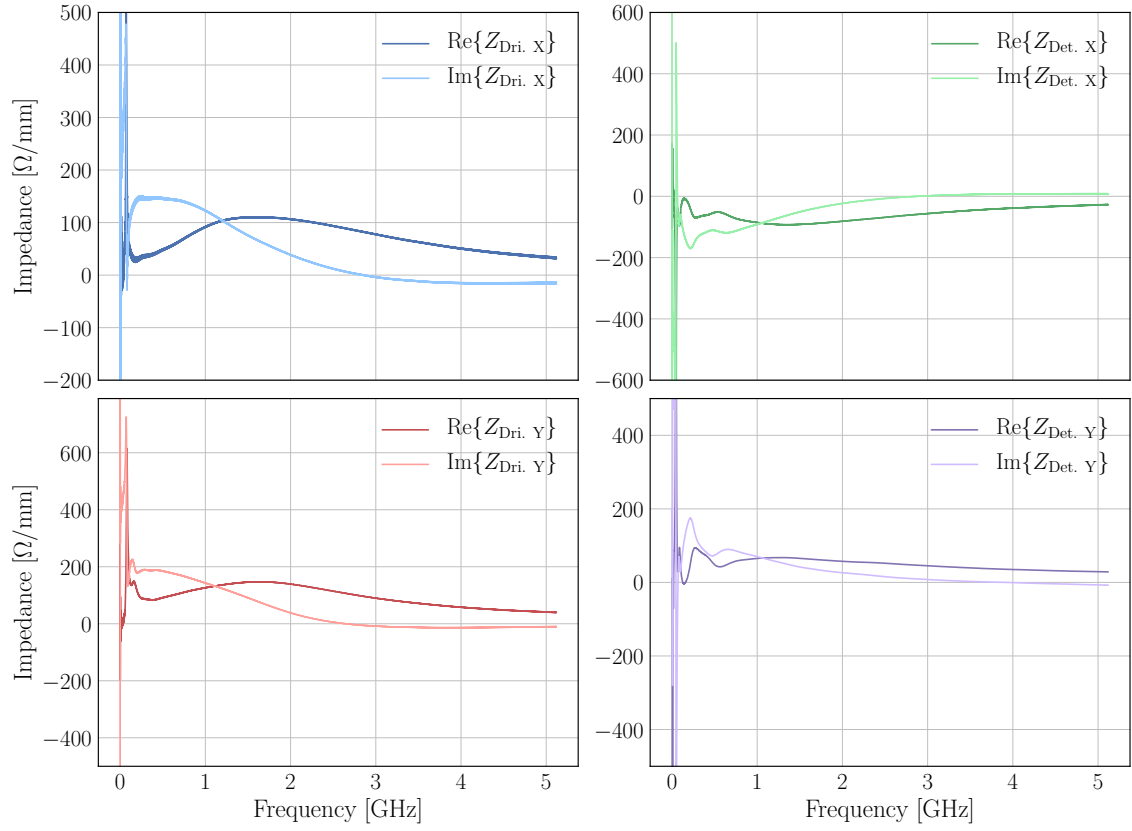
Figure 3.22: The simulated complex transverse impedance, driving and detuning components, of the MKE-L with the 180 mm serigraphy.
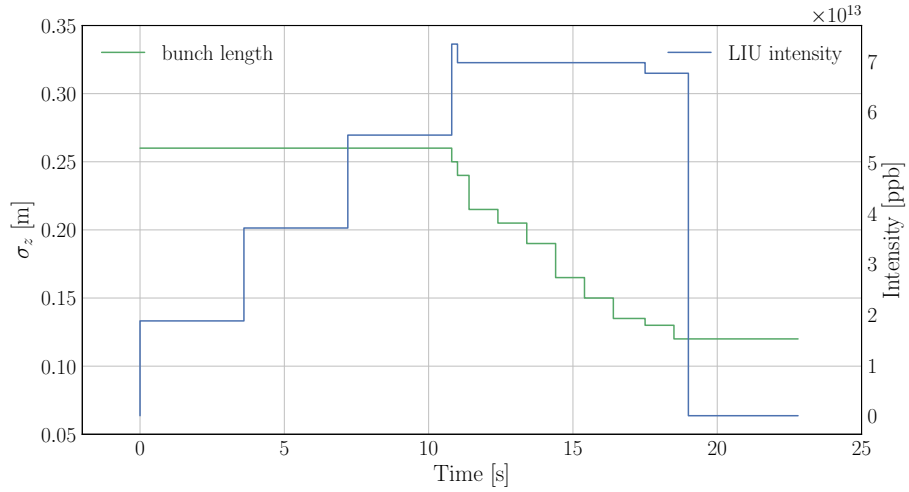
Figure 3.23: Mock-up of the LIU-SPS cycle for filling the HL-LHC.
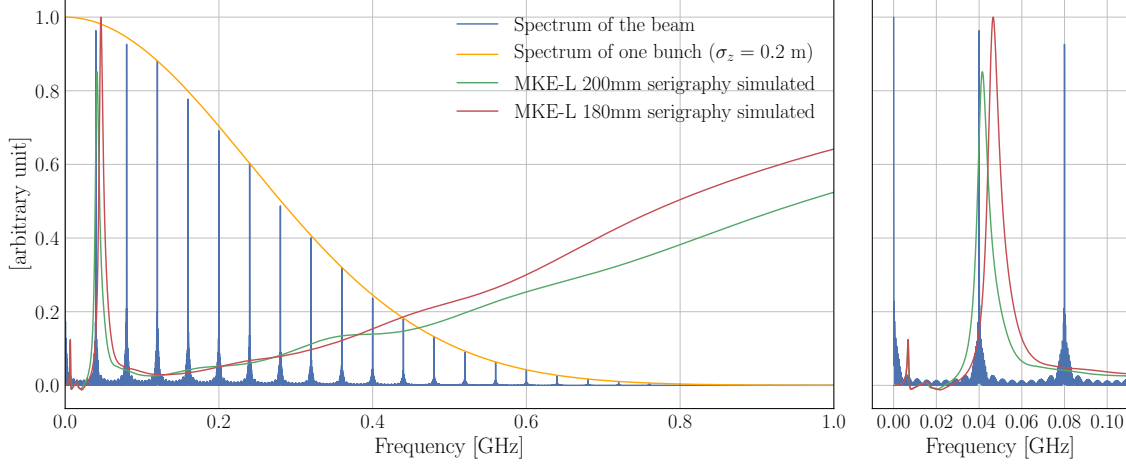
Figure 3.24: The spectrum of an LHC type 25 ns beam with Gaussian shaped bunches together with the simulated MKE-L kicker impedance for different serigraphy lengths. The zoom on lower frequency regions attached on the right-hand-side shows the reduction of the overlap between the beams spectrum and impedance for the 180 mm serigraphy length.

3.4 Investigation of the injection kicker

As discussed in Subsec. 3.2.2, the power loss in the MKP-L lead to limitations when operating the SPS with higher than nominal beam intensities. Ideally these kickers should be shielded from the circulating beam in a similar fashion as the MKEs. However, due to the shorter cell length of the MKPs, there is not enough space to install the serigrahy used in the MKEs. The coupling between the resulting stripes would be insufficient. Beside the reduction of the power loss in the kickers, a shielding of the four MKP-L kickers installed is also desirable because it could reduce the broadband impedance and increase the threshold for impedance-driven instabilities.

The simulation model for the MKP has been improved and validated with measurements in [Bec15]. The serigraphy adapted to the MKPs, originally proposed in the same thesis, consists of five stripes spaced by 12 mm as depicted in Fig. 3.25 (a). The serigraphy extends over the full kicker length and is connected to the transition plates installed between the MKPs and their vacuum tanks, to shield the cavity. To avoid any deterioration of the kicker function, an insulation between HV plates and serigraphy is essential. A good insulation is achieved by sliding a 2 mm thick alumina plate in grooves introduced into the GND- and HV bus-bar. Similar to the serigraphy, the alumina plate extends over the whole kicker length and is offset by 2 mm from the kicker's aperture surface. This creates a vacuum layer between the HV plates and the alumina plate that further improves the insulation.

For this thesis several aspects of the CST model have been updated:
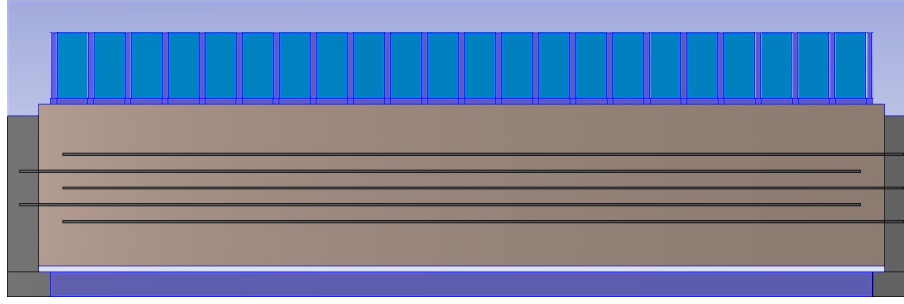
(a) Five stripes 12 mm spaced
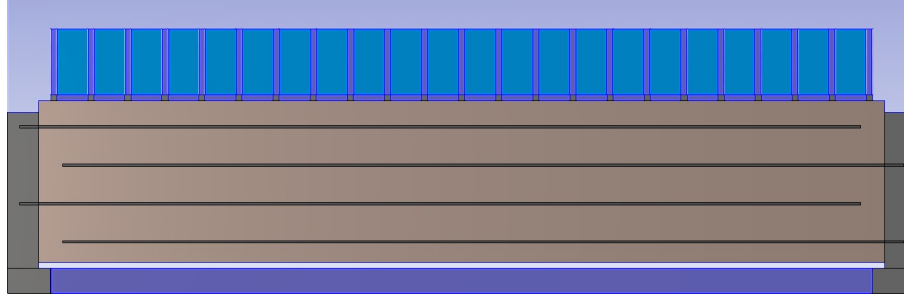
(b) Four stripes 30 mm spaced

Figure 3.25: The serigraphy layouts proposed for the MKP-L. For visualisation, the kicker is cut in the vertical plane, so the lower plane of the aperture is visible with the alumina insulation plate depicted in brown. Between the ferrite and the alumina plate a 2 mm thick vacuum layer expands for additional insulation. On the left / right side of the pictures the transition plates between the kicker and the tank, connected to the GND busbar, are shown. The serigraphy is electrically connected to them.

- The model of the 8C11 ferrite has been updated with the measured relative permeability μ_r values also used for the MKE.

- The serigraphy is now implemented as a thin panel material.

- Recent simulations of the MKP's field suggested a possible detrimental effect for a serigraphy layout that situates a stripe directly below and above the beam [ABD17, BFA$^+$12]. To overcome this limitation, a serigraphy with four stripes spaced by 30 mm is proposed in this thesis and shown in Fig. 3.25 (b). The wider spacing was chosen to avoid electrical breakdowns between the stripes.

The resulting impedance curves of the unserigraphed MKP-L and MKP-S kicker simulated with the updated model are depicted in Fig. 3.26. It is immediately visible why MKP-L shows higher temperature values than the MKP-S during operation (see Fig. 3.9). Its impedance contribution is higher at frequencies where the beam spectrum (Fig. 2.4) extends, which leads to a higher power loss (Eq. (2.16)). The

frequency of the TEM mode excited between the bus-bars is dependent on the length of the kicker and thus at a higher frequency for the shorter MKP-S.
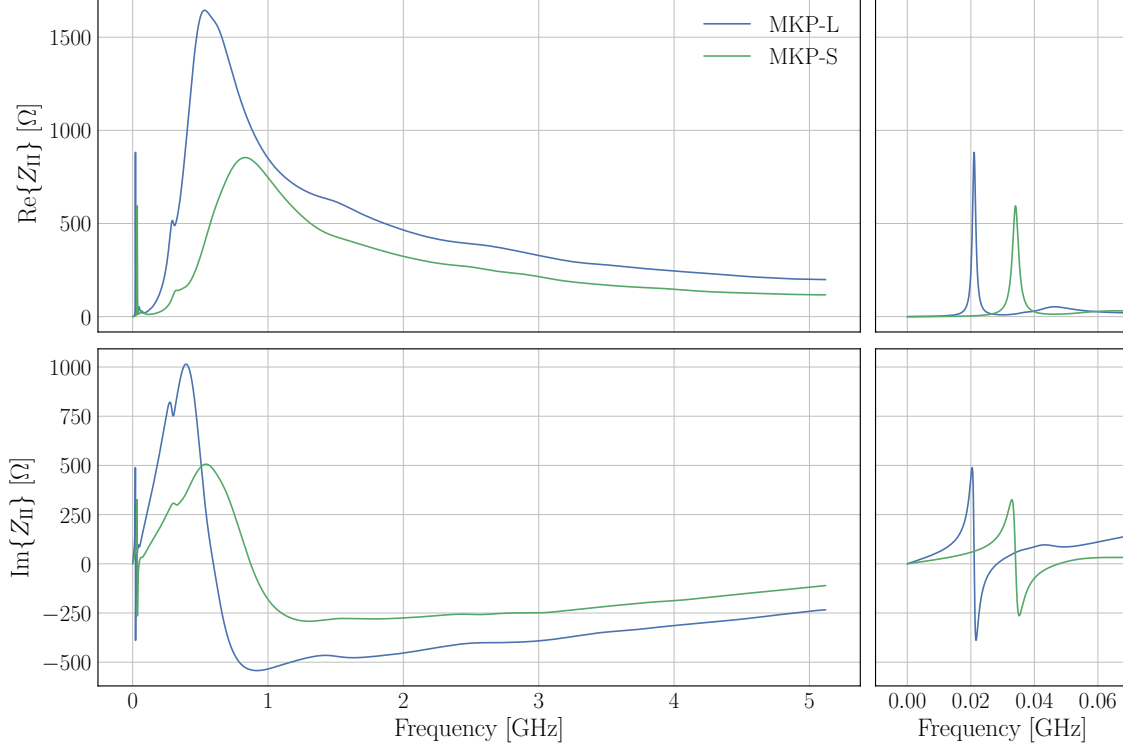
Figure 3.26: Simulated impedance curves of the MKP-L and the MKP-S. On the right-hand-side a zoom on lower frequency regions is attached.

The simulated impedances of the MKP-L equipped with the different serigraphy layouts shown in Fig. 3.25 are compared in Fig. 3.27. For frequencies below $1.2\,\text{GHz}$, they both reduce the impedance with respect to the unserigraphed kicker, which leads to a reduction of the power loss for both cases. The serigraphies introduce a resonance peak in addition to the resonance of the TEM mode excited between the two bus-bars. As all resonances are far enough disparate from the first beam spectrum line at $40\,\text{MHz}$ they are not expected to contribute to the power loss.

The power loss in this case is therefore only dependent on the broadband impedance in the region of the beam spectrum. Hence, the power loss of a kicker shielded with the five stripes serigraphy is lower than the one of a kicker shielded with the four stripes serigraphy. This is visible in Tab. 3.7 where the power loss ratio for the two serigraphy layouts is reported. The five stripes layout reduces the power loss more effectively than the four stripes layout. The power loss here is computed for one LIU SPS cycle as explained in Subsec. 3.3.4.

The proposed serigraphies would also be beneficial for the instability threshold in the SPS, as they shift the broadband longitudinal impedance of the MKP-L
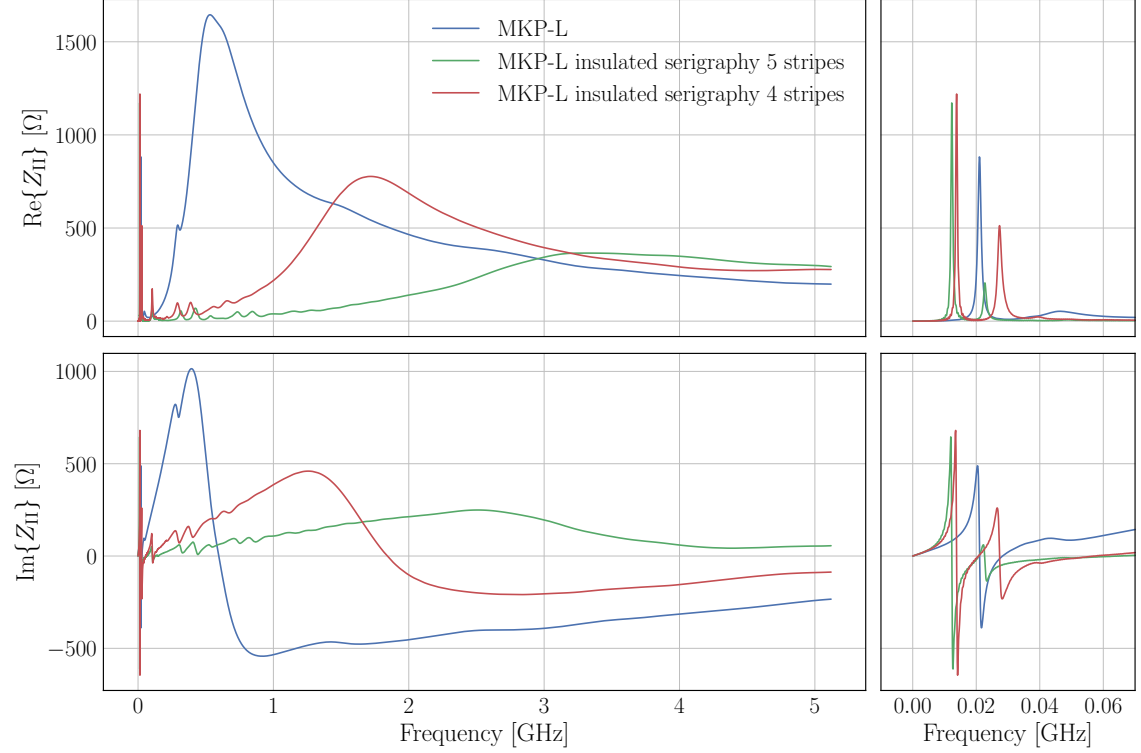
Figure 3.27: Comparison of the simulated impedances of the MKP-L kicker not serigraphed and with the two proposed serigraphy layouts installed. On the right-hand-side a zoom on lower frequency regions is attached.

Table 3.7: Predicted difference in MKP power loss for the high intensity beam.

Power loss ratio	MKP-L
$W_{\mathrm{noser}}/W_{\mathrm{ser5stripes}}$	20.8
$W_{\mathrm{noser}}/W_{\mathrm{ser4stripes}}$	8.0

to frequencies further away from the beam spectrum. However, the broadband impedance of the serigraphed kicker at frequencies over $3\,\mathrm{GHz}$ worsens. This should not influence the intensity threshold due to longitudinal instabilities as it is far away from the beam spectrum, but has to be further studied in longitudinal beam dynamics simulations for certainty.

The transverse impedance of the unshielded MKP-L and of the MKP-L shielded with the five and four stripes serigraphies, respectively, are shown in Figs. 3.28, 3.29 and 3.30. The impedance reduction die to the shielding is visible also in both transverse planes. The simulation of the MKP-L with a wake length of $500\,\mathrm{m}$ and 10.5 million mesh cells, as used for the computation of the longitudinal and transverse

impedances, on a 16 cores HPC node described in Sec. 2.2 lasts approximately 16 hours.
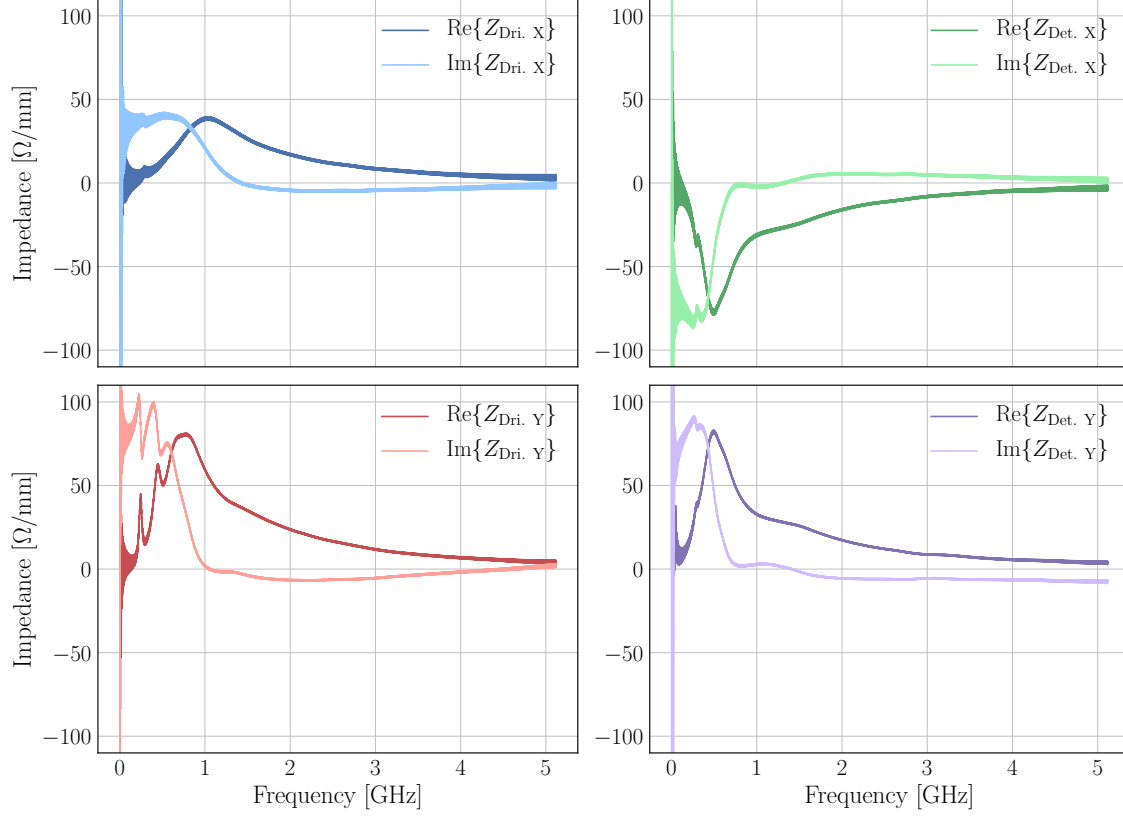
Figure 3.28: The simulated complex transverse impedance, driving and detuning components, of the MKP-L without serigraphy.
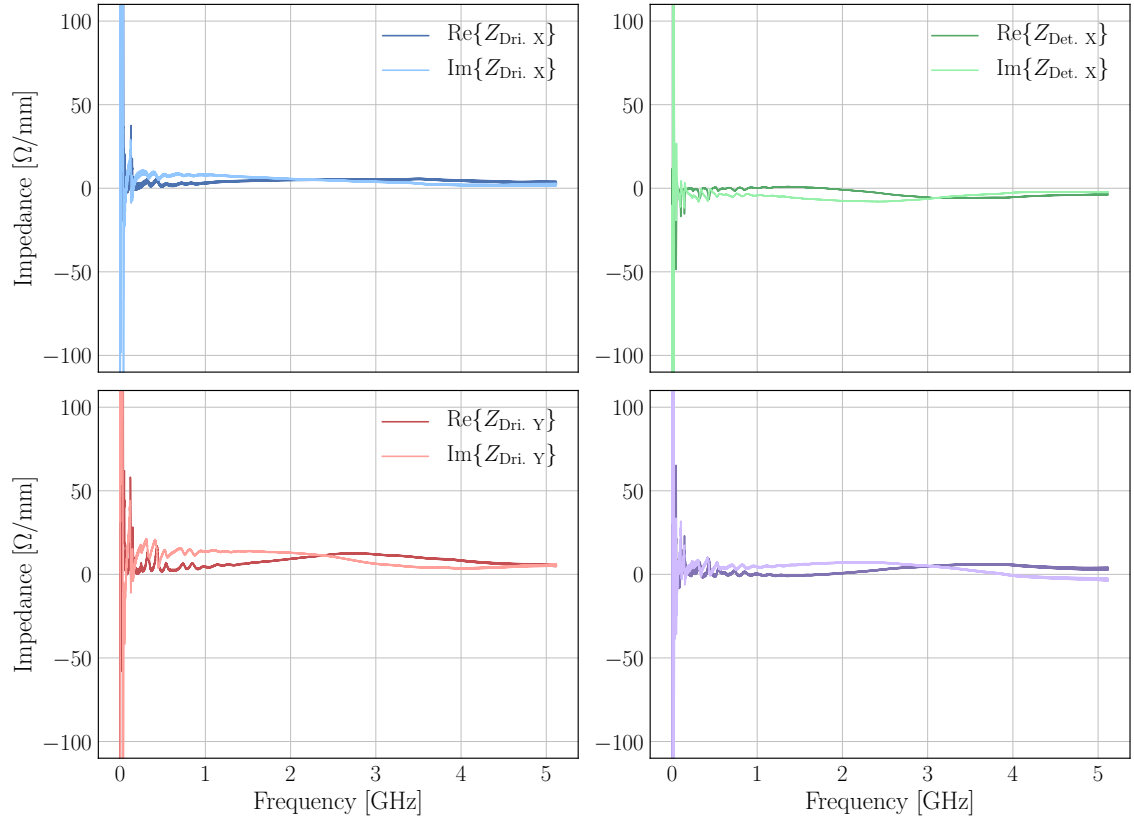
Figure 3.29: The simulated complex transverse impedance, driving and detuning components, of the MKP-L with the insulated 5 stripes serigraphy.
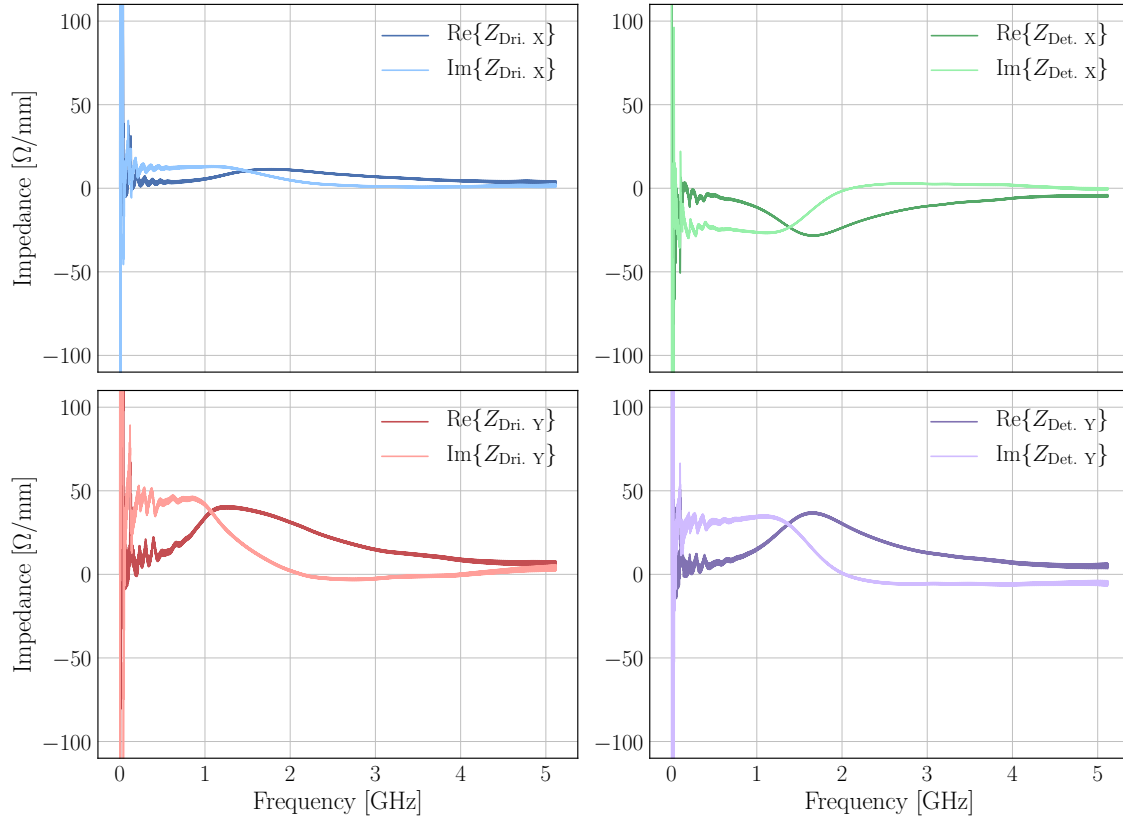
Figure 3.30: The simulated complex transverse impedance, driving and detuning components, of the MKP-L with the insulated 4 stripes serigraphy.

3.5 The Electrostatic Septa (ZS)

In addition to the two fast extraction schemes in the SPS for the LHC beams, with the MKE kickers discussed in the section above, a slow multi-turn extraction scheme is in place to deliver beam to the fixed target experiments. This extraction scheme relies on a series of five Electrostatic Septa (ZS) (In the SPS Z indicates electrostatic systems and S stands for septa). The septa provide a field-free region for the circulating beam, and a region with a deflecting field for the beam to be extracted. The regions are separated by vertical wires, shielding the circulating beam from the electrostatic field. The tanks are also equipped with cleaning electrodes, supposed to catch secondary particles (electrons or ions) that are released when beam particles hit the aperture or the wires. The cleaning electrodes are realised by plates, extending above and below the beam. They are electrically separated and connected to different potentials creating an electrostatic field between them. Due to problems with sparking and the resulting high vacuum activity, a general upgrade of the ZS system has been launched [BBBR16]. This also includes an improvement of the impedance performance. The upgrade will be installed during the Long Shutdown (LS) lasting from end of 2018 to beginning of 2021 (LS2). The current and upgraded ZS chains are depicted in Fig. 3.31. Two major changes are visible:

- The shielded vacuum pumps currently mounted in between the tanks have been moved under the tanks.

- The connecting round beam pipe is replaced by a flat one, the so-called racetrack beam pipe with a flat aperture and rounded walls left and right.

For this thesis, approaches to reduce the impedance for the upgrade have been investigated. The results of the impedance simulations and calculations of the current as well as the upgraded setup are presented here. The beam is always simulated in its circulating position.

In this section, first the different interconnects situated between the tanks and depicted in Fig. 3.31 are studied in terms of methods to reduce their contribution to the impedance. Second, the tanks themselves are investigated with the same goal. Finally, the interconnects and the tanks are combined to compare the impedance of the complete ZS as it is currently installed to the impedance of the upgraded version. To ensure the reproducibility of the results the technical drawings of all the components discussed in this section can be found in Appendix C.

3.5.1 Upgrade of the interconnects

First, the interconnects between the five septa tanks have been investigated. After the current one, four versions proposed for the update have been studied. They
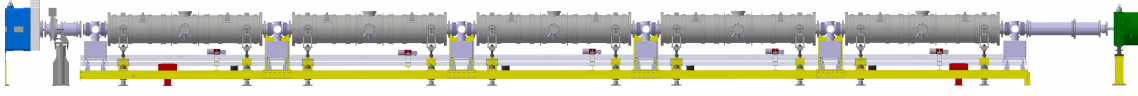
(a) Current setup
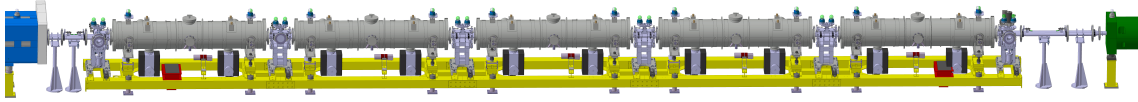
(b) Post-LS2 setup

Figure 3.31: The complete ZS extraction chain in the SPS pre- (a) and post- (b) LS2. The beam travels from left to right. Downstream, a quadrupole is visible and upstream the a device (a metallic mask) protecting the next quadrupole from missteered beams. [Courtesy: Bruno Balhan]

differ in the beam instrumentation equipment that they accommodate. The different versions are summarized in Tab. 3.8. The simulation of those interconnects lasts up to six hours for a model with 3.5 million mesh cells on a HPC node with 16 cores described in Sec. 2.2.

Table 3.8: Overview of the interconnects for the ZS upgrade.

Interconnect*	beam instrumentation equipment installed
ST0734834	No instrumentation (only racetrack beam pipe).
ST0734696	One beam profile scanner (horizontal).
ST0728011	One grid for one shot transverse beam profile measurements.
ST0733918	Two beam profile scanners (horizontal and vertical).

* The interconnects are identified by their CERN equipment number here.

Current interconnect

Currently, massive 215 mm internal diameter round beam pipes, with two T-shaped instrumentation flanges attached on each side, are used. Their CST simulation model is shown in Fig. 3.32. In reality EM-shielded vacuum pumps are attached to the flanges facing downwards. They are assumed to be perfectly shielded and therefore not considered in the simulations. Beside most of the flanges conceived for housing beam instrumentation, most of them are not used and act as massive cavities contributing to the impedance of the machine because of trapped modes. As the aim of simulating the current interconnect is only to form an idea of a reference

impedance, all flanges are closed with metal for the simulations. The two bellows that are part of the interconnect have a larger internal radius than the beam pipe and create additional cavities.

(a) Complete view   (b) Horizontal cut
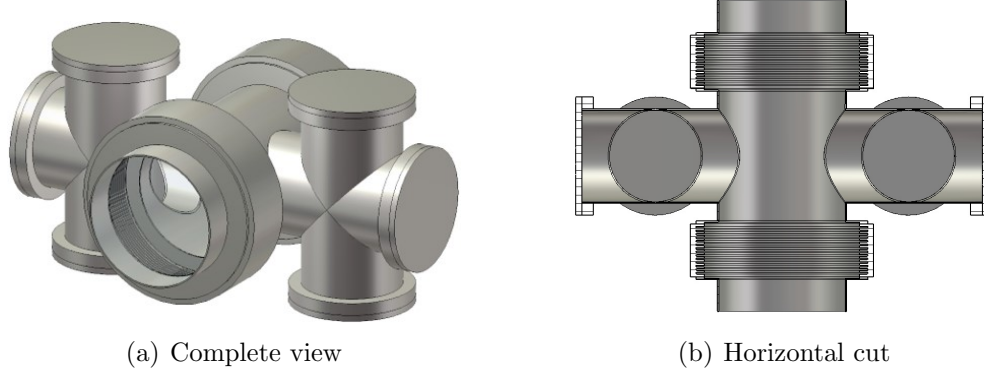
Figure 3.32: The current interconnect between the ZS tanks. On the right, a cut through the horizontal plane is shown. The beam is passing through the middle from bottom to top.
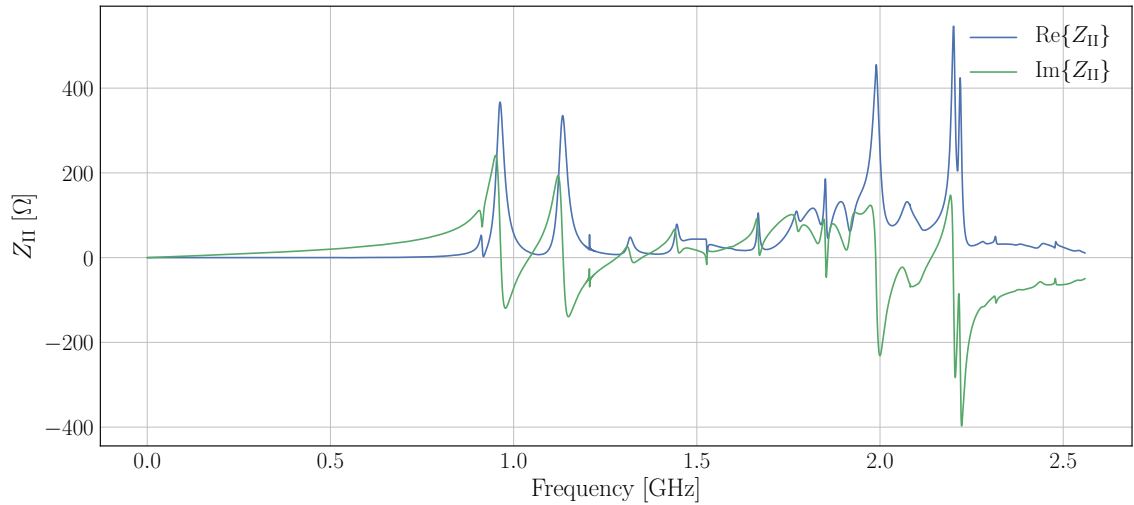
Figure 3.33: Simulated impedance of the current ZS interconnect.

The simulated impedance of this structure is shown in Fig. 3.33. From around 0.90 GHz, very close to the beam spectrum, contributions to the impedance are visible. The cut-off frequency f_c of the beam pipe is around 820 MHz. The first high peak in the simulated impedance spectrum at 0.96 GHz is the contribution of the fundamental mode of the cavity created by the bellows. As six of those interconnects are installed, their contributions add up. For the current interconnect, the frequencies

of all modes are above the cut-off frequency of the beam chamber. In this case the power can also dissipate through the ports, an effect which is not taken into account in eigenmode simulations. For this reason, eigenmode simulations of this model are con only indicate the positions of the resonance peaks, but cannot correctly predict the impedance. Their wake field simulations have been optimized in cooperation with CST AG in Darmstadt, Germany, to converge to reliable results.

Racetrack beam pipe interconnect

A first step to reduce the impedance in general is to smoothen the transition from the round beam pipe to the flat rectangular aperture of the septa. With the ZS upgrade, the interconnects are changed to the racetrack beam pipe, a flat aperture with rounded walls left and right, as shown in Fig. 3.34. The bellows, mounted to align the tanks during installation in the machine, follow the same type of aperture now. As no vacuum pumps need to be attached to the interconnect any more, no flanges are needed. The cut-off frequency of this type of beam pipe is found at 720 MHz. The simulated impedance of this interconnect is plotted in Fig. 3.35. The only impedance contribution in the region of interest up to 2.5 GHz, is the resonance frequency of the cavity created by the bellows at 2.26 GHz.

(a) Complete view
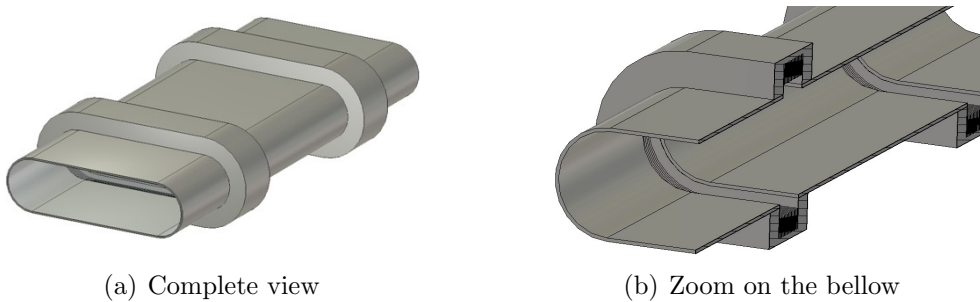
(b) Zoom on the bellow

Figure 3.34: The racetrack beam pipe interconnect. On the right, a vertical cut through the bellows is shown.

Racetrack beam pipe interconnect with one horizontal scraper

In three of the six interconnects, beam instrumentation is necessary to investigate the shape of the extracted beam if needed. To add the instruments to the racetrack aperture ZS interconnect, a cylindrical tube housing the beam instrumentation tools is inserted in between the two bellows, as shown in Fig. 3.36. The rod holding the scraper (the part of the instrument that interacts with the beam) can scan through the extracted beam over multiple shots and determine the horizontal beam profile. The rod is driven by an engine that is flanged vacuum tight to the left side of the tube. The engine is ignored in the simulations because it is perfectly shielded. The scraper
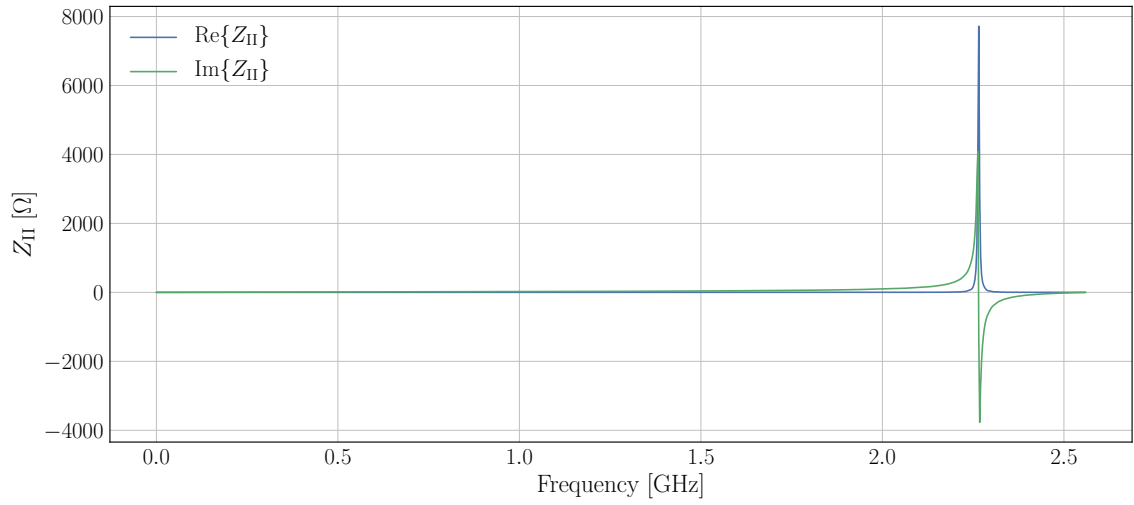
Figure 3.35: Simulated impedance of the racetrack beam pipe interconnect.

tool is simulated in its parking position. As the measurement is destructive and the beam is dumped after measurements, other scenarios do not need to be considered. In Fig. 3.37 the impedance of this interconnect is presented. The tube orthogonal to the beam introduces multiple modes down to approximately $1.2\,\mathrm{GHz}$. Especially the first two modes contribute a higher impedance than the bellows discussed before.

(a) Complete view   (b) Horizontal cut
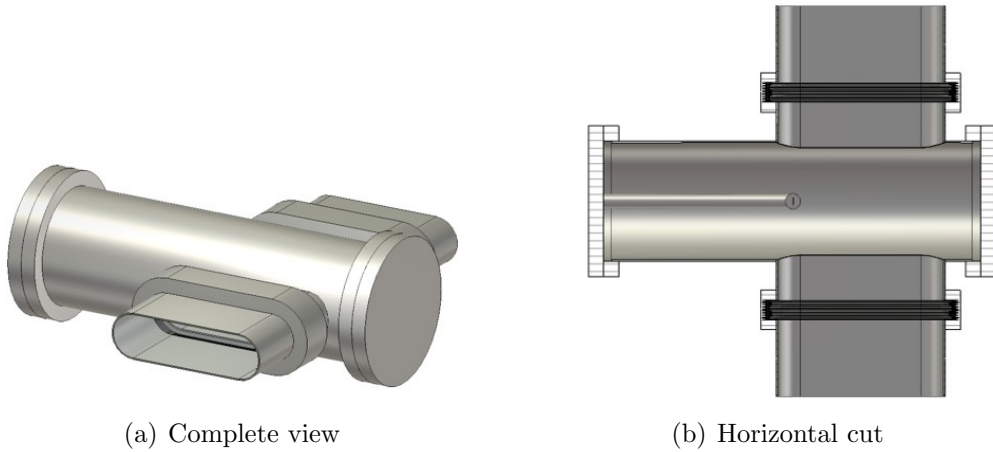
Figure 3.36: The racetrack beam pipe interconnect housing a horizontal beam profile scanner for the extracted beam. On the right, the horizontal cut is shown. The beam is passing from bottom to top.

To avoid the creation of these modes a shield is proposed. The shield should hide the tube from the beam, but the instrumentation has to move in and out as needed. In addition, notches are required to enable the vacuum pumps to evacuate the area
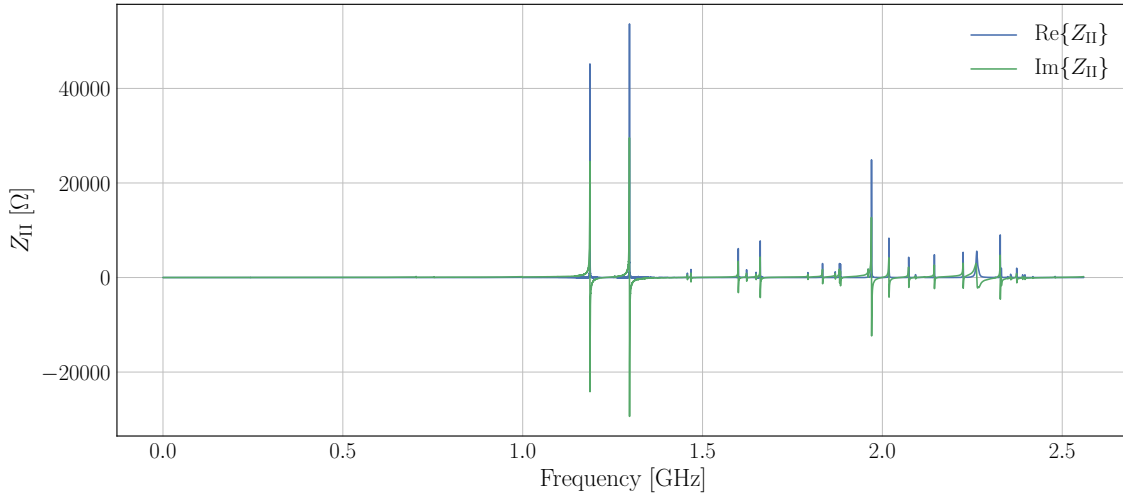
Figure 3.37: Simulated impedance of the racetrack beam pipe interconnect housing a horizontal beam profile scanner for the extracted beam.

behind the shield sufficiently fast. The resulting shield is shown in Fig. 3.38(b). The notches for vacuum pumping are executed in the form of stripes, as drilled holes could lead to small breakdowns introduced by the image current. The movement of the beam instrumentation is accounted for by a recess. The shield will be welded into the tube to ensure perfect electrical contact. The impact on the simulated impedance is remarkable (see Fig. 3.39), as only the already observed bellows mode at 2.26 GHz remains.

(a) Complete view
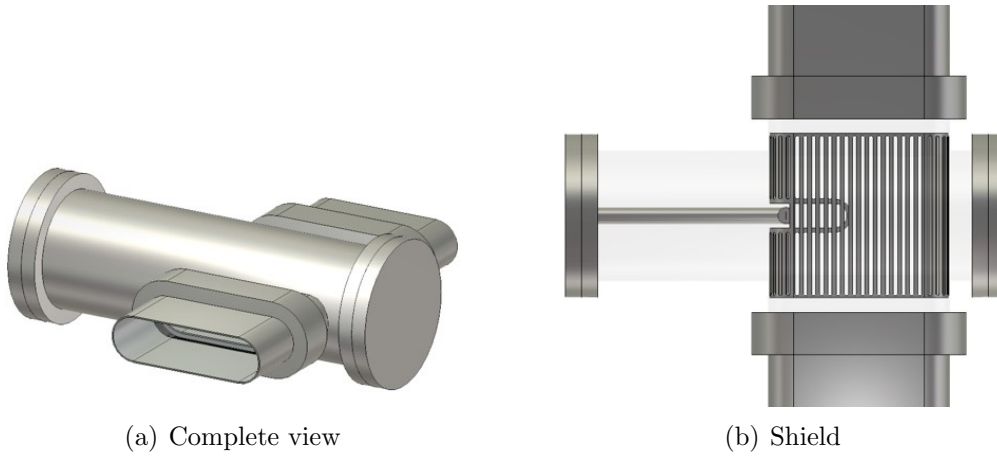
(b) Shield

Figure 3.38: Simulated impedance of the racetrack beam pipe interconnect housing a shielded horizontal beam profile scanner for the extracted beam. On the right, the horizontal cut is shown. The beam is passing from bottom to top.
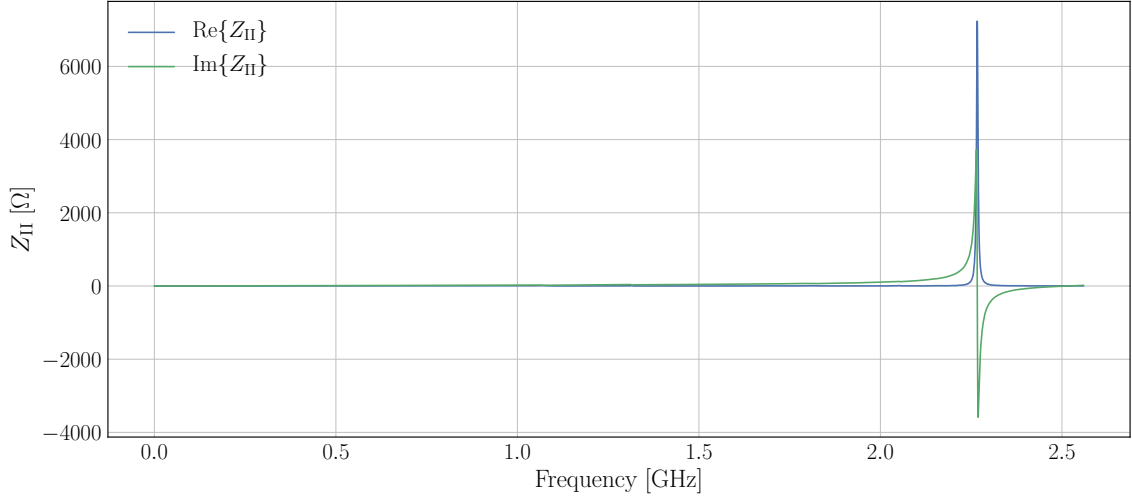
Figure 3.39: Simulated impedance of the racetrack beam pipe interconnect housing a shielded horizontal beam profile scanner for the extracted beam.

Racetrack beam pipe interconnect with a grid

Another interconnect houses a grid that allows measuring the transverse beam profiles in one shot, as shown in Fig. 3.40. As the support of the grid is substantial, it requires a larger cut into the shield, as depicted in Fig. 3.40(b). The simulated impedance of this shielded interconnect housing the grid is plotted in Fig. 3.41. The spectrum now shows multiple modes besides the known mode at 2.26 GHz. Investigating the excited modes in CST shows that they are trapped between the support of the grid and the shield. As only one of the interconnects is supposed to house a grid and these modes are relatively weak they can be tolerated. Notable is also that, due to the fact that only one bellows is mounted to this interconnect, the resonance peak at 2.26 GHz is only half as high as the peak from an interconnect with two bellows (for example, see the standard racetrack interconnect without instrumentation in Fig. 3.35).

The additional tube connected to the right of the interconnect in Fig. 3.40 models an attached vacuum valve. If shielded from the beam, no contribution to the impedance is observed.

Racetrack beam pipe interconnect with two scrapers

The last interconnect houses a horizontal and a vertical beam profile scanner. The shield for the interconnect in Fig. 3.38(b) is therefore adapted with a second recess and shown in Fig. 3.42(b). The simulated longitudinal impedance of the resulting model is plotted in Fig. 3.43. Again, the results only show the bellows mode so the second recess does not degrade the shield. As one bellows is used, the impedance of

(a) Complete view   (b) Shield
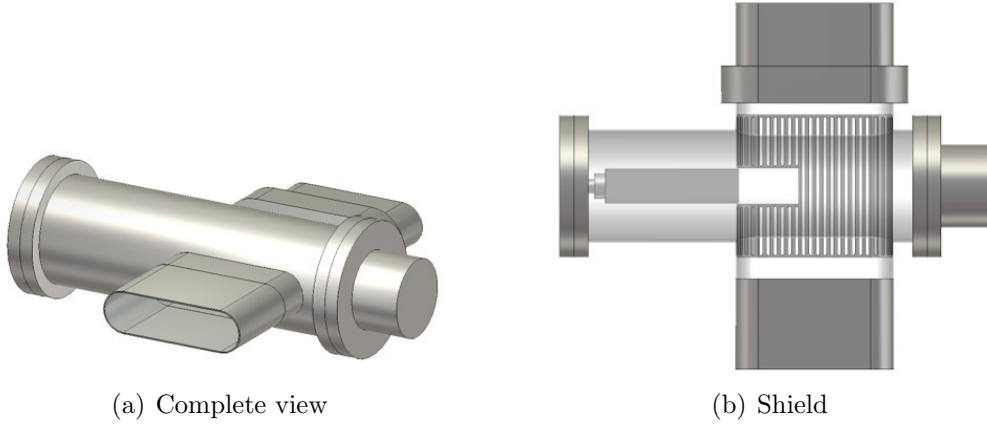
Figure 3.40: The racetrack beam pipe interconnect housing a shielded grid for horizontal beam profile measurements in one shot. On the right, the horizontal cut is shown. The beam is passing from bottom to top.
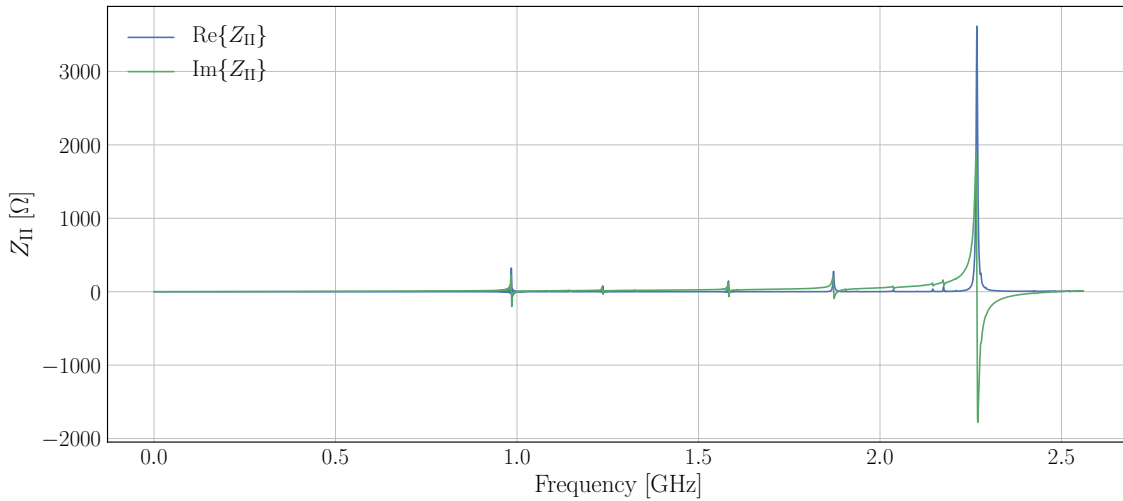
Figure 3.41: Simulated impedance of the racetrack beam pipe interconnect housing a shielded grid for horizontal beam profile measurements in one shot.

this mode is again ca. $4\,\text{k}\Omega$.

Mitigation of the bellows mode

With the different shields, the impedances of all the new ZS interconnects are dominated by the bellows resonance frequency peak. The bellows are compressed or stretched when installed in the machine. This however does not influence the frequency of the mode trapped in the bellows as the frequency of a pillbox cavity is only dependent on the radius/height of the cavity and not on its length. In total,

(a) Complete view

(b) Shield

Figure 3.42: The racetrack beam pipe interconnect housing a horizontal and a vertical shielded beam profile scanner for the extracted beam. On the right, the horizontal cut is shown. The beam is passing from bottom to top.
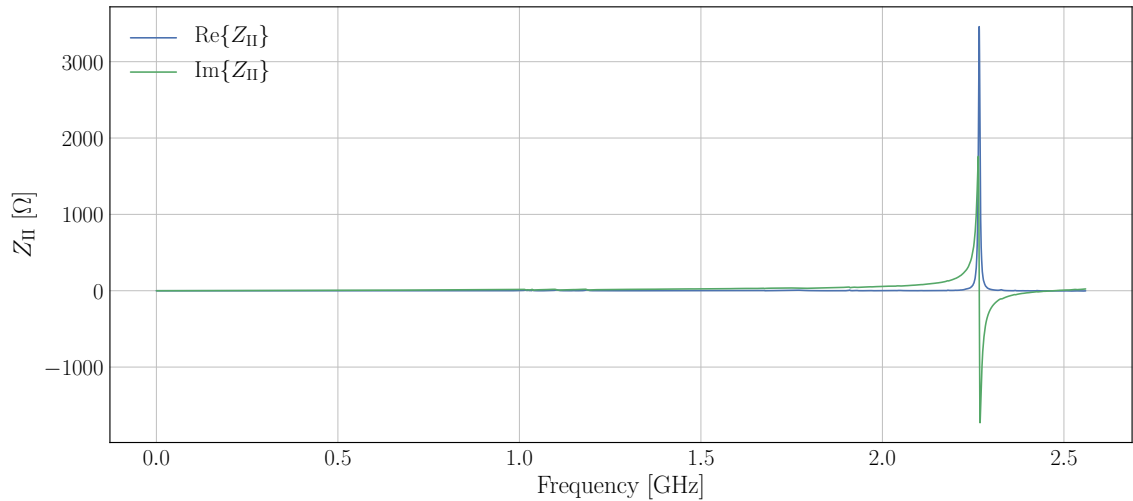
Figure 3.43: Simulated impedance of the racetrack beam pipe interconnect housing a shielded horizontal and vertical beam profile scanner for the extracted beam.

ten bellows will be installed in the post-LS2 ZS (three times the racetrack beam pipe interconnect and one of each of the different beam instrumentation housing interconnects). If all of the impedance contributions add up, the height of the bellows could have a large impact.

To move this frequency to higher values, the offset between the beam pipe and the bellows, i.e. the height of the bellows, should be varied. The influence of this height on the resonant mode's frequency is investigated in the following. A reduction of the bellows height should not only shift the resonance frequency further away from the

beam spectrum but should also increase the damping of the mode. The damping of a resonant mode can be expressed by its dimensionless quality factor Q. It is defined as the ratio between the average energy stored in the mode and the energy lost per second [Poz12]. Thus, the higher the Q value of a mode is, the less the mode is damped. In this context the R/Q factor, which is found by dividing the impedance of a mode by its Q factor, is also used to characterize modes.

The impact of the bellows height on the impedance is demonstrated on the standard racetrack interconnect without beam instrumentation as shown in Fig. 3.34. The simulated impedance results plotted in Fig. 3.44 show the expected shift of the resonance frequency to higher values for cavities with a lower height. Wake field simulations are compared to eigenmode simulations in the same figure to validate the height of the resonance peak. As the bellows mode is trapped, eigenmode simulations are adequate also above f_c. The reduction in impedance due to the degraded Q values is observed in both eigenmode and wake field results. Therefore, it was decided to produce all bellows with a height of 1 mm. For the 1 mm bellows the resonance frequency is at 2.46 GHz and the mode has a Q value of 3800 (from eigenmode simulations).
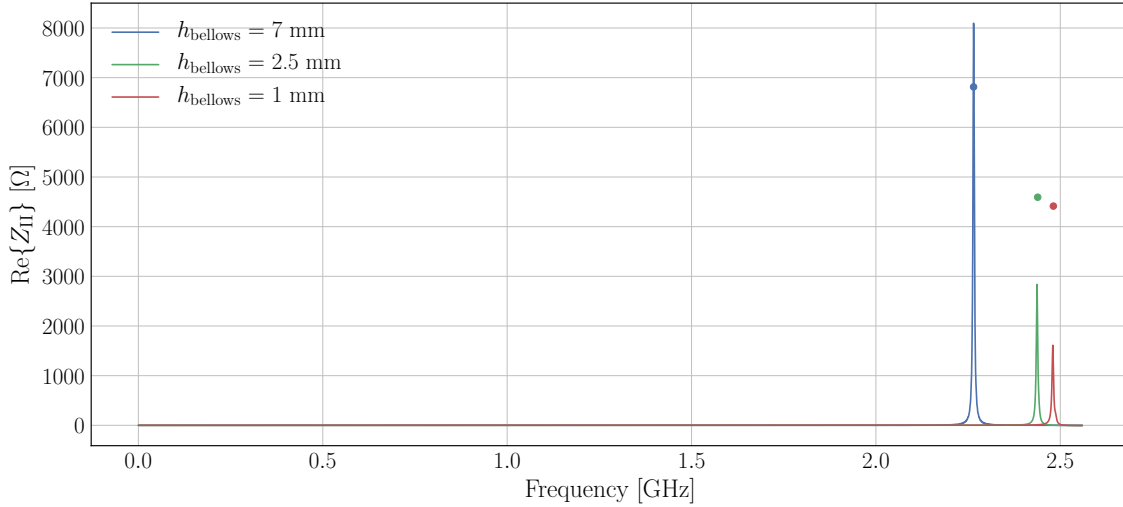
Figure 3.44: Simulated impedance of the impedance for the interconnect shown in Fig. 3.34 for different heights of the bellows. The drawn lines were obtained by wake field simulations and the dots represent the impedance values of the resonant modes calculated from eigenmode simulation results.

To crosscheck the CST eigenmode simulations they were compared to eigenmode simulations in HFFS [ANS]. The values in Fig. 3.45 show a nearly perfect agreement.
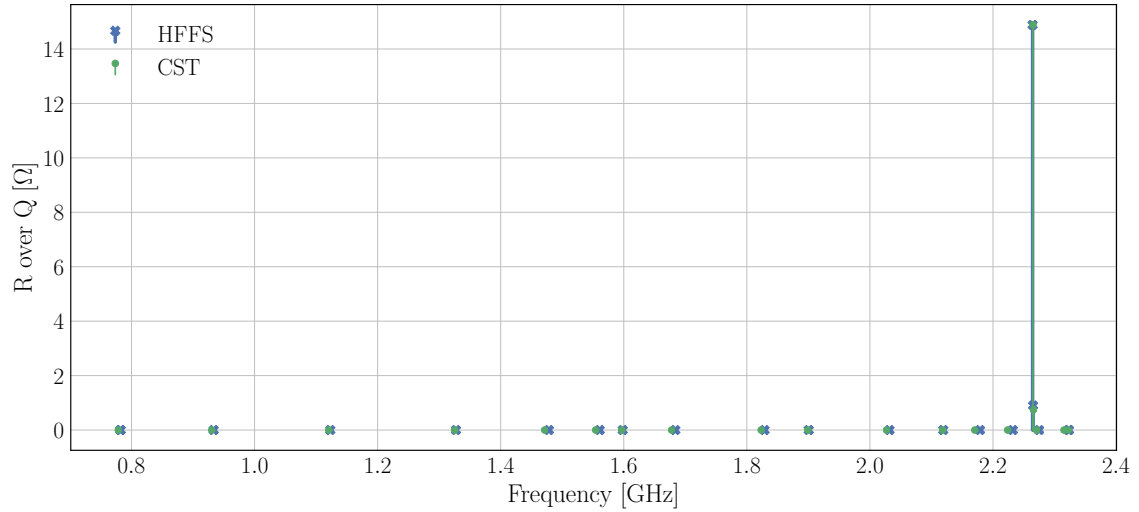
Figure 3.45: Comparison of the R over Q value obtained by eigenmode simulations in CST and HFFS for the interconnect shown in Fig. 3.34 with a h_{bellows} of $7\,\text{mm}$.

3.5.2 Upgrade of the tanks

The main structural change to the tanks housing the septa is the already mentioned shift of the vacuum pumps, which will be now installed beneath the tank. These pumps, as well as the ports connecting them, are shielded and therefore not taken into account in the simulations. Otherwise, the simulation model of the ZS tank includes the complete septa, including the wires shielding the field as well. All material parameters are modelled as in reality. For the upgrade of the ZS, a shield was designed to further reduce the impedance by screening the whole tank from the beam. This tank shield is shown in Fig. 3.46. The RF contacts are compressed against the flange of the tank to ensure a constant path for the image current from the updated racetrack aperture interconnects into the septum. The effect of this shield on the tank impedance has been studied for this thesis.

Figure 3.47 shows the impact that this shield has on the simulated impedance of one tank. Most important is that for frequencies up to $0.75\,\text{GHz}$, where the beam spectrum has its main contribution, nearly all modes have been strongly damped. Investigating this effect shows that most of the modes are excited in between the extensions of the cleaning electrodes (see Fig. 3.46) and radiate into the tank. With the attached tank shield, the fields of these modes are shielded from the tank and damped. Removing the extensions of the cleaning electrodes, but leaving the tank shield attached, leads to an even lower impedance. However, these extensions are mandatory to achieve the demanded field uniformity and removing them is not an option. As the vacuum pumping ports are neglected, the two impedance curves in Fig. 3.47 show the tank impedance before and after the ZS upgrade, with the
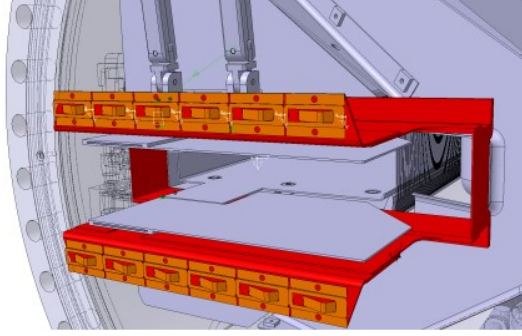
Figure 3.46: The shield proposed to screen the beam from the ZS vacuum tank is marked in red. Inside the shield, on top and bottom the extensions of the cleaning electrodes to catch secondary particles are visible. [Courtesy: Bruno Balhan]

green one being the upgraded tank impedance. Simulating the around 3 m long ZS tanks with 15 million mesh cells and a wake length of 200 m on a 16 core HPC node described in Sec. 2.2 needs around 17 hours .

The simulations of the ZS tank could not be validated by wire measurements for the following reasons: Compared to the MKE, which has mainly broadband impedance contributions, the tank accommodates a lot of high Q modes excited in cavities created by insertions. The introduction of a wire changes the modes in these cavities to TEM modes and a measurement would not fully represent the real structure.

3.5.3 Simulation of the complete ZS chain

For beam dynamics simulations the interest lies in the impedance of the whole ZS chain. The chain is composed of five tanks in series, each one being 3 m long and connected through the interconnects, as shown in Fig. 3.31. The accumulated length makes the simulation of the whole system in CST hardly possible. The possibility of scaling the impedance of one tank up to the full chain has been studied for this thesis and is presented in the following.

The connection of two tanks through one interconnect is shown in Fig. 3.48 (a) for the current ZS setup and in Fig. 3.48 (b) for the upgraded ZS setup. Comparing the two pictures, the changes realized for the ZS upgrade, namely the new interconnect aperture and the tank shield, are well observable. It has been calculated that the updated interconnects, despite their reduced size, will not lead to any aperture restriction for the SPS beam and thus will not impact beam dynamics neither in the horizontal nor in the vertical plane.

To investigate the possibility of scaling the impedance, twice the impedance of one tank was compared to a chain of two tanks. The two tanks of the chain were connected through an interconnect, as that is how they are installed in the machine
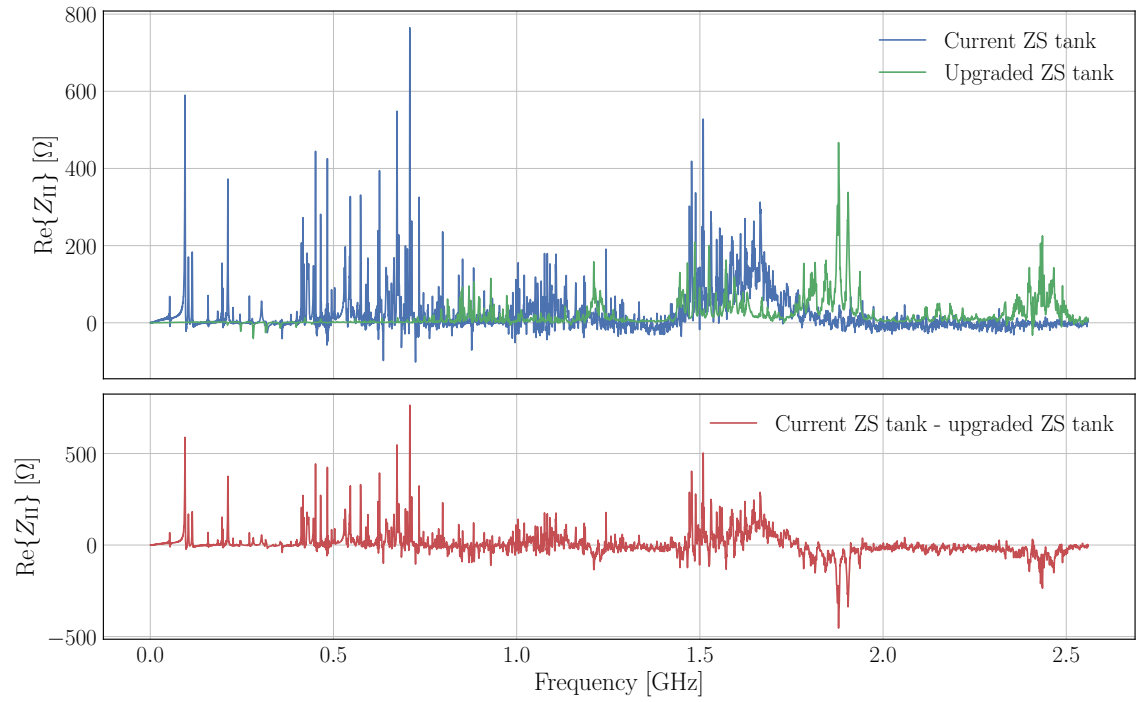
Figure 3.47: Simulated real part of the tank impedance tank with (upgraded version), and without (current version) the tank shield shown in Fig. 3.46. The difference of the curves in the upper plot is shown in the lower one.

(a) Current setup

(b) Updated setup
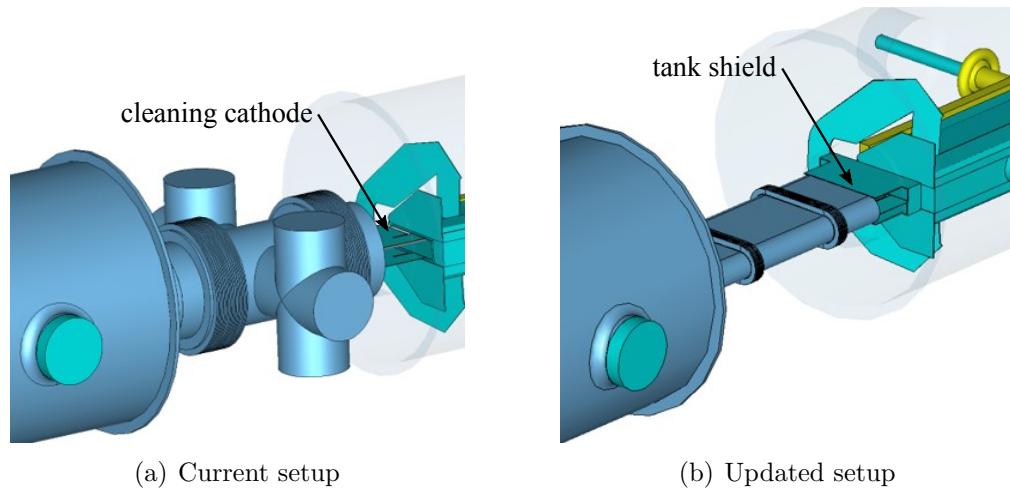
Figure 3.48: Two ZS tanks with an interconnect before and after the upgrade. Here, as an example, only the connection between two tanks is shown.

(see Fig. 3.48 (a)). In addition, interconnects were also attached to the far ends of both tanks. For a better description of the simulated arrangement henceforth an interconnect will be represented by IC and a tank by TA. The two-tank chain arrangement described above is then identified by: IC-TA-IC-TA-IC. The simulated impedance of this arrangement with the current tanks and interconnects is compared to the summarized impedance of one current tank multiplied by the factor two and of the current interconnect multiplied by three in Fig. 3.49. The results are found to be significantly different. This is expected, as the attached interconnects have an additional effect on the beam and may couple with the tanks above their cut-off frequencies. This could influence the resulting impedance.
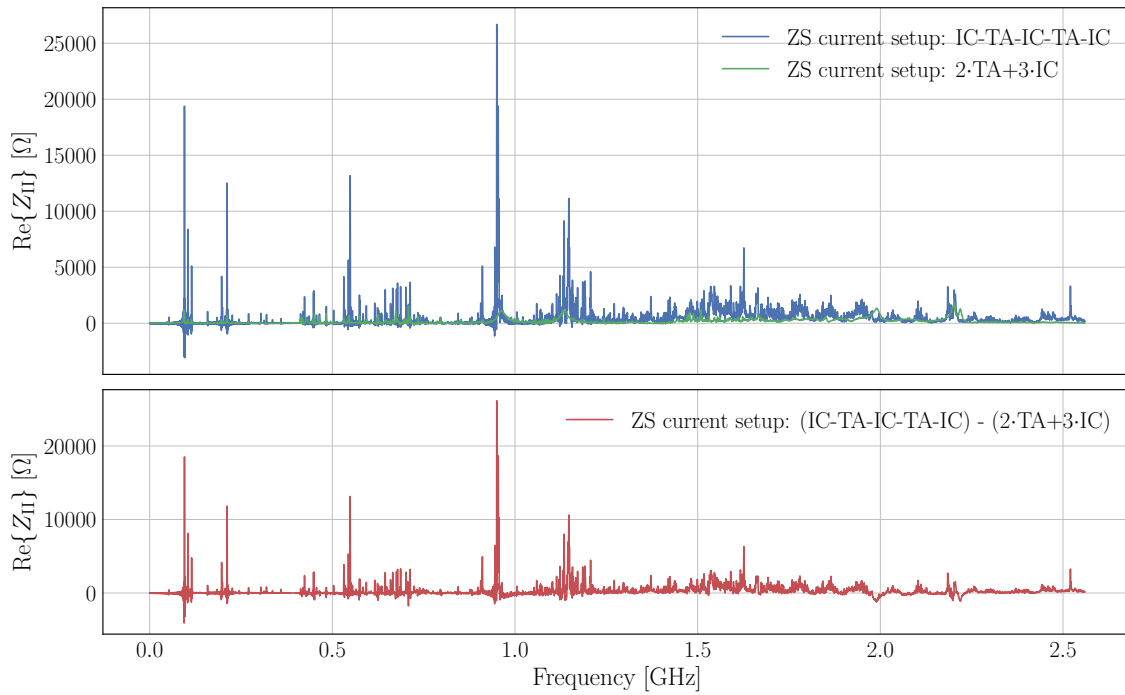
Figure 3.49: The doubled simulated impedance of one tank is compared to the simulated impedance of two tanks connected and terminated by interconnects. Tanks and interconnects as currently installed in the SPS were simulated. The difference of the curves in the upper plot is shown in the lower one.

Therefore, to achieve scalability, the interconnects have to be taken into account. The simulated impedance of the IC-TA-IC-TA-IC arrangement is compared to the simulated impedance of an IC-TA-IC arrangement, meaning one current tank with one interconnect attached at each end. The impedance results of these simulations are plotted in Fig. 3.50. Generally, a good agreement is observed. Frequencies under $0.75\,\mathrm{GHz}$ show identical results, which is important because the beam spectrum has its largest contribution in that frequency range. At higher frequencies there are

differences. This observation can be explained as follows: Doubling the impedance of one IC-TA-IC arrangement, leads to a contribution of four interconnects to the impedance, whereas the IC-TA-IC-TA-IC arrangement considers only three interconnects as in reality. As the interconnect currently installed only contributes to frequencies above 0.75 GHz (see Fig. 3.33), the effect only occurs in that frequency regime. But also a slight frequency shifts through coupling above the cut-off frequency of the interconnects and /or numerical errors occur. This is visible in the difference curves in Fig. 3.50 where the real parts of the peaks at 950 MHz in the first plot show a difference of about $10 \, k\Omega$ but the difference plot of the real part shows values of $\pm 25 \, k\Omega$.

The same scaling was done for the upgraded setup of the ZS chain shown in Fig. 3.48 (b). To double-check the scalability of more tanks, the IC-TA-IC-TA-IC arrangement was compared to an IC-TA-IC-TA-IC-TA-IC-TA-IC arrangement. Here, only the standard racetrack beam pipe interconnects without beam instrumentation were used. The simulated impedances of these two scenarios are compared in Fig. 3.51, where the result of the simulation with four tanks is divided by two. Again, a very good accordance is observed for frequencies below the cut-off frequency of the interconnect beam pipe. The peak of the 1 mm bellows resonance frequency shifts to 2.55 GHz when the interconnect is attached to the tank. This peak also shows the largest disagreement of ca.400 Ω in the first plot of Fig. 3.51, as the contribution of five bellows is compared to the contribution of six bellows. Here again a frequency shift above. The drift of the imaginary part can be attributed to numerical errors occurring when calculating the impedance out of the wake functions (see Sec. 2.2).

The studies presented above show that the impedance of the complete ZS chain can be found by scaling one tank terminated by two interconnects (IC-TA-IC). The simplification that this method represents in terms of simulation time and resources is very significant. For example the simulation of the IC-TA-IC-TA-IC-TA-IC-TA-IC arrangement (4 tanks) takes 105 hours with a wake length of 300 m and 67 million mesh cells on the 16 core HPC node described in Sec. 2.2. The IC-TA-IC arrangement with 18 million mesh cells the same wake length on the same type of HPC node only takes 29 hours. When assuming a computing time of 29 hours per tank, the scaling approach reduces the simulation times by a factor of five.

To reduce the simulation time of the already demanding simulations the wake length for the scaling investigations was chosen to be 300 m. Thereby the wake did not completely decay for the model of the current setup, which was tolerated to reduce the simulation time. The final results of the current model were obtained by simulations with a wake length of 3 km. Simulations of the IC-TA-IC arrangement with the 3 km long wake and 36 million mesh cells takes 544 hours on the HPC node introduced in Sec. 2.2. If a symmetry plane can be defined (possible for all simulations except for those of the driving and detuning components in the vertical plane) the number of mesh cells reduces to 18 million and the simulation is finished after 278 hours. As the generated wake of the updated model decays faster, due
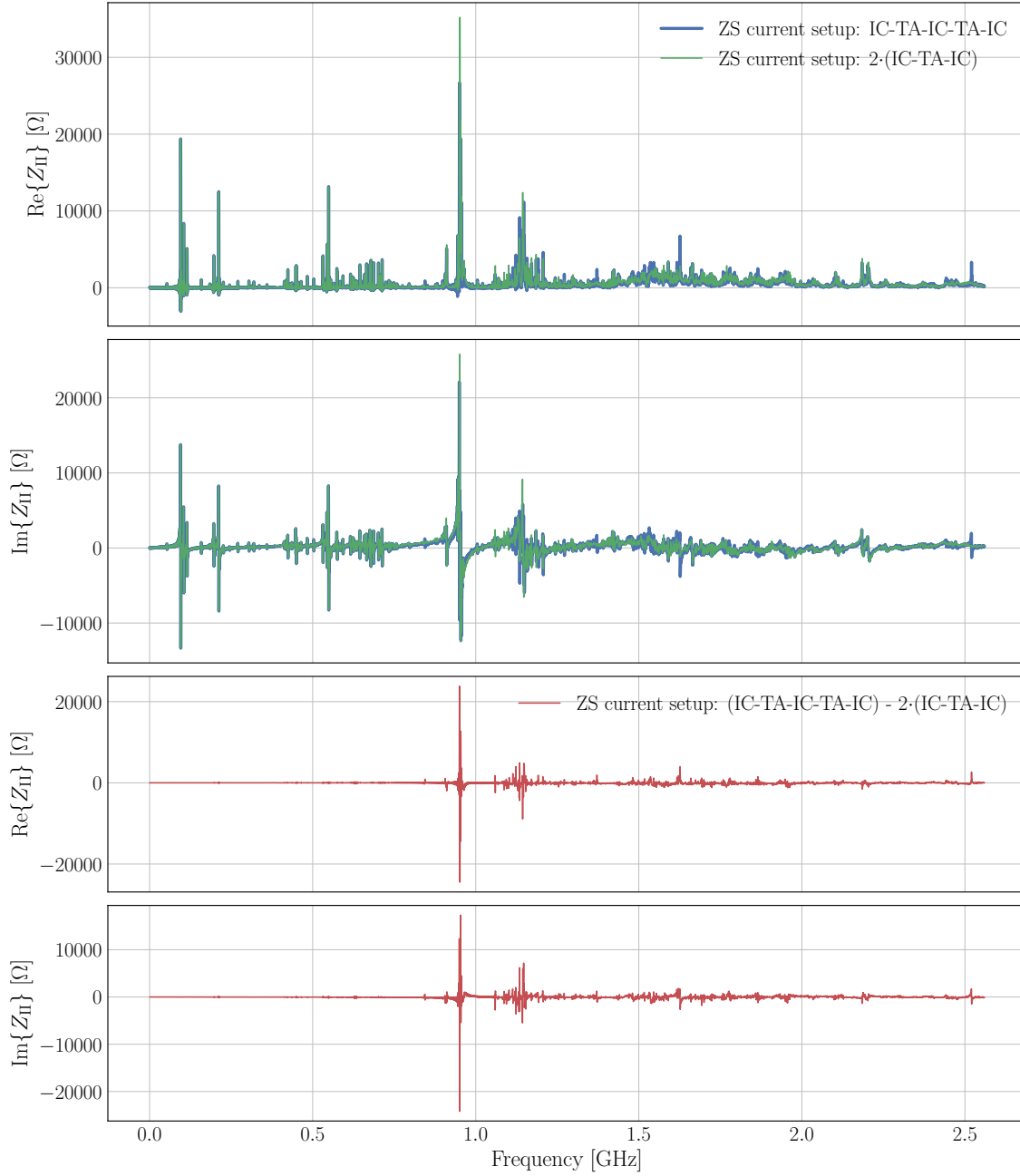
Figure 3.50: The doubled simulated impedance of one tank enclosed by two interconnects is compared to the simulated impedance of two tanks connected and terminated by interconnects. Tanks and interconnects as currently installed in the SPS were simulated. The differences of the curves in the upper two plots are shown in the lower two.
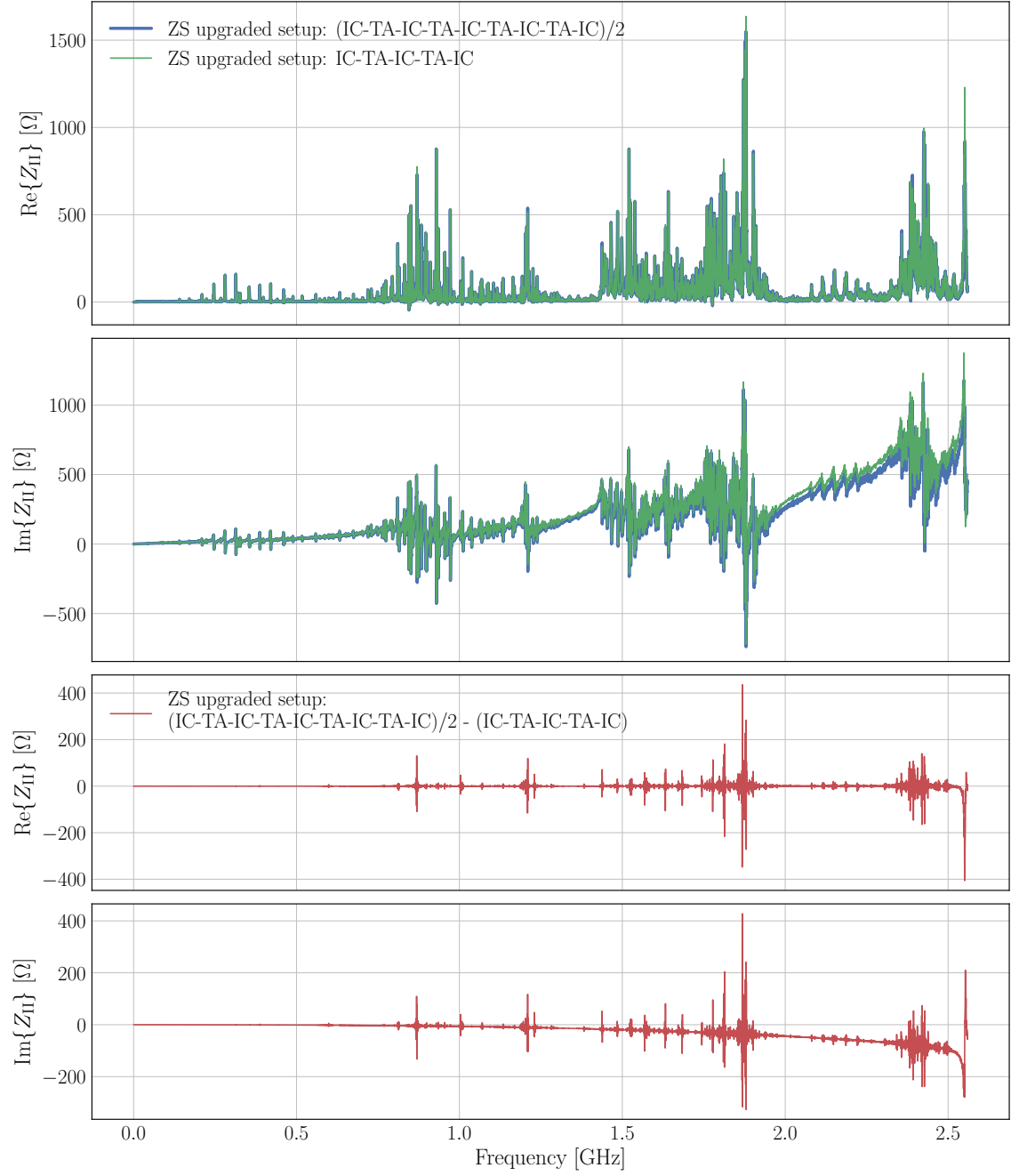
Figure 3.51: The halved simulated impedance of four tanks connected and terminated by interconnects is compared to the simulated impedance of two tanks connected and terminated by interconnects. Tanks and interconnects of the upgraded ZS setup were simulated. The differences of the curves in the upper two plots are shown in the lower two.

to the implemented modifications, a wake length of 300 m was kept for the final simulations and thus simulation times as discussed in the paragraph above apply.

The resulting simulated impedances for the complete ZS chains are presented in Fig. 3.52 for the current setup and in Fig. 3.53 for the updated setup. Comparing the results, the drastic impedance reduction for the upgraded ZS setup is observed (note that there is a factor 30 between the scales of the ordinates). The effect of the longer wake length in the simulations of the current model is visible in a different relation of the impedance amplitude in the spectra in Fig. 3.50 and Fig. 3.52, especially for frequencies below 1 GHz. The final simulations presented here are implemented in the impedance model. The scaling approach was also demonstrated for the transverse impedance and wakes, respectively.
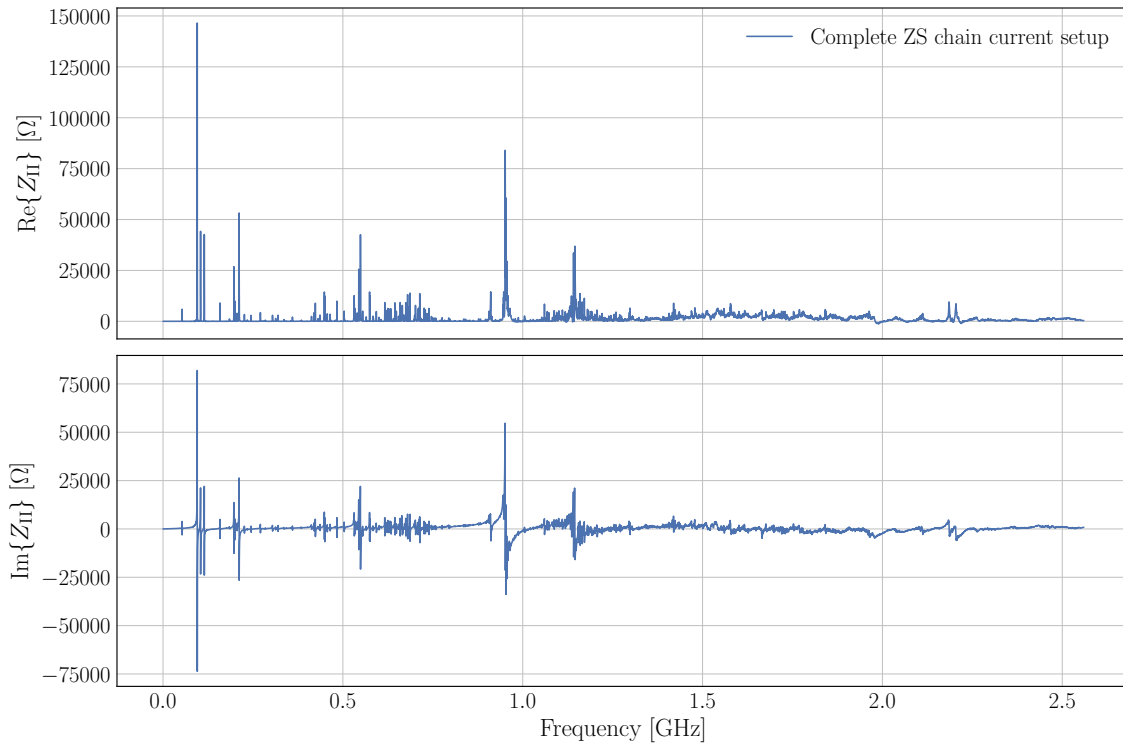
Figure 3.52: The simulated impedance of the complete current ZS chain.
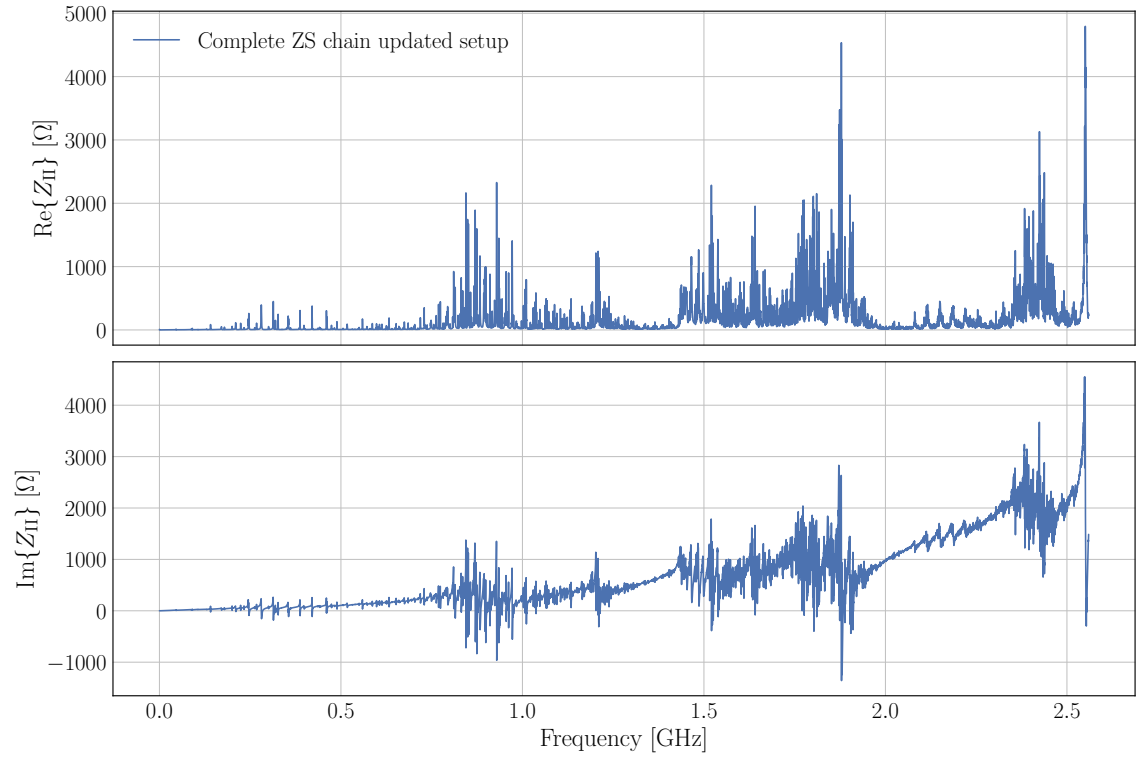
Figure 3.53: The simulated impedance of the complete updated ZS chain.

4 From impedance to beam dynamics

This chapter bridges the computed impedance to its effects on the simulated beam dynamics. First, the basic concepts of beam dynamics relevant for this thesis are introduced shortly. The following section discusses the construction of an impedance model together with the impedance model of the SPS. Next, a description of the code used for beam dynamics simulations in this thesis is presented. Finally, the chapter closes with an overview of beam measurements in the SPS.

4.1 Introduction to beam dynamics

The following section introduces the modelling of the particle motion in an accelerator and gives a short overview over selected collective effects. The section closely follows [Cha93] and [Lee12] in the discussed topics.

To completely describe the motion of particles in an accelerator a six dimensional phase space Γ is needed. Every particle is then completely described by a vector $\vec{\Psi}$:

$$\vec{\Psi} = \begin{pmatrix} x \\ x' \\ y \\ y' \\ z \\ \delta \end{pmatrix}, \vec{\Psi} \in \Gamma. \tag{4.1}$$

All variables in Γ are defined with respect to the reference orbit designated by the synchronous particle. The synchronous particle has the design energy and always follows the design orbit s in its trajectory, as shown in Fig. 4.1. The transverse (horizontal and vertical) positions x and y thus describe the distance to the reference orbit (in meters). The variable s has the meaning of the time variable (with $s = v \cdot t$ and the velocity v). The transverse angles $x' = dx/ds$ and $y' = dy/ds$ are also referred to as the transverse momenta of the particle [Lee12], as (x, x') and (y, y') define pseudo phase spaces. The concept of a phase space itself is not introduced here, but can be found in [Lee12]. The absolute longitudinal position in meters is indicated by z and $\delta = \Delta P/P$ is the relative momentum offset of a particle, defined with respect to the synchronous particle.
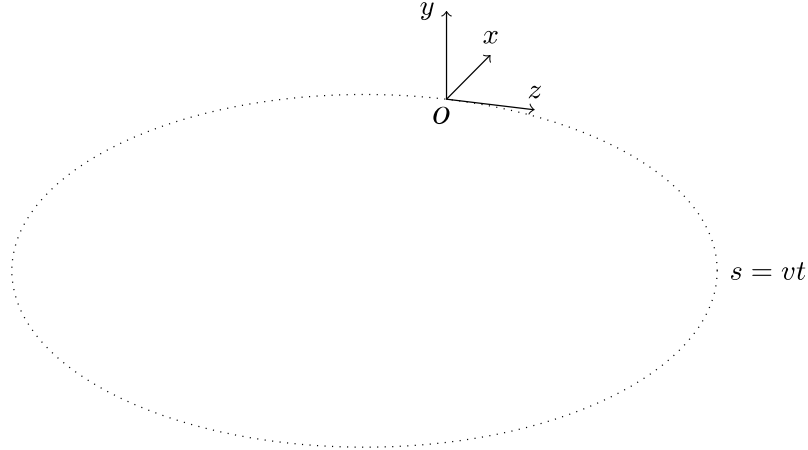
Figure 4.1: The coordinate system in a circular accelerator with the radius R. The reference particle O travels along the accelerator's circumference $2\pi R$ with $s = v \cdot t$. The horizontal, vertical and longitudinal positions of a particle with respect to the reference particle are x, y and z. Adapted from: [Cha93]

4.1.1 Longitudinal motion

The longitudinal dynamics for a bunched beam is mainly governed by the RF cavities. Here a sinusoidal voltage on a single RF system with $\omega_{RF} = h\omega_0$, where h is the so-called harmonic number, is assumed. The cavity produces a time-dependent electromagnetic field that focuses the particles longitudinally. The unperturbed longitudinal motion of a particle with the charge e, travelling with the relativistic speed $v = \beta c$ in a circular accelerator with the circumference $C = 2\pi R$, is therefore defined by [Lee12, CMTZ13]:

$$z' = -\eta\delta,$$
$$\delta' = \frac{eV}{p_0 \beta c C}\left(\sin\left(\frac{hz}{R}\right) - \frac{\Delta E}{eV} \right). \tag{4.2}$$

Hereby V is the integrated RF cavity voltage, ΔE the energy change per revolution period, p_0 is the momentum of the synchronous particle, the so-called reference momentum, and e the charge of a particle. The phase slippage factor η is defined as $\frac{\Delta\omega_0/\omega_0}{\Delta P/P}$ and describes the relative change in revolution frequency with momentum.

With the momentum compaction factor $\alpha = \frac{\Delta C/C}{\Delta P/P}$, which is defined as the relative orbit change with momentum, and the Lorentz factor γ the slippage factor η can be expressed as:

$$\eta = \frac{1}{\gamma^2} - \alpha. \tag{4.3}$$

The slippage factor therefore adapts to the momentum of a particle. The transition energy is defined at $\eta = 0$ by a gamma at transition γ_{tr} of $1/\sqrt{\alpha}$. This value is a

property of the transverse layout of an accelerator. When the transition energy is crossed during acceleration, the following phenomena occur:

- Below the transition energy ($\eta < 0$) the velocity change dominates over the path length change, so particles with positive momentum offset δ show a higher revolution frequency $f_{rev} = \omega_0/2\pi$ than the synchronous particle.

- At transition ($\eta = 0$) the velocity change and path length change exactly cancel each other. The revolution frequency of a particle is thus independent of its momentum offset δ.

- Above the transition energy ($\eta > 0$) the path length change dominates over the velocity change, so particles with a positive momentum offset δ show a lower revolution frequency f_{rev} than the synchronous particle.

The classical linear equation of motion for the longitudinal plane can be found by linearising the second equation in (4.2) around the synchronous phase ϕ_s and implementing it in the derivation of the first equation in (4.2):

$$z'' + \underbrace{\frac{eV\eta h}{p_0 \beta c C R} \cos(\phi_s)}_{\left(\frac{\omega_s}{\beta c}\right)^2} \; z = 0. \tag{4.4}$$

This notation allows to extract the synchrotron tune Q_s, which describes the number of longitudinal periods per turn in the machine [Lee12]:

$$Q_s = \frac{\omega_s}{\omega_0} = \sqrt{\frac{eV\eta h}{2\pi p_0 \beta c} \cos(\phi_s)} = \sqrt{\frac{eV\eta h}{2\pi E_0 \beta^2} \cos(\phi_s)}, \tag{4.5}$$

where E_0 represents the reference energy. This number is typically in the range of $10^{-4} - 10^{-1}$, except for large lepton machines where it can approach unity. The synchrotron tune in the SPS is $Q_s^{SPS} = 0.015$ [Bar]. Equation (4.5) also shows the absence of the synchronous particle motion ($Q_s = 0$) at transition ($\eta = 0$).

4.1.2 Transverse motion

The transverse motion in an accelerator is mainly defined by the dipole and quadrupole magnets. The equation of motion in the horizontal plane can be defined by the harmonic oscillator function, the so-called Hills equation, given in Eq. (4.6).

$$x'' + K(s)x = 0. \tag{4.6}$$

The effective focusing function $K(s)$ is periodic for an accelerator ring. In the following, all concepts are introduced for the horizontal plane but can be derived analogously for the vertical plane. The vertical plane thus can be described by exchanging x with y.The solution of an ordinary second order linear equation in the form of Eq. (4.6) is uniquely determined by the initial values of x and its derivative x':

$$x(s) = C(s, s_0)x(s_0) + S(s, s_0)x'(s_0),$$
$$x'(s) = C'(s, s_0)x(s_0) + S'(s, s_0)x'(s_0). \tag{4.7}$$

$C(s, s_0)$ and $S(s, s_0)$ are the cosine and sine-like solutions. The equations in (4.7) can also be written in matrix notation, which will become handy for the tracking of particles:

$$\left. \begin{pmatrix} x \\ x' \end{pmatrix} \right|_s = \left. \begin{pmatrix} C & S \\ C' & S' \end{pmatrix} \right|_{s,s_0} \left. \begin{pmatrix} x \\ x' \end{pmatrix} \right|_{s_0} = M(s|s_0) \left. \begin{pmatrix} x \\ x' \end{pmatrix} \right|_{s_0}. \tag{4.8}$$

The matrix $M(s|s_0)$ in Eq. (4.8) is called the transfer matrix. To find this matrix, equation Eq. (4.6) has to be solved. For rings its solution is [Lee12]:

$$x(s) = \sqrt{2J_x \beta_x(s)} \cos(\psi_x(s) + \psi_{x,0}),$$
$$x'(s) = \sqrt{\frac{2J_x}{\beta_x(s)}} (\alpha_x \cos(\psi_x(s) + \psi_{x,0}) + \sin(\psi_x(s) + \psi_{x,0})), \tag{4.9}$$

with the horizontal action of the particle J_x, the phase advance $\psi_x(s)$ of the transverse (betatron) oscillation and the initial betatron phase of $\psi_{x,0}$. The values α_x and β_x are part of the Twiss or Courant-Snyder parameters $(\alpha_{x,y},\ \beta_{x,y},\ \gamma_{x,y})$, corresponding to the optics functions in the machine (not to confuse with the Lorentz factor and the relativistic beta). In particular, the value β_x determines the local amplitude of the horizontal oscillation and α_x is defined as $\beta'_x/2$. Inserting the solution (Eq. (4.9)) in Eq. (4.7) the following transfer matrix is obtained:

$$M(s_1|s_0) = \begin{pmatrix} \sqrt{\beta_1} & 0 \\ -\frac{\alpha_1}{\sqrt{\beta_1}} & \frac{1}{\sqrt{\beta_1}} \end{pmatrix} \begin{pmatrix} \cos(\Delta\psi_{0\to1}) & \sin(\Delta\psi_{0\to1}) \\ -\sin(\Delta\psi_{0\to1}) & \cos(\Delta\psi_{0\to1}) \end{pmatrix} \begin{pmatrix} \frac{1}{\sqrt{\beta_0}} & 0 \\ -\frac{\alpha_0}{\sqrt{\beta_0}} & \sqrt{\beta_0} \end{pmatrix}, \tag{4.10}$$

where $\Delta\psi_{0\to1}$ describes the betatron phase advance from s_0 to s_1.

The trajectory of particle motion defined by the solution in Eq. (4.9) follows an ellipse defined by $2J_x$ with the starting phase $\psi_{x,0}$ in the phase space (x, x') with the properties shown in Fig. 4.2. The phase space area enclosed by the ellipse is called the emittance ϵ_x. The emittance is invariant for a particle that is travelling through an accelerator at a constant energy. But the shape and orientation of the ellipse change, as the Twiss parameters defining it are dependent of the position in the accelerator.
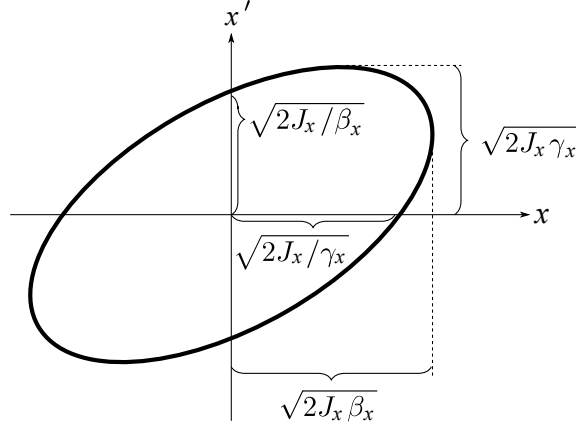
Figure 4.2: Properties of the Twiss parameter ellipse in the horizontal phase space (x, x'). Adapted from: [Lee12]

When the energy of the particle is changed, its emittance changes as well. Therefore, the so-called normalized emittance,

$$\epsilon_{x_N} = \beta\gamma\epsilon_x, \tag{4.11}$$

can be defined. As it is independent of the energy of a particle it stays constant during acceleration. For a bunch of particles in an accelerator the emittance describes the ellipse in phase space which includes all its particles. But for practical reasons the emittance is often found by fitting the particle distribution in a bunch with a Gaussian distribution. The so-called rms emittance $\epsilon_{x_{rms}}$ can be found from the second order momentum (variance) of the obtained distribution which equals $\beta_x\epsilon_{x_{rms}}$ [Lee12]. The variance of a beam is also referred to as its bunch length.

As for the longitudinal plane the tune can also be defined in the transverse planes. The horizontal tune Q_x is defined by the number of betatron oscillations in the horizontal plane per particle revolution in the accelerator.

$$Q_x = \oint \frac{1}{\beta_x(s)} ds. \tag{4.12}$$

Linear effects due to the momentum distribution   Next, linear effects occurring due to the momentum distribution of particles in a beam are discussed. The focus here lies on the phenomena introduced by dipole and quadrupole magnets, namely dispersion and chromaticity. In a circular accelerator the dispersion $D(s)$ occurs due to the fact that dipoles bend particles dependent on their momentum. The value of the dispersion thus changes with the bending strength of the dipoles and the layout of the machine.

Quadrupole magnets in a machine provide focusing depending on the particle momentum, which leads to a tune shift for individual particles and a tune spread

over a particle distribution. This effect is described by the (natural) chromaticity parameter Q' which is defined as:

$$Q' = \frac{d\Delta Q}{d\delta}. \tag{4.13}$$

Non-linear effects due to the momentum distribution   Until now, only linear particle motion was introduced. When studying collective effects, some non-linear aspects of the transverse motion have an important impact. Here, the focus lies on the non-linearities introduced by sextupole and octupole magnets. To correct the chromaticity, sextupole magnets can be employed. Then, the chromaticity Q' of the respective transverse planes can be also written as [Lee12]:

$$Q'_x = -\frac{1}{4\pi} \oint \beta_x(s)(K_1(s) - K_2(s)D(s))ds,$$

$$Q'_y = +\frac{1}{4\pi} \oint \beta_y(s)(K_1(s) - K_2(s)D(s))ds, \tag{4.14}$$

where $K_1(s)$ and $K_2(s)$ are the effective normalized magnetic strengths of the quadrupoles and sextupoles, respectively.

Octupole magnets provide a focusing dependent on the transverse offset of particles from the center of the magnet (J_x or J_y). This effect is called detuning with amplitude and introduces a transverse tune spread. The detuning coefficients can be written as:

$$\alpha_{xx} = \frac{d\Delta Q_x}{dJ_x}, \alpha_{xy} = \frac{d\Delta Q_x}{dJ_y},$$

$$\alpha_{yy} = \frac{d\Delta Q_y}{dJ_y}, \alpha_{yx} = \frac{d\Delta Q_y}{dJ_x}. \tag{4.15}$$

Similar to the chromaticity, they can be linked to the beta functions and the magnet strength [Lee12]:

$$\alpha_{xx} = +\frac{3}{8\pi} \oint K_3(s)\beta_x(s)^2 ds,$$

$$\alpha_{xy} = -\frac{3}{4\pi} \oint K_3(s)\beta_x(s)\beta_y(s)ds = \alpha_{yx},$$

$$\alpha_{yy} = +\frac{3}{8\pi} \oint K_3(s)\beta_y(s)^2 ds, \tag{4.16}$$

where K_3 is the effective normalized magnetic strength of the octupoles.

With Eq. (4.13) and Eqs. (4.15) the complete tune shift introduced due to chromaticity and amplitude detuning per turn results in:

$$\Delta Q_x = Q_x^{'}\delta + \alpha_{xx}J_x + \alpha_{xy}J_y,$$
$$\Delta Q_y = Q_y^{'}\delta + \alpha_{yy}J_y + \alpha_{yx}J_y. \tag{4.17}$$

4.1.3 Collective effects

So far all particles have been treated as independent from another and their surroundings. They were only influenced by the RF-cavity's electrical field in the longitudinal plane and by the fields of the magnets in the transverse plane. The phenomena related to particles interacting with another and with their surrounding are called collective effects. When collective effects are considered in the transverse planes, a single particle is not only influenced by the external focusing (optics functions) but also perturbed by the forces created by those effects. Adapting the transverse description of particle motion to that scenario, leads to a perturbation of the Hills equation (Eq. (4.6)) by a force F_c generated due to collective effects [Ng06]:

$$x'' + K(s)x = F_c(\Psi, s). \tag{4.18}$$

Hereby, the force F_c is dependent on the distribution of all the particles in the phase space, which means that it is dependent on the collective particle distribution in the beam. For realistic cases the force F_c has to be determined numerically.

If the perturbation of the transverse particle motion becomes strong enough, it can lead to instabilities. Instabilities are characterised by an exponential growth of one or more momenta of the particle distribution. The kind of instability occurring depends on the machine configuration. Instabilities lead to a degradation of beam quality and to beam loss. Unstable beams may have to be dumped in order to protect the machine from uncontrolled particle loss. The instability onset can be mitigated by changing the chromaticity, activating a damper or introducing octupoles. Also the tune spread created by octupoles (Eq. (4.15)) may introduce so-called Landau damping, which can suppress instabilities [Lee12, Cha93]. The damping effect can explained by assuming parasitic tune shift, which could provoke an instability. If the beams exhibits an incoherent tune distribution, this parasitic tune shift may not affect the collective beam motion, as only single particles may be affected. Thus the instability is damped by Landau damping. In the following, the collective effects and instabilities of interest in the context of this thesis are introduced.

Space charge   As first collective effect, the so-called space charge is discussed. It is only of marginal interest for this thesis and therefore introduced briefly and only in the transverse plane. A deeper discussion can be found e.g in [Wie15, Cha93, Lee12].

The space charge mechanism arises from the strong repelling forces within a beam. Due to the self-fields of a beam the Lorentz force acts on particles within the beam. For a beam with a size a and a line density λ that travels along an accelerator, the horizontal Lorentz force F_x acting on a particle at a position x within it, can be written as:

$$F_x = \frac{2\lambda e\beta}{a^2\gamma^2}x. \tag{4.19}$$

In the ultra-relativistic case ($\gamma \to 0$) this force vanishes (see Eq. (4.19)). Physically that can be explained by the compensation between the electric and magnetic components of the Lorentz force. From Eq. (4.19) follows, that the space charge usually affects low energy beams with small transverse dimensions and a high line density. Besides, since it adds a defocusing term to the equation of motion, it shifts the particle tune to lower values [Cha93].

Indirect space charge describes the phenomena of image charges, created by the introduction of boundary conditions, acting back on the relativistic beam in a manner similar to space charge. Indirect space charge also introduces a transverse tune shift [Cha93].

Wakes fields Another kind of collective effects is introduced by the wake fields discussed in Ch. 2. As for the power loss calculation in the same chapter, the bunch is assumed to be sliced in the following. When wakes are considered, a single particle in a witness slice feels the force from the external focusing and from the wake created by all source particles travelling ahead of it (see Fig. 4.3). The resulting equation of motion is:

$$\begin{aligned}
x'' + K(s)x = &- \frac{e^2}{p_0\beta cC} \int_{-\infty}^{\infty} \lambda(z') \, W_x^{drive}(z-z') \, \overline{x}(z') \, dz' \\
&+ \int_{-\infty}^{\infty} \lambda(z') \, W_x^{det}(z-z') \, x \, dz.'
\end{aligned} \tag{4.20}$$

Here, $\lambda(z')$ is the line density of the source slice at its longitudinal position z' and $\overline{x}(z')$ refers to the average horizontal position of the particles in the source slice creating the wake. $W_x^{drive}(z-z')$ and $W_x^{det}(z-z')$ describe the driving and detuning component of the wake field at the position of the trailing slice.

Assuming that the action of the wake field only happens at a discrete point and using the matrix notation (Eq. (4.8)) leads to [Li17]:

$$\begin{pmatrix} x_{s_1} \\ x'_{s_1} \end{pmatrix} = M(s_1|s_0) \begin{pmatrix} x_{s_0} \\ x'_{s_0} - \frac{e^2}{p_0\beta cC} \int_{-\infty}^{\infty} \lambda(z')[W_x^{drive}(z-z')\overline{x}(z')+ \\ +W_x^{det}(z-z')x_{s_0}]dz' \end{pmatrix}, \tag{4.21}$$

where $M(s_1|s_0)$ is the transfer matrix in Eq. (4.10). In this approximation, the wake only influences the momentum of the transverse particle motion. The driving and detuning parts of the wake influence the particles in the trailing slice as follows:
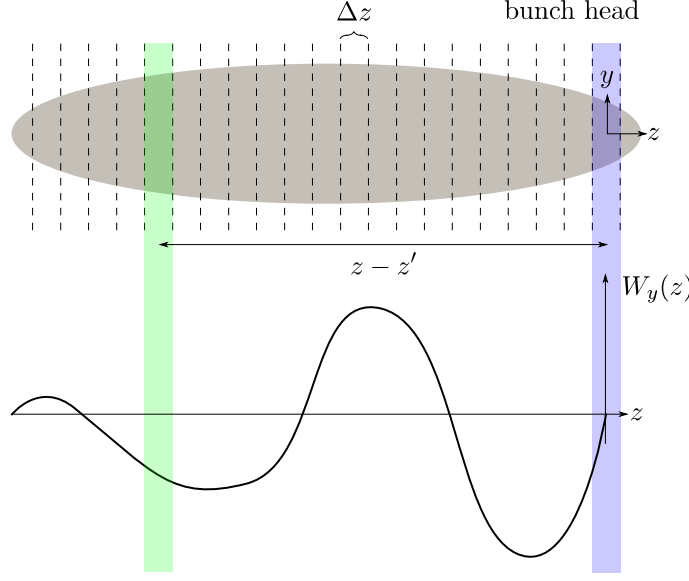
Figure 4.3: The slicing of the bunch (in grey). The particles in a source slice, in blue, create a wake that influences the particles in every trailing slice for example, the one in green.

- The driving (dipolar) wake generates a dipolar type kick, dependent on the intensity (through $\lambda(z')$) but also on the transverse position (through $\overline{x}(z')$) of each source slice. This leads to an intra bunch coupling.

- The contribution of the detuning (quadrupolar) wake is dependent on the intensity but also on the position of the particle influenced by the wake (through x_{s_0}). Therefore, it generates a tune shift, similar to quadrupoles (see Eq. 4.13). In addition, as the tune shift is slice-dependent, the detuning wake creates a tune spread. Contrary to the driving wake, the detuning wake themselves cannot drive a beam unstable.

The discussion above refers to the case of a wake field that has decayed after one turn. In the case of a wake surviving over multiple turns, the integral in Eq. (4.21) has to be summed over all the turns and becomes:

$$\sum_{k=0}^{\infty} \int_{-\infty}^{\infty} \lambda(z'+kC)[W_x^{drive}(z-z'-kC)\overline{x}(z'+kC) + W_x^{det}(z-z'-kC)x_{s_0}]dz'. \quad (4.22)$$

As usual, the integrals in this paragraph have been extended to $-\infty$, as the wake functions vanish for positive values of z due to causality.

Transverse Mode Coupling Instability (TMCI)   The TMCI is one of several instability meachanisms. It is also known as the strong head-tail instability. As in

[Rum14] and in [Lee12] it can be explained by a simple two macro-particle model. Therefore, it is assumed that the regarded beam consists out of two macro-particles that both have the same longitudinal amplitude and intensity $N/2$ but perform synchrotron oscillations with opposite phases. Furthermore zero chromaticity shall be assumed and therefore no coupling between the horizontal and transverse planes. During the first half synchrotron period $T_s = 2\pi/\omega_s$ the second particle (particle 2) experiences the wake created by the first one (particle 1). Thus, the transverse equations of motion of the two particles can be, for $0 < s < \pi c/\omega_s$, written as:

$$
\begin{aligned}
y_1'' + \left(\frac{\omega_\beta}{c}\right)^2 y_1 &= 0, \\
y_2'' + \left(\frac{\omega_\beta}{c}\right)^2 y_2 &= -\frac{e^2 N W_0}{2 p_0 \beta c C} y_1,
\end{aligned}
\tag{4.23}
$$

with the transverse wake W_0 which is integrated over the machine circumference C and assumed to be constant but vanishing within one turn. Note, that the focusing function $K(s)$ in Eq. (4.6) has been written as ω_β/c with the vertical betatron frequency ω_β.

In the following, this two particle system shall be studied for its stability. For this, a solution of the first equation in (4.23) can be found by [Lee12]:

$$
\tilde{y}_1(s) = \tilde{y}_1(0) e^{-j\omega_\beta s/c} \quad \text{with} \quad \tilde{y}_1(s) = y_1(s) + j\frac{c}{\omega_\beta} y_1'(s).
\tag{4.24}
$$

Inserting this solution in the second equation of (4.23) and evaluating the result at the position of the particles after half a synchrotron period (at $s = \pi c/\omega_s$) leads to the solution [Lee12]:

$$
\left. \begin{pmatrix} \tilde{y}_1 \\ \tilde{y}_2 \end{pmatrix} \right|_{s=\pi c/\omega_s} = e^{-j\pi\omega_\beta/\omega_s} \begin{pmatrix} 1 & 0 \\ j\Upsilon & 1 \end{pmatrix} \left. \begin{pmatrix} \tilde{y}_1 \\ \tilde{y}_2 \end{pmatrix} \right|_{s=0},
\tag{4.25}
$$

where Υ has been defined as a positive dimensionless parameter:

$$
\Upsilon = \frac{\pi c N e^2 W_0}{4 p_0 \beta C \omega_\beta \omega_s}.
\tag{4.26}
$$

As the particles change positions for the second half of the synchrotron period ($\pi c/\omega_s < s < 2\pi c/\omega_s$) the scenario described above is reversed, meaning particle 1 experiences the wake created by the particle 2. The solution for this scenario can be found by exchanging the equations of motions in Eq. (4.23). The solution for the complete synchrotron period results in [Lee12]:

$$
\left. \begin{pmatrix} \tilde{y}_1 \\ \tilde{y}_2 \end{pmatrix} \right|_{s=\pi c/\omega_s} = e^{-j\pi\omega_\beta/\omega_s} \begin{pmatrix} 1 & j\Upsilon \\ 0 & 1 \end{pmatrix} \begin{pmatrix} 1 & 0 \\ j\Upsilon & 1 \end{pmatrix} \left. \begin{pmatrix} \tilde{y}_1 \\ \tilde{y}_2 \end{pmatrix} \right|_{s=0}.
\tag{4.27}
$$

The eigenvalues of the product of the two matrices determine the stability of the two particle system. The eigenvalues $\lambda_\pm$ are:

$$\lambda_\pm = (1 - \Upsilon^2/2) \pm \sqrt{(1 - \Upsilon^2/2)^2 - 1}. \tag{4.28}$$

The product of the two eigenvalues results in one. Thus, to reach the requirements for stability the eigenvalues have to be purely imaginary ($\lambda_\pm = e^{\pm jv}$ with a real variable v) [Rum14].This information defines the condition for stability as:

$$\lambda_+ + \lambda_- = 2 - \Upsilon^2 = 2 \cdot \cos(v) \quad \Rightarrow \quad 1 \geq \sin\frac{v}{2} = \frac{\Upsilon}{2} \quad \Rightarrow \quad \Upsilon \leq 2. \tag{4.29}$$

Combinung this stability condition with Eq. (4.26) reveals the intensity threshold N_{thr} [Rum14]:

$$N_{thr} = \frac{8}{\pi e}\frac{p_0 \omega_s}{\beta_y}\left(\frac{C}{W_0}\right), \tag{4.30}$$

The threshold is proportional to the energy of the beam (by p_0) and inversely proportional to the wake field along the ring. The value of the transverse beta function β_y also influences the threshold, as the kick, which a particle experiences due to a wake, is always proportional to the beta function at the position where the wake is created. Increasing the synchrotron frequency can also influence the stability range, as in this chase if the particles change their position in phase space faster, the duration of disturbance caused by the wake decreases.

When analysing the spectrum of the beam motion below N_{thr}, several spikes, azimuthal and radial modes, arise from the interaction of the bunch with the dipolar wake field in presence of synchrotron motion. Stepwise increasing the intensity to N_{thr} reveals that two of these modes couple at N_{thr} [Li17]. Hence, the name TMCI.

Besides the two particle model several analytical formalisms exist to describe the TMCI. For example by modelling the driving impedance as a broadband resonator Z^{BB}:

$$Z_y^{BB}(\omega) = \frac{\omega_r}{\omega}\frac{R_s}{1 + iQ(\frac{\omega}{\omega_r} - \frac{\omega_r}{\omega})}. \tag{4.31}$$

Here R_s is the resistance of the resonator, with the angular resonating frequency ω_r and the quality factor Q. Then, the TMCI intensity threshold N_{thr}^{TMC} can be estimated by [Rum14]:

$$N_{thr}^{TMC} = \frac{16\sqrt{2}}{3\pi}\frac{R|\eta|\varepsilon_z}{\beta_y e\beta^2 c}\frac{\omega_r}{|Z_y^{BB}|}\left(1 + \frac{Q_y'\omega_0}{\eta\omega_r}\right), \tag{4.32}$$

where ω_0 describes the angular revolution frequency of the machine, and Q_y' the vertical chromaticity. It is important to distinguish between the vertical beta function β_y and the relativistic beta β.

Strategies to increase the TMCI threshold consist of the reduction of the impedance to reduce the wake created, or increasing the synchrotron tune in the machine.

Head-tail instability   It can be demonstrated that, apart from TMCI, individual coherent modes develop, which may be intrinsicly unstable [Rum14]. These modes develop for finite chromaticities different from zero. When an accelerator is running above transition energy, the mode zero is only stable for positive chromaticity and gets unstable for negative values. The number of a mode reveres to the number of nodes that appear when the transverse particle positions ($x(z)$ or $y(z)$) in an unstable bunch are observed over multiple turns. Modes with a higher order tend to be unstable for positive chromaticity values, but stable for negative ones. However, the mode zero shows the fastest rise-time and thus is the most dangerous in practice. For that reason, particle accelerators operating at high energy (above transition) need to ensure a positive chromaticity. Therefore, they need chromaticity correction with sextupoles. The occurring higher order modes would exhibit slower growth and can be usually damped by other mechanisms.

4.2 Generating an impedance model

Beam dynamics simulations are used to investigate instabilities in an accelerator. Simulation codes need information about the wakes generated in a machine in order to compute impedance-related instabilities. Therefore, wake functions and/or impedances are pre-calculated and stored in accelerator-specific databases.

Nowadays, the impedance of most accelerators is modelled and controlled right from the design phase, as impedance-related effects influence the performance reach of a machine. Also impedance or wake models for existing rings are used to understand the behaviour of a beam during operation, or to investigate the possibility of upgrading a machine. The the wake model can be transferred into the impedance model via a Fourier transform.

An impedance model includes the longitudinal impedance and the driving and detuning parts of the transverse impedance [BSZ16], as they impact the beam differently. Higher order transverse impedance contributions can be neglected when studying instability thresholds. Depending on needs and knowledge, the impedance model of an accelerator can vary from a simple number, over broadband resonator models, to detailed and complex models taking into account the contributions of the individual elements in the machine. The last approach is extremely helpful when the evaluation of the impedance model is studied in the context of installing or removing components from the accelerator.

The impedance model should cover at least the same frequency range as the spectrum created by the beam. The impedances of the different machine components contributing to the model are mostly computed from the simulated wake potentials and plotted over frequency (as described in Ch. 2). The beam therefore defines the parameters for the impedance simulations. For example very short excitation pulses are needed to access high frequencies, but to reproduce multi-bunch effects, or to

resolve the impedance at low frequencies, long wake lengths have to be simulated. This is more demanding in terms of computational resources. As discussed in Ch. 2, the simulations for the transverse impedance model can be simplified in special cases. For example, if the structure is rotationally symmetric the detuning component vanishes and thus does not have to be calculated. However, this simplification is not valid for axis symmetric or for non-symmetric structures (Kickers etc.). The same relations hold for the creation of transverse wake potentials (Eq. (2.17)) [HWZ98].

As the dipolar and quadrupolar impedances are normalized by the offset of the source or test beam (Eq. (2.18)), they can be scaled to the offsets needed in simulations.

To create a longitudinal impedance model from the different machine components, it is sufficient to sum up all the longitudinal impedance contributions. In the transverse planes the impedance of the different contributors have to be weighted by the local beta function before the summation. The transverse impedance model $Z_{x,y}^{acc}(f)$ therefore consists of the impedances of the components $Z_{x,y}^{i}(f)$, weighted by the ratio between the beta function $\beta_{x,y}^{i}$ at the position of the components in the accelerator and the average beta function $\overline{\beta}_{x,y}$ over the whole machine [BSZ16]:

$$Z_{x,y}^{acc}(f) = \sum_{i=1}^{N} \frac{\beta_{x,y}^{i}}{\overline{\beta}_{x,y}} Z_{x,y}^{i}(f) \tag{4.33}$$

An impedance model has to be constantly adapted to changes in the accelerator and always verified by measurements, to best reproduce the effects in the machine (see Fig. 1.2). For this thesis this has been done for the transverse impedance and wake models of the SPS as documented in the following. Impedance models are also available for other CERN machines for example the PS [Per15], the LHC [SAA+12] and the HL-LHC [BLM+16].

4.2.1 The SPS impedance model

The impedance model of the SPS is divided into a longitudinal [VAB+15a, KCV17] and a transverse [Sal10, SAA+12, Zan13] part. This thesis focuses on impedance effects in the transverse planes, hence, on the transverse impedance model. Nevertheless, the impedances of the components studied in Ch. 3 were included in the longitudinal model.

For the transverse plane, an impedance and a wake model are available. The models are created independently but include the contribution of the same components, which were obtained by the same CST simulation results. The wake model includes the driving and detuning wakes in the horizontal and vertical planes and the impedance model combines the complex driving and detuning impedances in both planes. In general the impedance model of the SPS includes frequencies up to 2.5 GHz.

Instead of the wake function, the wake potential is used in the transverse wake model, assuming that the bunch length used to calculate the wake potential is much smaller than the bunch length used in beam dynamics simulations. The wake potentials and impedances of the different accelerator components are weighted with the corresponding β-function value at their position, as demanded by Eq. (4.33). Furthermore, the SPS can operate with different beta functions, so-called optics configurations, resulting in different β values. Therefore, the different optics have to be considered in the SPS models. This is done by the generation of optics-dependent versions. Three optics are currently used: Q20, Q22 and Q26. Their names refer to the transverse integer tune with which they are associated. The β values for the different optics are obtained with the optics simulation software Methodical Accelerator Design (MAD) [CERb] in its current version (MAD-X). For each machine optics, the code uses information about the positions and the strengths of the magnets in the SPS to calculate the β-function at the positions of interest. The average beta function values $\overline{\beta}$ for the different optics are shown in Tab. 4.1.

Table 4.1: The average beta function values for the different machine optics.

Optics	$\overline{\beta}_{x,y}$
Q20	55.1
Q22	49.7
Q26	42.1

Initially, the transverse models have mainly focused on reproducing single bunch intensity effects and tune shifts. Therefore, the interest lay in the broadband impedance and the wakes could be limited to a length of 5 ns, corresponding to the size of the longitudinal RF buckets in the SPS (200 MHz RF system). But, elements that introduce sharply peaked impedances (narrowband impedances) close to beam spectrum lines could couple bunches and lead to instabilities. Besides, multi-turn wakes could even affect single bunches. For future multi-bunch and multi-turn simulations, all the narrow band impedances with their long-lasting wakes, have to be considered. For example, the impedance of the ZS, shown in the previous chapter to feature several sharp peaks, was adequately included in the upgraded impedance model of the SPS. In particular, all simulations of accelerator components in this thesis (see Ch. 3) have been executed such as to provide long wakes and to create a wake model for multi-bunch and multi-turn simulations.

The machine elements considered in the transverse SPS models are the following:

- **Kickers:** As already mentioned before, the kickers are the main contributors to the broadband impedance in the SPS. Besides the MKEs and MKPs the two Magnetic Tune Kicker (MKQ) (one in the horizontal and one in the vertical

plane) and the five Magnetic Dump Kicker (MKD) (three in the horizontal and two in the vertical plane [FHS73]) are considered in the model. The refined simulations of the MKEs and the MKPs presented in Ch. 3 and in [Bec15] are included.

- **Wall:** The contribution of the beam pipe (resistive wall) is included with an analytic formula. It was calculated with the exact analytical model for a circular chamber and adapted with a form-factor to the different beam pipe apertures [ZLR12]. The different apertures are also weighted with the corresponding β values.

- **Indirect Space Charge (ISC):** The ISC is represented as an impedance in the model. Similar to the resistive wall it was calculated with the exact analytical model, adapted with a form-factor to the different beam pipe apertures and individually weighted with the corresponding β values. Therefore, the ISC is included in the wall data.

- **Cavities:** The impedance and wake contributions of the 200 MHz and 800 MHz cavities in the SPS were accessed in CST simulations and are implemented in the model.

- **Beam Position Monitor (BPM):** The horizontal and vertical BPMs, modelled and simulated with CST in [Sal10], are included in the model.

- **Flanges:** There are several flanges installed in the SPS. They create unwanted cavities and thus contribute to the imaginary broadband impedance. The flanges were simulated in CST and are considered in the impedance/wake models.

- **Transitions between different beam pipe apertures:** The transitions are integrated using a simplified CST model to take into account their broadband impedance contribution.

- **ZS:** The impedance/wake results of the ZS obtained by the simulations presented in Sec. 3.5 are newly included in the models.

The list above includes also the refinement of the impednace models done during the studies described in this thesis. In addition, to adapt the models to changes in the machine, different versions are introduced. The versions represent the machine configurations in different years; 2015, 2018 and as expected after LS2. The 2015 version is the legacy version to be used for benchmark or to reproduce old measurements. The main changes in the 2018 version of the model are the introduction of the pre-LS2 version of the ZS and the removal of one MKE-L from the SPS together with the shortening of the serigraphy (see Tab .3.2). In adition, the updated kicker models

presented in Ch. 3 are included. On the other hand, the post-LS2 version models the SPS impedance/wake as foreseen after the implementation of the LIU upgrades. Besides including the post-LS2 version of the ZS, it also accounts for the shielding of the flanges and the installation of an additional MKD-V with the moving of the beam dump from LSS1 to LSS5 during LS2 [VAB⁺14, VAB⁺15b, HBC⁺18]. As the MKD kickers are installed at the same position in yet another sextant of the SPS, the beta function at their positions does not change (the super-periodicity gives identical values at the same position in different sextants). The diffent position of the dump kickers does thus not have to be considered in the models. The flanges are assumed as perfectly shielded [KV17, ASV15] and thus excluded from the post-LS2 version of the model. The main differences between the model versions are summarized in Tab. 4.2.

Table 4.2: The different versions of the SPS impedance model. All items that are not mentioned are equal in all three versions.

Version	2015 (legacy)	2018	Post-LS2
Number of MKE	8	7	7
MKE ser. length	200 mm	180 mm	180 mm
MKE model	first model*	updated model⋆	updated model⋆
MKP model	first model*	updated model⁺	updated model⁺
Number of MKD	5	5	6
Flanges	included	included	shielded (excluded)
ZS version	not included	pre-LS2	post-LS2

* Model presented in [Zan13].   ⁺ Model presented in [Bec15] and in Ch. 3.

⋆ Model presented in Ch. 3.

A Python script has been developed to combine the different simulated components to the complete wake or impedance model, taking into account the version and the optics needed. The script can be found on GitLab [1]. The complete wake model in the 2018 version is displayed in Fig. 4.4 for the different optics. A difference between the optics is mainly visible on the horizontal detuning wake over the first 0.2 ns. This wake is also the only component of the transverse wake model which is constantly negative. The post-LS2 version of the wake model and a comparison of all three versions can be found in Appendix B.

Table 4.3 summarizes the modelling approaches for the different components that are included in the SPS wake model. Most of the components are modelled in CST and simulated in time domain. The impedance is then determined by means of the Fourier transform. Only the impedance of the resistive wall and the impedance representation of the ISC are modelled analytically.

---

[1]`https://gitlab.cern.ch/IRIS/SPS_IW_model`
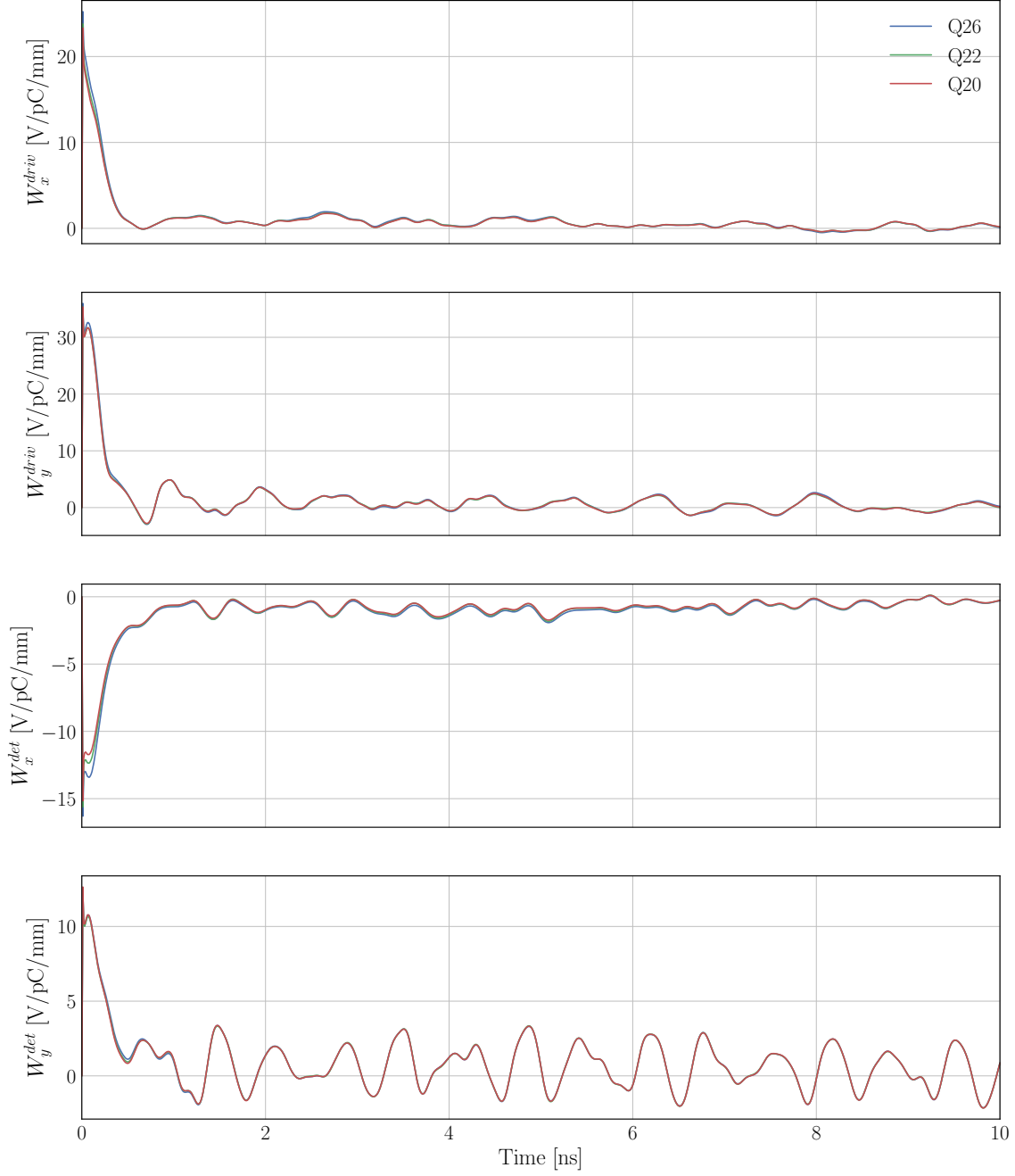
Figure 4.4: The 2018 version of the transverse SPS wake model for the three different optics used in the SPS: Q20, Q22 and Q26.

Table 4.3: The machine components included in the SPS impedance/wake model, and the method with which their impedance is obtained.

Machine component	Implementation
Kickers	CST simulation
Wall	Analytic model
ISC	Analytic model
BPMs	CST simulation
Cavities	CST simulation
Transitions	CST simulation
Flanges	CST simulation
ZS	CST simulation

4.3 Methods - Beam dynamics simulations

Beam dynamics codes use either the impedance or the wake as input to simulate the effects on particles in machines.

The BLonD code [CERa], for example, used for longitudinal beam dynamics simulations at CERN, relies on a resonator model fit of the longitudinal impedance as input. On the other hand, transverse beam dynamics simulations at CERN are mainly done with the PyHEADTAIL code [CERc], which relies on a full wake model of a machine. Generally, simulations can be distinguished between single-bunch and multi-bunch/multi-turn simulations. As already discussed above, in the case of multi-bunch/multi-turn simulations the wake or impedance model has to be created with a very long wake length to give realistic results.

In the following, the PyHEADTAIL code is introduced briefly as it is the only beam dynamics simulation code of interest for this thesis.

4.3.1 The PyHEADTAIL code

PyHEADTAIL is a particle tracking code to study beam dynamics and collective effects. It was developed at CERN. It is based on the HEADTAIL [RZ02] code which is written in the C language. Due to the growing complexity of the code it was decided to rewrite HEADTAIL in the Python language in an object-oriented approach. Hence, the name PyHEADTAIL. The code is freely available on GitHub [CERc] and can compute the effects of space charge, electron clouds, impedance and feedback systems on single bunches. Furthermore, the posibility to simulate multiple bunches is currently implemented. PyHEADTAIL simulations are launched via a Python script containing all the parameters and commands for the simulation. The effect of a wake field can be included with a wake file that has to be provided as an input. Bunch and slice monitors are available to store the computed evolution

of bunch momenta and intra-bunch motion in files for further evaluation. The most impotant beam dynamics modelling approaches in PyHEADTAIL are briefly introduced in the following. This subsection follows the article [Li17] closely, where more details can be found.

Modelling of beam dynamics

The general approach of PyHEADTAIL is the representation of an accelerator by ring segments. The particles are tracked along the segments with linear transfer maps. The perturbations due to collective effects are computed and applied in so-called interaction points between these segments. The large number of particles in a real bunch ($> 10^{11}$) makes the tracking of each particle computationally unpractical. PyHEADTAIL therefore introduces macro-particles to reduce the total particle number. Typically around 10^7 of those macro-particles are tracked in their six-dimensional phase space. Below, the implementations of the tracking, the collective effects and the dampers are introduced.

Longitudinal tracking   In PyHEADTAIL the longitudinal tracking can be executed either linearly or non-linearly. The linear case assumes that every particle has the same synchrotron tune Q_s. However, the synchrotron motion can influence the growth rates and thus is crucial for realistic simulations. Therefore, a non-linear tracking method is available, which creates an RF bucket of arbitrary shape to which the beam is matched. Then every particle possesses a synchrotron tune dependent on its amplitude within the bucket.

Transverse tracking   The benefit of the transfer matrix notation in Eq. (4.10) is that the one-turn transfer matrix can be split into subintervals:

$$M(s_1|s_0) = M(s_1|s_{0.5})M(s_{0.5}|s_0). \tag{4.34}$$

This is used in PyHEADTAIL for the segmentation of the machine during the simulation. Interaction points can be inserted between the subintervals, and used to distribute collective effects around the machine. Pure wake simulations in this thesis use a one-turn wake which is modelling the machine as a single segment (see e.g Fig. 4.4). For this thesis only the smooth approximation of the transfer matrix in Eq. (4.10) with

$$\alpha = 0 \text{ and } \beta = \frac{R}{Q_x} = constant, \tag{4.35}$$

is used. PyHEADTAIL can also employ Twiss parameters provided externally, by MADX for example. With the periodic optics function known (or approximated), the accelerator can be represented by the transfer matrix of each segment. The

propagation of the macro-particles in the machine can then be defined by:

$$\begin{pmatrix} x_k \\ x_k' \end{pmatrix}\bigg|_{s_{i+1}} = M_x(s_{i+1}|s_i) \begin{pmatrix} x_k \\ x_k' \end{pmatrix}\bigg|_{s_i},$$
$$i \in [0,..,N_{segments}-1], \quad k \in [0,...N_{macro-particles}-1]. \tag{4.36}$$

The detuning, introduced at the beginning of this chapter, is implemented via an additional phase shift in the matrix M. From Eq. (4.17) the phase shift of a macro-particle k after one segment (s_i, s_{i+1}) can written as:

$$\Delta\psi_{k,i\to i+1} = (Q'\delta_k + \alpha J_k)\frac{\Delta\psi_{i\to i+1}}{2\pi Q}. \tag{4.37}$$

Collective effects   As the wake fields only influence the angle of a macro-particle (Eq. (4.21)), the momenta have to be updated to include their effect. To calculate the updated momenta, the slicing in the longitudinal plane, which is displayed in Fig. 4.3, is used. The number of slices has to be adapted to the wake potential used. In that, the wake potential should not exhibit a large variation over a given slice. When sliced, the effect of the wake potential has to be evaluated only once for all the macro-particles in a slice. This reduces the number of computations and with it the simulation time.

The updated change in momenta for every macro-particle x_i in a slice i due to the wake can be calculated from:

$$\Delta x_i'{}^{drive} = -\frac{e^2}{p_0\beta cC}\sum_{j=0}^{N_{slice}} N(z_j)\langle x_j\rangle W_x^{drive}(z_i - z_j), \tag{4.38}$$

$$\Delta x_i'{}^{det} = -\frac{e^2}{p_0\beta cC}\sum_{j=0}^{N_{slice}} N(z_j)x_i W_x^{det}(z_i - z_j). \tag{4.39}$$

Here z_j is the longitudinal position of the center of a slice j and $N(z_j)$ are the number of macro-particles of the slice in this position. These momenta then have to be added to the momentum of the macro-particles in the slice (see Eq. (4.21)).

Transverse damper   A damper represents a feedback system analysing the motion of a beam and trying to mitigate potential unwanted collective motion by creating a counteracting EM field. The simplest numerical implementation of a transverse damper is achieved by correcting the momentum x' of every particle by the angle $\Delta x'$, which is proportional to the average momentum of all particles in the bunch $\overline{x}'$:

$$\Delta x' = -g_x\overline{x}'. \tag{4.40}$$

The strength of the mitigation is defined by the gain factor g_x. As the correction is dependent on the average momentum, this kind of damper can only mitigate coherent motion in a bunch.

4.4 Methods - Measuring with beam

Measurements with beam are necessary to check if the observations in the machine are fully covered by beam dynamics simulations in combination with the wake model. Therefore an overview of tools used for measurements and methods to evaluate the gathered data follows.

The SPS is a cycle-based machine. Multiple cycles are combined in a super-cycle. Depending on the number and length of the single cycles the length of the super-cycle varies. Typically a super-cycle is between 30 s and 60 s long. An example of a super-cycle in the SPS is displayed in Fig. 4.5. The different cycles can be attributed to different users. Measurements in the SPS are therefore carried out as so-called Machine Development (MD) sessions in parallel to daily operation for physics.

Target	I/E11	MUL	%SYM	Experiment
T2	21.3	3	90 a	H2/H4
T4	38.1	4	85 a	H6/H8
T6	118.8	13	94 a	COMPASS
T10	21.9	0	42	NA62
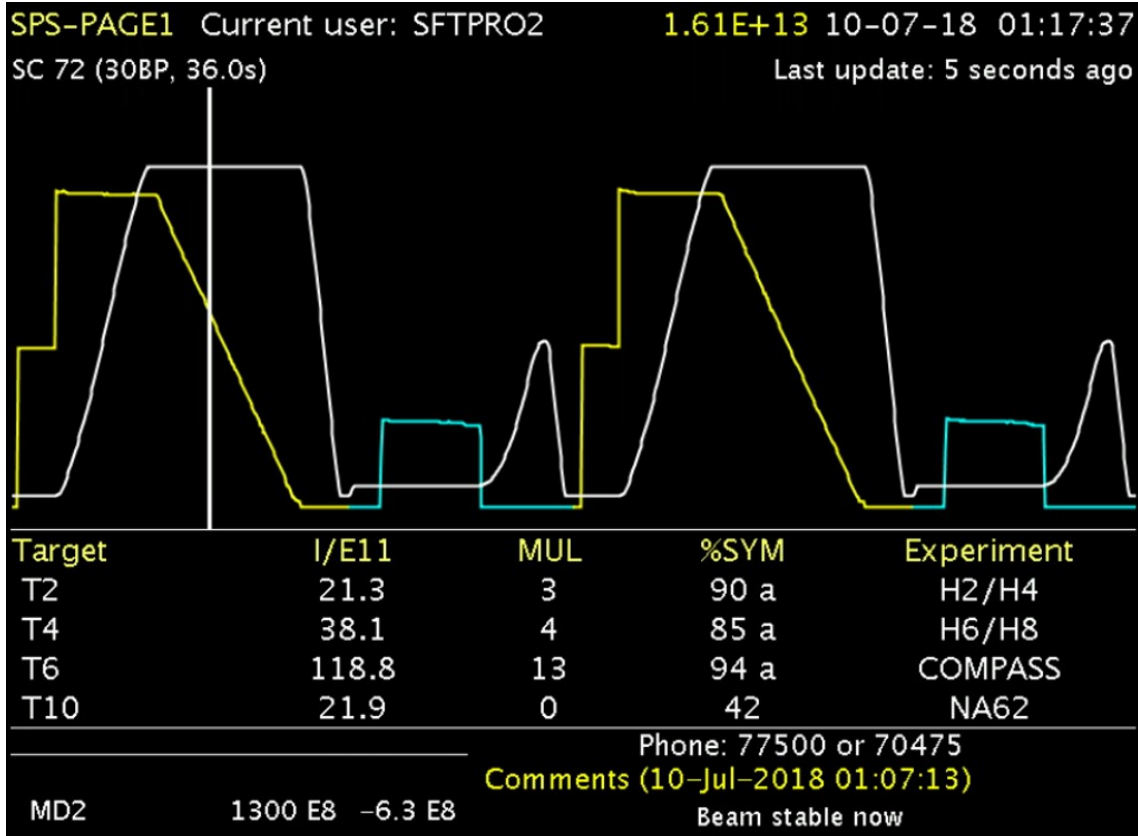
Figure 4.5: An SPS super-cycle. The coloured line shows the development of the intensity over the super-cycle. The different colours separate the cycles. The white line shows the magnetic field strength at a given time in the super-cycle.

In the SPS, a variety of beam instrumentation tools are available to monitor the behaviour of the different beam properties. The tools used for measurements in the SPS that were employed in the studies described in this thesis are:

- **BPMs** are installed around the machine so that the path of the beam can be monitored [FKL09].

- To lobserve the intra-bunch motion a **head-tail monitor** is installed in the SPS. The data is collected with so-called stripline pickups which allow a good time resolution within a bunch length [LLL16]. A screenshot of the head-tail viewer available to visualize the gathered data during a MD is shown in Fig. 4.6.

- The **Beam Current Transformer (BCT)** is used to monitor the intensity of the beam and to detect losses [Den09].

- **Wire scanners** in the horizontal and transverse planes are available to determine the transverse bunch sizes and the emittances of the beam [Bra09].
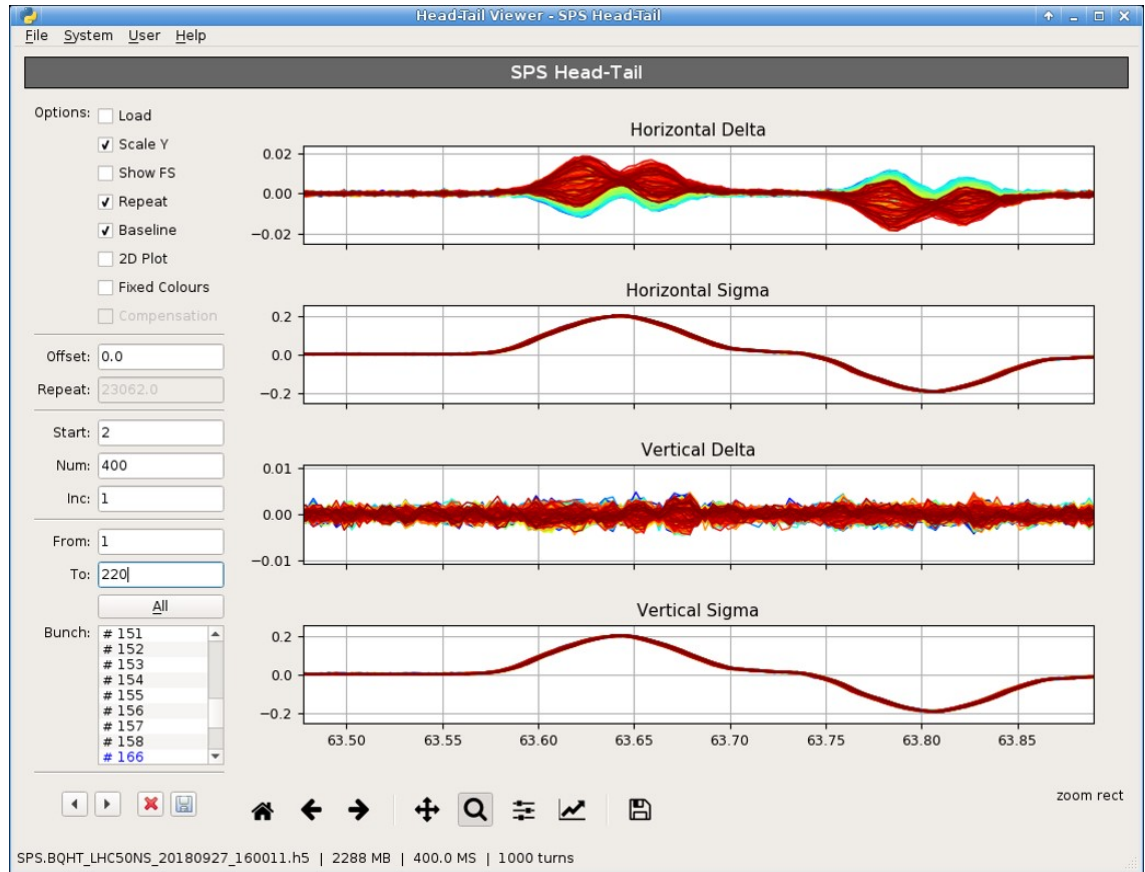
Figure 4.6: Screenshot of the SPS head-tail viewer. The sums (sigma) and differences (delta) of the pickup signals in both planes are displayed. A bunch with an instability in the horizontal plane is shown. The right, mirrored, side of the signal occurs due to a reflection on the stipline pickup and is artificial.

Besides, multiple machine parameters can be changed in the SPS. For example, the chromaticity value and the value of the magnetic octupole strength K are adjusted, among others, in the **Trim editor**. The set values, also referred to as trimmed values, are therefore converted into the corresponding magnet currents.

Measurements for this thesis were mainly conducted with a single bunch. Before each MD session the beam was corrected in orbit and injection phase. In addition, the MD cycle used was always situated behind the fixed target cycle (SFTPRO, shown in Fig. 4.5) which ensures a reproducible magnetic history in the dipole and octupole magnets. The intensity and length of the bunch are defined in the pre-accelerators.

4.4.1 Obtaining beam and machine parameter

In the following, the methods used for the evaluation of the data collected during measurements are presented. Several approaches were also used to evaluate the data obtained by simulations.

Fractional tune

The fractional tune is determined by observing the position of the beam with one BPM over multiple turns. The Fourier transform of this signal reveals a peak at the position of the fractional tune. For fractional tune measurements in the SPS the beam has to be excited to obtain a good BPM signal. The tune kickers MKQ-H and MKQ-V, introduced before, are used to kick the beam and thus to measure the fractional tune in the horizontal and vertical plane, respectively. For measured data a Python version of the SUSSIX code [BS98] was used to determine the fractional tune. It fits the measured points with a sinus function first and then transforms it in the frequency domain. This is especially important for fast-decaying BPM signals. Results of beam dynamics simulations are treated in the same way to determine the simulated fractional tune.

Chromaticity

The chromaticity Q' is determined by measuring the fractional tune over a large range of relative momentum offset δ and fitting the measured points by a curve. Higher order chromaticity values are obtained by a higher order fit. In Fig. 4.7, the results of such a measurement in the Q20 optics is shown. The results for the other optics can be found in [CBB+18].

Growth rates of instabilities

The growth rate g_r of an instability is found by fitting the evolution of the beam position, measured by BPMs or obtained from simulations, with an exponential
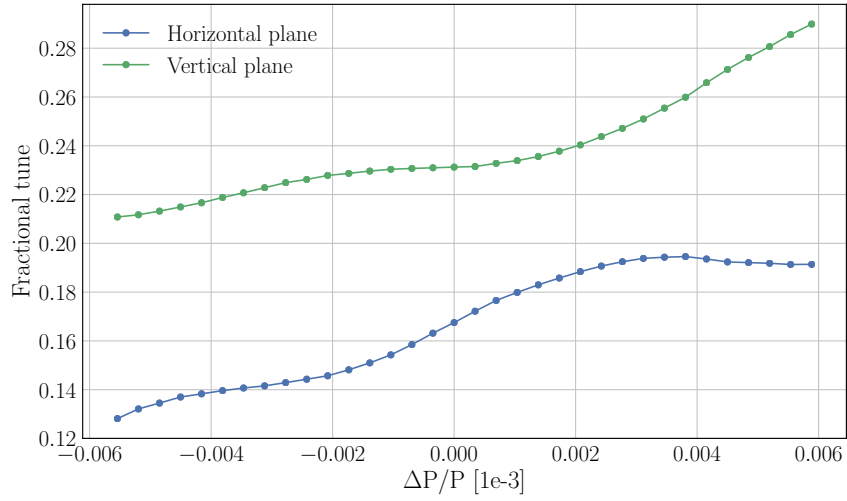
Figure 4.7: The measured fractional horizontal and vertical tunes in the SPS Q20 optics. The fractional tune is plotted against the relative momentum offset. Every dot represents a measured value, which is determined as a mean of multiple cycles.

function with an amplitude A:

$$f(t) = A \cdot e^{(g_r t)} \tag{4.41}$$

The inverse of the growth rate is the rise time $\tau = 1/g_r$. To improve the fit, only turns during which the instability grows are considered. A fit of a measured signal is plotted in Fig. 4.8.

Some instabilities in the machine are so violent, that it is not possible to monitor them early enough. Then the available number of turns are not enough to find the growth rate. In such a case, a ratio of the injected intensity and the intensity remaining in the machine at the end of the cycle is used to visualize the instability.
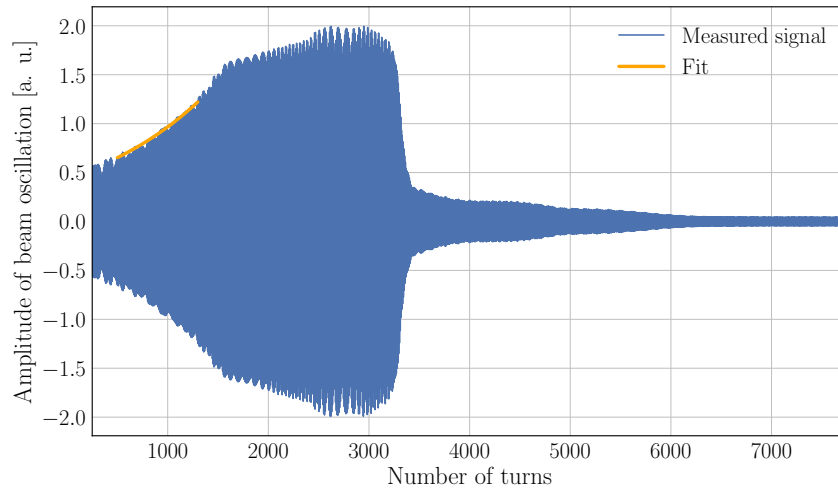
Figure 4.8: A fit for the growth rate calculation of an instability that was observed during measurements in the SPS. After around 1500 turns particle losses occur. With less particles the beam gets stable again.

5 Beam dynamics simulations and experimental observations

This chapter presents the beam dynamics simulations and the measurements with beam in the SPS performed for this thesis. First, the wake model introduced in the previous chapter is validated by measurements. Second, the intensity threshold in the Q22 optics is investigated in measurements and reproduced in simulations. Finally, possible instabilities developing in the horizontal plane and methods to stabilize the beam are investigated. Parts of the simulations and measurements in this section have been published in [BBC+18b] and in [BBC+18a].

5.1 Validation of the SPS wake model

Validation measurements were executed, to check the results obtained by beam dynamics simulation using the PyHEADTAIL code in combination with the wake model. Simulating 1,000 turns of a particle bunch with 100 slices in the SPS with PyHEADTAIL takes around three minutes on a computer using an Intel Core i7-4790 CPU with a frequency of 3.6 GHz and 12 GB RAM. The simulations presented below run for 60,000 turns and thus each run takes three hours to finish.

The discussion in Ch. 4 shows that the wake (impedance) and the intensity of a bunch influence its tune (see Eq. 4.21). Thus, to validate the detuning components of the wake model, the fractional tune of bunches with different intensities are measured in the SPS and compared to beam dynamic simulations reproducing the measurement. The measurements have been executed in the Q20 and Q22 optics as those two are foreseen to be used after the LIU. A single-bunch which was kept at the constant energy of 26 GeV (the injection energy of the SPS) was used for the measurements. The fractional tunes of the horizontal and vertical planes were determined as described in Sec. 4.4. The machine parameters set for the measurements were used in simulations and are documented in Tab. 5.1. The 2018 version of the SPS wake model is used for the PyHEADTAIL simulations, as in this year the measurements took place.

The results of these measurements and simulations are presented in Fig. 5.1 for the Q20 optics and in Fig. 5.2 for the Q22 optics, respectively. In both cases the results obtained from measurements are satisfactorily reproduced in simulations. The measured tune in the vertical plane changes by about 0.04 points in the Q20 optics (0.05 points in the Q22 optics), whereas the horizontal tune only changes around 0.01

Table 5.1: Parameters for SPS beam dynamics simulations in PyHEADTAIL.

	Q20	**Q22**
Betatron tunes Q_x/Q_y	20.13/20.18	22.13/22.18
Average beta function $\overline{\beta}_{x,y}$	55.1	49.7
Gamma at transition γ_t	18	20
Gamma at injection γ_0	27.7	27.7
RF voltage at 200 MHz V_{200} [MV]	4	2.7
RF voltage at 800 MHz V_{800} [MV]	0.4	0.27
Chromaticity $Q_x^{'}/Q_y^{'}$	7.4/1.7	7.2/4
2nd order chromaticity $Q_x^{''}/Q_y^{''}$ (10^2)	2.7/6.6	3.7/12
3nd order chromaticity $Q_x^{'''}/Q_y^{'''}$ (10^6)	-1.8/1.4	-1.8/1.6
Normalized transverse emittance ϵ_n [μm]	2	2

points over the covered intensity range. This is expected as the horizontal detuning wake is negative (see Fig. 4.4) and thus the effects of driving and detuning wakes on the tune shift with intensity compensate each other.

Figure 5.3 compares measurements of the vertical fractional tune in the Q20 optics obtained in 2014, to the vertical fractional tune measurements shown in Fig. 5.1. Note that an additional MKE kicker was installed in the machine (see Tab. 3.2) in 2014. Simulations executed with the 2015 and 2018 versions of the SPS wake model are presented in the same plot. The reduction of the created wake, due to
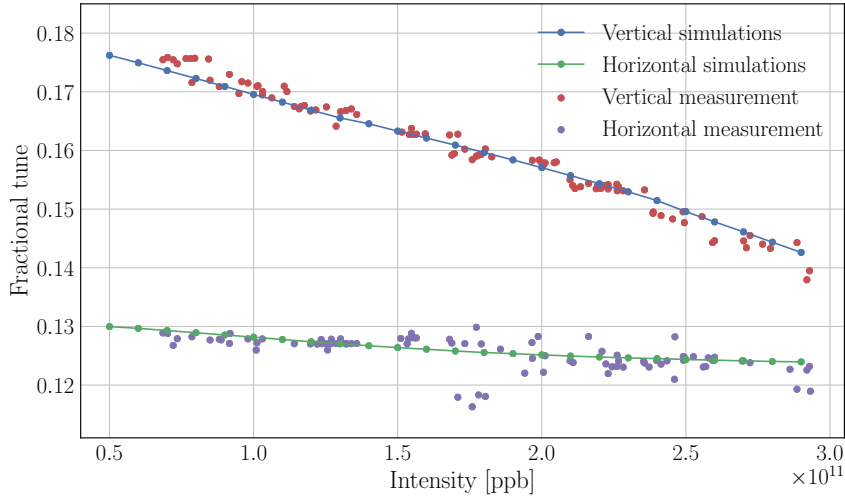
Figure 5.1: A scan of the fractional tune against the intensity for the SPS Q20 optics. Beam dynamics simulation results are compared to measured values. Each dot represents a simulation or a measured cycle, respectively.
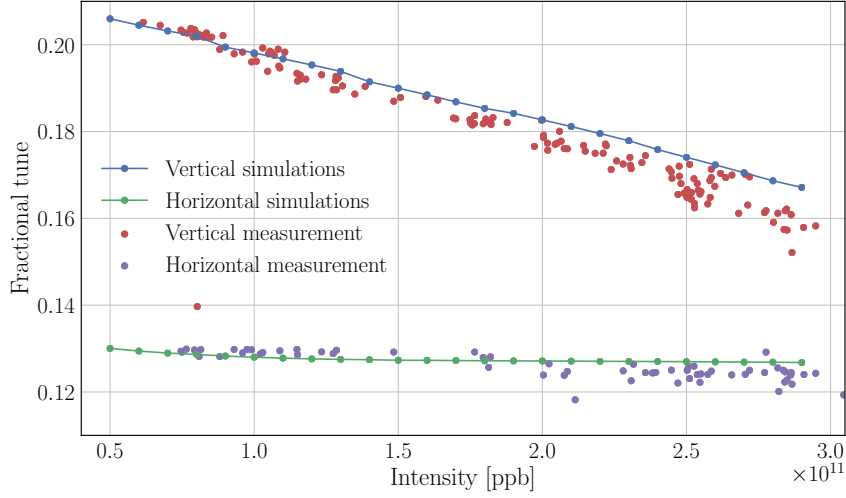
Figure 5.2: A scan of the fractional tune against the intensity for the SPS Q22 optics. Beam dynamics simulation results are compared to measured values. Each dot represents a simulation or a measured cycle, respectively.

the removal of one MKE kicker, can be observed in the evolution of the tune shift measurements. The measured tune shifts are reduced by about 0.005 points for the 2018 case in the intensity region from $1 \cdot 10^{11}$ particles per bunch (ppb) to $2.5 \cdot 10^{11}$ ppb. These measured results are reproduced in simulations.

Simulations of the post-LS2 version of the wake model in the Q20 optics predict a further, very slight reduction in tune shift over intensity due to the shielded flanges.
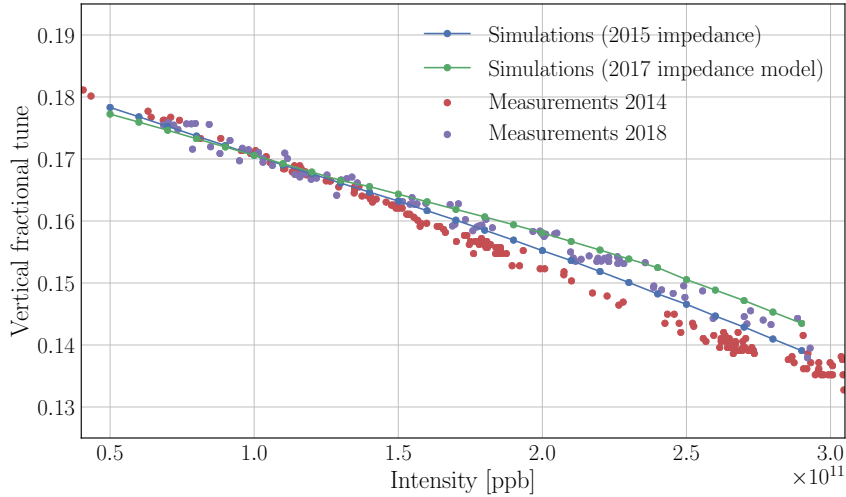
Figure 5.3: A scan of the fractional tune against the intensity for the Q20 optics. Simulations are compared to the measured fractional tune of shots with different intensities.

This is shown in Fig. 5.4 where the simulation results of the post-LS2 model are compared to the results of the 2018 version. Over the intensity range from $0.5 \cdot 10^{11}$ ppb to $3.9 \cdot 10^{11}$ ppb the fractional tunes of the post-LS2 simulations shift 0.0014 points less in vertical plane and 0.0007 points less in the horizontal plane respectively, than in the simulations with the 2018 model.
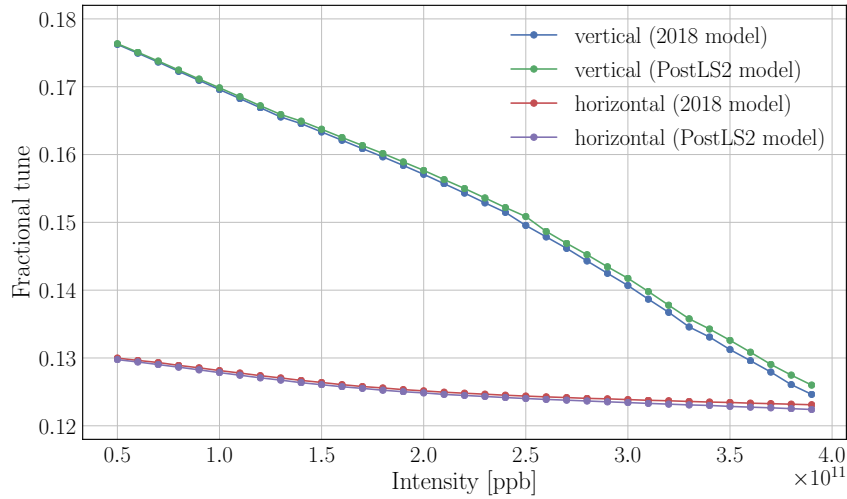
Figure 5.4: A simulated scan of the fractional tune against the intensity for the Q20 optics. Results obtained with the post-LS2 version of the wake model are compared to results obtained with the 2018 version of the wake model.

As already discussed, in the past the focus lay on the vertical part of the SPS wake model [MAB+08, Sal10, Zan13], as intensity limitations in the SPS arose mostly from the vertical plane. With the increased intensity after LIU, intensity limitations could also occur in the horizontal plane. To validate the horizontal driving (dipolar) part of the SPS wake model in particular, a single-bunch chromaticity scan was performed in the SPS in the Q20 optics. As a driving wake acts as a kick on the trailing particles (see Ch. 4) it influences the growth rate of wake-driven instabilities. The measurements were realised using bunches with $2 \cdot 10^{10}$ particles and the growth rates were calculated as described in Sec. 4.4. The simulations to validate these measurements employed the same intensity values and the simulation parameters for the Q20 optics which are presented in Tab. 5.1 with changing horizontal chromaticity values. In Fig. 5.5 the measured growth rates are compared to the simulated ones. The agreement is good. The small difference can be attributed to an uncertainty in the determination of Q'_x in measurements. Also marginal amplitude detuning that could occur in the machine and is not considered in the simulation could have an influence.

The instability occurring for negative chromaticity values is the expected head-tail instability with the mode zero developing for negative chromaticity. The head-tail

monitor installed in the SPS was used to observe this mode during the measurements. The instability is plotted in Fig. 5.6 for a chromaticity of $Q'_x \approx -6$. The mode zero is equally observed in simulations.
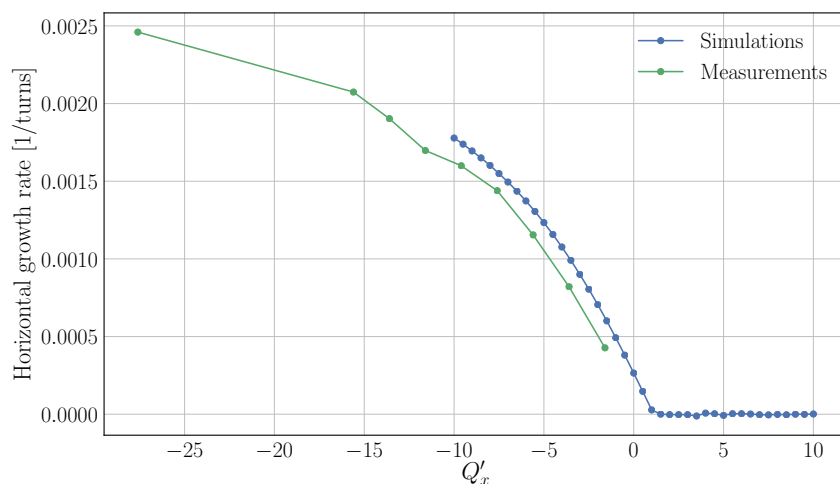
Figure 5.5: A comparison between a measured and a simulated chromaticity scan for an intensity of $2 \cdot 10^{10}$ ppb. The horizontal instability growth rate is plotted against the chromaticity Q'_x. Each dot represents a simulation or a measured value averaged over multiple cycles, respectively.
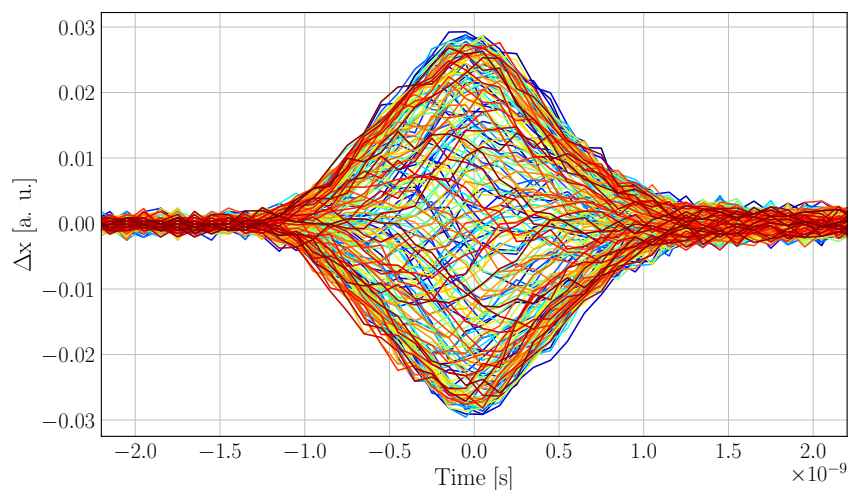
Figure 5.6: The measured horizontal mode zero instability developing for a chromaticity of $Q'_x \approx -6$. The amplitude of the instability is plotted against time with respect to the center of the RF bucket over 200 consecutive turns.

5.2 Intensity threshold in the SPS Q22 optics

Before the LHC era the SPS was operated with the so-called Q26 optics with a transverse integer tune of 26 and characterized among others by its low intensity threshold N_{thr} measured at approximately $1.6 \cdot 10^{11}$ ppb for a longitudinal emittance of $\epsilon_z \approx 0.28\,\text{eVs}$ [Bar13]. This threshold would have limited the maximum intensity delivered to the LHC. To improve the intensity threshold the low gamma transition optics, the Q20 optics with a transverse integer tune of 20, was introduced. The measured intensity threshold of this optics is $N_{thr} \approx 3.4 \cdot 10^{11}$ ppb for a longitudinal emittance of $\epsilon_z \approx 0.28\,\text{eVs}$ [Bar13], enabling operation with LHC intensities and even leaving margins for future intensity goals.

However, the low gamma transition in combination with LIU intensities leads to an increased beam loading[1] that probably cannot be compensated by the RF power amplifiers, not even after the upgrade of the RF system foreseen by LIU [DFG+14]. Therefore, a Q22 optics with a transverse integer tune of 22 and intermediate transition energy has been proposed [BAB+15] as an option, relaxing the demands on the RF power amplifiers but also leading to a intermediate stability threshold.

As described above, the intensity threshold in the SPS has already been studied for the Q26 and the Q20 optics in measurements and simulations [BIP+14, RSV05]. Here, for the first time, it has been investigated in depth for the newly proposed Q22 optics. The influence of the changeable machine parameters on the threshold is investigated in the following. The measurements are then compared to simulations.

The intensity limitation in the SPS has been long suspected to be imposed by TMCI. An overview of the TMCI in the SPS can be found in [MAA+18]. Recent measurements and simulations, unpublished when this thesis was finished, suggest that other mechanisms may also contribute to the threshold. As the threshold in the SPS behaves as predicted by the TMCI formalism (as shown below) it is still referred to as TMCI.

5.2.1 Measurements

For the threshold measurements, the Q22 optics is set up with a slightly positive vertical chromaticity ($Q'_y \approx 0.7$) to ensure the suppression of the mode zero head-tail instability excited at negative chromaticities. Again a single-bunch at injection energy ($26\,\text{GeV}$) was used as the TMCI imposes the most severe limitations at low energies (see Ch. 4.1). An RF voltage of $2.7\,\text{MV}$ was used for measurements.

The intensity threshold is measured by injecting single-bunches into the SPS while ramping up the intensity over consecutive cycles. The TMCI instability is too fast to be captured on the BPMs. Therefore, the intensity measured in the SPS after $200\,\text{ms}$

---

[1]A voltage induced by the beam on the accelerating cavities that acts opposite to the RF voltage used for acceleration.

with the BCT is compared to the intensity extracted from the PS, its direct injector. Whenever the intensity in the SPS is significantly lower, a very fast instability, the TMCI, is observed. The head-tail monitor then shows a travelling wave pattern as displayed in Fig. 5.7, which was observed for TMCI before [Bar13].
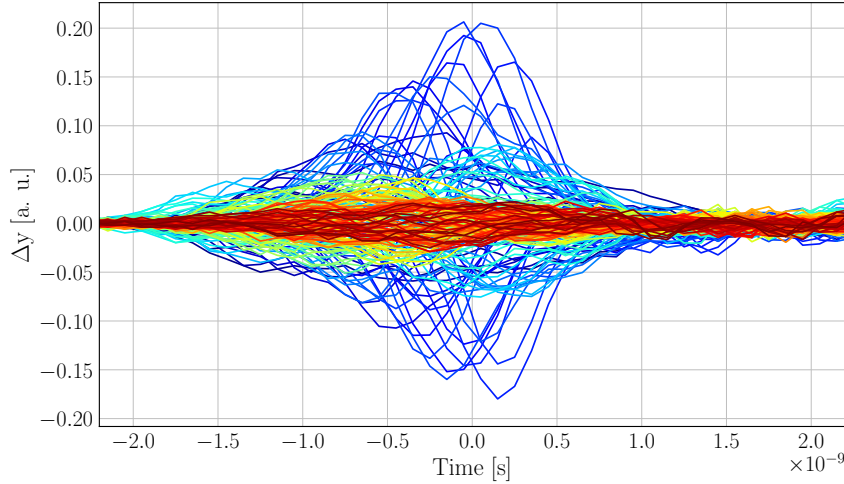
Figure 5.7: The measured travelling wave pattern in the vertical plane. The amplitude of the instability is plotted against the size of one RF bucket with respect to the center of the bucket over 200 consecutive turns. Blue colours refer to earlier turns.

Influence of longitudinal emittance

For a first characterization of the intensity threshold, bunches with a longitudinal emittance of $\epsilon_z \approx 0.32\,\mathrm{eVs}$ were measured to compare the threshold to the measurements in [Bar13] noted above. The measured longitudinal emittances presented here always refer to the longitudinal emittances measured in the PS before the rotation of the bunch is done when extracting the beam to the SPS (as described in [Bar13]). The threshold for a longitudinal emittance of $\epsilon_z \approx 0.32\,\mathrm{eVs}$ is found at $N_{thr} \approx 2.5 \cdot 10^{11}$ ppb as shown in Fig. 5.8.

For the next measurement the longitudinal emittance is reduced to $\epsilon_z \approx 0.22\,\mathrm{eVs}$. Figure 5.9 shows a threshold of about $\approx 1.8 \cdot 10^{11}$ ppb for this scenario. The linear dependency predicted by Eq. (4.32) is confirmed as the ratio of longitudinal emittance to intensity threshold is constant for both measurements.

Influence of RF voltage

A change of the cavity's RF voltage influences the synchrotron motion of the particles (Eq. (4.5)). The synchrotron motion affects the TMCI threshold (Eq. (4.30)), as a faster synchrotron motion can intuitively slow down or even prevent the instability
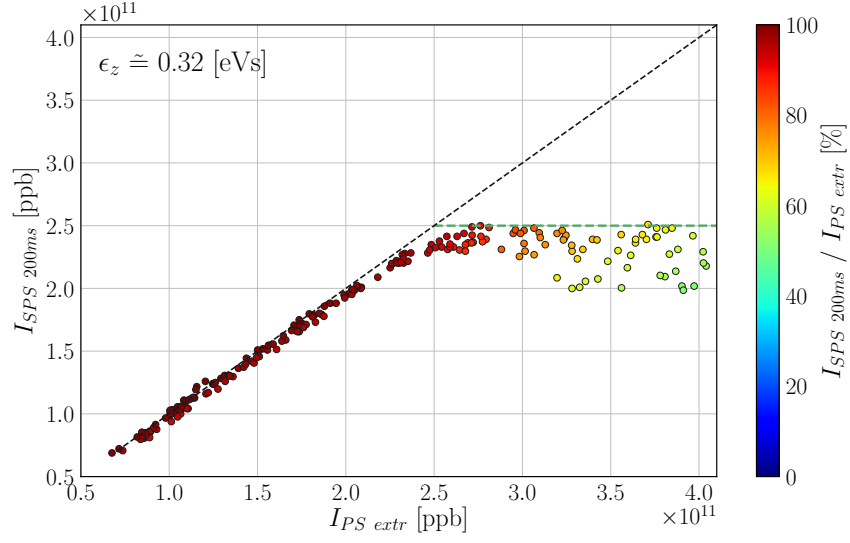
Figure 5.8: The intensity measured in the SPS 200 ms after injection is plotted against the intensity extracted from the PS. Color-coded is the percentage of particles left in the SPS after 200 ms with respect to the number of particles extracted from the PS. The green dashed line represents the intensity threshold obtained from the measured data for a longitudinal emittance $\epsilon_z \approx 0.32$ eVs in the Q22 optics.
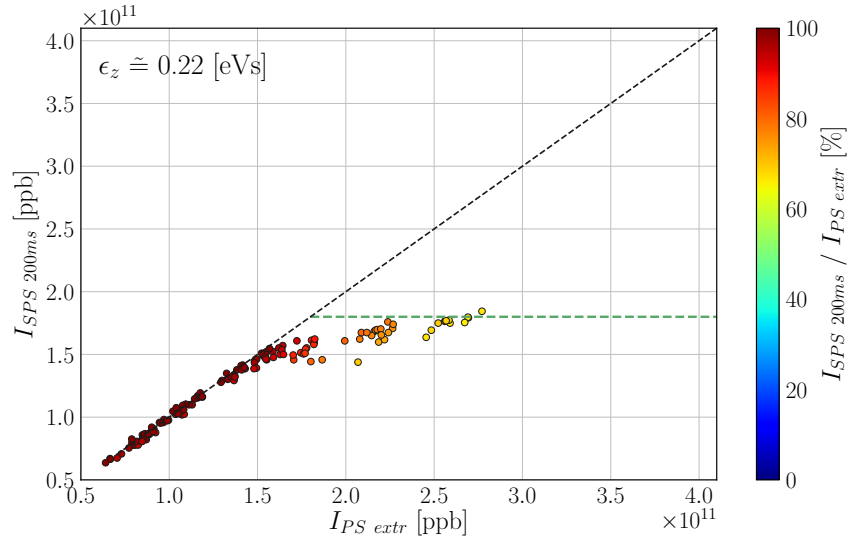
Figure 5.9: The intensity measured in the SPS 200 ms after injection is plotted against the intensity extracted from the PS. Color-coded is the percentage of particles left in the SPS after 200 ms with respect to the number of particles extracted from the PS. The green dashed line represents the intensity threshold obtained from the measured data for a longitudinal emittance $\epsilon_z \approx 0.22$ eVs in the Q22 optics.

from building up over the bunch length in successive turns. As the TMCI threshold is linearly dependent on the synchrotron tune Q_s (Eq. (4.30)) which scales with the square root RF voltage V (Eq. (4.5)), the intensity threshold in the machine should also show a square-root dependency on the RF voltage. The measurements shown in Fig. 5.10 roughly confirm that dependency. This scaling does not hold for RF voltages $V_{RF200} \geq 3\,\mathrm{MV}$ as losses already dominate in this case.
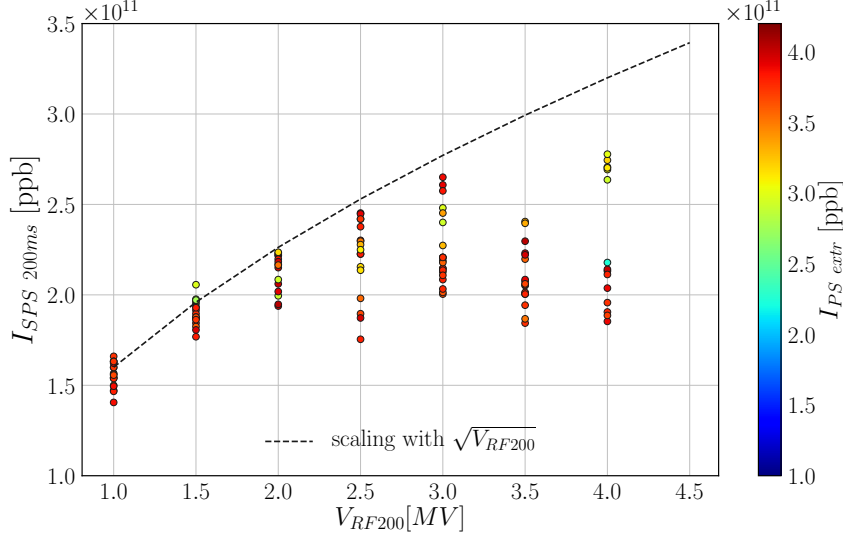
Figure 5.10: The intensity measured in the SPS 200 ms after injection is plotted against the RF voltage of the SPS main cavities (V_{RF200}). Color-coded is the number of particles extracted from the PS. The dashed black line scales with the square root of the voltage.

Influence of chromaticity

Theoretically, the TMCI threshold is dependent on the transverse chromaticity (Eq. 4.32). To investigate this dependency in measurements, different values of the vertical chromaticity Q'_y have been probed for their threshold. The results of this scan, which are shown in Fig. 5.11, confirm the theoretical prediction. The threshold is clearly found to increase for higher chromaticity values.

Beam condition after the instability

To investigate the beam condition after the occurrence of the instability, its transverse emittances in the SPS have been studied after the TMCI. Therefore, the horizontal and vertical rotational wire scanners were used. A rotational wire scanner measures the emittance two times, once swinging into the beam and once going back to its parking position. Unfortunately, it was not possible to measure the emittance before the instability occurs. For that reason, the transverse emittance of measurements
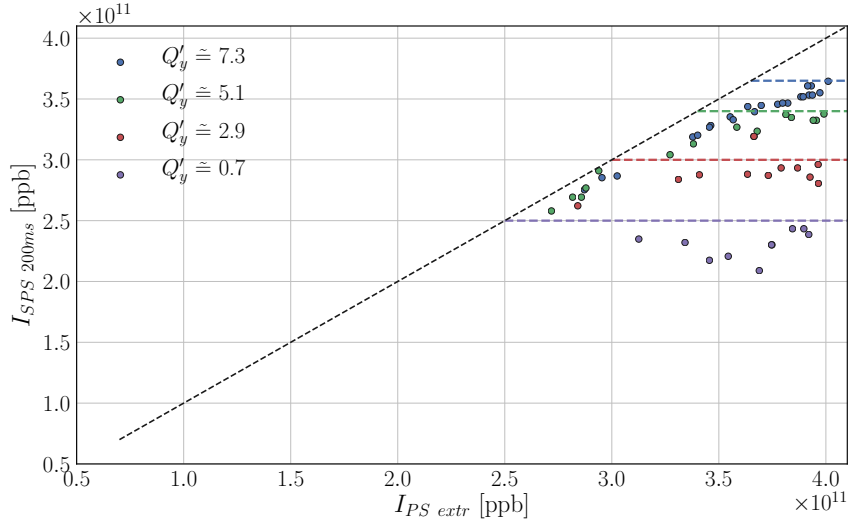
Figure 5.11: The intensity measured in the SPS 200 ms after injection is plotted against the intensity extracted from the PS. Every dot represents one measured cycle. Color-coded are the different values of the vertical chromaticity Q'_y as labeled.

where the TMCI occurs are compared to measurements where no instability occurred. In Fig. 5.12, the results of these measurements are shown. A larger vertical emittance is clearly observed after an occurrence of the TMCI. The horizontal emittance is not affected by the instability. Thus, besides the intensity loss, the increased vertical emittance also would prevent the beam to be used for physics after the occurrence of the instability.

5.2.2 Comparison of measurements and simulations

To compare the measured development of the intensity threshold with beam dynamics simulations in PyHEADTAIL, a scan over intensity and longitudinal emittance was executed in measurements. The results are shown in Fig. 5.13. A general behaviour where lower emittance values result in a lower intensity threshold is observed. Unfortunately it was not possible to fit the growth rate of the instability. Therefore, the ratio between the intensity measured in the SPS 200 ms after injection and the intensity extracted from the PS is used.

The simulations of the instability threshold in PyHEADTAIL employ the same parameter values as used for the measurement in the machine (except for the vertical chromaticity of $Q'_y = 0.7$ the same values as in the Q22 column of Tab. 5.1). The 2018 version of the SPS wake model was used for the simulations. The simulation results are shown in Fig. 5.14. Even if the quantities are different and cannot be compared directly, the behaviour of the intensity threshold is well reproduced in simulations. Especially the intensity thresholds of $N_{thr} \approx 2.5 \cdot 10^{11}$ and $N_{thr} \approx 1.8 \cdot 10^{11}$ found
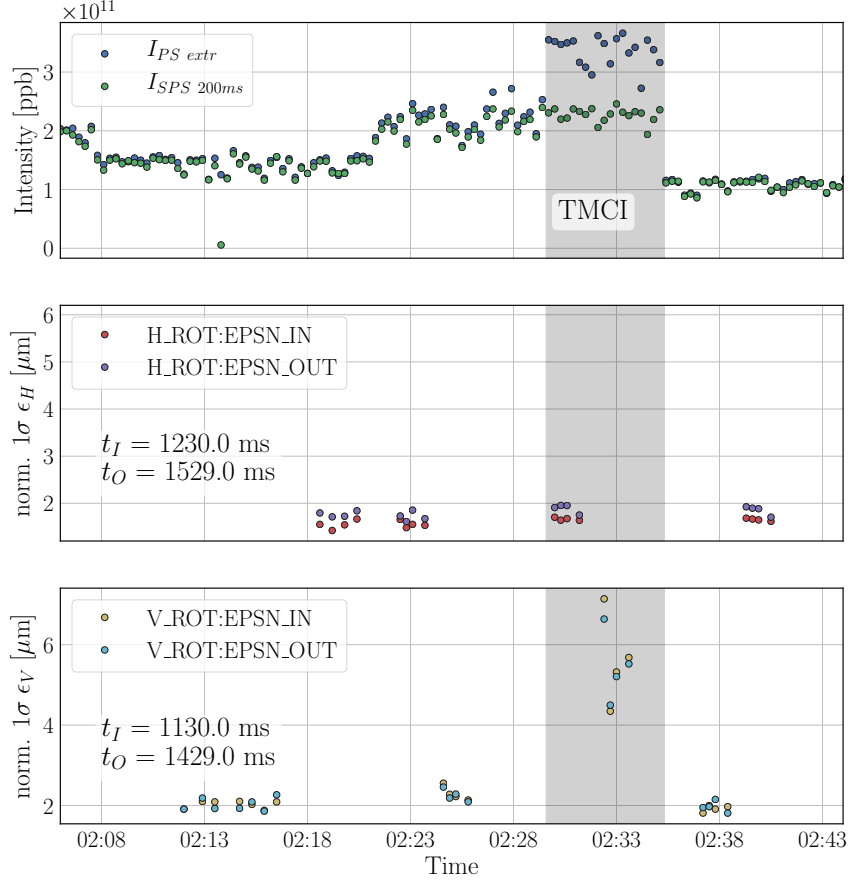
Figure 5.12: The intensity history and emittances obtained by wire scans in the horizontal and the vertical plane are shown. t_I and t_O denote the time of the measurement in the SPS cycle (injection at 1015 ms). If the intensity measured in the SPS after 200 ms is significantly lower than the intensity extracted from the PS, losses due to TMCI occurred.
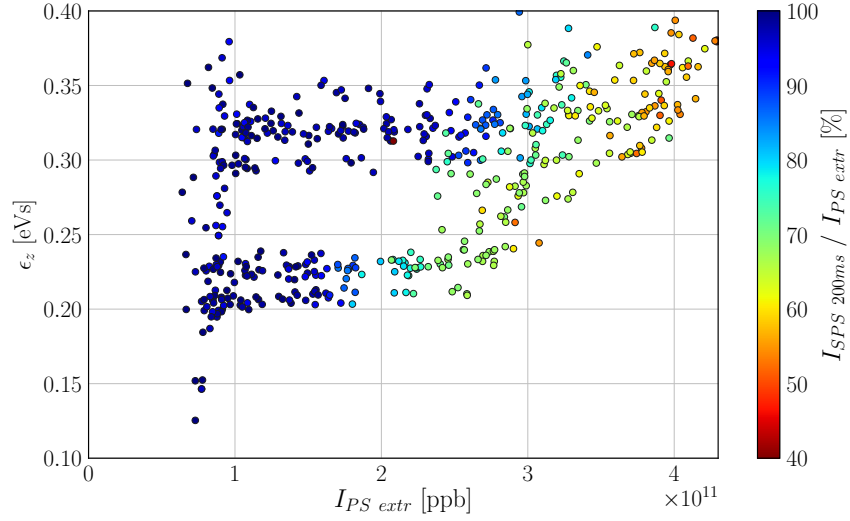
Figure 5.13: The measured longitudinal emittance is plotted against the intensity extracted from the PS. Color-coded is the percentage of particles left in the SPS after 200 ms with respect to the number of particles extracted from the PS.
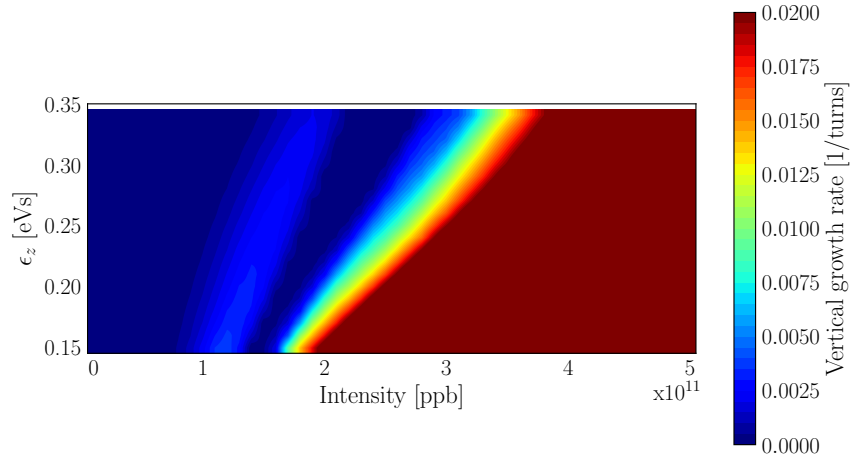
Figure 5.14: The longitudinal emittance is plotted against the intensity. Color-coded is the simulated vertical growth rate of occurring instabilities.

in measurements with longitudinal emittances of $\epsilon_z \approx 0.32$ eVs (Fig. 5.8) and $\epsilon_z \approx$ 0.22 eVs (Fig. 5.9), respectively, are well reproduced in simulations. This is shown in Fig. 5.15 where the growth rates of the simulations in Fig. 5.14 with an emittance of $\epsilon_z = 0.32$ eVs and an emittance of $\epsilon_z = 0.22$ eVs are plotted over intensity. The intensity threshold of the simulations with an emittance of $\epsilon_z = 0.32$ eVs is found at $N_{thr}^{sim} = 2.6 \cdot 10^{11}$ ppb and for an emittance of $\epsilon_z = 0.22$ eVs at $N_{thr}^{sim} = 1.9 \cdot 10^{11}$ ppb.
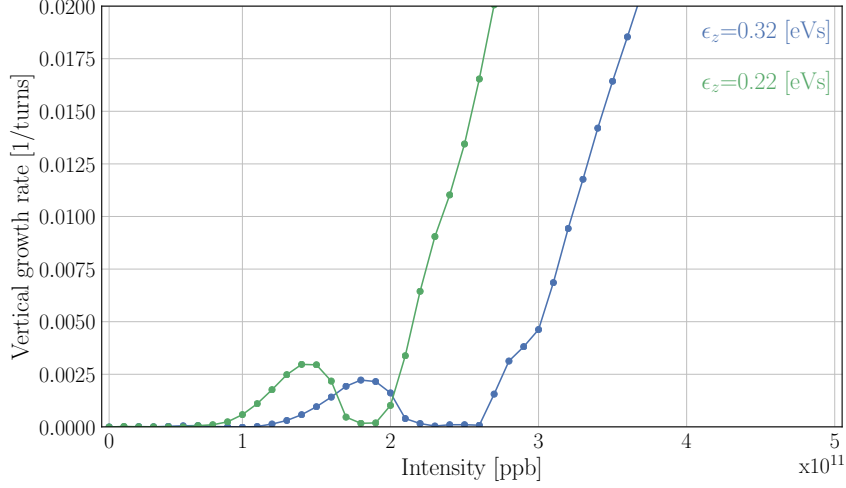
Figure 5.15: The simulated growth rates are plotted against intensity for the emittances of $\epsilon_z = 0.32$ eVs and $\epsilon_z = 0.22$ eVs. Every dot represents the results of a simulation.

The island of slow growth rate observable around $1.5 \cdot 10^{11}$ ppb in simulations could not be observed in measurements. However, the travelling wave pattern of the instability observed during measurements (see Fig. 5.7) is reproduced in simulations and presented in Fig. 5.16. In the measured case, a mitigation of the instability can be observed due to the loss of bunch particles. This effect is not observed in simulations as losses are not considered. The measured amplitude of the head-tail monitor depends on its signal processing and thus cannot be compared directly to the simulated values.
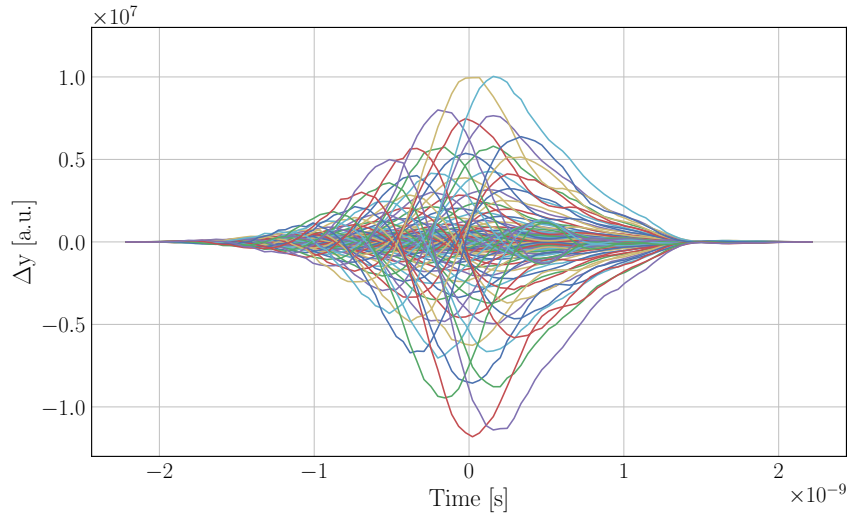
Figure 5.16: The simulated travelling wave pattern in the vertical plane. The amplitude of the instability is plotted against the size of one RF bucket with respect to the center of the bucket over 200 consecutive turns.

5.3 Horizontal instabilities in the SPS

As discussed in Ch. 1, the SPS is supposed to accelerate nearly double the amount of particles with respect to currently operated intensities after the LIU project. In recent high intensity multi-bunch runs in the SPS, a horizontal single-bunch mode one instability (see Fig. 5.17) was observed and is currently being studied and characterized. As the horizontal plane could thus become a potentially limiting factor, a campaign to investigate horizontal high intensity instabilities and possible damping mechanisms was launched. The studies concentrate on the Q20 optics as the instability was observed in this optics and it is the baseline for the LIU project. Therefore, beam dynamics simulations have been performed to study unstable behaviour and possible limitations. The simulations were done with the PyHEADTAIL code and used the SPS wake model in the 2018 version.

First scans over the horizontal chromaticity Q'_x have been done using both a linear and a non-linear optics model of the SPS. In the linear case all the higher order terms of chromaticity are set to zero and only linear synchrotron motion is assumed. These assumptions allow for instabilities to develop and are used for studies. For the more realistic non-linear case, besides assuming a non-linear synchrotron motion, the higher order chromaticity is set to values obtained by measurements and presented in Tab. 5.1. As there is no coupling between the transverse planes activated in the simulation, the vertical plane is neglected here. This is a valid assumption as coupling between these planes is indeed negligible in the SPS [Bar]. As the instability occurred on occasional bunches in the beam, single-bunch simulations are used for the
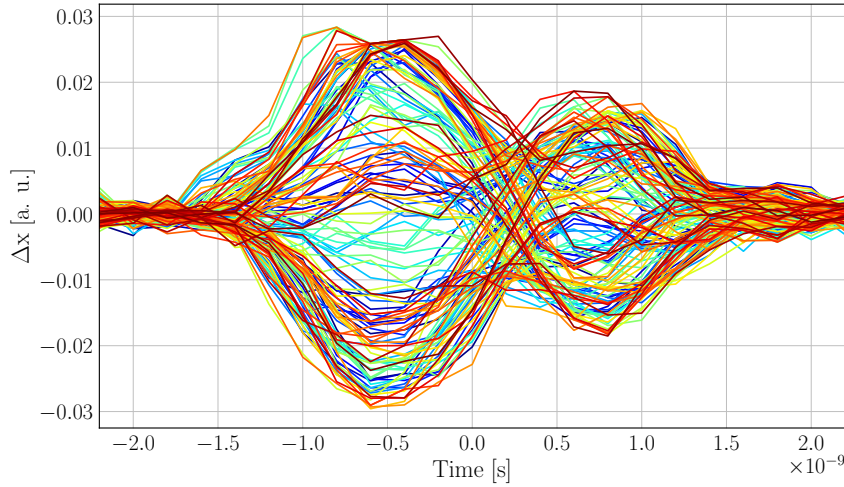
Figure 5.17: Measured horizontal mode one instability. The amplitude of the instability is plotted against time with respect to the center of the bucket over 200 consecutive turns.

investigation. The intensity was set to $2 \cdot 10^{11}$ ppb, which was the bunch intensity used when the instability was observed, and the longitudinal emittance to $\epsilon_z = 0.35$ eVs , i.e. the nominal SPS value at injection. Both, the linear and non-linear scenarios have been simulated with an active damper to investigate its effect on the growth rate. The damping time has been set to 100 turns.

In Fig. 5.18 the results of the beam dynamics simulations for the linear case are shown. For negative chromaticity, the expected mode zero head-tail instability is observed again. Between a horizontal chromaticity Q'_x of zero and five, an area with higher growth rates develops. The higher growth rate occurs due to a mode one instability which is shown in Fig. 5.19.

Using the more realistic non-linear machine model for the simulations changes the growth rate development (as seen in Fig. 5.20). Instead of being damped by a horizontal chromaticity Q'_x of zero as in the linear case, the mode zero needs a horizontal chromaticity Q'_x larger than one to be suppressed (see Figs. 5.18 and 5.20 blue curves). This can be expected due to the contributions of the higher order chromaticities (Fig. 4.7). The growth rate does not show large variations for higher chromaticity values anymore. Especially the bump around $Q'_x = 3$ is not observed anymore. The mode one instability shown in Fig. 5.19 can still be observed but with marginal growth rates thus it is not visible in Fig. 5.20.

Simulations show that the damper acts very efficiently on the mode zero instability seen at negative chromaticities. For both, the linear and the non-linear model, the damper stabilizes bunches for small negative chromaticity values as long as the instability growth rate is lower than 1/100 turn. For the linear case it is interesting to observe that the damper mitigates the bump of the mode one instability for chro-
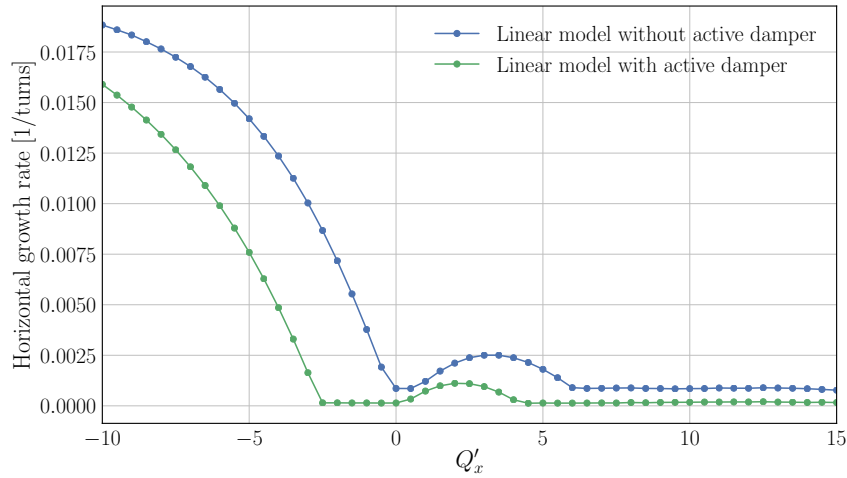
Figure 5.18: Simulated chromaticity scan for the linear machine model. The horizontal instability growth rate is plotted against the horizontal chromaticity Q_x'. The simulations have been run without (blue) and with active bunch-by-bunch damper with a damping time of 100 turns (green).
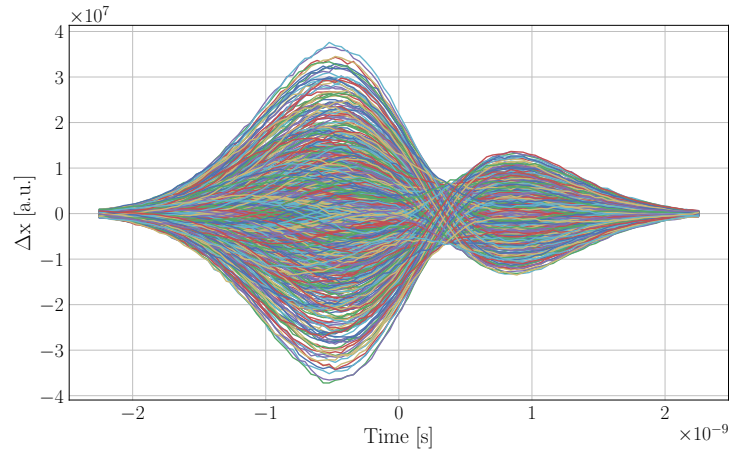
Figure 5.19: Simulated horizontal mode one instability developing for a horizontal chromaticity $Q_x' = 3$. The amplitude of the instability is plotted against time with respect to the center of the bucket over 200 consecutive turns.

maticity values larger than two, but does not completely suppress it (see Fig. 5.18). This is expected as the damper cannot act on intra-bunch motion. For the non-linear simulations with damper (Fig. 5.20) the mode one instability can again be observed around a horizontal chromaticity Q_x' of three with marginal growth rates.

The mode one observed in simulations could not be observed in single-bunch measurements with the 3.4 s long MD cycle in the SPS. As the growth rate is so
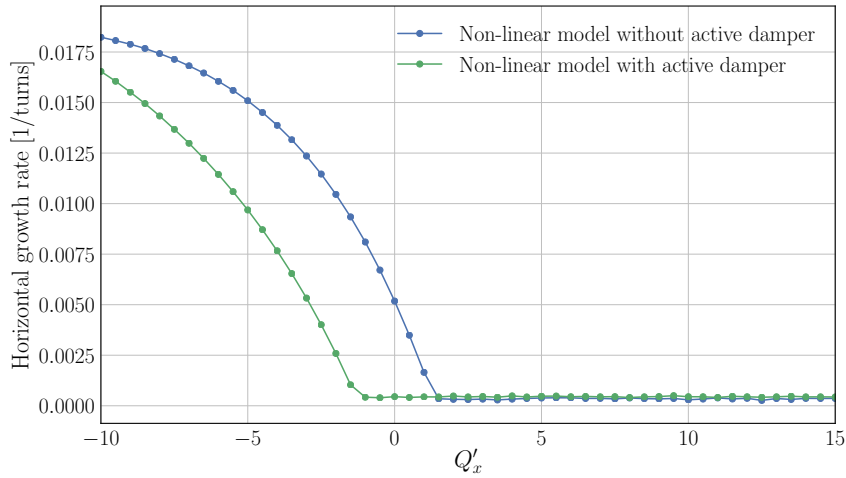
Figure 5.20: Simulated chromaticity scan for the non-linear machine model. The horizontal instability growth rate is plotted against the horizontal chromaticity Q'_x. The simulations have been run without (blue) and with active bunch-by-bunch damper with a damping time of 100 turns (green).

marginal, the instability probably cannot develop in such a short time or is completely damped by non-linearities of the machine.

When the simulation results with a bunch intensity of $2 \cdot 10^{10}$ ppb in Fig. 5.5 are compared to the simulations with a bunch intensity ten times higher in Fig. 5.20 a factor ten can also be observed between the growth rates. The growth rate thus proves to scale linearly with the intensity. This is expected as no mode coupling is occurring.

5.4 SPS octupole studies

For the future operation of the SPS with LIU intensities and the instabilities developing in the horizontal plane discussed above, the octupoles could become an important tool to keep the beam stable. Octupoles can damp an instability by introducing a betatron tune spread as a function of the transverse particle oscillation amplitude. This tune spread can lead to Landau damping which then mitigates the instability. The possibility of using this mechanism to stabilize the beam has been investigated in measurements for this thesis.

Three groups of so-called Landau octupoles are installed in the SPS; the group next to the focusing quadrupoles, the Horizontal Landau Octupoles (LOF), is acting mainly on the horizontal plane, the group next to the defocusing quadrupoles, the Vertical Landau Octupoles (LOD), is acting mainly on the vertical plane, and the group of the Landau Octupoles for Extraction (LOE), which is also acting mainly

on the horizontal plane. For this thesis only LOE1202 and LOE3302 of the LOE family were used in measurements, as they are situated in regions of the accelerator with a small horizontal dispersion and thus mainly create amplitude detuning and hardly any second order chromaticity.

First, a simple scan for different magnetic strengths of the LOF K_{LOF} has been carried out in the machine. For this purpose single-bunches with an intensity of $N \approx 2 \cdot 10^{10}$ ppb were used. While the vertical chromaticity was kept at a positive value ($Q'_y \approx 2$), the horizontal chromaticity was set to $Q'_x \approx -2$ in order to provoke the mode zero head-tail instability as shown in Fig. 5.6. This instability should then be mitigated by the octupoles. The results of the measurement are plotted in Fig. 5.21. For absolute magnetic strengths of $|K_{LOF}| = 6 \ m^{-4}$ the instability is damped by the octupoles.

However, the LOF do not only introduce amplitude detuning a_{xx} but also second order chromaticity Q''_x in the horizontal plane. To investigate the damping mechanism, a scan over the second order chromaticity Q''_x was done. For this measurement the general idea is to set up the LOE to compensate the amplitude detuning a_{xx} introduced by the LOF and the LOD to compensate the introduced amplitude detuning cross term a_{xy}. MADX was used to calculate the magnetic strength K of all three octupole groups needed to obtain the demanded second order chromaticity Q''_x with the constraint that the amplitude detuning a_{xx} and the amplitude detuning cross term a_{xy} have to be zero. Measurements of the amplitude detuning a_{xx} verified a good compensation at different values of the second order chromaticity Q''_x. The results of this scan are shown in Fig. 5.21.

Note, the growth rates obtained without octupoles ($K_{LOF} = 0 \ m^{-4}$) show a nearly identical value of around 0.0003/turn in both measurements, which indicates a good quality of the measurements. However, comparing the growth rates to the one obtained for the chromaticity scan in Fig. 5.5 a discrepancy occurs, as the measured growth rate for a chromaticity of $Q'_x \approx -2$ without active octupoles is around 0.0005/turn. This difference can be attributed to the fact that the measurements were not executed during the same MD session and the longitudinal beam distributions delivered by the pre-accelerators might have been slightly different.

The curve of the measured second order chromaticity scan in Fig. 5.21 follows remarkably well the scan of the magnetic strength of the LOF K_{LOF} in the same figure. This leads to the impression that the damping of the LOF mainly arises from chromatic effects, as the compensation of the amplitude detuning does not seem to influence the results significantly. Investigations revealed a non-negligible offset that the beam had from the center of the octupoles. When a beam passes an octupole out of its axis the so-called feed down effect leads to an additional sextupolar field contribution [Lee12]. This field changes the chromaticity in the machine as the measurement in Fig. 5.22 shows. When the second order chromaticity values were set, the different magnetic strengths of the LOF K_{LOF} led to significant changes in chromaticity.
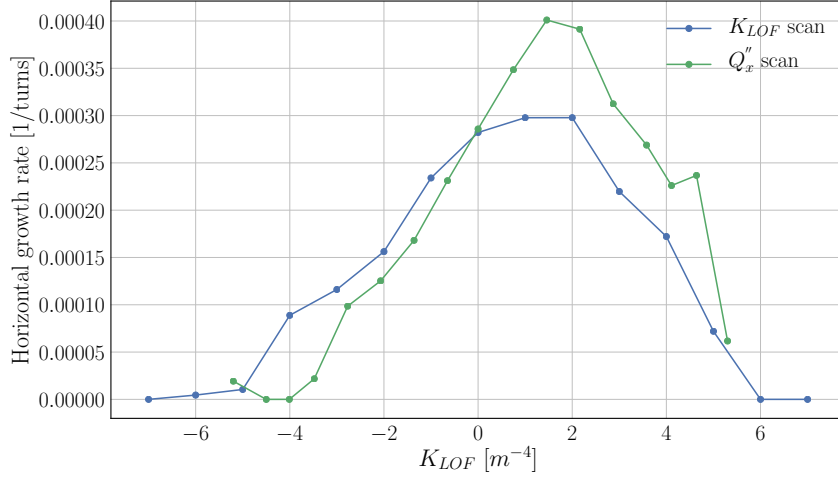
Figure 5.21: The measured growth rate is plotted against the magnetic strength of the LOF K_{LOF}. For the horizontal second order chromaticity $Q_x^{''}$ scan, the LOE and LOD were used to compensate the amplitude detuning produced by the LOF. The growth rate for every measured point is determined as the mean of multiple cycles. Intensities of $N \approx 2 \cdot 10^{10}$ ppb were used for the measurement.

In the SPS only selected octupoles are connected to power supplies. The reason for the off-center orbit lay in the fact that the octupoles, which were connected at that time, were chosen for the orbit of the Q26 optics and thus did not have ideal positions for the orbit of the Q20 optics. After connecting octupoles at low orbit positions in the Q20 optics, measurements of amplitude detuning a_{xx} and second order chromaticity $Q_x^{''}$ for different the magnetic strengths K_{LOF} revealed the introduction of pure amplitude detuning with marginal chromatic effects. Therefore, a second scan for the magnetic strength K_{LOF} was executed and is presented in Fig. 5.23. Unfortunately, it was not possible to fit the growth rate for these measurements, which is why the percentage of particles lost over one cycle is used as a substitute. Note, even if, compared to the measurements in Fig. 5.21, a more than seven times higher intensity ($N \approx 1.5 \cdot 10^{11}$) was used for the measurements, magnetic strengths of $K_{LOF} = -9 \ m^{-4}$ and $K_{LOF} = 6 \ m^{-4}$ stabilized the beam. The stabilization mechanism is thus suspected to be Landau damping introduced by the amplitude detuning of the octupoles [Bar].
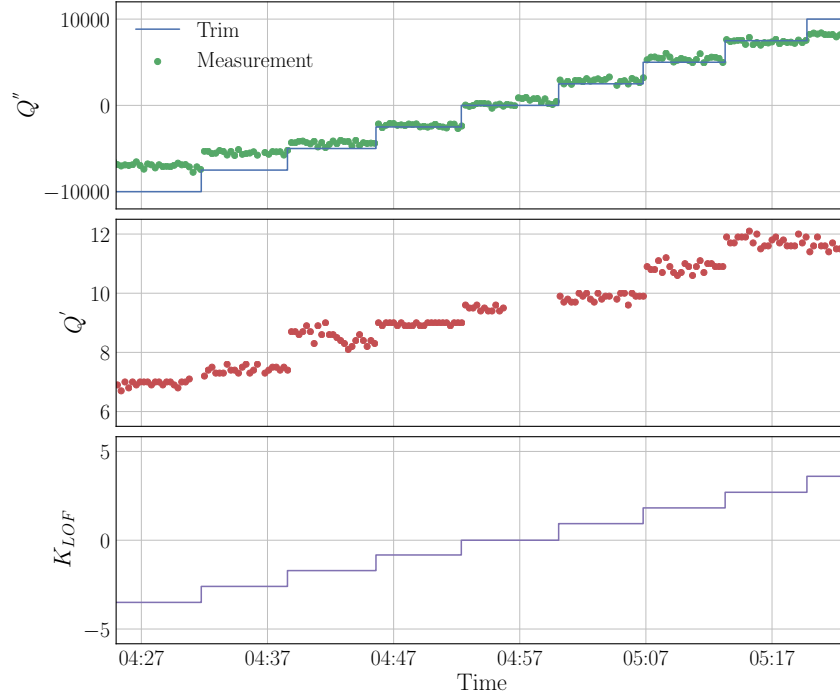
Figure 5.22: The measured first and second order chromaticities for different set of second order chromaticity values. The the magnetic strength of the LOF K_{LOF} used in the measurement are shown in addition. Intensities of $N \approx 2 \cdot 10^{10}$ ppb were used for the measurement.
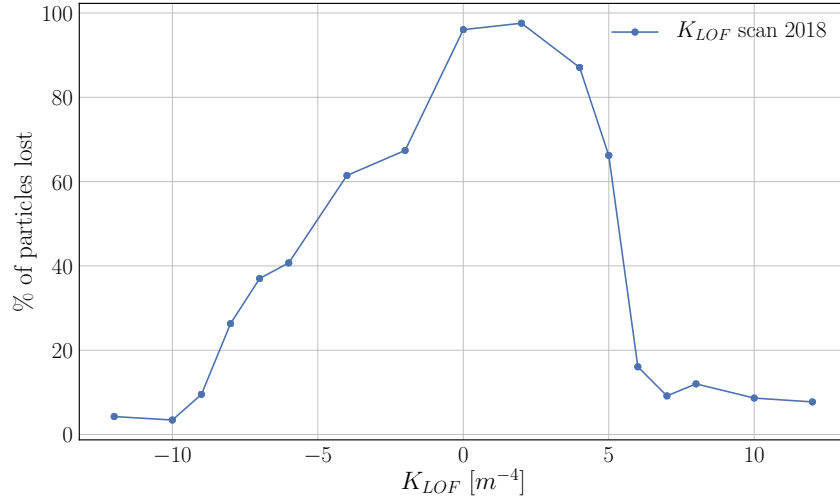
Figure 5.23: The measured percentage of particles lost over one cycle is plotted against the magnetic strength of the LOF K_{LOF}. The growth rate for every measured point is determined as a mean of multiple cycles. Intensities of $N \approx 1.5 \cdot 10^{11}$ ppb were used for the measurement.

6 Conclusion

This thesis provides new contributions in simulating the impedance of individual accelerator components and modelling the impedance of a complex accelerator. Universally applicable methods to reduce the impedance of accelerators, to emulate impedance measurements and to scale the impedance contribution of repeated structures in an accelerator were presented. A impedance model of an accelerator was assembled out of the contributions of different components. The model was validated by measurements and used to investigate intensity-dependent beam instabilities in beam dynamics simulations. Instabilities in high intensity beams and possibilities to stabilize those beams were also investigated in measurements. The following paragraphs conclude the studies presented.

The CST code was used to investigate the impedance of a discontinuous transition from one into two beam pipes (Y-chamber). The results show that adding a simple metal sheet, which is cut in the shape of a smooth aperture transition, can significantly reduce the impedance generated by the transition.

CST simulations were also used to characterize the impedance of the Electrostatic Septum (ZS) chain, which is used to extract the beam from the SPS. After modelling the impedance of all of its specific components, a new scaling approach allowed to characterize the impedance of the complete ZS chain for the first time. During the shutdown during 2019 and 2020 (LS2), a newly developed dedicated shielding to reduce the ZS impedance is planned to be implemented. Simulations investigating the shielding predict that it will reduce the impedance of the complete ZS chain by a factor of 30.

A new kicker model for impedance simulations in CST was presented and validated by bench measurements and heating observations in the SPS. An emulation of the bench measurements by simulations showed a very good agreement with measurements. But the emulations also exhibited a discrepancy when the impedance is calculated out of the measured S-parameter by means of the LOG-formula. The modelling of the so-called serigraphy, which was applied to the SPS extraction kickers to reduce their impedance, was studied in depth. Multiple parameters were investigated in simulations and measurements. The relative permittivity of the ferrite ϵ_r was found to have a significant influence on the resonance frequency of the serigraphy. This resonance frequency is decisive for the emulation of the heating observed for the MKE type extraction kickers. For the SPS injection kickers, two adapted insulated serigraphy layouts were proposed. Calculations predict that these serigraphies can reduce the heating of a MKP-L type injection kicker by up to a factor of 20.

Two new versions for the SPS impedance and wake models have been introduced. Compared to the legacy model of 2015, the first new version, the 2018 version, takes into account the modifications in the SPS within the last three years, i.e. the removal of one extraction kicker and the adaptation of the serigraphy length. The model now also considers the impedance contribution of the ZS. The second new version, the post-LS2 version, takes into account all changes foreseen in the machine during the upcoming shutdown. Beside the update of the ZS, the shielded flanges are included as well. With all this considerations, the post-LS2 version permits to study the beam dynamics in the upgraded SPS by simulations. The impedance and wake model scripts were implemented in Python. The output of the wake model can now be directly used as an input for the beam dynamics simulation code PyHEADTAIL. To validate the SPS impedance model, multiple machine measurements were compared to beam dynamics simulations in PyHEADTAIL. The good agreement suggests a highly realistic machine model. Moreover, the long wake lengths used for the impedance simulations can be beneficial for future multi-bunch simulations.

Post-LIU operation of the SPS may benefit from a newly proposed setup of the SPS, the so-called Q22 optics. The intensity threshold in this optics has been measured in depth for the first time and was found at $N_{thr} = 2.5 \cdot 10^{11}$ ppb for a longitudinal emittance of $\epsilon_z = 0.32\,\text{eVs}$. Furthermore, the dependency of the threshold on multiple theoretical parameters has been investigated and was found to scale like predicted by the analytical formula describing a transverse mode coupling instability (TMCI) in the vertical plane. The measured results are in very good agreement with PyHEADTAIL beam dynamics simulations, which resort to the newly introduced SPS wake model in the 2018 version.

The so-called mode one instability, that has been observed on a single-bunch during first operations with a high intensity multi-bunch beam in the SPS, was investigated in beam dynamics simulations. The studies show, that for higher single-bunch intensities in the SPS a mode one instability can develop in chromaticity regions where it has not been observed before. The instability can be damped using higher chromaticity. Furthermore, it has been shown that an active bunch-by-bunch damper can help to reduce these chromaticity values. Future multi-bunch simulations can be used to further study this instability.

The effect of the SPS octupoles magnets on a deliberately created beam instability was studied in measurements. It has been shown that before the reconfiguration of the octupoles, their chromatic detuning dominated the stabilization mechanisms. After the reconfiguration, the octupoles damp the instability more efficiently. The so-called Landau damping is believed to stabilize the beam now. A scan over different magnetic strengths of the octupoles showed that reasonable values are sufficient to damp instabilities. Thus, the octupoles could be used stabilize the horizontal mode one instability observed in multi-bunch operation.

With all this research this thesis contributes to the impedance modelling of accelerators and to their operation with high intensity beams.

A Further studies and results

This appendix documents the sensitivity and convergence studies executed on the MKE kicker model within this thesis. In addition, further simulation and measurement results of the different MKE versions are presented.

A.1 Convergence and sensitivity studies

Besides the sensitivity studies for the MKE model already presented in Ch. 3, the sensitivity of the simulated kicker impedance on the serigraphy paste conductivity σ_{ser} and the ferrite conductivity σ_{ferrite} were investigated, as well.

The results of the serigraphy paste conductivity scan are presented in Fig. A.1. For serigraphy paste conductivity values of $1.0 \cdot 10^7\,\text{S/m}$, which was used in simulations, $4.2 \cdot 10^7\,\text{S/m}$, which is the value for the silver paste given by the supplier, and $6.2 \cdot 10^7\,\text{S/m}$, which is the value of silver, the resulting impedance curves are in very good accordance. The difference plots show negligible values of $15\,\Omega$ maximum between the simulated impedances of the resonance peaks.

The results of the ferrite conductivity scan in Fig. A.2 show an influence on the height of the resonance peak for a conductivity that is a factor of 10^4 smaller than the value given by the supplier $(1.0 \cdot 10^{-5}\,\text{S/m})$. A ferrite conductivity value which is a factor of 100 higher than the value given by the supplier does not show a remarkable effect on the impedance.

Mesh convergence studies were executed to check if the mesh is able to resolve the EM penetration into the ferrite. Therefore, the model was simulated with a higher number of mesh cells (57.5 million). In Fig. A.3 the resulting impedance is compared to the results of the same model employing 44.1 million mesh cells. This kind of mesh was also used for the simulations described in this thesis and is referred to as the standard mesh henceforth. The results show that the larger number of mesh cells has no remarkable influence on the impedance (less than two percent), which leads to the conclusion that the ferrite is sufficiently resolved by the standard grid.

However, both grids used above resolve the serigraphy stripe width with only two mesh cells. As the serigraphy has a strong influence on the impedance, a mesh with a tripled number of cells over the serigraphy width was tested as well. In Fig. A.4 the results are compared to the standard mesh. Besides a marginal shift in the serigraphy resonance frequency by $1.2\,\text{MHz}$ the broadband frequency over ca. $300\,\text{MHz}$ slightly differs, as well. But the simulation with the finer mesh needs seven times longer, i.e. around 395 hours instead of 56.5 hours, to finish on the HPC node with 16
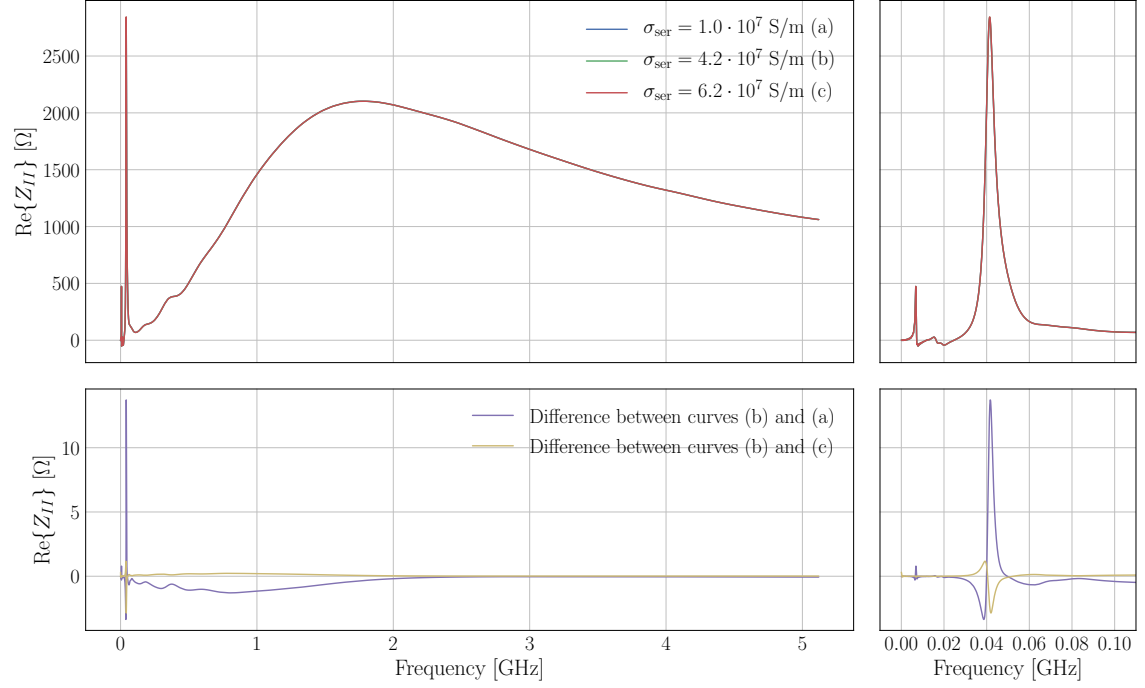
Figure A.1: Comparison of the influence of the serigraphy paste conductivity σ_{ser} for three different values on the impedance of a MKE-L kicker with the 200 mm serigraphy installed. The differences of the curves in the upper plots are shown in the lower ones.
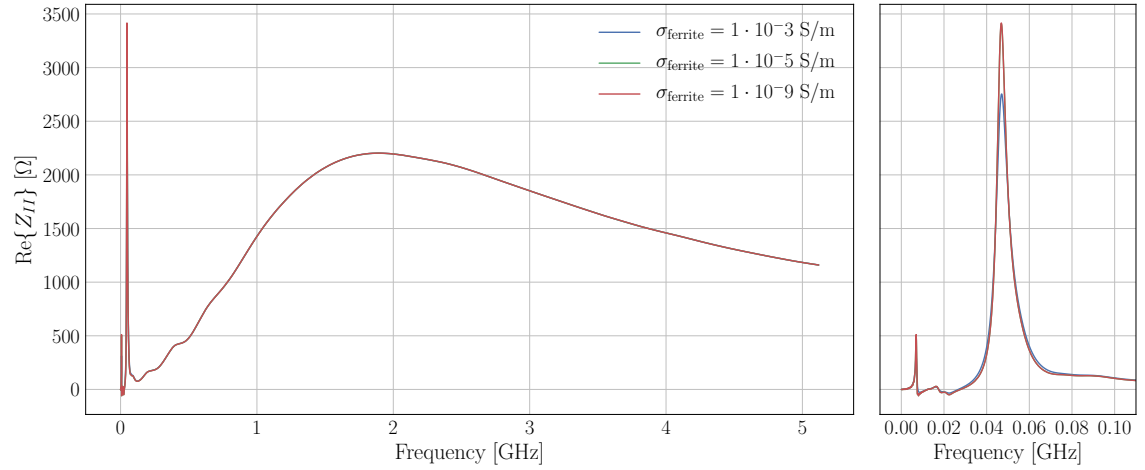
Figure A.2: Comparison of the influence of the ferrite conductivity $\sigma_{\mathrm{ferrite}}$ for three different values on the impedance of a MKE-L kicker with the 200 mm serigraphy installed.

cores described in Sec. 2.2. For this reason, the standard mesh with ca. 44 million mesh cells was chosen for MKE simulations within this thesis. Parallelization of the simulations was not possible as it was not supported by the CERN HPC grid.
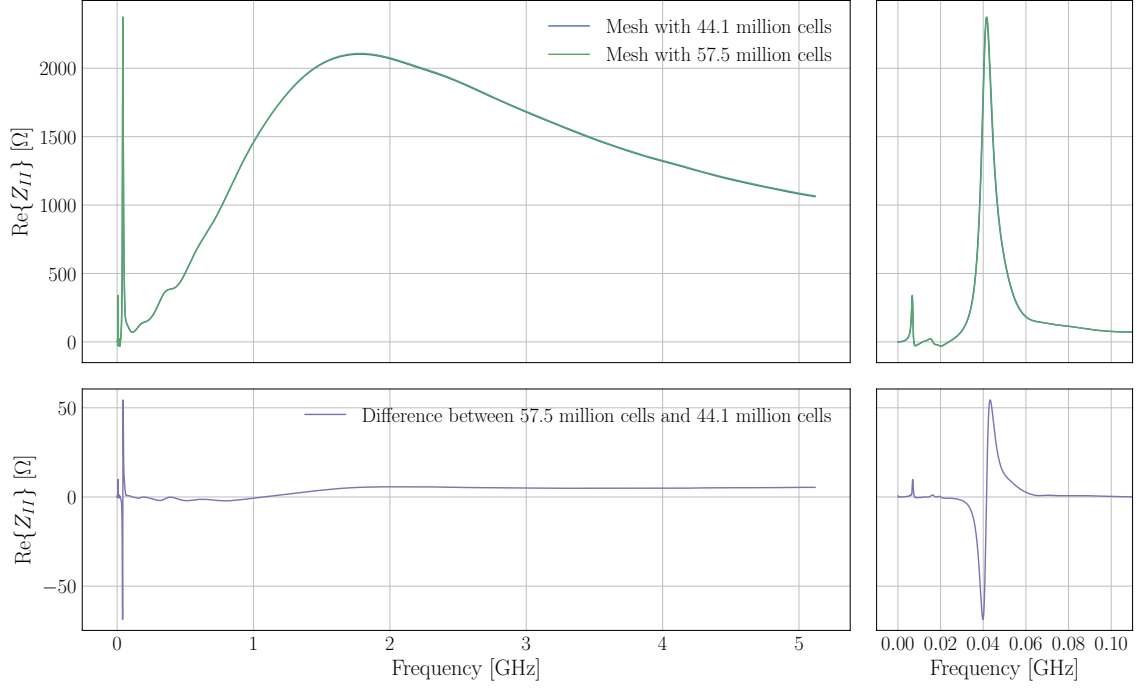
Figure A.3: Mesh convergence studies for the MKE-L with the 200 mm serigraphy installed. The results of simulations with different numbers of mesh cells are plotted. The serigraphy width is resolved by two mesh cells in both cases. The difference of the curves in the upper plots is shown in the lower ones.
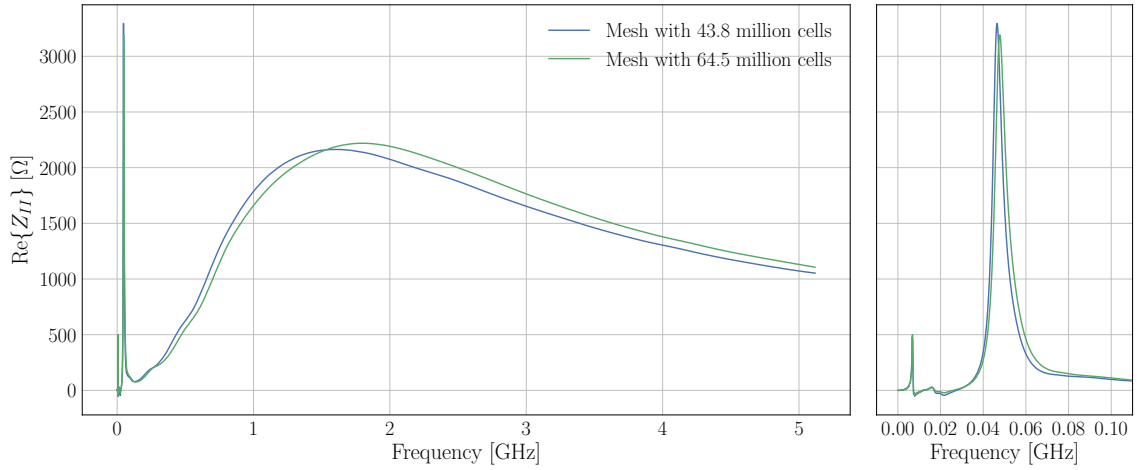
Figure A.4: Mesh convergence studies for the MKE-L with the 180 mm serigraphy installed. The results of simulations with different numbers of mesh cells are plotted. The serigraphy width is resolved by two mesh cells in the first case and by six mesh cells in the second case.

The numbers of mesh cells and computing times of the different simulations in this section are summarized in Tab. A.1. If not stated otherwise, all simulations were computed with the parameters of the final model presented in Sec. 3.3.

Table A.1: Influence of the discretisation mesh on the simulation time.

	MKE-L			
Length of serigraphy stripes	180 mm		200 mm	
Total number of mesh cells [in million]	64.5	43.8	44.1	57.5
Simulation time [in hours]	395	56.5	58.0	76.5
Resolution of ser. width	6 cells	2 cells	2 cells	2 cells

A.2 Further results

This section presents further results of MKE simulations and measurement executed within this thesis. A comparison of measurements and simulations of the MKE-L with the 180 mm serigraphy attached, is presented in Fig. A.5. Taking into account the effects of the LOG formula, the wire introduced for the measurements and the plates closing off the tank that accommodates the measured kicker as discussed in Sec. 3.3, the results are in very good agreement.

The transverse impedance of the MKE-S as it is installed in the SPS, with the 180 mm long serigraphy stripes, was also calculated and is presented in Fig. A.6.
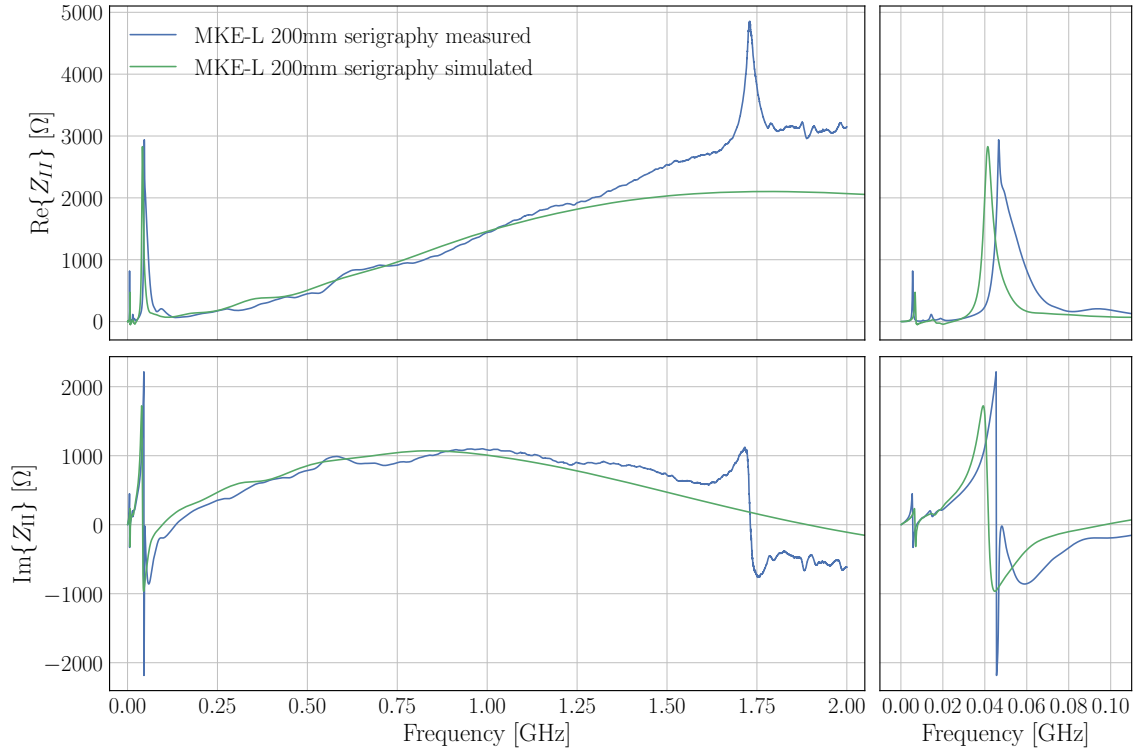
Figure A.5: MKE-L 200 mm serigraphy: Comparing impedance measurements to wakefield simulations of the model shown in Fig. 3.10. The impedance of the measurement has been calculated from the S-parameters by means of the LOG-formula.
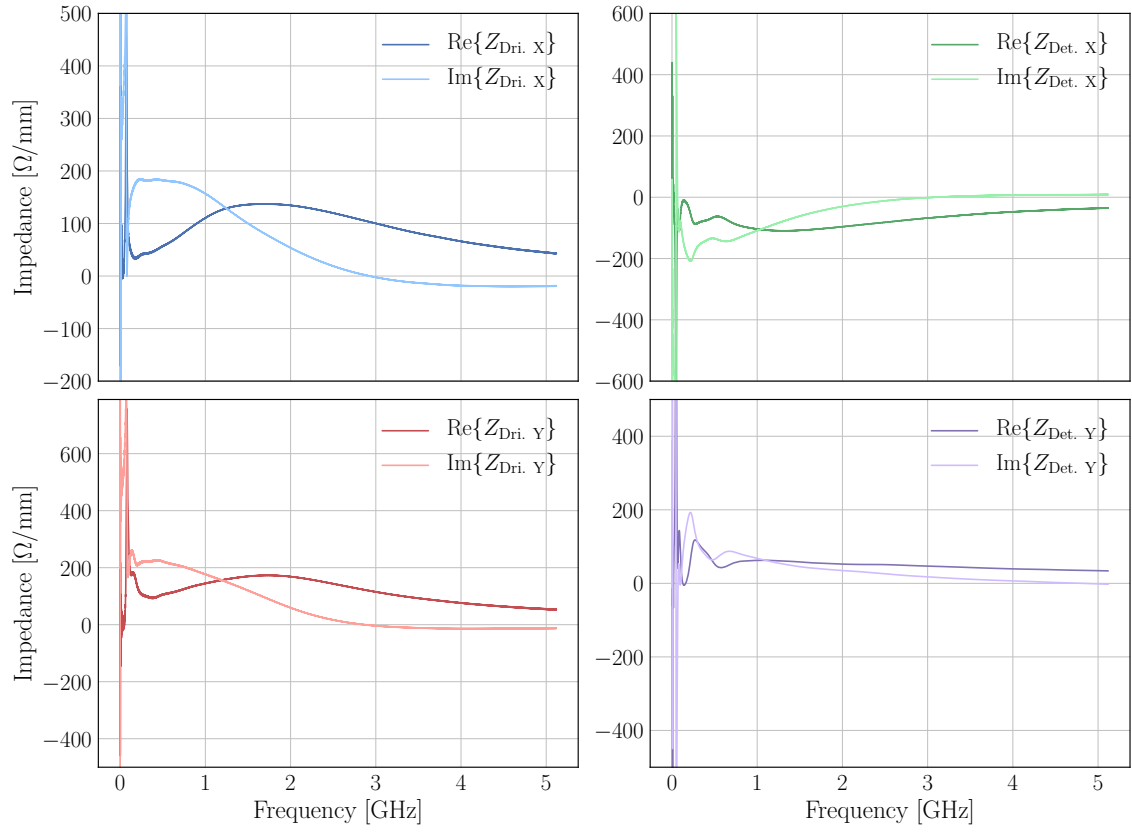
Figure A.6: The simulated complex transverse impedance, driving and detuning components, of the MKE-S with the 180 mm serigraphy.

B Versions of the wake model

This chapter presents and compares the different versions of the SPS wake model. Its post LS2 version for the different optics is shown in Fig. B.1.

The different versions of the wake model summarized in Tab. 4.2 are compared in Fig. B.2. The difference between the 2015 version, the legacy version, and the 2018 and post LS2 versions arises mainly from the fact that one MKE kicker magnet less is considered in the 2018 version. The different MKE models used for the simulations also have an additional influence. A visible difference between the curves of the 2018 and post LS2 models arises from the shielding (exclusion) of the flanges. The contribution of the ZS is negligible for the regarded wake length.
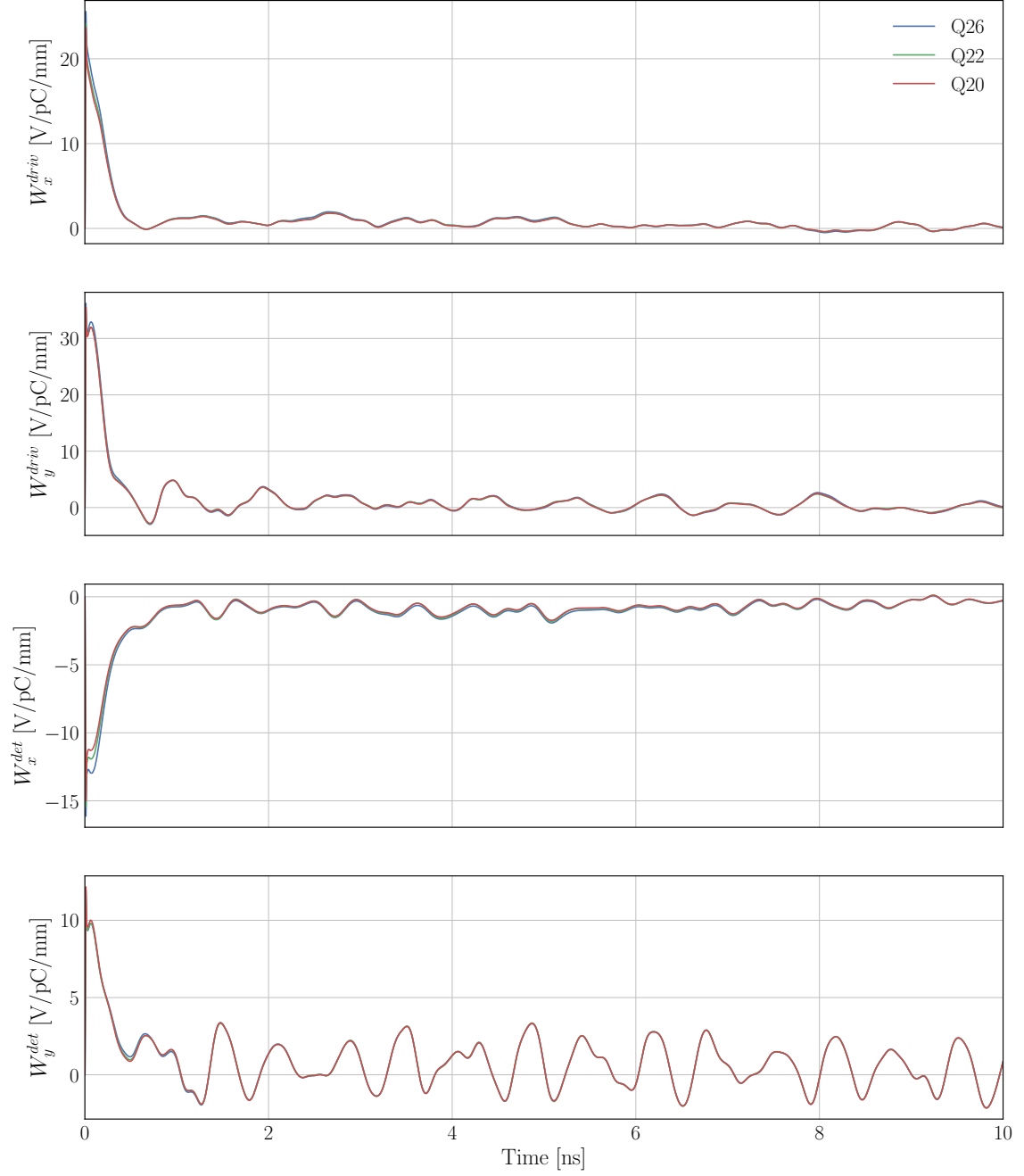
Figure B.1: The post LS2 version of the SPS wake model for the three different optics used in the SPS: Q20, Q22 and Q26.
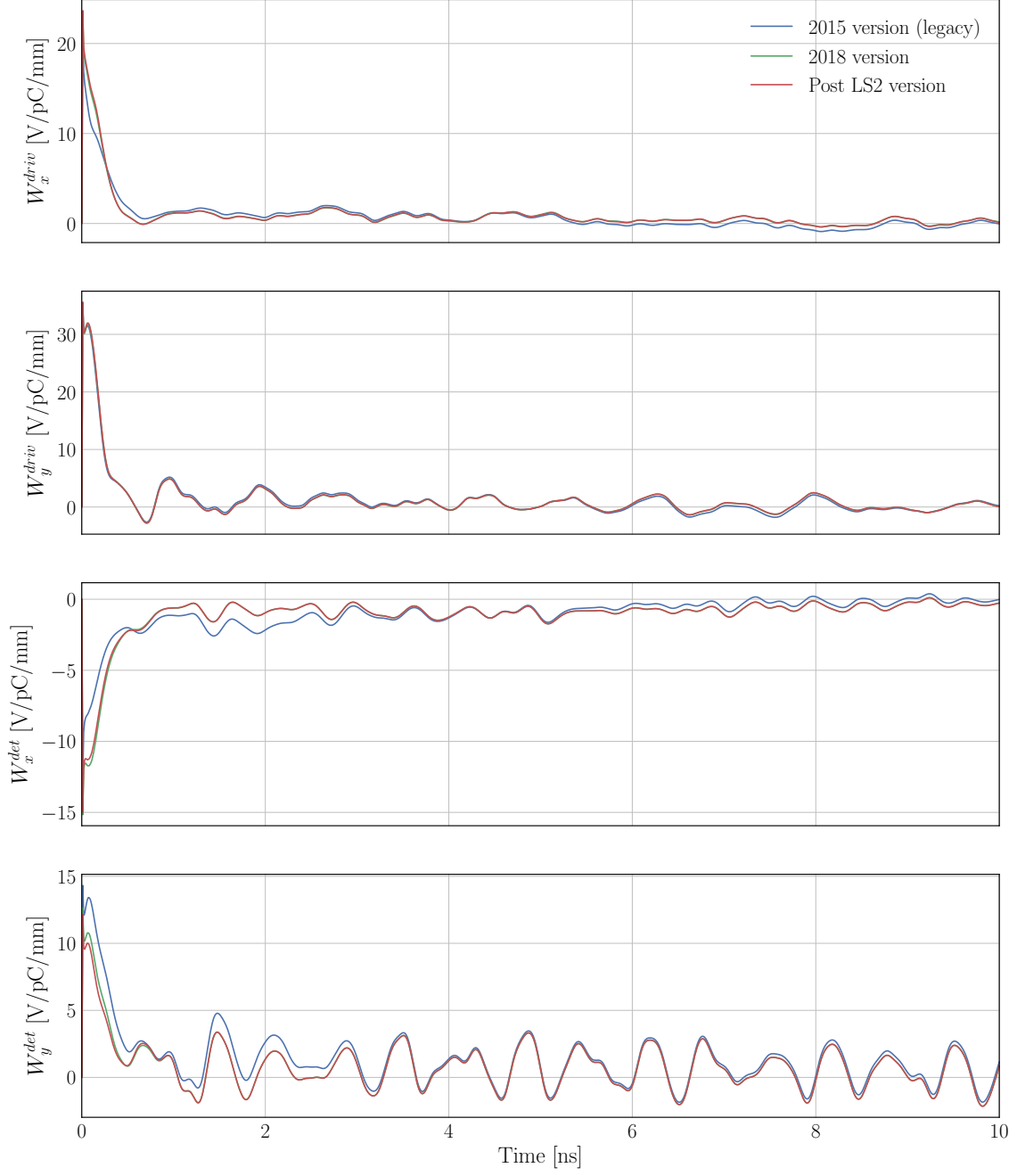
Figure B.2: Comparison of different versions of the SPS wake model for the Q20 optics.

C Technical drawings

This section contains technical drawings of the ZS. The list below gives an overview of the drawings attached on the following pages. Bold text identifies the drawing or figure numbers, respectively.

- The current interconnect.
  8035.3.563.0

- The interconnect without instrumentation (only racetrack beam pipe).
  SPSVMZS_0033

- The interconnect with one beam profile scanner (horizontal).
  SPSVMZS_0032

- The shield for one beam profile scanner (horizontal).
  SPSVMZS_0039

- The interconnect with one grid for transverse beam profile measurements.
  SPSVMZS_0007

- The shield for one grid for one shot transverse beam profile measurements.
  SPSVMZS_0037

- The interconnect with two beam profile scanners (horizontal and vertical).
  SPSVMZS_0035

- The shield for two beam profile scanners (horizontal and vertical).
  SPSVMZS_0038

- The tank shield.
  SPS8032051072

- Three Figures of the tank.
  Front view **Fig. C.1** cut A-A **Fig. C.2** cut B-B **Fig. C.3**.

Vue suivant Coupe A.A

Coupe B.B

Vue suivant D

Beam

Beam

⊕ → Axes de visée LABO ALIGN.

Poids approximatif de l'ensemble: 325 daN

Dimensions: ~370, 165, 436, ~720, 646, 909, 430, 215, 340, Ø214, 528, 470, ~1418, ~200

Repères: 16-22, 36, 35, 17.23, 15-21, 4, 1, 2, 7, 5, 33, 31, 6, 27.28.29, 12.20, 3, 32, 34, 16-22

		Nb	Désignation		
45					
44					
43					
42					
41					
40					
39					
38					
37		1	Vanne entrée d'air	VVAM	LEYBOLD
36		1	Jauge déclench. HP		LEYBOLD
35		1	Jauge vide PIRANI	VGS0	BALZERS
34		1	Jauge vide PENNING	VGHA	8095.5098.2
33		1	Tê spécial p/Jauges	VGHB	8032.3.534.3
32		1	Transition p/Jauges		s/ens
31					s/ens
30	200		Rondelle plate M8	inox A4.90	47.78.15.008.1
29				inox A4.90	47.43.78.108.0
28	140		Ecrou M8		47.62.83.124.0
27	140		Vis HM 8×60		
26				Amico	18.60.55.432.0
25		2	Joint NW40	Amico	18.60.55.410.0
24		2	Joint NW16	VSA	8095.0171.4
23		1	Joint AL Ø77	Cuivre	18.60.55.965.0
22		1	Joint UHV Ø17³,3		
21					
20		1	Couvercle UHV OD150	VCA	LEYBOLD n°83506
19					
18		2	Connex.ⁿᵉ rapide NW40		
17		2	Connex.ⁿᵉ rapide NW16		
16		2	Connex.ⁿᵉ rapide OD70		
15					Special BT.5E 8032.3.554.2
14					
13					
12		2	Pompe Ionique 400 l/s	VIPSB	8095-6028-1
11		1	Sublimateur UHV 8"	VIPTC.2	8032.11.611.0
10		1	Support module pompage		s/ens
9		1	Miresₑₛ alignement	type II	8032.11.697.2
8		1	Cadre de maintien	type II	8032.3.519.1
7		1	Résistance RF	Al₂O₃	Gr ME.VA
6		1	Module type II	VEBY	8032.3.501.1

Réf. Pl. d'ens. 8032.1.501.0/511.0

Mass = 25.66kg

UNLESS OTHERWISE MENTIONED, APPLICABLE ISO GPS STANDARDS
ARE THOSE PRIOR TO 2010-08-01 REGARDLESS OF THE DRAWING DATE

QUA	DESCRIPTION	MAT.	OBSERVATIONS	POS
2	MIDDLE TANK CHAMBER SUPPORT	EN 1.4306 (St. Steel 304L)	SPSVMZS_0034 ST0735046	6
2	STIFFENER + PIVOT	EN 1.4306 (St. Steel 304L)	SPSVMZS_0008 ST0730508	5
2	INTERCON. SHORT RACETRACK SHAPE	EN 1.4306 CERN	SPSVMZS_0042 ST0725789	4
2	PROFILE OBLONG COURT INTERCON.	ENG 7R07R7 (304L)	ST0725789	4
2	INTERCON. RACETRACK SHAPE CHAMBER	EN 1.4306 CERN	SPSVMZS_0043 ST0725786	3
2	PROFILE OBLONG CHAMBRE INTERCON.	ENG 7R07R7 (304L)	ST0725786	3
2	ZS INTERCONNECTION BELLOW+COLLAR		SPSVBZS_0001 ST0725100	2
2	SOUFFLET+COLLET INTERCONNEXION ZS		ST0725100	2
2	RACETRACK OPENED CON FLANGE Ø286	EN 1.4306 CERN	SPSVCZS_0008 ST0724583	1
2	BRIDE CONIQUE Ø286 OUVERTE OBLON	ENG 7R044 (304L)	ST0724583	1

ZS interconnections
ZS INTERCONNECTIONS
INTERCONNECTION CHAMBER
INTERCONNEXIONS ZS
CHAMBRE INTERCONNEXION

ISO 2768-mK

Ra 1.6

ISO 13715

		DESIGN	D.RUCK	2017-03-08
		CONTROLLED	B.RIFFAUD	2017-03-28
		RELEASED	B.BALHAN	2017-03-30
		APPROVED		

SCALE 1:2

REF. CERN

S.ENS/S.ASS

ENS/ASS

DAO Document Number ST0725780_02

REPLACES

SPSVMZS_0033

SIZE 1 / IND.

REF: CERN

REPLACES

RELEASED BY
PROJECT ENGINEER FOR PRODUCTION

EUROPEAN ORGANIZATION FOR NUCLEAR RESEARCH
ORGANISATION EUROPÉENNE POUR
LA RECHERCHE NUCLÉAIRE
GENÈVE

DESSIN RUGOSITÉ TOLÉRANCES
SELON NORMES ISO
DRAWING RUGOSITY TOLERANCES
ACCORDING TO ISO STANDARDS

AFTER WELDING

A-A
1:1

D
5:1 (2x)

C
5:1 (4x)

(219)
(09)
0.5 A B
0.2 AFTER WELDING

(2x)84
(2x)95.2
((2x)101.7
(2x)(66)
(192.6)
(4)
(15)
(15)
125

0.4 B A
0.1 CZ
0.4 B A

B-B (2x)
In every sleeved areas
Dans toutes les zones emmanchées

A-A

C (2x) 2:1

SANS REPRISE

AFTER WELDING

spots weld

Mass = 31.008kg

POS	DESCRIPTION	QUA	MAT.	REF. CERN	OBSERVATIONS
11	ECRAN BBSV21638 SCREEN	1	EN 1.4306	CERN SPSVMZS_0039	BBSV21638 ST0831743
10	SUPPORT MIRES / TARGET SUPPORT	1	EN8 79067 304L	ST0831743	
9	MP AND BI CHAMBER PART 3 / PARTIE 3 CHAMBRE MP ET BI	1	(St. Steel 304L)	CERN SPSVMZS_045	ST0739364
8	CHAMBER SUPPORT LEG / PATTE SUPPORT CHAMBRE	2	EN 1.4306	CERN SPSVMZS_0045	ST0734574
7	STIFFENER + PIVOT / RENFORT + PIVOT	2	(St. Steel 304L)	CERN SPSVMZS_0009	ST0732397
6	MP AND BI CHAMBER PART 2 / PARTIE 2 CHAMBRE MP ET BI	1	EN 1.4306	SPSVMZS_0008	ST0730508
5	MT AND BI ROUND PIPE / TUBE ROND MT ET BI	1	Stainless Steel	SPSVMZS_0041	ST0727826
4	UNV CF FIXED FLANGE / UNV CF BRIDE FIXE Ø202-159x2	1	Stainless Steel	ST0727736	
3	CONICAL FLANGE / BRIDE CONIQUE Ø206-TUBE Ø159/156	2	EN 1.4429 CERN 30F	STDVFUHV0242	ST0447415
2	ZS INTERCONNECTION BELLOW+COLLAR / SOUFFLET+COLLET INTERCONNEXION ZS	2	EN8 79075 (316LN)	STDVFCONG082	ST0660771
1	RACETRACK OPENED CON FLANGE Ø266 / BRIDE CONIQUE Ø266 OUVERTE OBLON	1	EN8 79094 304L	SPSVBZS_0001	ST0725100
			EN 1.4306 CERN SPSVCZS_0008	ST0724583	

1:2

96.75

(501)

5
5
5
5

66.75
82.75
82.75
8
3

218.8

1.5

0.2

59.8

218.8

14

(2x) R15

30

193.5

Mass = 0.666kg

UNLESS OTHERWISE MENTIONED, APPLICABLE ISO GPS STANDARDS
ARE THOSE PRIOR TO 2010-08-01 REGARDLESS OF THE DRAWING DATE

ISO 13715 $-0.5 \atop -0.5$

√ Ra 3.2

ISO 2768-mK

ZS interconnections

| QUA | | POS | MAT. | OBSERVATIONS | REF.CERN |

1 EN 1.4306 CERN
1 EENS 700767 (304L)

DESCRIPTION

ENS/ASS

S.ENS/S.ASS

ZS INTERCONNECTIONS
BBSV21638 SCREEN
INTERCONNEXIONS ZS
ECRAN BBSV21638

CAD Document Number: ST0831743_02

REPLACES

SCALE 1:1
R. RICOL 2017-02-23

SPSVMZS_0039

SIZE 2 B

- GMC

IND.	DATE	NOM/NAME	ZONE	MODIFICATION
B	2017-04-27	R. RICOL		4 strips removal for manufacturing
A	2017-03-30	R. RICOL		Strips shape modification for strenght
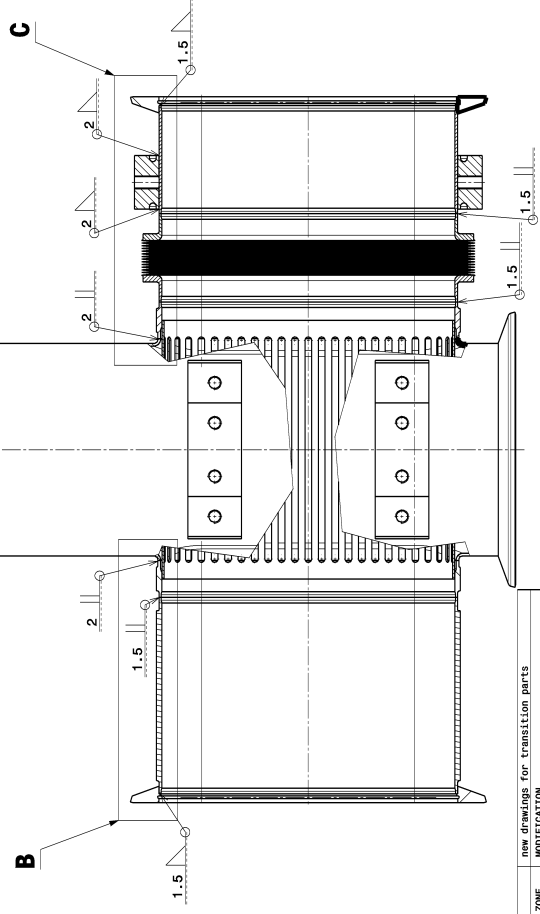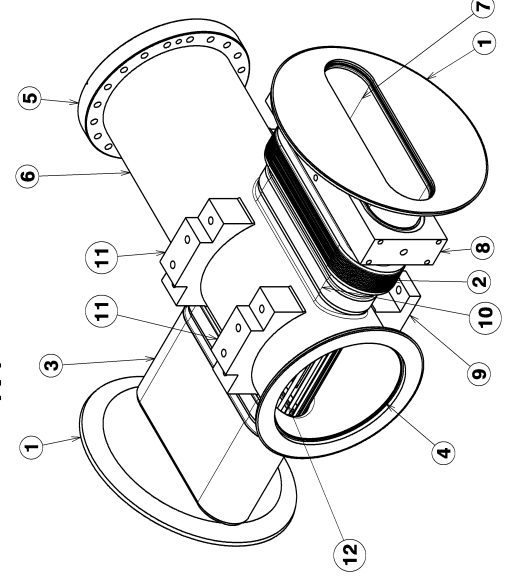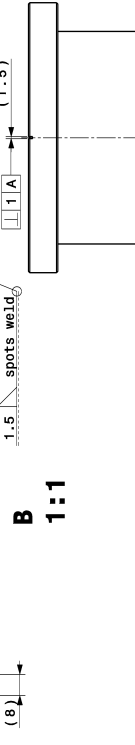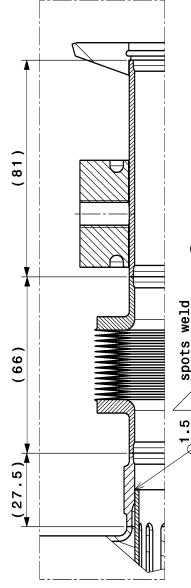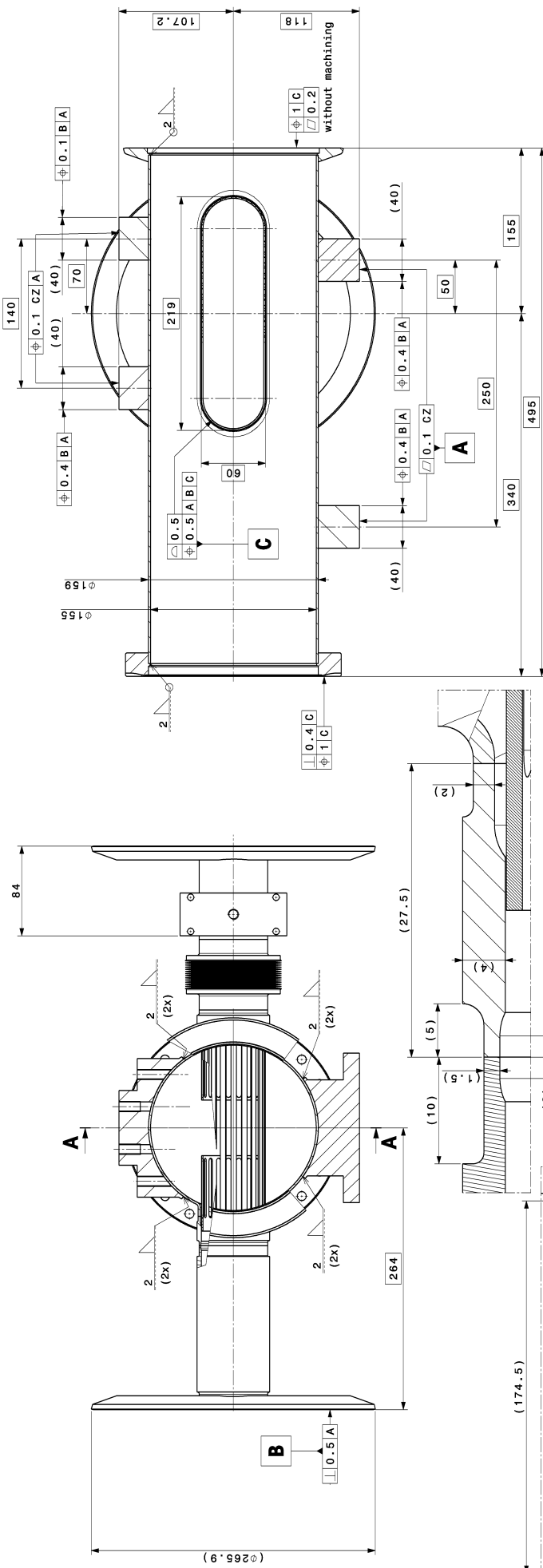
Mass= 27.819kg

UNLESS OTHERWISE MENTIONED, APPLICABLE ISO GPS STANDARDS
ARE THOSE PRIOR TO 2010-08-01 REGARDLESS OF THE DRAWING DATE

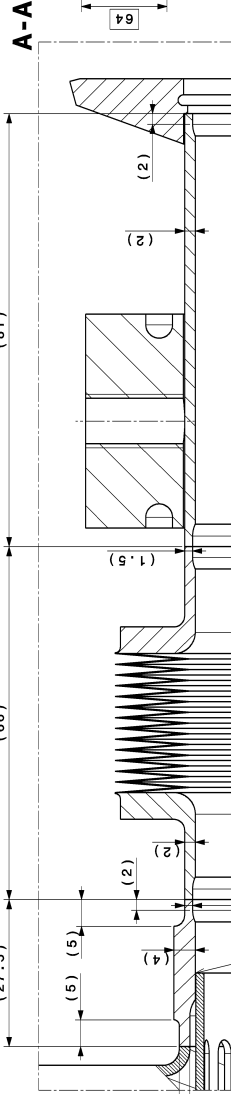|	POS	DESCRIPTION	MAT.	OBSERVATIONS
1	12	BSGH21632 SCREEN	EN 1.4306 CERN	SPSVMZS_0037
1		ECRAN BSGH21632	EDMS 790767 (304L)	ST0753763
2	11	TARGET SUPPORT	EN 1.4306	SPSVMZS_0010
		SUPPORT MIRES	(St. Steel 304L)	ST0739384
1	10	MP AND BI CHAMBER PART 3	EN 1.4306 CERN	SPSVMZS_0045
1		PARTIE 3 CHAMBRE MP ET BI	EDMS 790767 (304L)	ST0734574
1	9	CHAMBER SUPPORT LEG	EN 1.4306	SPSVMZS_0009
		PATTE SUPPORT CHAMBRE	(St. Steel 304L)	ST0732397
1	8	STIFFENER + PIVOT	EN 1.4306	SPSVMZS_0008
		RENFORT + PIVOT	(St. Steel 304L)	ST0730508
1	7	MP AND BI CHAMBER PART 2	Stainless Steel	SPSVMZS_0041
		PARTIE 2 CHAMBRE MP ET BI		ST0727826
1	6	MT AND BI ROUND PIPE	Stainless Steel	ST0727736
		TUBE ROND MT ET BI		
1	5	UNV CF FIXED FLANGE Ø202-159x2	EN 1.4429 CERN 3DF	STDVFUHVO242
		UNV CF BRIDE FIXE Ø202-159x2	EDMS 790075 (316LN)	ST0447415
1	4	CONICAL FLANGE Ø206-TUBE Ø159/156	EN 1.4306 CERN	STDVFCONO082
		BRIDE CONIQUE Ø206-TUBE Ø159/156	EDMS 790944 (304L)	ST0560771
1	3	MP AND BI CHAMBER PART 1	EN 1.4306 CERN	SPSVMZS_0044
		PARTIE 1 CHAMBRE MP ET BI	EDMS 790767 (304L)	ST0727694
2	2	ZS INTERCONNECTION BELLOW+COLLAR		SPSVBZS_0001
		SOUFFLET+COLLET INTERCONNEXION ZS		ST0725100
1	1	RACETRACK OPENED CON FLANGE Ø286	EN 1.4306 CERN	SPSVCZS_0008
		BRIDE CONIQUE Ø286 OUVERTE OBLON	EDMS 790944 (304L)	ST0724583
QUA.				

ISO 2768-mK   /Ra 3.2

ISO 13715   -0.3   +0.3
             -0.3   +0.3

S.ENS/S.ASS
ENS/ASS

DESIGN	R.RICOL	2017-02-23
CONTROLLED	B.RIFFAUD	2017-03-28
RELEASED	B.BALHAN	2017-03-30
APPROVED		

DAO Document Number   ST0727609_02
REPLACES

REF.CERN

SCALE   1:2

ZS interconnections
ZS INTERCONNECTIONS
MP AND BI UPSTREAM CHAMBER
INTERCONNEXIONS ZS
CHAMBRE MP ET BI AMONT

RELEASED BY   FOR
PROJECT ENGINEER   PRODUCTION   -

SIZE
SPSVMZS_0007   1   A

A-A

C
1:1

D
5:1

B
1:1

107.2
118
without machining

140   (40)   (40)   70
0.1 CZ A
0.4 B A
0.1 B A

219
Ø159
Ø155
155
250
50
(40)
495
340
(40)

60
C
A

0.5 A B C
0.5 A B C
0.1 CZ

0.4 C
1 C

0.4 B A
0.4 B A
0.1 CZ

(81)
(66)
(27.5)
spots weld
1.5

84
264
(174.5)
(27.5)
(2)
(4)
(5)
(10)
(1.5)
(2)
(2)
(Ø265.9)
(8)
spots weld
1.5
(4)

1 A
0.5 A

1.5
1.5
1.5
2
2

DRAWING RUGOSITY, TOLERANCES
ACCORDING TO ISO STANDARDS
DESSIN RUGOSITE, TOLERANCES
SELON NORMES ISO

PROJECTION

IND.	DATE	NOM/NAME	ZONE	MODIFICATION
A	2017-06-07	R.RICOL		new drawings for transition parts

1:2
Developped lenght

(501)

96.75

5
5
5
5
5

207

21.95

55.75

82.75

82.75

12.5
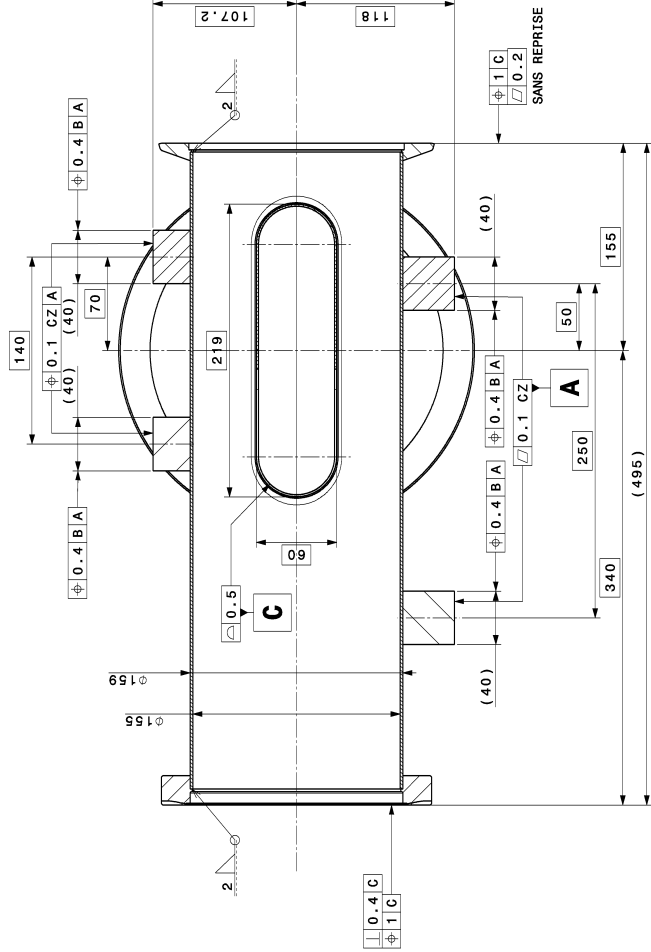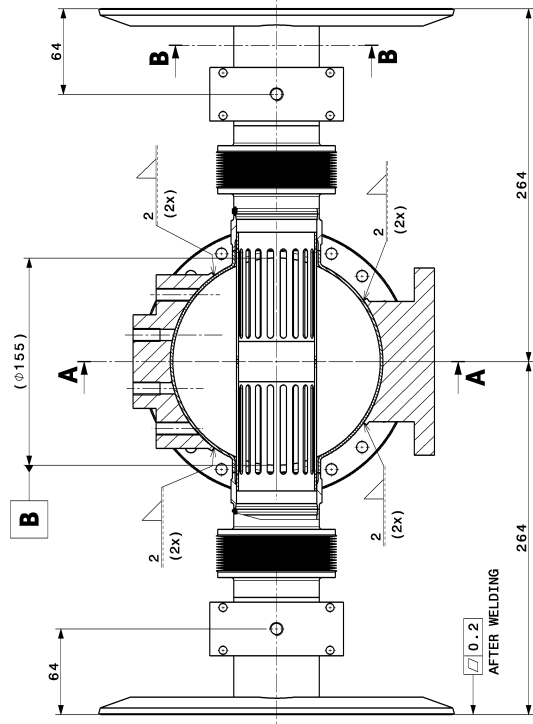
8

3

218.8

1.5

0.4

59.8

218.8

22

(4x) R5

193.5

70.75

52

Mass = 0.639kg

UNLESS OTHERWISE MENTIONED, APPLICABLE ISO GPS STANDARDS
ARE THOSE PRIOR TO 2010-08-01 REGARDLESS OF THE DRAWING DATE

ISO 2768-mK

√ Ra 3.2

ISO 13715 -0.5 -0.5 $+0.5$

ZS interconnections

| QUA | DESCRIPTION | POS | MAT. | OBSERVATIONS | REF.CERN |

ENS/ASS

EN 1.4306 CERN

ENS 700767 (304L)

S.ENS/S.ASS

ZS INTERCONNECTIONS
BSGH21632 SCREEN
INTERCONNEXIONS ZS
ECRAN BSGH21632

SCALE 1:1

DRAWN R. RICOL 2017-02-23
CONTROLLED
RELEASED
APPROVED
CAD Document Number: ST07763763_02
REPLACES

SPSVMZS_0037

SIZE 2 B

NON VALABLE POUR EXECUTION
NOT VALID FOR EXECUTION

IND.	DATE	NOM/NAME	ZONE	MODIFICATION
B	2017-04-27	R. RICOL		4 strips removal for manufacturing
A	2017-03-30	R. RICOL		Strips shape modification for strenght

Mass = 29.988kg

D 1:1

C-C

A

B-B

A 2:1

Spot welded

Without machining

POS	QUA	DESCRIPTION		MAT.		
13	1	BBSV21691 AND BBSH21691 SCREEN	ECRAN BBSV21691 ET BBSH21691	EN 1.4306 CERN	SPSVMZS_0038	ST0802369
12	2	TARGET SUPPORT	SUPPORT MIRES	EN6 79076 (304L)	SPSVMZS_0010	ST0738364
11	2	MP AND BI CHAMBER PART 3	PARTIE 3 CHAMBRE MP ET BI	EN 1.4306 CERN	SPSVMZS_0045	ST0734574
10	2	MP AND BI CHAMBER SPOOL PIECE	MANCHETTE CHAMBRE MP ET BI	(St. Steel 316LN)	ST0733984	
9	2	CHAMBER SUPPORT LEG	PATTE SUPPORT CHAMBRE	EN 1.4429	SPSVMZS_0009	ST0732397
8	1	STIFFENER + PIVOT	RENFORT + PIVOT	EN 1.4306	SPSVMZS_0008	ST0730508
7	1	MP AND BI CHAMBER PART 2	PARTIE 2 CHAMBRE MP ET BI	Stainless Steel	SPSVMZS_0041	ST0727826
6	1	DOWNSTREAM MP AND BI PIPE	TUBE ROND MP ET BI AVAL	Stainless Steel	ST0733983	
5	1	UNV CF FIXED FLANGE Ø202-159x2	UNV CF BRIDE FIXE Ø202-159x2	EN 1.4429 CERN 3DF	STDVFUHV0242	ST0447415
4	1	CONICAL FLANGE Ø206-TUBE Ø159/156	BRIDE CONIQUE Ø206-TUBE Ø159/156	EN6 79076 (316LN)	STDVFCONCO082	ST0560771
3	1	MP AND BI CHAMBER PART 1	PARTIE 1 CHAMBRE MP ET BI	EN6 79044 (304L)	SPSVMZS_0044	ST0727694
2	1	ZS INTERCONNECTION BELLOW+COLLAR	SOUFFLET+COLLET INTERCONNEXION ZS	EN 1.4306 CERN	SPSVBZS_0001	ST0725100
1	1	RACETRACK OPENED CON FLANGE Ø266	BRIDE CONIQUE Ø266 OUVERTE OBLON	EN6 79044 (304L)	SPSVCZS_0008	ST0724583
POS		DESCRIPTION		MAT.	OBSERVATIONS	

ISO 2768-mK
ISO 13715

SCALE 1:2

PROJECT ENGINEER

FOR EXECUTION

1:2

96.75

(501)

(6x) R5

5
5

4

61.75

82.75

82.75

3

218.8

1.5

59.8

0.2

96.75

40

10

R15

55

40

15

30

20

193.5

Thickness from 1mm to 1.5mm
MODIFICATION

A 2017-04-24 R. RICOL
IND. DATE NOM/NAME ZONE

A-A 1:1

B 2:1

C 3:1

253.5

112

Mass : 0.82kg

QUA	DESCRIPTION	POS	MAT.		OBSERVATIONS
4	HEXAGON NUT M4 FOR UHV FLANGE ECROU HEXAGONAL M4 PR BRIDE UHV	7	St. Steel M-100		ST0396361
4	PLAIN WASHER 4X9 UHV FLANGES RONDELLE PLATE 4X9 BRIDES UHV	6	St. Steel M-100		ST0431798
6	Ion TRAP TABLET	5	Ceramic A1203 97-98%		SPS8032051280 ST0373901
2	Brace Clamp Clamp Entretoise	4	EN 1.4306		SPS8032050894
1	Sheet 4 Sym Welding Soudage Tole 4 Sym	3	(St. Steel 304L)		ST0895017 SPS8032050899
1	Sheet 4 Welding Soudage Tole 4	2			SPS8032050898 ST0900127
1	Sheets 1 Welding Soudage Toles 1	1			ST0900124 SPS8032050896 ST0894675

ISO 2768-mK

√Ra 3.2

ISO 13715 ±0.3 / -0.30 / +0.3

ZS

ENS/ASS S.ENS/S.ASS

ZS RF SCREEN
ASSEMBLY
ZS ECRAN RF
ENSEMBLE

SCALE 1:1

REF.CERN

47.43.78
104.8
OLD 47.7
108.5

DRAWN (E) Dessolis 2017-10-19
CONTROLLED
RELEASED
APPROVED
CAD Document Number: ST0900143_02
REPLACES

NON VALABLE POUR EXECUTION
NOT VALID FOR EXECUTION

DAC - No. SPS8032051072 SIZE 2 IND. A

A | 2017-10-30 | A. PROST | Modification SPS8032050896
IND. | DATE | NOM/NAME | MODIFICATION
ZONE

Figure C.1: Front view of the ZS tank.

Figure C.2: Cut A-A of the ZS tank in Fig. C.1.

Figure C.3: Cut B-B of the ZS tank in Fig. C.1.

D List of publications and presentations

This list contains the publications and presentations during the course of this PhD thesis related to its subject.

- **Publications:**
  - M.J. Barnes, A. Adraktas, M. Beck, G. Bregliozzi, H. Day, L. Ducimetière, J. Ferreira, B. Goddard, T. Kramer, C. Pasquino, G. Rumolo, B. Salvant, L. Sermeus, J. Uythoven, L. Vega Cid, F.M Velotti, W. Weterings, C. Zannini, "Studies of impedance-related improvements of the SPS injection kicker system", Proceedings of the 7th International Particle Accelerator Conference (IPAC2016) 8-13 May 2016. Busan, Korea.
  - M.J Barnes, M. Beck, H. Day, L. Ducimetière, E. Garcia-Tabares, B. Goddard, H. Neupert, A. Romano, L. Vega Cid, W. Weterings, C. Zannini, "Upgrading the SPS fast extraction kicker systems for HL-LHC", Proceedings of the 8th International Particle Accelerator Conference (IPAC2017) 14-19 May. 2017. Copenhagen, Denmark.
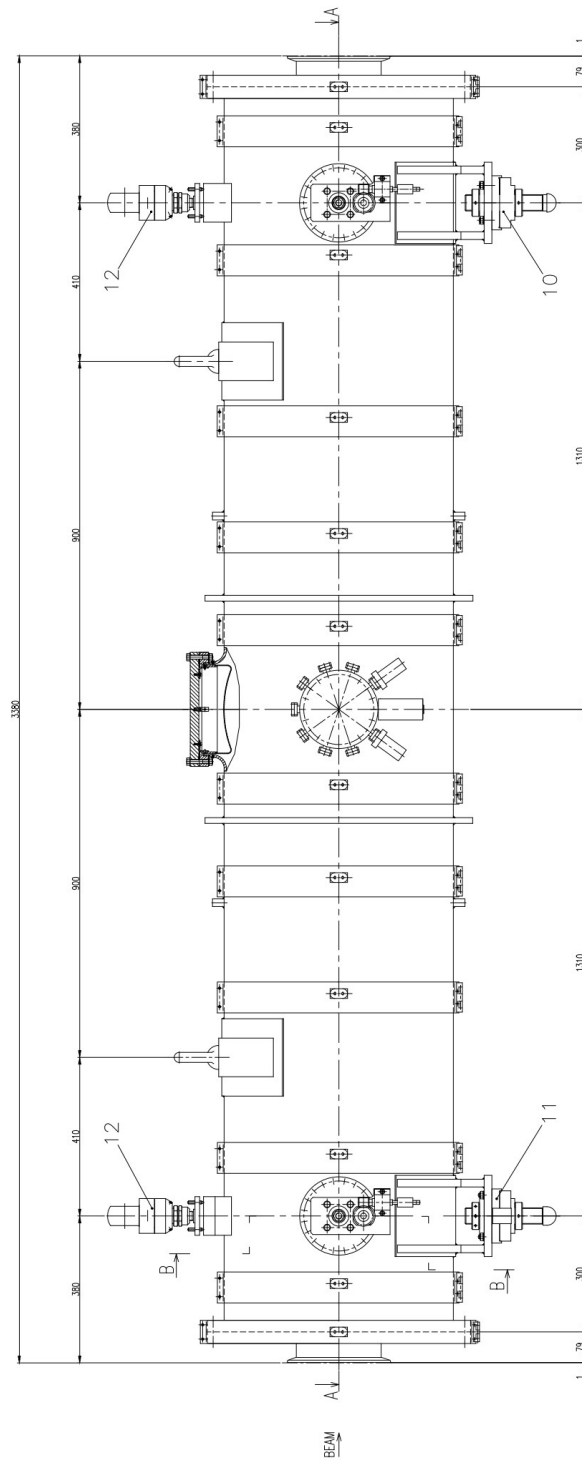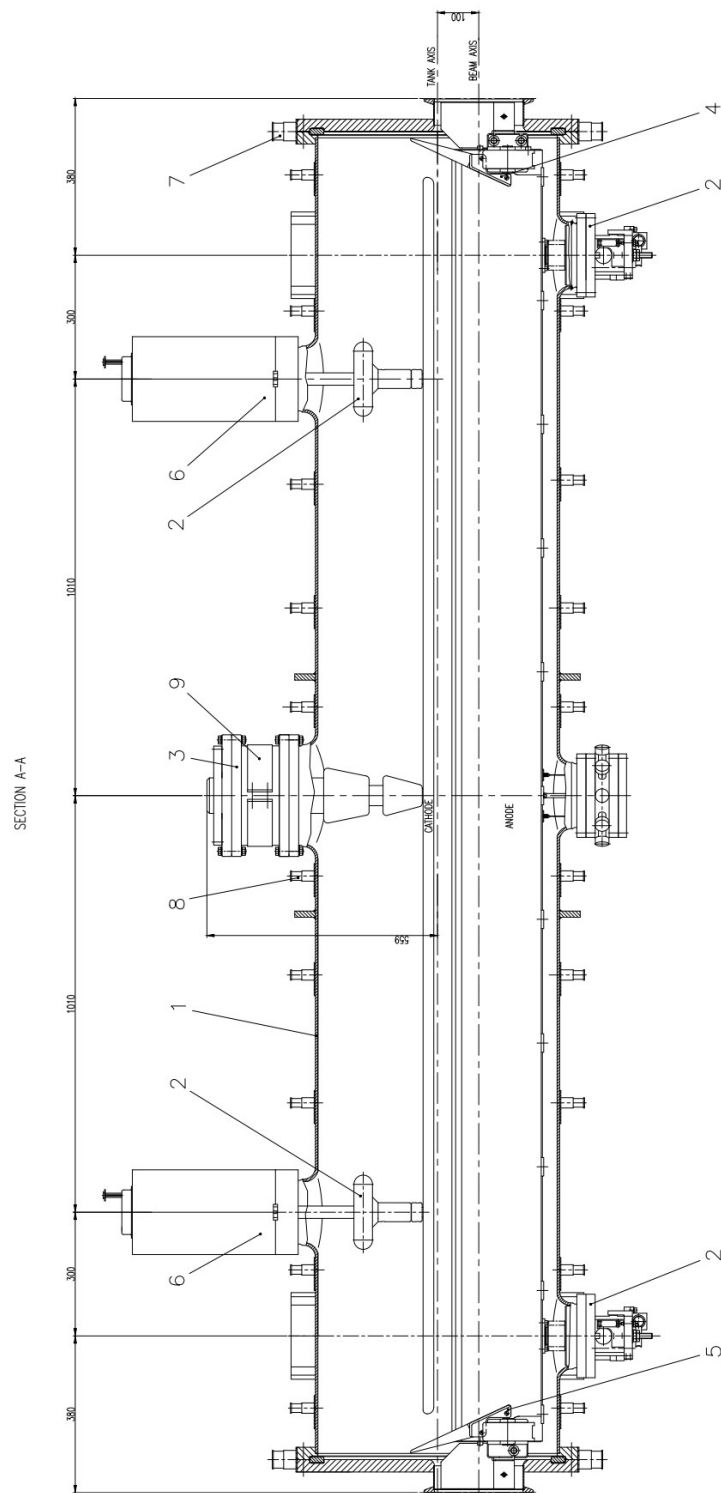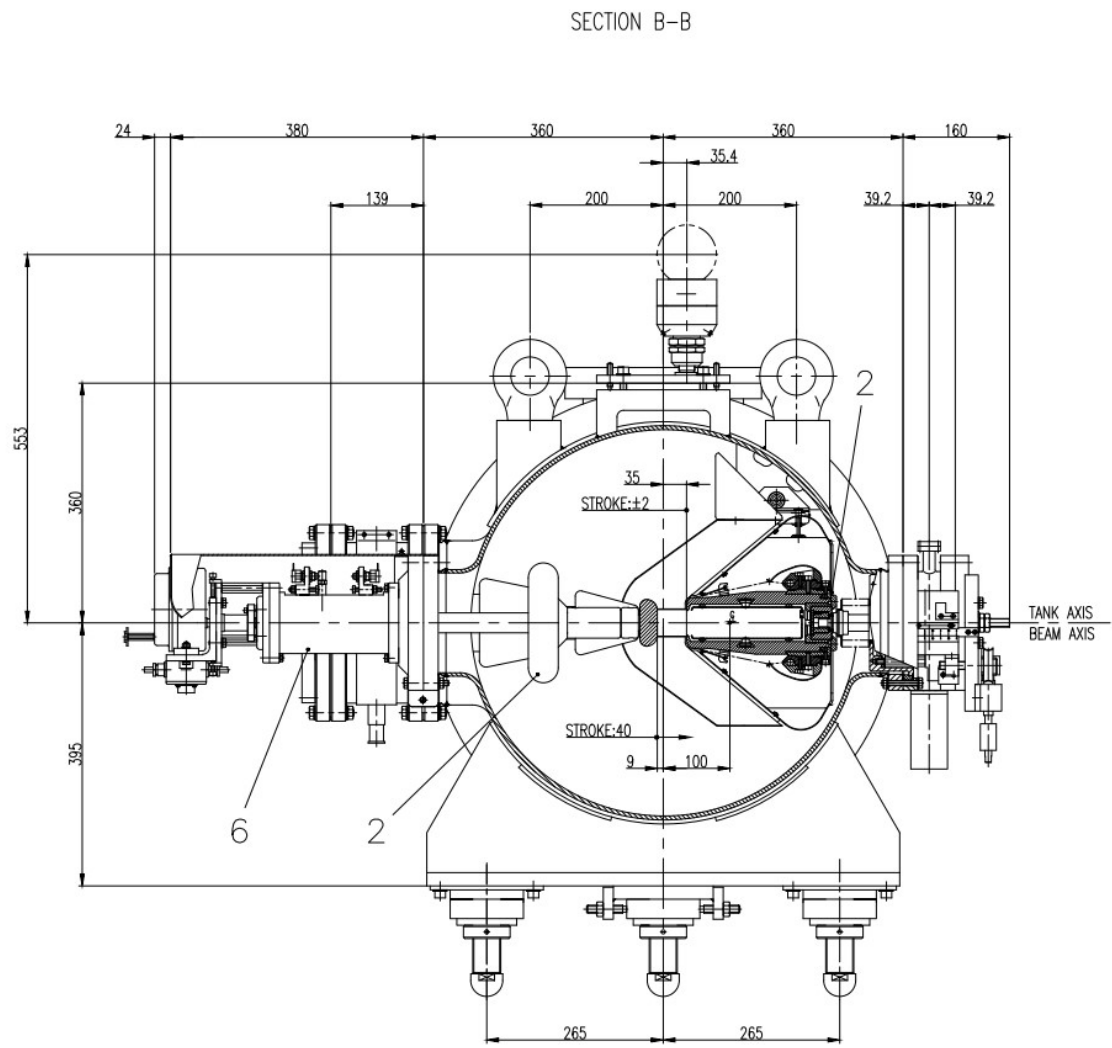 - M. Beck, H. Bartosik, M. Carlà, K.S.B. Li, U. van Rienen, G. Rumolo, M. Schenk, "Studies of horizontal instabilities in the CERN SPS", Proceedings of the 9th International Particle Accelerator Conference (IPAC2018) 29 Apr-4 May 2018. Vancouver, Canada.
  - M. Carlà, H. Bartosik, M. Beck, K.S.B. Li, M. Schenk, "Studies of a new optics with intermediate transition energy as alternative for high intensity LHC beams in the CERN SPS", Proceedings of the 9th International Particle Accelerator Conference (IPAC2018) 29 Apr-4 May 2018. Vancouver, Canada.
  - M. Beck, H. Bartosik, M. Carlà, K.S.B. Li, U. van Rienen, G. Rumolo, M. Schenk, "Studies of transverse instabilities in the CERN SPS", Proceedings of the 61st ICFA Advanced Beam Dynamics Workshop on High-Intensity and High-Brightness Hadron Beams (HB2018) 17-22 Jun 2018. Daejeon, Korea.
  - A. Farricker, M. Beck, J. Repond, C. Vollinger, "Effect of the extraction kickers on the beam stability in the CERN SPS", Proceedings of the 61st ICFA Advanced Beam Dynamics Workshop on High-Intensity and High-Brightness Hadron Beams (HB2018) 17-22 Jun 2018. Daejeon, Korea.

- K.S.B. Li, H. Bartosik, M. Beck, E.R. Bjørsvik, W. Höfle, G. Kotzian, T.E. Levens, M. Schenk, "Recent results from the wideband feedback system tests at the SPS and future plans", Proceedings of the 61st ICFA Advanced Beam Dynamics Workshop on High-Intensity and High-Brightness Hadron Beams (HB2018) 17-22 Jun 2018. Daejeon, Korea.

- **Selected presentations:**

  - "Simulation, measurement and reduction of the beam induced power loss in the SPS injection kickers", CST European User Conference in Strasbourg, France from 26-27 April 2016.

  - "Impedance of the SPS accelerator", Workshop on Advances in Electromagnetic Research in Hirschegg, Austria from 3-9 September 2016.

  - "Impedance reduction techniques", IFCA Mini-workshop on Impedance and Beam Instability in Particle Accelerators in Benevento, Italy from 18-22 September 2017.

  - "Beam coupling impedance reduction campaign in the SPS", Workshop of the Chair of Electromagnetic Field Theory in Binz, Germany from 4-6 October 2017.

Bibliography

[ABAB+17] G. Apollinari, I. Béjar Alonso, O. Brüning, P. Fessia, M. Lamont, L. Rossi, and L. Tavian. *High-Luminosity Large Hadron Collider (HL-LHC): Technical Design Report V. 0.1.* CERN Yellow Reports. CERN, Geneva, 2017.

[ABC+04] G. Arduini, T. Bohl, F. Caspers, E.H. Gaxiola, T. Kroyer, M. Timmins, L. Vos, and J. Uythoven. Beam induced heating of the SPS fast pulsed magnets. *Proceedings of the 9th European Particle Accelerator Conference (EPAC2004) 5-9 Jul 2004. Lucere, Switzerland*, 2004.

[ABD17] A. Adraktas, M.J. Barnes, and L. Ducimetière. Influence of conducting serigraphy upon field pulse shape of the SPS extraction kicker systems. *Proceedings of the 8th International Particle Accelerator Conference (IPAC2017) 14-19 May 2017. Copenhagen, Denmark*, 2017.

[ANS] ANSYS. HFFS®. https://www.ansys.com/products/electronics/ansys-hfss.

[ASV15] T. Argyropoulos, E. Shaposhnikova, and J.E. Varela. Other means to increase the SPS 25ns performance - longitudinal plane. *Proceedings of the Chamonix 2014 Workshop on LHC Performance 22-25 Sep 2014. Chamonix, France*, 2015.

[BAB+15] H. Bartosik, G. Arduini, A. Blas, C. Bracco, T. Bohl, K. Cornelis, H. Damerau, S. Gilardoni, S. Hancock, B. Goddard, W. Höfle, G. Iadarola, M. Meddahi, E. Métral, G. Papotti, Y. Papaphilippou, G. Rumolo, E. Shaposhnikova, B. Salvant, G. Sterbini, F.M. Velotti, and C. Zannini. Other means to increase the SPS 25ns performance - transverse plane. *Proceedings of the Chamonix 2014 Workshop on LHC Performance 22-25 Sep 2014. Chamonix, France*, 2015.

[Bar] H. Bartosik. Private communication. 2018.

[Bar13] H. Bartosik. *Beam dynamics and optics studies for the LHC injectors upgrade.* PhD thesis, Technische Universität Wien, Vienna, Oct 2013. Presented 13 Nov 2013.

[BBBR16] B. Balhan, R.A. Barlow, J. Borburgh, and G. Raffaele. Improvement of the CERN SPS electrostatic septa ion traps. *Proceedings of the 27th International Symposium on Discharges and Electrical Insulation in Vacuum (ISDEIV2016) 18-23 Sep 2016. Suzhou, China*, 2016.

[BBC+18a] M. Beck, H. Bartosik, M. Carlà, K.S.B. Li, U. van Rienen, G. Rumolo, and M. Schenk. Studies of horizontal instabilities in the CERN SPS. *Proceedings of the 9th International Particle Accelerator Conference (IPAC2018) 29 Apr-4 May 2018. Vancouver, Canada*, 2018.

[BBC+18b] M. Beck, H. Bartosik, M. Carlà, K.S.B. Li, U. van Rienen, G. Rumolo, and M. Schenk. Studies of transverse instabilities in the CERN SPS. *Proceedings of the 61st ICFA Advanced Beam Dynamics Workshop on High-Intensity and High-Brightness Hadron Beams (HB2018) 17-22 Jun 2018. Daejeon, Korea*, 2018.

[BBD+17] M.J. Barnes, M. Beck, H. Day, L. Ducimetière, E. Garcia-Tabares, B. Goddard, H. Neupert, A. Romano, L. Vega Cid, W. Weterings, and C. Zannini. Upgrading the SPS fast extraction kicker systems for HL-LHC. *Proceedings of the 8th International Particle Accelerator Conference (IPAC2017) 14-19 May 2017. Copenhagen, Denmark*, 2017.

[BCC+09] M.J. Barnes, F. Caspers, K. Cornelis, L. Ducimetière, E. Mahner, G. Papotti, G. Rumolo, V. Senaj, and E. Shaposhnikova. Measurement and analysis of SPS kicker magnet heating and outgassing with different bunch spacing. *Proceedings of the 29th Particle Accelerator Conference (PAC2009) 4-9 May 2009. Vancouver, Canada*, 2009.

[BCK+09] M.J. Barnes, F. Caspers, T. Kroyer, E. Métral, F. Roncarolo, and B. Salvant. Measurement of the longitudinal and transverse impedance of kicker magnets using the coaxial wire method. *Proceedings of the 29th Particle Accelerator Conference (PAC2009) 4-9 May 2009. Vancouver, Canada*, 2009.

[BCM+04] M. Benedikt, P. Collier, V. Mertens, J. Poole, and K. Schindl. *LHC Design Report*. CERN Yellow Reports. CERN, Geneva, 2004.

[BDF+10] M.J. Barnes, L. Ducimetière, T. Fowler, V. Senaj, and L. Sermeus. Injection and extraction magnets: Kicker magnets. *Proceedings of the CERN Accelerator School (CAS): Specialised course on magnets 2009. Bruges, Belgium*, 2010.

[Bec15] M. Beck. Simulation, measurement and mitigation of the beam induced power loss in the SPS injection kickers. Master's thesis, Karlsruhe Institut of Technology, Karlsruhe, Sep 2015. Presented 23 Sep 2015.

[BFA+12] M.J. Barnes, T. Fowler, M.G. Atanasov, T. Kramer, and T. Stadlbauer. Effect of a metallized chamber upon the field response of a kicker magnet: Simulations results and analytical calculations. *Proceedings of the 3rd International Particle Accelerator Conference (IPAC2012) 20-25 May 2012. New Orleans, USA*, 2012.

[BIP+14] H. Bartosik, G. Iadarola, Y. Papaphilippou, G. Rumolo, B. Salvant, and C. Zannini. TMCI thresholds for LHC single bunches in the CERN SPS and comparison with simulations. *Proceedings of the 5th International Particle Accelerator Conference (IPAC2014) 16-20 Jun 2014. Dresden, Germany*, 2014.

[BLM+16] N. Biancacci, K.S.B Li, E. Métral, N. Mounet, and B. Salvant. The HL-LHC impedance model and aspects of beam stability. *Proceedings of the 7th International Particle Accelerator Conference (IPAC2016) 8-13 May 2016. Busan, Korea*, 2016.

[Bra09] E. Bravin. Transverse beam profiles. *Proceedings of the CERN Accelerator School (CAS): Specialised course on beam diagnostics, 2008. Dourdan, France*, 2009.

[BS98] R. Bartolini and F. Schmidt. A computer code for frequency analysis of non-linear betatron motion. Technical Report SL-Note-98-017-AP, CERN, Geneva, Feb 1998.

[BSZ16] N. Biancacci, B. Salvant, and C. Zannini. Building the impedance model of a real machine. *ICFA Beam Dynamics Newsletter*, (No. 69), December 2016.

[BW96] M.J. Barnes and G.D. Wait. Comparison of measured and predicted inductance per cell for a travelling wave kicker magnet. *Proceedings of the 5th European Particle Accelerator Conference (EPAC1996) 10-14 Jun 1996. Sitges, Spain*, 1996.

[CBB+18] M. Carlà, H. Bartosik, M. Beck, K.S.B. Li, and M. Schenk. Studies of a new optics with intermediate transition energy as alternative for high intensity LHC beams in the CERN SPS. *Proceedings of the 9th International Particle Accelerator Conference (IPAC2018) 29 Apr-4 May 2018. Vancouver, Canada*, 2018.

[CBC+18] A. Chmielinska, M.J. Barnes, F. Caspers, B.K. Popovic, and C. Vollinger. Measurements of electromagnetic properties of ferrites as a function of frequency and temperature. *Proceedings of the 9th International Particle Accelerator Conference (IPAC2018) 29 Apr-4 May 2018. Vancouver, Canada*, 2018.

[CERa] CERN. BLonD - Beam Longitudinal Dynamics. http://blond.web.cern.ch.

[CERb] CERN. MAD - Methodical Accelerator Design. http://mad.web.cern.ch.

[CERc] CERN. PyHEADTAIL. https://github.com/PyCOMPLETE.

[CER72] CERN. *The 300 GeV programme.* Number CERN-1050-E. CERN, Geneva, 1972.

[CGD⁺00] F. Caspers, C. González, M. Dyachkov, E. Shaposhnikova, and H. Tsutsui. Impedance measurement of the SPS MKE kicker by means of the coaxial wire method. Technical Report CERN-PS-RF-NOTE-2000-04, CERN, Geneva, Feb 2000.

[Cha93] A.W. Chao. *Physics of Collective Beam Instabilities in High Energy Accelerators.* Wiley Series in Beam Physics and Accelerator Technology. Wiley, 1993.

[CMS01] F. Caspers, A. Mostacci, and B. Spataro. On trapped modes in the LHC recombination chambers: experimental results. Technical Report LHC-PROJECT-NOTE-266, CERN, Geneva, Aug 2001.

[CMT00] F. Caspers, A. Mostacci, and H. Tsutsui. Impedance evaluation of the SPS MKE kicker with transition pieces between tank and kicker module. Technical Report CERN-SL-2000-071-AP, CERN, Geneva, Oct 2000.

[CMTZ13] A.W. Chao, K.H. Mess, M. Tigner, and F. Zimmermann. *Handbook of accelerator physics and engineering; 2nd ed.* World Scientific, Singapore, 2013.

[CST] CST. CST STUDIO SUITE®. https://www.cst.com.

[DBC⁺11] H. Day, M.J. Barnes, F. Caspers, E. Metral, B. Salvant, C. Zannini, and R. Jones. Coaxial wire measurements of ferrite kicker magnets. *Proceedings of the 2nd International Particle Accelerator Conference (IPAC2011) 4-9 Sep 2011. San Sebastian, Spain*, 2011.

[Den09] J.C. Denard. Beam current monitors. *Proceedings of the CERN Accelerator School (CAS): Specialised course on beam diagnostics, 2008. Dourdan, France*, 2009.

[DFG⁺14] H. Damerau, A. Funken, R. Garoby, S. Gilardoni, B. Goddard, K. Hanke, A. Lombardi, D. Manglunki, M. Meddahi, B. Mikulec, G. Rumolo, E. Shaposhnikova, M. Vretenar, and J. Coupard. LHC

Injectors Upgrade, Technical Design Report, Vol. I: Protons. Technical Report CERN-ACC-2014-0337, Dec 2014.

[Duc05] L. Ducimetière. Advances of transmission line kicker magnets. *Proceedings of the 25th Particle Accelerator Conference (PAC2005) 16-20 May 2005. Knoxville, USA*, 2005.

[FBRV18] A. Farricker, M. Beck, J. Repond, and C. Vollinger. Effect of the extraction kickers on the beam stability in the CERN SPS. *Proceedings of the 61st ICFA Advanced Beam Dynamics Workshop on High-Intensity and High-Brightness Hadron Beams (HB2018) 17-22 Jun 2018. Daejeon, Korea*, 2018.

[Fer08] Ferroxcube. *8C11 material specification*, September 2008.

[FFH⁺76] P.E. Faugeras, E. Frick, C.G. Harrison, H. Kühn, V. Rödel, G. Schröder, and J.P. Zanasco. The SPS fast pulsed magnet systems. Technical Report CERN-SPS-BT-76-1, CERN, Geneva, Mar 1976.

[FHS73] P.E. Faugeras, C.G. Harrison, and G.H. Schröder. Design study of the SPS beam dumping system. Technical Report CERN-OPEN-2013-015, CERN, Geneva, Jul 1973.

[FKL09] P. Forck, P. Kowina, and D. Liakin. Beam position monitors. *Proceedings of the CERN Accelerator School (CAS): Specialised course on beam diagnostics, 2008. Dourdan, France*, 2009.

[GCD⁺06] E. Gaxiola, F. Caspers, L. Ducimetière, P. Faure, T. Kroyer, B. Versolatto, and G. Vossenberg. The SPS fast extraction kicker system in LSS6. *Proceedings of the 10th European Particle Accelerator Conference (EPAC2006) 5-9 Jul 2006. Edinburgh, UK*, 2006.

[HBC⁺18] C. Hessler, W. Bartmann, E. Carlier, L.Ducimetière, B. Goddard, and F.M. Velotti. Beam simulation studies for the upgrade of the SPS beam dumping system. *Proceedings of the 9th International Particle Accelerator Conference (IPAC2018) 29 Apr-4 May 2018. Vancouver, Canada*, 2018.

[HDD⁺14] K. Hanke, H. Damerau, A. Deleu, A. Funken, R. Garoby, S.S. Gilardoni, N. Gilbert, B. Goddard, E.B. Holzer, A.M. Lombardi, D. Manglunki, M. Meddahi, B. Mikulec, E. Shaposhnikova, and M. Vretenar. Status of the LIU project at CERN. *Proceedings of the 5th International Particle Accelerator Conference (IPAC2014) 16-20 Jun 2014. Dresden, Germany*, 2014.

[Her11] Heraeus. *C 1075 SD (LPA 411-076) - REACH compliant silver conductor paste*, November 2011.

[Hin08] F. Hinterberger. *Physik der Teilchenbeschleuniger und Ionenoptik : mit durchgerechneten Beispielen und 105 Übungsaufgaben mit vollständigen Lösungen.* Springer, Berlin, 2. Aufl. edition, 2008.

[HM06] W. Herr and B. Muratori. Concept of luminosity. *Proceedings of the CERN Accelerator School (CAS): Intermediate course on accelerator physics, 2003. Zeuthen, Germany*, 2006.

[HWZ98] S. Heifets, A. Wagner, and B. Zotter. Generalized impedances and wakes in asymmetric structures, Jan 1998.

[Jen00] E. Jensen. An improved LOG-formula for homogeneously distributed impedance. Technical Report CERN-PS-RF-NOTE-2000-001, CERN, Geneva, Jan 2000.

[KCG07] T. Kroyer, F. Caspers, and E. Gaxiola. Longitudinal and transverse wire measurements for the evaluation of impedance reduction measures on the MKE extraction kickers. Technical Report CERN-AB-Note-2007-028, CERN, Geneva, Jul 2007.

[KCV17] T. Kaltenbacher, F. Caspers, and C. Vollinger. Machine element contribution to the longitudinal impedance model of the CERN SPS. *Proceedings of the 57th ICFA Advanced Beam Dynamics Workshop on High-Intensity and High-Brightness Hadron Beams (HB2017) 3-8 Jul 2017. Malmö, Sweden*, 2017.

[KV17] T. Kaltenbacher and C. Vollinger. Characterization of shielding for the CERN-SPS vacuum flanges with respect to beam coupling impedance. *Proceedings of the 8th International Particle Accelerator Conference (IPAC2017) 14-19 May 2017. Copenhagen, Denmark*, 2017.

[Lee12] S.Y. Lee. *Accelerator physics; 3rd ed.* World Scientific, Singapore, 2012.

[Li17] K.S.B Li. Numerical methods I and II. *Proceedings of the CERN Accelerator School (CAS): Specialised course on intensity limitations in particle beams, 2015. Geneva, Switzerland*, 2017.

[LLL16] T. Levens, K. Lasocha, and T. Lefèvre. Recent developments for instability monitoring at the LHC. *Proceedings of the 5th International Beam Instrumentation Conference (IBIC2016) 11-15 Sep 2016. Barcelona, Spain*, 2016.

[LS17]   A. Lasheen and E. Shaposhnikova.   Evaluation of the CERN Super Proton Synchrotron longitudinal impedance from measurements of the quadrupole frequency shift. *Physical Review Accelerators and Beams*, Vol. 20, 2017.

[MAA+18] E. Métral, D. Amorim, G. Arduini, H. Bartosik, E. Benedetto, H. Burkhardt, K.S.B. Li, A. Oeftiger, D. Quatraro, G. Rumolo, B. Salvant, and C. Zannini.   Space charge and transverse instabilities at the CERN SPS and LHC. *Proceedings of the 13th International Computational Accelerator Physics Conference (ICAP2018) 20-24 Oct 2018. Key West, USA*, 2018.

[MAB+08] E. Métral, G. Arduini, T. Bohl, H. Burkhardt, R. Calaga, F. Caspers, H. Damerau, T. Kroyer, H. Medina, G. Rumolo, B. Salvant, M. Schokker, E. Shaposhnikova, B. Spataro, and J. Tückmantel. CERN SPS impedance in 2007.   *Proceedings of the 11th European Particle Accelerator Conference (EPAC2008) 23-27 Jun 2008. Genoa, Italy*, 2008.

[MLGL92] H.H. Meinke, K. Lange, F.W. Gundlach, and K.H. Löcherer. *Taschenbuch der Hochfrequenztechnik: Band 1: Grundlagen*. Taschenbuch der Hochfrequenztechnik. Springer, 1992.

[Mos16]   A. Mostacci. Beam coupling impedance and wakefield - bench measurements. *ICFA Beam Dynamics Newsletter*, (No. 69), December 2016.

[Ng06]   K.Y. Ng.   *Physics of intensity dependent beam instabilities*.   World Scientific, Hoboken, NJ, 2006.

[NG16]   U. Niedermaiyer and E. Gjonaj.   Wake field and beam coupling impedance simulations. *ICFA Beam Dynamics Newsletter*, (No. 69), December 2016.

[Per15]   S. Persichelli.   *The beam coupling impedance model of CERN Proton Synchrotron*. PhD thesis, Universitá di Roma La Sapienza, Rome, Feb 2015. Presented 25 Feb 2015.

[Poz12]   D.M. Pozar. *Microwave engineering*. Wiley, Hoboken, NJ, 4th edition, 2012.

[RSV05]   G. Rumolo, E. Shaposhnikova, and V.G. Vaccaro. Simulations of the fast transverse instability in the SPS.   Technical Report CERN-AB-2005-088, CERN, Geneva, Dec 2005.

[Rum14]   G. Rumolo. Beam instabilities. *Proceedings of the CERN Accelerator School (CAS): Advanced accelerator physics course, 2013. Trondheim, Norway*, 2014.

[RvR18]   F. Reimann and U. van Rienen. Wakefields - An overview. *Proceedings of the CERN Accelerator School (CAS): Specialised course on free electron lasers and energy recovery linacs, 2016. Hamburg, Germany*, 2018.

[RZ02]   G. Rumolo and F. Zimmermann. Practical user guide for HEADTAIL. Technical Report SL-Note-2002-036-AP, CERN, Geneva, Nov 2002.

[SAA⁺12] B. Salvant, O. Aberle, G. Arduini, R.W. Aßmann, V. Baglin, and M.J. Barnes et al. LHC impedance model: Experience with high intensity operation in the LHC. *Proceedings of the 52nd ICFA Advanced Beam Dynamics Workshop on High-Intensity and High-Brightness Hadron Beams (HB2012) 17-21 Sep 2012. Beijing, China*, 2012.

[Sal10]   B. Salvant. *Impedance model of the CERN SPS and aspects of LHC single-bunch stability.* PhD thesis, Ecole Polytechnique, Lausanne, Mar 2010. Presented 04 Mar 2010.

[SMZ⁺10] B. Salvant, N. Mounet, C. Zannini, E. Metral, and G. Rumolo. Quadrupolar transverse impedance of simple models of kickers. *Proceedings of the 1st International Particle Accelerator Conference (IPAC2010) 23-28 May 2010. Kyoto, Japan*, 2010.

[Stu01]   G.V. Stupakov. Wake and impedance. *Proceedings of the Joint US-CERN-Japan-Russia Accelerator School (JAS) on frontiers of accelerator technology: High quality beams, 2000. St. Petersburg and Moscow, Russia*, 2001.

[TBGU06] M. Timmins, A. Bertarelli, E. Gaxiola, and J. Uythoven. SPS extraction kicker magnet cooling design. Technical Report CERN-AB-Note-2004-005-BT, CERN, Geneva, 2006.

[TCV03]   H Tsutsui, Friedhelm Caspers, and L Vos. Calculation of MKE kicker heating. Technical Report AB-Note-2003-051-MD, CERN, Geneva, Jul 2003.

[Tsu00a] H Tsutsui. Longitudinal impedances of some simplified ferrite kicker magnet models. *Proceedings of the 7th European Particle Accelerator Conference (EPAC2000) 26-30 Jun 2000. Vienna, Austria*, 2000.

[Tsu00b] H. Tsutsui. Some simplified models of ferrite kicker magnet for calculation of longitudinal coupling impedance. Technical Report CERN-SL-2000-004-AP, CERN, Geneva, Jan 2000.

[TV00] H. Tsutsui and L. Vos. Transverse coupling impedance of a simplified ferrite kicker magnet model. Technical Report LHC-PROJECT-NOTE-234, CERN, Geneva, Sep 2000.

[TWK98] M.K.A. Thumm, W. Wiesbeck, and S. Kern. *Hochfrequenzmeßtechnik: Verfahren und Meßsysteme.* Teubner, Stuttgart, 2., durchges. aufl. edition, 1998.

[VAB+14] F.M. Velotti, O. Aberle, C. Bracco, E. Carlier, F. Cerutti, K. Cornelis, L. Ducimetiere, B. Goddard, V. Kain, R. Losito, C. Maglioni, M. Meddahi, F. Pasdeloup, V. Senaj, and G.E. Steele. Performance studies of the SPS beam dump system for HL-LHC beams. *Proceedings of the 5th International Particle Accelerator Conference (IPAC2014) 16-20 Jun 2014. Dresden, Germany*, 2014.

[VAB+15a] J.E Varela, T. Argyropoulos, T. Bohl, F. Caspers, J. Esteban, J. Ghini, A. Lasheen, D. Quartullo, B. Salvant, E. Shaposhnikova, and C. Zannini. An extended SPS longitudinal impedance model. *Proceedings of the 6th International Particle Accelerator Conference (IPAC2015) 3-8 May 2015. Richmond, USA*, 2015.

[VAB+15b] F.M Velotti, J.L. Abelleira, M. Barnes, C. Bracco, E. Carlier, F. Cerutti, K. Cornelis, R. Folch, B. Goddard, V. Kain, M. Meddahi, R. Morton, J. Osborne, F. Pasdeloup, V. Senaj, G. Steele, J. Uythoven, and H. Vincke. Feasibility study of a new SPS beam dump system. *Proceedings of the 6th International Particle Accelerator Conference (IPAC2015) 3-8 May 2015. Richmond, USA*, 2015.

[Wie15] H. Wiedemann. *Particle Accelerator Physics.* Graduate Texts in Physics Springer Link : Books. Springer, Cham, 4th edition, 2015.

[Wil89] P.B. Wilson. Introduction to wakefields and wake potentials. *Proceedings of the U.S. Particle Accelerator School (USPAS) 1987. Batavia, USA*, 1989.

[WW91] T. Weiland and R. Wanzenberg. Wake fields and impedances. *Proceedings of the US-CERN Joint International Accelerator School on frontiers of particle beams: Intensity limitations, 1990. Hilton Head, USA*, 1991.

[Zan13]   C. Zannini. *Electromagnetic simulation of CERN accelerator components and experimental applications.* PhD thesis, Ecole Polytechnique, Lausanne, Mar 2013. Presented 15 Apr 2013.

[ZLR12]   C. Zannini, K.S.B. Li, and G. Rumolo. Effects of an asymmetric chamber on the beam coupling impedance. *Proceedings of the 3rd International Particle Accelerator Conference (IPAC2012) 20-25 May 2012. New Orleans, USA*, 2012.

[ZMS+10] C. Zannini, N. Mounet, B. Salvant, E. Metral, and G. Rumolo. Electromagnetic simulations of simple models of ferrite loaded kickers. *Proceedings of the 1st International Particle Accelerator Conference (IPAC2010) 23-28 May 2010. Kyoto, Japan*, 2010.

[ZRV12]   C. Zannini, G. Rumolo, and V.G. Vaccaro. Effect of the TEM mode on the kicker impedance. *Proceedings of the 3rd International Particle Accelerator Conference (IPAC2012) 20-25 May 2012. New Orleans, USA*, 2012.

[ZVM+11] C. Zannini, V.G. Vaccaro, E. Metral, G. Rumolo, and B. Salvant. Electromagnetic modeling of C shape ferrite loaded kickers. *Proceedings of the 2nd International Particle Accelerator Conference (IPAC2011) 4-9 Sep 2011. San Sebastian, Spain*, 2011.

Selbstständigkeitserklärung

Hiermit erkläre ich, dass ich die vorliegende Dissertation mit dem Titel "Numerical and experimental studies to model and reduce the impedance in the CERN Super Proton Synchrotron (SPS)" selbstständig und ohne fremde Hilfe und nur unter Verwendung der von mir angegebenen Quellen und Hilfsmittel verfasst habe.

Genf,

Mario Beck

Mario Beck

Address:	Rue de la Servette 34	**Date of Birth:**	August 10th, 1988
	1202 Geneva	**Place of Birth:**	Stuttgart, Germany
	Switzerland		
E-mail:	mario-beck@outlook.de	**Phone:**	+49 162 4497027

Education

University of Rostock, Rostock, Germany   2015 - 2019
- Electrical engineering PhD student with the 'CERN doctoral student program' on numerical and experimental studies to model and reduce the beam impedance in the CERN Super Proton Synchrotron (SPS) particle accelerator
- Trainings: JUAS, Advanced CAS and Beam Instrumentation CAS

Karlsruhe Institute of Technology (KIT), Karlsruhe, Germany   2009 – 2015
- Bachelor and Master of Science in Electrical Engineering and Information Technology with focus on communications technology and high frequency technology
- Master's thesis with the 'CERN technical student program' on the simulation measurement and mitigation of the beam induced power loss in the SPS injection kickers

Technical High School, Esslingen Zell, Germany   1999 - 2008
- General qualification for university entrance (Abitur)
- Bilingual classes in English and German

Work Experience

CERN, Geneva, Switzerland – *Master and PhD student / R&D engineer*   March 2015 – May 2019
- Bench measurements and electromagnetic simulations of accelerator components in CST
- Beam dynamics measurements in the SPS; evaluation in Python and MATLAB
- Beam dynamics simulations in PyHEADTAIL
- In charge of maintaining and upgrading the transverse SPS impedance model
- Poster price winner of the International Particle Accelerator Conference (IPAC) 2018

CNES, Toulouse, France - *intern*   March – September 2014
- Centre National d'Etudes Spatiales antenna department: Development and evaluation of a software for the simulation of passive intermodulation products occurring on space borne reflector antennas

KIT, Karlsruhe, Germany - *student research assistant*   October 2011 – February 2014
- Institute for High Frequency Technology and Electronics (IHE): Designing a Radar baseband board on basis of a FPGA, comparing different methods of RF signal synthesis
- Communications Engineering Lab (CEL): Designing a Kalman filter for position estimation of a mobile user

Design of an electrical circuit, CW2, Fellbach, Germany - *engineer*   February – May 2013
- Design, construction and testing of an Uninterruptible Power Supply (UPS)

INDEX, Esslingen, Germany - *intern*   August 2009
- Introduction into circuit design, circuit production and soldering

Radio Operator, German Armed Forces   October 2008 – June 2009

Skills

Languages: German (native), English (fluent), French (fluent)
Computing: Python, CST, MATLAB, C++, Altium Designer, Eagle, Fortran90, PSpice